THE UNIVERSITY *of* EDINBURGH

Verification and Validation of a DEM-CFD Model and Multiscale Modelling of Cohesive Fluidization Regimes

by

Prashant Gupta

A dissertation submitted in partial fulfilment
for the degree of
Doctor of Philosophy

in the

Institute for Infrastructure and Environment
School of Engineering
UNIVERSITY OF EDINBURGH

2014

Declaration of Authorship

This thesis entitled, "*Verification and Validation of a DEM-CFD Model and Multiscale Modelling of Cohesive Fluidization Regimes*" is submitted to the University of Edinburgh for the degree of Doctor of Philosophy. The research work described and reported in this thesis has been completed solely by *Prashant Gupta* under the supervision of *Dr. Jin Sun* and *Prof. Jin Y. Ooi*. I confirm that:

- Where I have consulted the published work of others, this is always clearly attributed. Where I have quoted from the work of others, the source is given.
- I have acknowledged all main sources of help.
- Where the thesis is based on work done by myself jointly with others, I have made clear exactly what was done by others and what I have contributed myself.

Publications based on this thesis:

Gupta, P., Sun, J. & Ooi, J.Y. DEM-CFD simulation of a dense fluidized bed: wall roughness and particle size effects. *To be submitted for to Powder Technology, September 2014*

Gupta, P. & Sun, J. Microstructural analysis of stably expanded fluidization regimes. *In preparation*

Conference presentations based on this thesis:

Gupta, P., Sun, J. & Ooi, J.Y. Validation and Verification of an open source DEM-CFD code. *World Congress of Particle Technology 7, Beijing, China, May 2014*

Gupta, P., Sun, J. & Ooi, J.Y. Micro-structural analysis of homogeneous fluidization of Geldart A particles using DEM-CFD. *World Congress of Particle Technology 7, Beijing, China, May 2014*

Gupta, P., Sun, J. & Ooi, J.Y. Effect of hydrodynamic interactions on the segregation rate in bidisperse gas–solid fluidised bed and validation studies. *7th International Conference for Conveying and Handling of Particulate Solids– CHoPS, Friedrichshafen, Germany, September 2012*

Gupta, P., Sun, J. & Ooi, J.Y. Study of drag force models in simulation of bidisperse gas–solid fluidised beds using a CFD–DEM approach. *The 8th European Congress of Chemical Engineering, Berlin, Germany, September 2011*

Signed: _____

Date: _____

UNIVERSITY OF EDINBURGH

Abstract

Institute for Infrastructure and Environment
School of Engineering

Doctor of Philosophy

by Prashant Gupta

Fluidization of solid particles using gas flow is an important process in chemical and pharmaceutical industries. The dynamics of fluidisation are intricately related to particle scale physics. Fluid-particle interactions dominate gas-solid fluidization behaviour for particles with average size and density greater than 10^{-4} m and 10^3 kg/m^3, respectively, classified as Geldart B and D particles. Inter-particle forces, such as cohesion, play an increasingly important role in the fluidization dynamics of smaller particles, which are classified as Geldart A and C. In particular, interesting fluidization regimes have been noticed for weakly cohesive Geldart A particles, exhibiting a window of uniform fluidization before the onset of bubbling behaviour. Despite widespread industrial interests, the fundamental understanding of the mechanisms that underlie these fluidization regimes is poor. The present study aims to improve the understanding of fluidization dynamics of Geldart A regimes using numerical simulations.

A DEM-CFD model was employed to capture the widely separated spatial and temporal scales associated with fluidization behaviour. The model couples the locally averaged Navier-Stokes equation for fluid with a discrete description of the particles. The methodology and its computer implementation are verified and validated to assess the extent of fluidization physics that it is able to capture. Verification cases check the implementation of the inter-phase momentum transfer term, drag model implementation and pressure-velocity coupling. The test cases are employed in order to cover a wide range of flow conditions. Robust validation tests for complex fluidization phenomena such as bubbling, spouting and bidisperse beds have been conducted to assess the predictive capabilities of the DEM-CFD solver. The simulation results for time and spatially averaged fluidziation behaviour are compared to experimental measurements obtained from the literature, and are shown to have capture fluidization physics qualitatively. Robust features of bubbling fluidization, such as minimum fluidization velocity, frequency of pressure drop fluctuations, segregation rates and solid circulation patterns were captured. Furthermore, the DEM-CFD model is critically assessed in terms of model conceptualization and parameter estimation, including those for drag closures, particle-wall boundary conditions, bed height and particle shape effects. The validation studies establish modelling best-practice guidelines and the level of discrepancy against the analytical solutions or experimental measurements.

Having developed the model and established its predictive capability, it is used to probe the hydrodynamics of weakly cohesive particles. Cohesive interactions are captured by employing a pair-wise van der Waals force model. The cohesive strength of the granular bed is quantified by the ratio of the maximum van der Waals force to the particle gravitational force, defined as the granular Bond number. The Bond number of the bed is increased systematically from 0-10 to examine the role of cohesion in the fluidization

behaviour of fine powders while keeping the particle size and density constant across all the simulations. The idea was to segregate the hydrodynamics associated with size and density of the particles from the inter-particle interactions. The size and density of the particles are carefully chosen at a scale where inter-particle forces are present but minimal [Seville *et al.*, 2000]. The Geldart A fluidization behaviour is captured for granular beds with Bond numbers ranging from 1 to 3. Many robust features of Geldart A fluidization, such as pressure drop overshoot, delay in the onset of bubbling, macroscopic U_{mf} predictions and uniform bed expansion are captured in the DEM-CFD framework. The expanded bed was characterized according to criteria that the particles are highly immobile in this regime and the expanded porosity is related to inlet velocity by Richardson–Zaki correlations.

Sudden jumps in the magnitudes of global granular temperature were found near the regime transitions. This observation was used an indicator of the onset of bubbling and quantification of minimum bubbling velocity (U_{mb}). The window of the expanded bed regime (quantified as $U_{mb} - U_{mf}$) was shown to be an increasing function of cohesive strength of the bed. Furthermore, the stability of the expanded bed was probed by studying the response of the expanded bed to sudden inertial and voidage shocks. A kinematic wave, generated as a response to the voidage shock, was shown to slow down with increasing cohesion and decreasing hydrodynamic forces. Furthermore, predictions of U_{mb} by DEM-CFD simulations for weakly cohesive beds were compared against empirical correlations by Valverde [2013] with an excellent match. Stress analysis of the expanded bed revealed the presence of tensile stresses. As the inlet velocity is increased beyond the minimum fluidization velocity, a longitudinal shift of these negative stresses is observed until they reach the top of the bed. Negative stresses were seen at the bed surface at the onset of bubbling. The role of cohesion stresses in the formation of expanded bed and suppression of bubbling was highlighted.

Finally, the microstructure of the expanded bed was probed at different local micro and mescoscopic length scales. Evidence of clustering, agglomeration and cavities were presented in the expanded bed. Expanded bed expansion was shown to have meso-structural inhomogeneities present, which is contrary to the belief of homogeneous expansion.

Summary

Interactions between the three fundamental forms of matter (gas, liquid and solid) forms basis of many industrial processes. Often, solid industrial raw materials are subjected to flowing air. Many of these industrial processes are ill-designed or not optimized enough to make full use of resources making them cost and energy inefficient. This is due to a lack of fundamental understanding of the interaction between these phases. Fluidization is a process of subjecting a bed of grains to a stream of fluid in order to achieve good mixing and transfer of heat and mass. It is a well-established knowledge that the fluidization behaviour depends upon the properties of the granular. However, the link between the two is far from obvious and difficult to establish. Characterization experiments of these processes are expensive and often do not produce data that could be directly useful to design the process itself. In this thesis, simulations of fluidization processes are conducted to gain fundamental insights on how the interactions between the particles can manifest in different modes. Different fluidization processes are simulated and compared against experimental results. Specifically, weakly cohesive or sticky particles are subjected to gas inflow and it is studied that how the assembly of particles evolves. The main contribution of this thesis is verified, validated and predictive multiphase solver and a fundamental understanding towards the bulk behaviour of fluid-particle interactions.

Acknowledgements

This work has been carried out as a part of the PARDEM project, an EU-funded Framework 7 Marie Curie Initial Training Network. The financial support provided by the European Commission is gratefully acknowledged.

First and foremost, I would like to express sincere gratitude to my supervisor Dr. Jin Sun, whose guidance and support have been invaluable in this project. His constructive suggestions, criticisms, and the willingness to generously give time to the project and the thesis during the last four years are much appreciated and duly acknowledged. While his exceptional domain expertise was imperative in shaping me as a rigorous scientist, his perspective on life and rational thinking were inspirational in my quest to be a better human being as well. He is undoubtedly on the best role models to look up to.

I would like to thank my co-supervisor Professor Jin Ooi for his relentless and critical questioning that often defogged my understanding of the subject. I am deeply indebted to him for being very approachable and available (some times even without appointments). I have enjoyed a great deal working under both of my supervisors and a student could not have asked for more.

I would like to thank Dr Heng Xiao for his initial help and time with the open-source code, which I used in this thesis.

I would also like to thank Dr. Lothar tekamp and other colleagues at ITASCA consultants for great time at Gelsenkirchen, Germany during summers of 2012.

A very sincere thanks to the ETO, IIE and PARDEM administrative staff, who have helped me through painstaking VISA processes and worked so hard to just to keep me present in the UK. Without them, this thesis was a far-fetched dream. In particular, I sincerely acknowledge the immense support Ms Nicola McRobbie provided me with to navigate through the administrative corridors of PARDEM and for keeping me in high spirits; Joan Birse, who has been patiently tolerated my frequent requests to switch desks while turning a blind eyes towards all those cookies which I stole from her safety boxes in the kitchen. Compared to how calmly she handled the grave matters mentioned earlier, providing any and all administrative letters that I required must have been a walk in the park for her and I am thankful for her efforts; Liz Patterson from the graduate school office, who did everything in her capacity to bring me from Germany to UK within 3-4 months of my moving out!

I would like to mention Subhash Thakur for his great help when I first came to Edinburgh, Mohammedreza Ebrahimi and Pratap Kasina for such a great time at Jean Armour Avenue and cleaning the house of course!

Sincere thanks to J.P. Morrissey who always solved inevitable errors occurring when I was writing thesis using a deadly combination of LATEX with a mac. Also for proof reading the chapter with minimal amount of grump possible. Providing shelter at some times. Thanks mate.

Many thanks to Christopher Ness and Dhiraj Patil, for their help in proof reading some parts of thesis. Chris gave me an overview of thumb and controversial rules of English language.

I would also like to thank my colleagues in the PARDEM network and the University of Edinburgh in particular Jiaming Xu, Harry, Payam Khazaeinejad, Alvaro Janda and Carlos Labra for their helpful comments, suggestions and great friendship.

Finally, a very special thanks to my family in India for their continued support and inspiration. My mother has always helped me through and dark times. A mother is always special :).

In particular, I would like to mention my friends Eshan Agarwal, Vaibhav Vashisht, Prashant Gautam, Anubhai Bhargava, Shivam Agarwal and Aashna Agarwal who have been around in both sorrow and joy.

Contents

List of Figures

List of Tables

Abbreviations

ASME	**A**merican **S**ociety of **M**echanical **E**ngineering
CCN	**C**ohesion **C**oordination **N**umber
CFD	**C**omputational **F**luid **D**ynamics
CPB	**C**onstant **P**orosity **B**lock
CoV	**C**oefficient **o**f **V**ariance
DIA	**D**igital **I**mage **A**nalysis
DBM	**D**iscrete **B**ubble **M**ethod
DEM	**D**iscrete **E**lement **M**ethod
DPM	**D**iscrete **P**article **M**ethod
DWT	**D**iffusive **W**ave **S**pectroscopy
DNS	**D**irect **N**umerical **S**imulation
ECT	**E**lectrical **C**apacitance **T**omography
FFT	**F**ast **F**ourier **T**ransformation
LBM	**L**attice **B**oltzmann **M**ethod
MCN	**M**echanical **C**oordination **N**umber
MD	**M**olecular **D**ynamics
MRI	**M**agnetic **R**esonance **I**maging
PEPT	**P**ositron **E**mission **P**article **T**racking
PIV	**P**article **I**mage **V**elocimetry
RDF	**R**adial **D**istribution **F**unction
RF	**R**ain-fall **F**illing method
SEM	**S**canning **E**lectron **M**icroscopy
SPS	**S**ingle **P**article **S**edimentation
TFM	**T**wo **F**luid **M**odel

Symbols

A	Hamaker constant	m
Ar	Archimedes constant	
Bo_g	Granular Bond number	
d_p	Particle diameter	m
d	Particle diameter	m
E_p	Particle Young's Modulus	Pa
e	Coefficient of restitution Particle-Particle	
e_w	Coefficient of restitutionParticle-Wall	
E	Young's Modulus	Pa
$\overrightarrow{F}$	Resultant force vector, the sum of all the contact forces	N
f_{ci}	Total contact forces acting on a particle i	N
f_{vdwi}	Total cohesion forces acting on a particle i	N
f_{fpi}	Total fluid-particle interaction force acting on a particle i	N
F_N	Normal component of the contact force	N
F_T	Tangential component of the contact force	N
Fr	Froude Number	-
$F_{n_{ij}}$	Normal contact force vector between particle i and j	N
$F_{t_{ij}}$	Tangential contact force vector between particle i and j	N
F_W	wall frictional force	
G	Shear modulus of the particle	
g	Gravitational constant	m/s^{-2}
I_f	Inter-phase momentum exchange term	kg $m^{-2}s^{-2}$
I_i	Moment of inertia of a particle i	kg m^2
h	Height of the granular bed assembly	
k_n	Normal contact stiffness	N/m
k_t	Tangential contact stiffness	N/m

m_i	Mass of particle i	kg
m_{eff}	Effective mass of particle assembly	kg
n_{ij}	Unit displacement vector between particle i and j	
P	Fluid pressure	Pa
r_i	Position vector of particle i	m
r_{ij}	Displacement vector between particle i and j	m
T_i	Total torque acting on particle i	kg m^2 s^{-2}
u_f	Fluid velocity	m/s
$u_{t_{ij}}$	The rate of change of the elastic tangential displacement	m/s
u_{bs}	Bed surface velocity	m/s
u_K	Kinematic wave velocity	m/s
u_D	Dynamic wave velocity	m/s
v_i	velocity vector of particle i	m/s
v_{ij}	Relative velocity between particle i and j	m/s
ϵ	Voidage	
δ_{ij}	Normal compression between particle i and j (overlap)	m
λ	Lubrication cut-off distance	m
μ_{mob}	Mobilised friction coefficient	
μ	Coefficient of sliding friction	
ρ_f	Fluid density	kg/m^3
ρ_p	Particle density	kg/m^3
τ_f	Viscous stresses	Pa
ω_i	Rotational velocity of particle i	1/s
$\overline{\sigma}_h$	Mean horizontal stress	Pa

This thesis is dedicated to my grandparents.
For their endless love and blessings.

Chapter 1

Introduction

This chapter introduces fluidization process of granular material with a brief description of different regimes. A new DEM-CFD solver is introduced along with its verification and validation. Furthermore, fluidization regimes of weakly cohesive powders are introduced along with simulation methodologies. Towards the end of the chapter, major objectives of the thesis and a structural layout of the rest of the thesis will be presented.

1.1 Fluidization

Particulate granular materials form bulk of food, chemical and pharmaceutical industrial raw materials and are important to the processes at even astrophysical scales [Jaeger *et al.*, 1996]. Interestingly, granular material display a wide range of mechanical properties and can be classified into any of three states of matter based on their bulk responses to deformations [Jaeger *et al.*, 2008]. Industries have benefited from such a versatile range of behaviour and also have been perplexed by it. A tremendous amount of research efforts has been put in the last many decades to achieve even a general understanding of the granular material behaviour. Of particular interests are fluid-like states of granular media which exhibit increased flowability, resembling a highly viscous fluid e.g. soil liquefaction. In order to benefit from the properties of these fluid-like states, industrial processes called fluidization were incepted in the early 1920's. In these processes, the granular bed is subjected to an influx of variety of fluids in controlled and sustained manner for variety of applications. The fluidization phenomenon combines advantages of increased flowability and homogeneity, along with bulk solid handling to provide industries with an opportunity to design many processes which are otherwise not feasible. Increased heat, mass transfer rates and uniform temperature distributions form the basis of many industrial processes such as chemical

reactors, combustors, fluid catalytic cracking and tablet coating. Based on industrial application, different macroscopic fluidization regimes can be classified as: fixed bed, homogeneous expansion, bubbling, spouting, turbulent or even pneumatic transport [Kunii and Levenspiel, 1969].

1.2 Fluidization Applications

For the past 70 years, industries have utilized almost all of the fluidization regimes because of the following advantages the fluidized systems offer:

- Bulk solids can be handled like a liquid with increased flowability, hence easier to transport.
- Iso-thermal conditions in the reactor are maintained by high mixing rates of bubbling, spouting or turbulent fluidization.
- Increased contact times between the particles lead to high heat and mass transfer rates.
- Uniform fluid-particle interaction in case of homogeneous expansion or fixed bed operations.

Owing to these advantages, the fluidization has been employed in various processes over chemical and pharmaceutical industries. Some of the wide industrial applications are enlisted here:

- Fluid catalytic cracking of kerosene [Elnashaie and El-Hennawi, 1979]
- Coal and biomass gasification [Li *et al.*, 2004]
- Fischer-Tropsch synthesis to convert natural gas to gasoline [Dry, 2002]
- Nuclear fuel preparation: producing refined Uranium from ore concentrates [Jonke *et al.*, 1958]
- Combustion of alternative solid fuels [Anthony, 1995]
- Photo-catalysis [Matsuda *et al.*, 2001]

1.3 Fluidization basics

Fluidization is the process by which particulate solid particles are transformed into a fluid-like state by contacting with a gas or liquid. A bed of particles is supported by

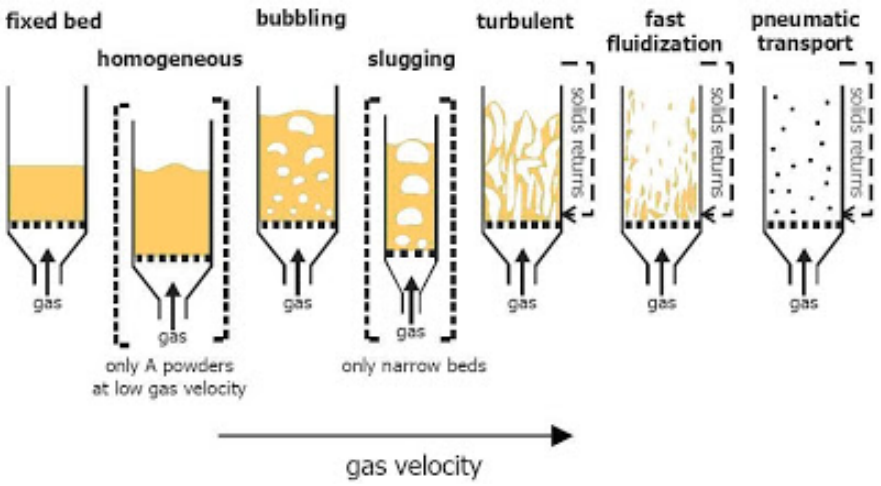

Figure 1.1: Schematic diagram of fluidization states with increasing inlet velocity, reproduced from Kunii and Levenspiel [1969]

a perforate plate, and the fluid is passed upwards. Role of the distributor is to allow equal distribution of the fluids and support the bed assembly. Resulting bed is aptly called a "fluidized bed", particle contacts make and break up almost instantly and the bed exhibits a fluid-like behaviour. Following properties are observed in the fluidized beds.

- Objects with the density greater than that of the bed float on the surface, otherwise they sink.
- When two unequal height fluidized beds are connected, the levels equalize.
- If a hole is made in the side walls at the bottom of the bed, solid will stream as a jet of liquid follows the Bernoulli's equation.
- Sound waves propagate through the bed but are dampened severely.

Structure of the bed evolves according to the imparted fluid velocity and the properties of particles comprising of the bed. A schematic diagram of the range of fluidization states with increasing velocity is shown in the figure 1.1. Almost all of these regimes are employed in the industries for efficient implementation of various physical and chemical processes and a brief descriptions of these are presented here:

- Fixed bed: Bed operated at sufficiently low flow rates, fluid percolates the voids or the gaps in between the stationary particles.
- Incipiently fluidized beds: As the flow rate is increased, the fluid-particle forces just counterbalance the weight of the bed. The particles are effectively suspended

in a state called "minimally fluidized" and the superficial velocity is called "Minimum fluidization velocity (U_{mf}). Typically, this is calculated by a simple force balance of the whole assembly. The pressure drop across the bed (calculated from empirical models), which is a function of bed voidage and inlet velocity, is equated to the weight of the bed. Correlations by Ergun [1952] and Abrahamsen and Geldart [1980] are popular methods to calculate U_{mf} from particle and fluid velocities.

- Homogeneously expanded beds: With increase in the flow rate beyond minimum fluidization, bed height increases almost linearly with the inlet velocity. This fluidization state depends upon the particle properties and is more common with liquid fluidization. This fluidization state will be studied in detail in the later chapters.

- Bubbling fluidized beds: Small pockets of fluid begin to rise rapidly, reminiscent of bubbles in a liquid column. The corresponding fluidizing velocity is called minimum bubbling velocity (U_{mb}). The bed is said to transit from "homogeneous" to "heterogeneous" state. A correlation by Abrahamsen and Geldart [1980] using the particle and gas properties is used to determine U_{mb}, given by equation 1.1. Here, d_p and ρ_g are the particle diameter and density, respectively. F_{45} is the mass fraction of the particles with size less than 45% of the total mass.

$$U_{mb} = \frac{2.07 d_p \rho_g^{0.06}}{\mu_g^{0.347}} \exp(0.716 F_{45}) \tag{1.1}$$

- Slugging fluidized beds: Big void spaces are created that slowly and collapse at the bed surface. The velocity of interstitial fluid is higher than the mesostructures.

- Turbulent fluidization: At very high inlet velocity, no organized structures like bubbles or slugs are apparent and instead particles move around chaotically.

- Fast fluidization: Particles have very high kinetic energy but not enough to escape the domain, they are fed back in to the system if elutrated. This is called circulating fluidized bed.

- Pneumatic transport: Lean phase with very low particle solid fractions. Almost all the particles escape the free board region. This velocity of the operation is called the terminal velocity. To calculate it, force balance equation of the free fall of a single isolated particle is solved (unlike U_{mf} when the force balance is solved on group of particles). The terminal velocity as a result of force balance is given by equation 1.2.

$$V_t = \left[\frac{4gd_p(\rho_p - \rho_f)}{3\rho_f C_d}\right]^{1/2} \tag{1.2}$$

Here, d_p and ρ_p are the diameter and density of particle, ρ_f is the fluid density and C_d is the drag coefficient, which is estimated as 0.43 for very high particle Reynolds number. A limiting condition for stable bed operation, without elutration of the particles is: $U_{mf} < U < V_t$. V_t/U_{mf}, is estimated for most particles to be around 8-9 [Kunii and Levenspiel, 1969].

With such multitude range of fluidization employed in industries, it is almost impossible to study the behaviour without clearly classifying them and identifying the boundaries. The next section reviews the literature on the fluidization regime classification.

1.4 Fluidization methodologies

A control over fluidization process is very necessary to eliminate some of the disadvantages of the process such as pulverization and elutriation of the raw materials and internal surface damage. Even with the widespread industrial usage, approaches to design of fluidization processes have been largely empirical due to a limited understanding at microscale and high costs of full-scale experiments required for optimization. Some of the industrial approaches are enlisted here:

- Completely empirical based on some dimensionless quantities.
- Semi-empirical with scientific principles applied with Buckingham-Pi theorems [Grace, 1986].
- Phenomenological models developed by solving governing equations of fluid and particle motion at a much coarser scale.

In a landmark empirical study, Geldart [1973] linked the particle properties (size and density) and the fluidizing medium properties (density) to macro-scopic bulk behaviour in a broad categorization which is now known as Geldart powder classification chart. Different regimes were recognized as Geldart A (Aeratable), B (Bubbling), C (Cohesive) and D (Spoutable). For any further distinction on the fluidization regimes, Geldart stated in 1986 that "*The arrival time of a space probe travelling to Saturn can be predicted more accurately than the behaviour of a fluidized bed chemical reactor!*" [Geldart, 1986]. Knowledge of the underlying mechanism of the fluidization regimes remains key to these predictions, design optimization and scaling up of the processes.

Experimental fluidization studies are difficult as the measurement techniques are largely ineffective due to inability to capture phenomena beyond walls [Goldschmidt *et al.*, 2003; Laverman *et al.*, 2008] or insufficient spatial or temporal scale resolutions [Holland *et al.*, 2008; Link *et al.*, 2008; Menon and Durian, 1997*a*; Warsito and Fan, 2001]. A better understanding can be achieved by employing tools with first principle derivation leading to an efficient bulk handling of materials and save substantial financial losses incurred by the industries due to poor optimization, design and scaling up procedures. Complex physics related to microscopic particle interactions with the presence of heterogeneous and length-scale dependent structures poses major challenges in attaining a greater understanding of the fluidization process.

1.5 Multi-scale Modelling

Rapid advancements in efficient numerical methods, algorithms and solutions along with increased computational powers provide us with an opportunity to numerically capture fluidization behaviour and study its robust features in great details [van der Hoef *et al.*, 2008]. Multi-scale modelling strategies are used to link phenomena occurring at different length and time scales [Deen *et al.*, 2007]. A trade-off between level of detail and the computational expense decides which modelling strategy is appropriate. On one end of spectrum, lie computationally inexpensive approaches wherein solid and gas phase are treated as inter-penetrating continuum phases and momentum exchange between them is modelled by constitutive relations. One of the major disadvantage of this approach is its inability to model inter-particle contacts accurately and instead prescribing solid and viscous stress tensors [Pain *et al.*, 2001] through constitutive modelling.

On the other extreme of the multiscale modelling lie fully resolved simulations. The fluid motion is solved with Lattice Boltzmann methods (LBM), each particle is tracked by Discrete Element Methods (DEM) and both the inter-particle and fluid-particle interactions are solved exactly [Guo *et al.*, 2013]. These Direct Numerical Simulations (DNS) for dense gas-solid fludized beds are rare and require immense computational power to run even for downsized laboratory scale simulations [Xiong *et al.*, 2010]. Nevertheless, these resolved simulations provide a route to micromechanical constitutive modelling of fluid-particle modelling to put at continuum scale (extensively reviewed in[van der Hoef *et al.*, 2008]). Taking advantages of both TFM and DNS, a hydrid approach employs DEM to accurately model inter-particle forces by contact models and fluid phase is described by the TFM fluid equations. In this approach (popularly referred as DEM-CFD), the governing equations for the fluid motion are spatially averaged [Anderson and Jackson, 1967], and each particle is separately tracked. This

avoids the DNS of fluid motion and can capture particle dynamics more accurately than any continuum description of solid phase[Kafui *et al.*, 2002; Tsuji *et al.*, 1993; Xu and Yu, 1997], hence maintaining computational tractability. This study employs DEM-CFD methodology implemented by coupling open source codes OpenFOAM and LAMMPS in C++ framework.

1.6 Verification and validation in multiphase flows

Numerous open source numerical codes and commercial soft-wares capable of solving multiphase flow equations are present in the literature (e.g. EDEM-Fluent, MFIX-DEM, LIGGGHTS-OpenFOAM). Prior to employing these codes for prediction of flow and design processes, quantification of model sensitivity is required. This provides a realistic expectation as to what extent physics of the system can be captured by the model. This essential step is known as verification and validation (VV). Verification can be refereed to as checking computer coding errors, such as uninitialized variables taking garbage values, unintended variable assignments and so on. These errors might be hidden and not show up as compilation or run time errors but affect predictive capabilities of the tool, like convergence to a wrong solution. Verification can be conducted by relatively simple cases which are targeted to check only one or two aspects of code and remain largely unaffected by rest of the code implementation. Assessing predictive capabilities and the extent to which mathematical models to reproduce the physical phenomenon can be referred to as validation process. Validation is conducted as comparison of the simulated data with experimental measurements. The validation and verification procedures are already well established in the CFD [Oberkampf and Blottner, 1998] and computational solid mechanics community [Schwer *et al.*, 2006], but similar efforts are lacking considerably in multiphase flow field. Recently, validation and verification test cases was presented and checked for open source code MFIX-DEM [Garg *et al.*, 2012; Li *et al.*, 2012*b*]. The study covered a wide range of test cases but was not comprehensive enough to address level of discrepancy with the analytical or experimental results based on mesh dependency, interpolation algorithms, fluid-particle time step ratio and various other known numerical issues.

In this work, a careful verification is conducted with simplistic cases such as sedimentation of a single particle and a constant porosity block in different density and viscosity fluids. The terminal velocity calculated from analytical solutions is compared with DEM-CFD code. To check convergence and numerical stability of the solution in high fluid velocity cases, pressure drop across in a controlled environment is checked against the analytical solution presented by Ergun [1952]. Analytical solutions are calculated in homogeneous conditions neglecting some physics which can introduce some

errors. However, careful quantification and justification of these errors, if at all present is required before proceeding to validation cases. Furthermore, validation studies are presented covering a wide range of dense-phase fluidization studies: Bubbling/slugging, Spouted, Bi-disperse beds. Bubbling bed experiments conducted using MR techniques [Müller *et al.*, 2008, 2009] will be used as a validation case. Measured voidage, solid velocity and granular temperature for a thin gas-solid fluidized bed with spatial resolutions comparable to the size of the fluidized particles will be compared against DEM-CFD simulation results. Time and spatially averaged particle velocity profiles are obtained from PEPT [Link *et al.*, 2008] to validate a spouting bed case. Segregation rates are taken from bidisperse bed studies by Goldschmidt *et al.* [2003] and used as validation data for bidisperse segregation case. With confidence in the DEM-CFD code to reproduce the hydrodynamics of fluidized beds, the tool is employed to study the intriguing behaviour of Geldart A particle fluidization.

1.7 Fluidization of weakly cohesive powders

Fluidization behaviour of sub micrometer sized Geldart A particles have brought out significant interests from both academics and industries. With increasing inlet velocity beyond U_{mf}, a uniform stable expansion is observed and bubbling is suppressed. An inlet velocity is identified ($U > U_{mf}$) when large void spaces, i.e. bubble start to appear and mark a transition from particulate to aggregative fluidization. From an industrial point of view, the uniform bed expansion is a highly desirable regime, owing to better fluid-particle contacts than a fixed bed and better control over the process than a bubbling bed. For example, pharmaceutical industries can be largely benefited for better table coating. However, the fluidization behaviour is intricately related to particle size and industrial coating materials are categorized as Geldart D or spoutable particles [Geldart, 1973]. A fundamental understanding of physics at the particle level can reveal mechanism behind the stable expansion and the origin of bubbling [Sundaresan, 2003]. Such understanding can help to design better optimized and up scaled apparatus. Even with such wide interests and practical applications, numerous outstanding questions remain to be answered definitely and the underlying theories have been heavily debated leading to controversies and divided opinions in fluidization community [Valverde and Castellanos, 2007*a*]. A few of these outstanding questions are summarized here:

- What is the fundamental mechanism behind uniform bed expansion? Whether it is fluid-particle interactions at that length scale or are non-hydrodynamic origin forces responsible? These questions have lead to divided opinions with both of

them having merits [Hou *et al.*, 2012]. The theory on non-hydrodynamic origin forces is further divided into frictional forces dominant or the cohesion forces.

- What is the criterion on the onset of bubbling and what are the fundamental parameters? Many researchers have tried to answer this question by taking a side on the two question mentioned [Foscolo and Gibilaro, 1984; Hou *et al.*, 2012; Mazzei and Lettieri, 2008; Yang *et al.*, 2013].

- What is the microstructural state of the uniformly expanded bed? Homogeneous expansion might only mean absence of bubbles, but the bed might not be homogeneous at micro level.

The present work attempts to address some these questions through multi-scale modelling approach DEM-CFD. Chapters 5,6 and 7 of the thesis will present more on the topics of DEM-CFD simulations of Geldart A fluidization, microstructure of uniformly expanded bed and its stability.

1.8 Objective and scope of thesis

The main objective of this research work is to provide insights into fluidization regimes of weakly cohesive particles using the multi-scale modelling approach. In order to achieve the objective, extensive validation and verification procedure of the numerical tool developed is laid out. The process of validation and verification is important to quantify the capability of the developed numerical tool to capture robust features of weakly cohesive fluidization. It is also noted that the simulation data produced is enormous and adequate post-processing has to be done in order to get meaningful information out of these simulations. To this end, different post-processing tools are developed such as coarse-graining from discrete data to continuum fields. The objectives and the overall methodology of this thesis is as follows:

- Verification of the open-source DEM-CFD code written from OpenFOAM and LAMMPS C++ libraries using simple test cases and comparison against analytical solutions.

- Quantify capability and validate of the DEM-CFD code in fluidization conditions with wide range of flow conditions and local particle concentration.

- With the gained confidence from validation and verification studies, employ the DEM-CFD code to check if it can reproduce hydrodynamics of weakly cohesive fluidization and its robust features such as pressure overshoot, uniform bed expansion and onset of bubbling.

- Study DEM-CFD parameters influencing the uniform bed expansion and quantify for prediction of U_{mb}.
- Quantify influence of particle cohesion forces in particular and relation to the delay in the onset of bubbling after U_{mf}. Idea is to keep the particle size and density in the region of Geldart A/B boundary and increase cohesive forces by changing cohesive model parameters. This would lead to systematic transition from Geldart B to C fluidization regimes. The focus is mostly on the Geldart A regimes reproduction and identification of the stable bed expansion window.
- Micromechanical characterization of Geldart A regimes by looking at the microstructure at different length scales such as coordination numbers, porosity, Vornoii cell tessellations. These are investigated for weak and strong force networks, shedding light on the claims of *homogeneous* bed expansion.
- Study stability of the expanded bed by shock wave criterion and prediction of onset of bubbling as a function of increasing cohesion strength.

1.9 Thesis layout

This dissertation is divided into 9 chapters including this chapter 1 on introduction, scope and objective of the research. The rest of the organization is as follows

Chapter 2 presents a state of the art review on the literature relevant to this research. The focus is on laying out fluidization regime classification, multi-scale modelling of fluidized beds and fluidization studies of weakly cohesive particles.

Chapter 3 provides a detailed DEM-CFD methodology employed to study fluidization regimes. An emphasis is laid on the implementation of drag model closures and interparticle adhesion. Furthermore, post processing tools for mapping the discrete data to the continuum domain developed in this work are presented.

Chapter 4 details the importance of verification of the computer codes and focusses on a detailed case-by-case verification of the DEM-CFD code. This is an importance step before employing the tool for prediction.

Chapter 5 is in continuation of the chapter 4 work and focuses on validation of the DEM-CFD code for capturing fluidized bed hydrodynamics. Importance of validation is emphasized and a lack of well-defined validation procedure for multiphase tools is highlighted. Validation guidelines are summarized. DEM-CFD code is validated against three validation cases testing bubbling, spouted and bidisperse fluidization dynamics against known experimental data.

Chapter 6 presents DEM-CFD simulation of weakly cohesive particles. After gaining confidence in DEM-CFD methodology capabilities from chapter 4 and 5, the code is used to simulate robust features of Geldart A fluidization regimes. Parameters such as mesh and cohesion effects are studied to capture macroscopic bulk behaviour. Post processing of DEM data is done for different fluidization regimes to study internal stresses.

Chapter 7 take clues from chapter 6 regarding the homogeneous claims and details in the microstructure characterization of fluidization regimes. Microstructure is quantified at different mesoscopic length scales. Also, a distinction is made on weak and strong force networks.

Chapter 8 concerns with the stability of expanded bed regimes, simulated from studies in chapter 6. Shock wave theory is tested with effects of cohesion tested. Cohesion effects on transformation from aggregative to particulate fluidization is studied and compared with the theoretical and experimental studies.

Chapter 9 concludes the dissertation and the research work and provides an outlook for future studies.

Chapter 2

Literature Review

2.1 Introduction

This chapter presents a brief overview of existing literature on gas-solid fluidization studies. The structure of the chapter is as follows. Section 2 will review existing state of the art on fluidization regimes. Section 3 will present multi-scale modelling of dense phase flows and the relevance of validation and verification of the tools. Section 4 will present previous experimental and simulation studies of weakly cohesive fluidization regimes, which will be the focus of this thesis. Last sections will present challenges identified from the literature and the objective of the thesis.

2.2 Fluidization regimes and their classification

The fluidization technology is employed with heaps of industrial raw materials that range from a few millimetres sized tablets to powders comprising of nano-particles to achieve intended results. A static granular bed when fluidized, can manifest itself into different regimes based on the raw material properties. A definitive control on the fludization regimes will allow industries to employ fluidization processes more efficiently and save costs related to inferior product delivery. An early attempt on broad classification of these regimes was based on the fluidization appearance [Wilhelm and Kwauk, 1948]. Criterion on the Froude number ($Fr = U_{mf}^2/(gd_p)$) was established to classify fluidization regimes:

- Particulate or non-bubbling ($Fr << 1$): Smooth uniform expansion with a progressive increase in the inlet velocity.
- Aggregative or bubbling: Appearance and rise of large void spaces in the bed similar to the gas bubbles in the liquid at the onset of fluidization ($U > U_{mf}$)

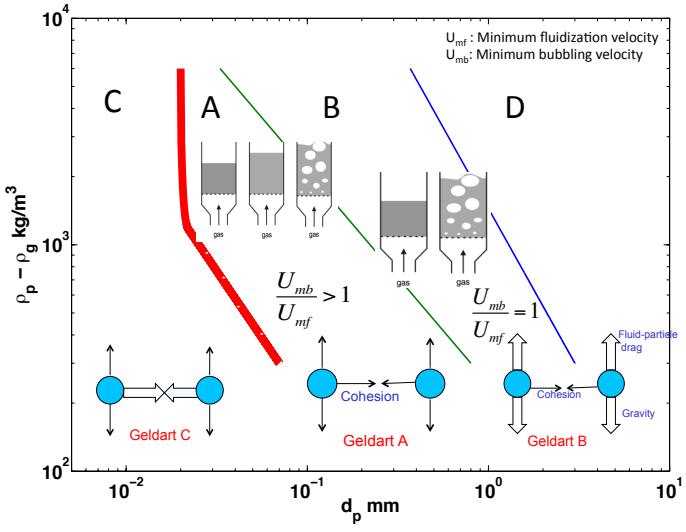

Figure 2.1: Geldart classification of fluidization powders and interpretation based on governing dynamics for each regime. d_p (particle diameter) is plotted on the X axis with the density difference between particle and fluid ($\rho_p - \rho_f$) on the Y axis, related to the macroscopic fluidization regimes. U_{mf} and U_{mb} are the minimum fluidization and minimum bubbling velocity. Thickness of arrows on the particle free body diagram tells the relative magnitude of forces.

The study provided some initial insights into a system too complex to be classified by such a simple criterion. In later years, evidence based on liquid-solid fluidization and sedimentation experiments revealed that these predictions are not that accurate. Different studies emerged in 1950's and 60's to differentiate between the particulate and aggregative fluidization. Criteria were proposed based on growth rates of disturbances by Jackson [1963] and Pigford and Baron [1965]; studies were complicated and could not provide a better answer than the Froude number criterion. Empirical relations given by studies were based on the assumptions that void spaces or bubbles are present but not observable on the surface. These studies are seldom used because of their complexity [Simpson and Rodger, 1961]. Later, more empirical studies emerged in search for more quantitative and accurate predictions covering a broad regime map. The pioneer work by Geldart [1973] stands out amongst these studies. These are reviewed here:

2.2.1 Geldart Classification

Geldart [1973] classified powders having similar fluidization behaviour when fluidized by gas. He linked the behaviour to the particle and gas properties in four major groups. These were all mapped altogether in what is popularly known as the Geldart chart presented in figure 2.1 with the governing dynamics of each regime indicated by the force

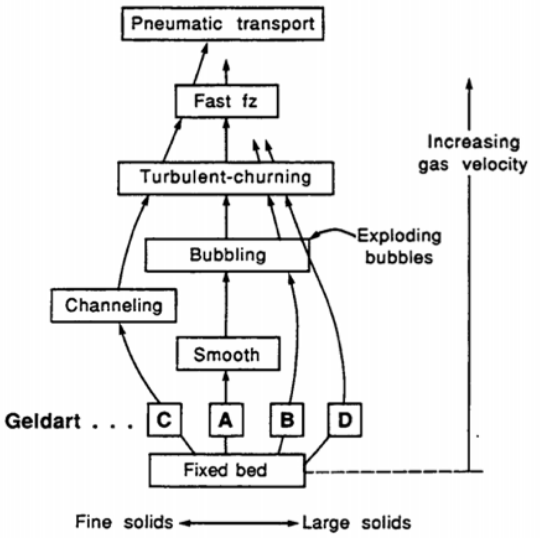

Figure 2.2: Flow chart of the bulk fludization behaviour path taken by different Geldart powders when fluidized, reproduced from Yates [1983]. The alphabets A,B,C and D indicate the Geldart powder groups.

body diagram of interacting particles. A flow chart of the bulk fludization behaviour path taken by different Geldart powders when fluidized, reproduced from Yates [1983], is given by figure 2.2.

Geldart A/B behaviour is of particular relevance to this thesis and highlighted in the figure 2.1. A remarkable feature of the Geldart A fluidization is the onset of bubbling much after the bed has completely fluidized. This is indicated by the bed states described in the figure 2.1. When the bed is subjected to an inlet velocity U such that $U < U_{mf}$, the granular bed is still static with solid appearance. With an increase beyond U_{mf}, a uniform expansion ($U_{mf} < U < U_{mb}$) of the bed is noticed. On further increase of inlet velocity ($U_{mb} > U_{mf}$), bubbling occurs. For Geldart B fluidization, these rising pocket of fluids i.e. bubbles, are apparent at the onset of fluidization itself and $U_{mb} = U_{mf}$ as given by the bed state diagram (figure 2.1). Origins of the boundary between this immediate aggregative behaviour (Geldart B) and delayed aggregative behaviour (Geldart A) behaviour is unclear and much debated in the literature. Geldart chart has been largely successful in providing this boundary roughly, but over last 50 years, a few exceptions to the chart and areas of improvement and were identified in the literature. Notable points related to Geldart classification studies are mentioned here:

- The chart is based on empirical studies and can not provide insights into the governing dynamics of each regime. Therefore, it fail to address the long standing issues of transitions between the regimes [Molerus, 1982]. Experimental works by Molerus [1982]; Seville and Clift [1984] suggested that the inter-particle forces might be a better parameter to investigate different regimes.

- The chart is only applicable at ambient temperature and pressure, whereas many of industrial processes are carried out at elevated conditions [Yang, 2007]. Recent work of Yang [2007] have attempted to modify and re-interpret Geldart chart at these conditions.

- The chart does not address on the transitions of the regime within the groups, for example with the increase in inlet velocity particulate behaviour of Geldart A particles transits to the bubbling regime. Geldart [1973] cautioned against making any generalizations between a group.

- Fluidization behaviour of nano-particles (NP) is shown to be deviating from what suggested by the Geldart chart [van Ommen *et al.*, 2012]. The behaviour is very counter-intuitive as the powders can be fluidized very well, even though placed in the Geldart C classification. NP are fluidized as agglomerates of high porosity instead of acting as individual particles [van Ommen *et al.*, 2012]. Great insights are provided on fluidization regimes in cohesive fluidization and especially relating to Geldart A/C boundary by Castellanos and his co-workers [Castellanos *et al.*, 1999; Valverde and Castellanos, 2007*b*, 2008].

In this thesis, interests lie in studying the Geldart A/B boundary. Key questions regarding Geldart A fluidization and the role of inter-particle forces in the formation of a uniform expanded bed, onset of the bubbling and the micro-structure of Geldart A beds are addressed in the chapters 5,6 and 7. A few attempts in literature addressing the Geldart chart criterion on A/B boundary and Geldart A fluidization regimes are summarized in the next few sub-sections.

2.2.2 Molerus interpretation

Molerus [1982] identified that by taking into account the inter-particle cohesion, limiting conditions can be derived to re-interpret Geldart classification. To demarcate the boundaries between the powder groups A, B and C, the following observations and deductions were made.

- A/C boundary: Particle movement is suppressed by adhesion forces, even at higher fluidizing velocity. A dimensionless quantity K_1 was defined for this condition by estimating adhesion force on a particle F_H and the average tensile force permitted per particle F_T. After simplification, expression for K_1 is given by equation 2.1.

$$K_1 = 10\frac{(\rho_p - \rho_f)d_p^3 g}{F_H} \tag{2.1}$$

  Here, ρ_p is the particle density, ρ_f is the fluid density, d_p is the particle diameter, g is the gravitational acceleration and F_H,estimated by Krupp [1967], is given by equation:

$$F_H = \frac{h_{lf}}{8\pi z_o^2} R\left(1 + \frac{h_{lf}}{8\pi^2 z_o^3 H}\right) \tag{2.2}$$

  Here, h_{lf} is the Lifschitz–Waals constant, z_o is the maximum separation between the surfaces of particles at which adhesion forces are observed, H is the hardness of the solid material and R is the characteristic measure of surface asperities. On the basis of parameter K_1, and its dependence on the material properties, Molerus [1982] explained the broad thickness of the A/C boundary (Geldart [1973]). For a catalysis particle on the boundary of A/C in the Geldart chart, K_1 was estimated to be around 0.01.

- A/B boundary: The distinction between the particulate and aggregative fluidization was explained by *the unimportance of cohesion forces on the fluidization behaviour in the case of powder type B*. A criterion K_2 was defined, much like granular Bond number (Bo_g) used later in thesis, given by the equation 2.3.

$$K_2 = \frac{(\rho_p - \rho_f)\frac{\pi d_p^3}{6} g}{F_H} \tag{2.3}$$

  K_2 at A/B transition was estimated roughly by experimental studies as 0.16. Since estimation of F_H is very surface asperity dependent, studies were not accurate enough to determine exact transition line in the Geldart chart. Together with K_1 as lower boundary and K_2 as upper boundary, a rough phenomenological regime for Geldart A was explained as: adhesion forces are important but the force chains are breakable after a minimum fluidizing velocity (identified as U_{mb}).

Distinction between B and D groups were also defined based on a non-dimensional Euler number of fluidization, B/D classification relates to the hydrodynamics at the particle size scale where the inter-particle forces are negligible.

2.2.3 Classification studies based on dimensionless numbers

The role of dimensionless numbers in the regime transition was highlighted by Grace [1986]. A group of variables which are fundamental to the fluidization process such as diameter, density and the fluidizing gas velocity were presented in their non-dimensioned forms d_p^* and U^* and given by equations 2.4 and 2.5 respectively.

$$d_p^* = d_p \left[\rho_p g \Delta\rho / \mu^2\right]^{1/3} \tag{2.4}$$

$$U^* = U \left[\rho^2 / \mu g \Delta\rho\right]^{1/3} \tag{2.5}$$

Here, d_p is the particle diameter, U is the superficial velocity, $\Delta\rho$ is the density difference between the particle and the fluid, μ is the static viscosity of the fluid. Other non-dimensioned groups were expressed as a function of d_p^* and U^*:

- Archimedes number: $Ar = (d_p^*)^3$
- Reynolds number: $Re = d_p^* U^*$
- Modified Froude number: $Fr = (U^*)^2 / d_p^*$
- Drag coefficient: $C_D = 4d_p^* / (3U^*)^2$
- Similarity Number: $M = (U^*)^3$

These dimensional groupings were instrumental in studying gas-solid fluidization regimes, and in particular Ar was used to differentiate between the A/B boundary. Ar was found empirically by fitting the experimental data as given by equation 2.6. In the general range of gas-solid fluidization, $\Delta\rho/\rho$ = 1000-2000 and Ar was found to be around 125, which was close to the Geldart predictions. Figure 2.4 reproduced from Grace [1986], gives the flow regime chart in terms of dimensionless quantities. The alphabets A, B, C and D indicate the Geldart powder groups.

$$Ar_{ab} = 1.03 \times 10^6 \left(\Delta\rho/\rho\right)^{-1.275} \tag{2.6}$$

Similar studies by Goossens [1998] differentiated A/B boundaries on the basis of critical values for the ratio between laminar and turbulent flow parameters, at the U_{mf} and U_{mb}. This gave Ar number equivalent to 88.5, close to the value 125 predicted by Grace [1986] and Geldart [1973]. Another critical transition number was proposed by

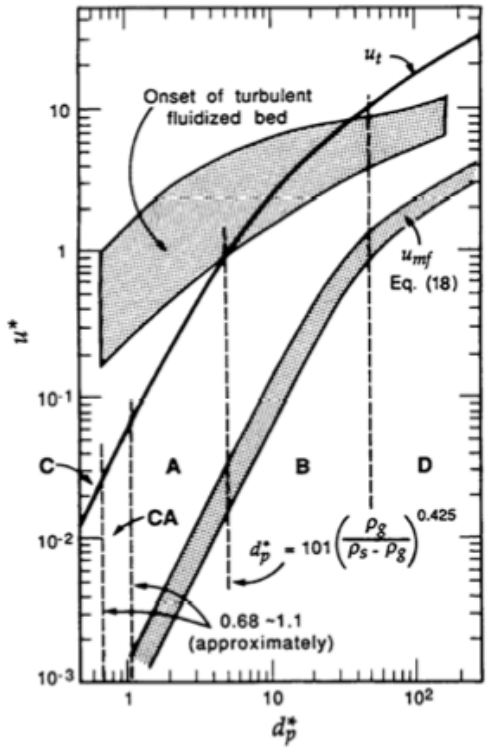

Figure 2.3: Flow regime chart for powder classification in terms of dimensionless quantities d_p^* andU^*, reproduced from Grace [1986]. The alphabets A,B,C and D indicate the Geldart powder groups

Verloop and Heertjes [1970] by employing the shock waves criterion to study transition at A/B boundary much before the work by Grace [1986]. This number, however can be rearranged as a product of Ar and $\Delta\rho/\rho$. Similar to equation 2.6, Verloop and Heertjes [1970] gave a criterion for bubbling fluidization to occur if the equation 2.7 is satisfied.

$$Ar(\Delta\rho/\rho) > 2.5 \times 10^7 \tag{2.7}$$

$$Ar_y = 2.24 \times 10^8 \left(\frac{\rho_p - \rho_f}{\rho_f}\right)^{-1.960} \tag{2.8}$$

Interestingly, experimental data by Oltrogge [1972] fitted according to the same dimensionless number proposed by Verloop and Heertjes [1970], the limiting conditions were found to be around 1.6×10^5, around 1 order of magnitude lower than the earlier predictions. These experiments by Oltrogge [1972] were conducted by covering a wide range of high pressure and temperature, unlike experiments by Geldart [1973], conducted at ambient conditions. Recent work by Yang [2007] modified the Geldart

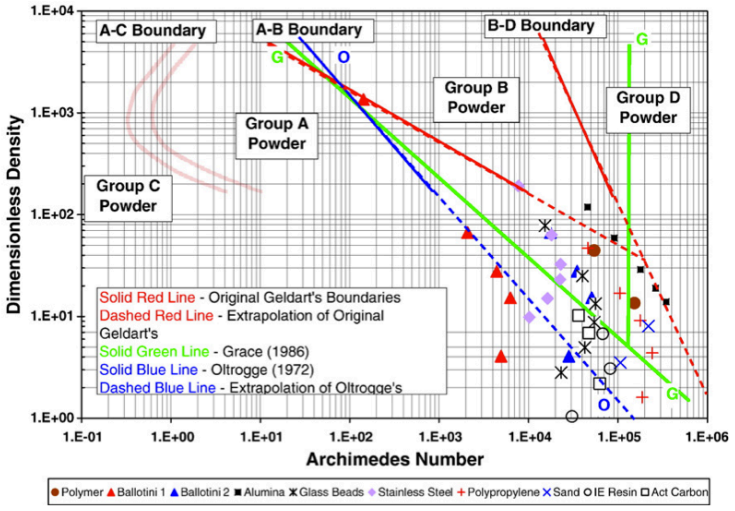

Figure 2.4: Modified Geldart's classification of powders employing dimensionless density and Archimedes number at elevated temperature and pressure, reproduced from Yang [2007]

A/B boundary equation to include effect of elevated pressure and temperature. It was reported that different Geldart B particles such as polypropylene, sand, alumina, silicon carbide behaved as Geldart A particles at elevated pressure fluidization using supercritical carbon dioxide as the fluidizing gas. Similar to Oltrogge [1972], Yang [2007] gave another correlation, with same dimensionless quantities Ar_y and $(\rho_p - \rho_f)/\rho_p$ given by equation 2.8. Moreover, according to the modified chart by Yang [2007], interpolated A/B boundary intersected B/D boundary in the high pressure and temperature conditions. It meant that even for a particle size as high as Geldart D particle can behave as Geldart A particles. The chart could confirm earlier studies by Liu *et al.* [1996] on Geldart D particles, fluidized with carbon dioxide at a pressure higher than 4 Mpa, behaving as Geldart A particles. Figure 2.4 gives the modified chart by Yang [2007].

In summary, extensive experimental work has been done to differentiate between the aggregative and particulate fluidization in the recent past. Strong evidence is inclined towards the role of inter-particle forces in this transition but a definitive understanding of the origins of these behaviours is still lacking. Numerical simulations have given us the opportunity to enhance our understanding of the fluidization regimes.

2.3 Numerical studies of fluidized beds

To overcome the practical difficulties in studying fluidization bed dynamics by experimental techniques, detailed numerical studies have provided an alternate route. Studies by computer codes, can measure evolution of local perturbations at the micro-scale

to macro-scale without disturbing the flow structures. However, simulating the reality of fluidization is extremely difficult due to limited understanding of the processes at a micro-scale. In fluidization processes, phenomenon occurring at micro scale give rise to organized flow-structures such as bubbles at the meso-scale which in turn affect the macro-scale bulk phenomenon. Studying fluidization dynamics at every scale and linking them to other relevant scales poses a difficult problem. Multi-scale modelling strategies have recently emerged to solve these problems at widely separated scales in various disciplines of science and engineering [Baeurle, 2009; de Pablo, 2011; Steinhauser, 2008]. Following sections will give an overview of multi-scale modelling in the context of dense multiphase flows.

2.3.1 Multi-scale modelling

A fundamental understanding of the smallest building blocks of matter and their interactions is believed to even answer the origins of the universe [Haber and Kane, 1985]. Breaking a macroscopic picture to a sub-level and further repeating this process till we can not do it any-more, lead to a standard model of physics and search for fundamental particles such as Boson [Aoki *et al.*, 2006]. Passing information from one level to the other is done by well defined strategies called constitutive models. This overall process is known as multi-scale modelling. Need for such modelling is apparent as the available phenomenological models are too inaccurate and miss out on the details. On the other hand, the micro scale models are too inefficient in providing just the relevant information and fail to capture the full spatial domain. Hence, a compromise between the accuracy and efficiency is required to devise a multi-scale modelling strategy. Multi-scale modelling approach has been successfully applied to the physical processes of manageable sizes of few metres. Following sub-level of interactions relevant to any physical/chemical system are identified in literature:

- Quantum mechanics models for interacting electrons (10^{-15} m, 10^{-12} s)
- Molecular Dynamics (MD) models at the atomistic scales (10^{-12} m, 10^{-9} s)
- Nano-scale models between interacting molecules or elements (10^{-8} m, 10^{-6} s)
- Continuum models when group of elements can be treated as continuous fabrics e.g. fluids (10^{-5} m, 10^{-3} s)
- Models between interacting continuum fabrics (10^{-3} m, 10^{-1} s)

Each of these levels describe the system over phenomenon occurring over a specific time and length scale. A major challenge of this modelling is to develop a constitutive model

at each level to link it to the next level with minimal loss of information. These models are based on input parameters identified from the lower level and output a coarse-grained quantity to be put at the second level. This approach has been successfully implemented to study processes in various disciplines of science and engineering such as meteorology, computational physics and chemistry, biological systems etc. In fact, Nobel prize in chemistry for the year 2013 was awarded *for the development of multi-scale models for complex chemical systems* [André, 2014]. Multi-scale modelling can be divided into three sub-components:

- Analysis of the system: assessment and identification of governing dynamics at different interacting levels.
- Constitutive models: formulation of models from parameters relevant at one scale and relating to parameters relevant to dynamics at another level
- Algorithms to solve: putting all the models together and solving each efficiently.

2.3.2 Multi-scale modelling of fluidized beds

For a dense phase fluidized system, hierarchy of multi-scale modelling is presented in the figure 2.5. Length scale of the interactions varies from 10^{-7} to 10^{-1} m whereas time scale varies from 10^{-5} to 10^{1} seconds. Collisions between the particles and the interaction between the fluid and the sub-particle surface are identified as the most microscopic level of physics that would be adequate to describe fluidized bed dynamics. These interactions result in mesoscopic flow structures such as bubbles and slugs. Interacting bubbles or slugs form the macroscopic bulk behaviour.

Efforts for developing multi-scale models from these fundamental interactions have rapidly increased with the recent advent of computational powers like high performance computing (HPC) and parallel computing. Based on the desired level of modelling details and computational facilities available, efficient multi-scale modelling strategies have been suggested. These models, classified by van der Hoef *et al.* [2008], according to the treatment of gas and solid phase are enlisted here:

1. Discrete Bubble Method (DBM): Phenomenological model employed at industrial scales. Bubbles are tracked in a Lagrangian framework.
2. Two-fluid model (TFM): Solid and gas phases are treated as inter-penetrating continuum in an Eulerian framework, extensively employed at engineering scale.
3. Discrete Particle Method (DPM): Each particle is tracked as a discrete entity with collisions, gas phase equations are solved in an Eulerian framework. Interactions

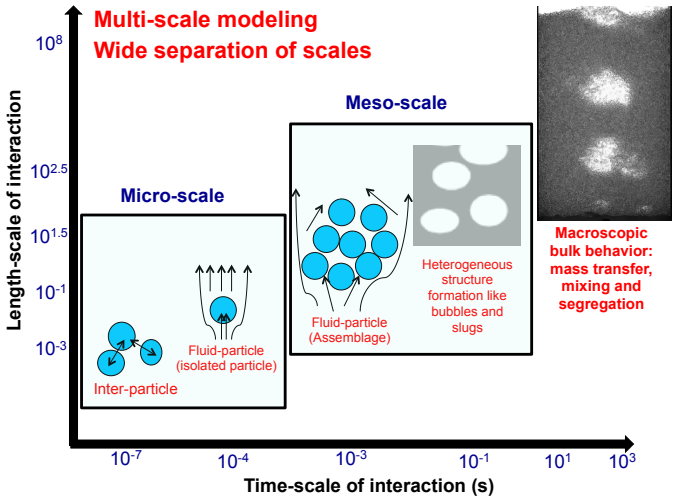

Figure 2.5: Hierarchy of multiscale modelling for a dense phase fluidization system.

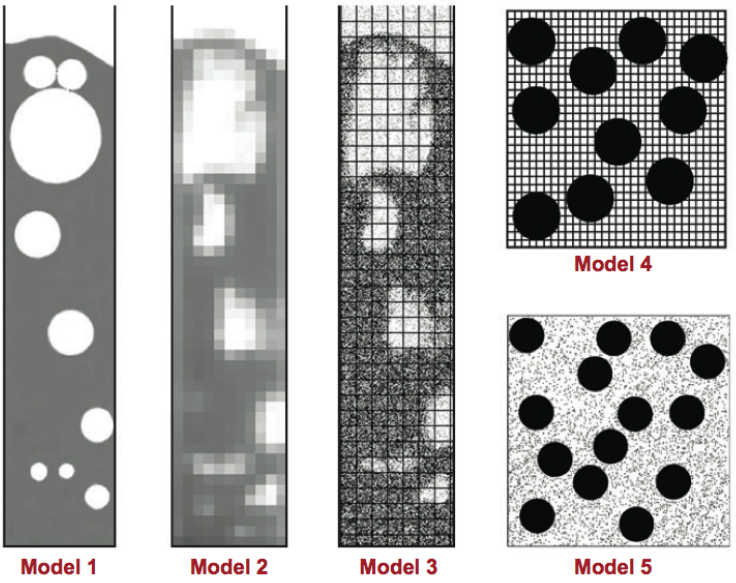

Figure 2.6: Graphical representation of different models employed to model dense phase multiphase flows (reproduced from van der Hoef *et al.* [2008].

between phases are unresolved and constitutive modelling is required. Employed at laboratory scales.

4. Lattice Boltzmann Method (LBM): Particles are tracked same way as DPM, gas-particle interactions are fully resolved. No constitutive modelling is required, slip boundary conditions are solved on the particle surface. Employed at sub-laboratory scales.

5. Molecular dynamics (MD): Both gas and particles are tracked in Lagrangian frames and interface momentum transfer is solved by treating it as elastic contacts at the particle surface. It is employed at the micro-scales (<0.001 m).

A graphical representation of these models is presented in figure 2.6, taken from van der Hoef *et al.* [2008]. The figure shows the relevance and level of spatial detail captured by each model. White colour in the figure indicates zero particle concentration, whereas shades of grey indicate dense, closely packed particles. DBM (Model 1) represent gas-particle interaction as bubbles in the solid phase. TFM (Model 2) treats solid phase as a continuum. White colour in the figure indicates no solid phase, whereas shades of grey indicate presence of dense solid phase. DPM (Model 3) and LBM (Model 4) treat particles as discrete entities, but the fluid mesh resolution is coarse for DPM while it is fine for LBM. Model 5 treats both particle and gas phase as discrete phases. In the context of modelling gas-solid fluidized beds, DBM and MD methods are not used for either being too simplified or being too complex. TFM, DPM, LBM are fairly popular methods in literature. In fact, coarser methods required at the TFM and DPM level are often supplied by LBM methods. Figure 2.7 (reproduced from van der Hoef *et al.* [2006]) presents how information provided by lower models can be used in development of higher models via closure relations along with experimental or theoretical data. Next sections will be provide a brief overview of these three models.

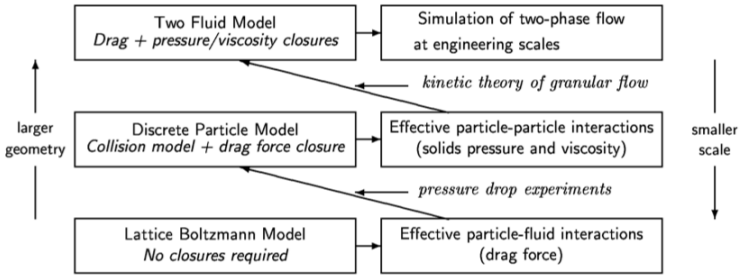

Figure 2.7: Multi-level modelling scheme (reproduced from van der Hoef *et al.* [2006].

2.3.3 Two fluid model

The model treats both the solid and fluid phases as inter-penetrating continua exchanging momentum. Both the phases are solved in the Eulerian framework hence, the model is often referred to as Euler-Euler (EE) method in the literature. Fluid phase equations are spatially averaged to incorporate the effect of particle phase [Anderson and Jackson, 1967]. Similar momentum equation is derived for the solid-phase, with reversed signs for momentum exchange terms as per Newton's third law. A significant challenge

lies in the accurate continuum description of the hydrodynamics of solid phase. The governing equations for TFM were developed from the first principle by both Anderson and Jackson [1967] and Ishii [1975] using different averaging techniques, but reaching at the same equations. During the averaging process, some of the terms lose their form and require another set of equations to close the solution. Figure 2.8 provides schematic of the averaging scheme, when particle discrete data is converted to the continuum data as an input parameter in the solid phase equation and the inter-phase momentum exchange term. Here ϕ is the fraction of the solid phase volume present in the discretization cell. The momentum exchange between the phases is calculated by the constitutive laws of these continuum quantities.

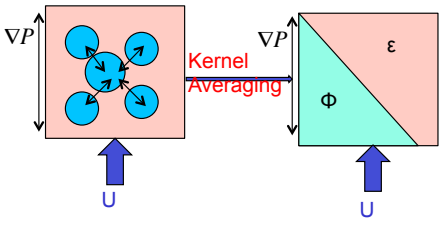

Figure 2.8: Schematics of the averaging scheme, when particle discrete data is converted to the continuum data as an input parameter in the solid phase equation and inter-phase momentum exchange term.ϕ is the fraction of the solid phase volume present in the discretization cell. ϵ is the porosity, calculated as 1-ϕ.

As evident in figure 2.7, TFM is employed at the engineering scales (1 m) but requires closure models for fluid-particle interactions, solid phase pressure and viscosity. The solid phase models are obtained from kinetic theory of granular flows (KTGF), which is a tool developed from the kinetic theory of gases [Ding and Gidaspow, 1990].

2.3.3.1 Limitations of TFM

TFM has been the most viable option at the engineering scale due to its derivation from the first principle itself and low computational expense. The model relies on different constitutive models for the information missed at the micro-scale. A review into studies has presented the following limitations in its applications:

- Averaging length scale: Derivation of TFM equations was based on an assumption that the resolution of the averaging is much less than the macroscopic scale but much greater than the microscopic scale. Such an assumption is difficult to overlook, as the TFM studies will be mesh-dependent. Role of scale resolution in TFM studies has been attributed as a probable cause of its failure in reproducing homogeneous expansion of Geldart A partcles [Wang *et al.*, 2011*b*].

- Solving solid phase mechanics: Fluidization regimes are often a result of an interplay between inter-particle forces and hydrodynamic forces. Flow of particulate solids have been well studied using continuum approaches in the absence of the fluid as well [Jop *et al.*, 2006; Savage, 1998] and it has been pointed out that some of the phenomena like local shearing have not been well captured by continuum models [Kamrin and Bazant, 2007].

- Particle phase stress: Even though TFM equations were derived for meso-scale averaging, the constitutive models are derived for microscopic homogeneous conditions [van der Hoef *et al.*, 2008]. The problem further complicates as the inhomogeneous structures occur at various length and temporal scales across the fluidized beds. One solution is to run simulations at very fine meshes at small time-steps. This is not always affordable and contradictory to the assumptions mentioned in the first point.

- Inter-phase momentum transfer: In addition to point 2, Coarse scale simulations are a compromise and leave unresolved structures affecting hydrodynamics of the study. However, it should be noted that drag closures modelled to account for inter-phase momentum transfer are mostly derived at a much coarser scale than the particle phase stresses. Problem of accounting for fluctuations arising from the sub-grid hydrodynamic instabilities remains unresolved.

Since the focus of this thesis is Geldart A fluidization, simulation studies using TFM will be reviewed in the later sections.

2.3.4 Discrete Particle Method (DPM)

Discrete Particle Model (DPM) lies on the second level of the multi-scale modelling as shown in the figure 2.7. Unlike TFM, DPM treats particles as discrete entities modelled as frictional contacting spheres. This numerical treatment is popularly known as Discrete Element Method (DEM) in literature [Cundall and Strack, 1979]. Fluid phase is described by the continuum TFM equations on a scale much greater than the particle size. Hydrodynamic, inter-particle, contact and gravitational forces are estimated and summed together on each particle and the resultant motion is governed by the Newton's second law of motion. Time integration is done on a time scale much smaller than the typical contact time, hence resolving each contact and particle positions are updated. As evident from figure 2.7, drag closures for the hydrodynamic interactions (same as TFM) and collision models at the particle scale are required for the model. DPM can help to validate and improve solid phase closures required for the TFM equations. A certain advantage of DPM over TFM is the realistic treatment of the particle

phase. Recent developments in the computational worlds have allowed the researchers to use computationally expensive DPM at least the laboratory scale.

DPM models have been applied extensively in literature to investigate underlying mechanics of the particulate material flow [Wu, 2012]. The strength of the discrete element methods is evident from the wide applications of it in the industrial processes. The method has been coupled with various numerical techniques such as finite element method (FEM) and computational fluid dynamics (CFD) and applied to study many different industrial processes [Wu, 2012]:

- Granular silo [González-Montellano *et al.*, 2011; Holst *et al.*, 1999]
- Fluidized beds [Guo *et al.*, 2013; Zhu *et al.*, 2008]
- Die filling and compaction [Nwose *et al.*, 2012; Wu and Guo, 2012]
- Pneumatic conveying [Ebrahimi *et al.*, 2014; Huber and Sommerfeld, 1998; Sturm *et al.*, 2010; Wee Chuan Lim *et al.*, 2006]
- Rock engineering [Jing and Stephansson, 2007]
- Ball milling [Cleary and Sawley, 2002; Mishra and Rajamani, 1992]
- Tumbling mills [Cleary, 2001]

The mechanics of inter-particle contacts in a granular assembly can be modelled via two approaches referred in literature as: Soft sphere and Hard sphere.

2.3.4.1 Hard sphere and soft sphere approach

- Hard Sphere Approach: It is an event driven approach and the collisions between particles are assumed as binary and instantaneous. Particles are treated as rigid spheres and the motion is only altered in case of a collision. Momentum conservation equation is solved and the resultant velocities of each particle are determined by the collisional parameters [Luding, 2004]. This approach was first combined with CFD to study bubble dynamics and effect of particle-particle interactions on gas-solid fluidized beds by Hoomans *et al.* [1996].
- Soft Sphere Approach: The model was first developed by Cundall and Strack [1979] and is now a very popular granular simulation technique. The soft sphere approach allows particles to overlap and calculates repulsive forces accordingly. The time scale of the contact is very low (10^{-7} s) and the simulations are run at 50 times lower than the contact time. Different contact models relating the force to the overlap can be found in the literature, reviewed here Shäfer *et al.*

[1996]. Multiple contacts are allowed between the particles, allowable overlap is typically less than 5% of the particle diameter. This approach is frequently coupled with CFD to model fluidization processes, and referred to as DEM-CFD in the literature. The method and fluidization studies will be discussed in detail in the later sections and chapter 3.

In order to compare collision modelling approach in different scenarios, van der Hoef *et al.* [2006] presented a table 2.1. This indicates that soft sphere approach is better to couple with CFD to simulate a dense weakly cohesive fluidization system. Coupling between soft sphere approach of DEM with CFD is a popular approach first developed by Tsuji *et al.* [1993] and rationalized by Xu and Yu [1997].

Table 2.1: Comparison between hard- and soft-sphere models. The symbols indicate good (++), normal (+), and not suitable (-). Reproduced from van der Hoef *et al.* [2006].

	Hard sphere	Soft sphere
Computer efficiency	++	+
Multiple contacts	-	++
Dense systems	-	++
Incorporation of cohesive force	+	++
Wide particle size distribution	++	+
Energy conservation during collisions	++	+

2.3.4.2 Coupling schemes

Different schemes have been addressed in literature for DEM-CFD coupling, according to incorporation of drag models and buoyancy terms in the momentum equation. First such classification of DEM-CFD coupling model was done by Gidaspow [1994]. Two models were proposed for gas-phase coupling equations given by Anderson and Jackson [1967].

- Model A: The pressure drop across the "mixture" phase is shared by both the gas and the solid phase. The momentum equation proposed accordingly is given as equation 2.9.

$$\rho_f \frac{\partial \epsilon \mathbf{u}_f}{\partial t} + \rho_f \nabla \cdot (\epsilon \mathbf{u}_f \mathbf{u}_f) = -\epsilon \boldsymbol{\nabla} p + \boldsymbol{\nabla} \cdot (\epsilon \tau_f) + \epsilon \rho_f \mathbf{g} - \mathbf{F}^A \qquad \textbf{(2.9)}$$

  where ϵ is porosity, $\mathbf{u}_f$, p, ρ_f and τ_f are the fluid velocity, pressure, density and viscous stress tensor, respectively, $\mathbf{g}$ is the gravitational acceleration; and $\mathbf{F}^A$ is the fluid–particle interactions force.

- Model B: The pressure drop is contributed by the gas phase only, equation 2.10

$$\rho_f \frac{\partial \epsilon \mathbf{u}_f}{\partial t} + \rho_f \nabla \cdot (\epsilon \mathbf{u}_f \mathbf{u}_f) = -\boldsymbol{\nabla} p + \boldsymbol{\nabla} \cdot (\epsilon \tau_f) + \epsilon \rho_f \mathbf{g} - \mathbf{F}^B \qquad \textbf{(2.10)}$$

Here ϵ is porosity; $\mathbf{u}_f$, p, ρ_f and τ_f are the fluid velocity, pressure, density and viscous stress tensor, respectively, $\mathbf{g}$ is the gravitational acceleration; $\mathbf{F}^A$ and $\mathbf{F}^B$ are the volumetric fluid–particle interactions forces for model A and B. $\mathbf{F}^B$ and $\mathbf{F}^A$ can be linked by a simple rearrangement [Feng and Yu, 2004].

Significant differences in the DEM-CFD simulations of bidisperse fluidized beds were first pointed out Feng and Yu [2004] and comparisons with experiments suggested Model B formulation should be more favourable. Di Renzo and Di Maio [2007] reviewed these formulation and established that the literature lacks in addressing these differences. The coupling force between the fluid and the particles is a function of the particle velocity relative to the fluid velocity and to the local concentration of the particle assembly. First, a question arises that on which scale to estimate inter-phase momentum and then how to transfer to the other scale ? As reviewed by Feng and Yu [2004], different schemes are presented in the literature:

- Scheme 1: Particle forces are calculated based on the instantaneous particle velocities and the locally averaged fluid velocity whereas the gas phase volume forces are calculated separately by a locally averaged method [Hoomans *et al.*, 1996; Kobayashi *et al.*, 2002; Tsuji *et al.*, 1993].

- Scheme 2: The gas-phase force term is estimated first by using locally averaged solid and fluid velocities as used by scheme 1. Force is then distributed back to the particles according to a weighting criterion [Mikami *et al.*, 1998; Rhodes *et al.*, 2001*a*].

- Scheme 3: Forces are estimated on the individual particles by using individual particle velocity and coarse grained fluid velocity . These forces are added together for the particles belonging to each cell and the volumetric force is calculated at the cell level [Feng and Yu, 2007; Hoomans *et al.*, 2000; Kafui *et al.*, 2002; Xu and Yu, 1997].

Scheme 1 was employed in the earliest reported DEM-CFD simulations of the fluidized systems [Tsuji *et al.*, 1993]. Since, this scheme do not satisfy Newton's third law, the approach was less preferred than scheme 2 and 3. Points of concern with the scheme 2 is how to distribute the forces back to the particles: is it based on surface area or volume of the particles? What weighting function to employ? How to calculate a mean solid phase velocity? There are many open question in the scheme 2 implementation,

however it should be pointed out that drag models available in the open literature (e.g. [Ergun, 1952; Syamlal and O'Brien, 1987]) are based on the meso-scopic variables as required by scheme 2. Scheme 3 was first implemented by Xu and Yu [1997], it is relatively straightforward than scheme 2 and has been most popular choice of three.

2.3.5 Direct Numerical Simulation (DNS)

Unlike DPM method, direct Numerical Simulation (DNS) solves the fluid flow at a smaller scale than the particle size. Particles are treated as discrete 3D spheres and solved by Newton's second law. Hydrodynamics is modelled accurately and flow details around the particles are fully resolved and instead of a constitutive law, a slip stick boundary condition is solved for particle-fluid contact. Latticle Boltzmann method is a popular DNS method to solve flow between the spheres, although other direct numerical simulation (DNS) techniques can be applied as well [van der Hoef *et al.*, 2006].

As indicated by the figure 2.7, the model is only suited for much smaller domains and computationally very expensive. DNS models are rarely applied at full laboratory scale, though recently studies have emerged with extremely high computational powers [Capecelatro *et al.*, 2014]. These models are mostly useful to provide the drag models for TFM or DPM studies ([Beetstra *et al.*, 2007*a*]) in dense gas-solid systems. Drag model derived is a function of Reynolds number and coarse grained solid fraction, expressed as a Carman Kozeny expression at lower Reynolds (Re) number and a fitting function for intermediate or high Re number added together [van der Hoef *et al.*, 2005]. A coefficient to each of the these terms is fitted on the basis of the pressure drop data, similar to the drag model derived by Ergun [1952].

2.4 Validation studies

Validation can be referred to as establishing the extent of the physics that can be captured by the model. In the CFD world, a more formal definition of validation is used: "*Process of determining the degree to which a model is an accurate representation of the real world from the perspective of the intended uses of the model*" [Oberkampf and Trucano, 2002]. Validation processes are well established in the CFD community [Oberkampf and Blottner, 1998] and benchmark cases and validation experiments are well defined. Best practice guidelines issued are available in open literature [Oberkampf and Trucano, 2002]. New tools or solution algorithms developed to optimize the working of code, can be rigorously tested against these benchmark cases. The European Research Community on Flow, Turbulence and Combustion (ERCOFTAC) maintains a classic database of benchmark cases to check validity of the code for a particular flow regime. Validation of turbulence models is a key challenge for the CFD community.

The computational solid mechanics community also benefits from guidelines published by the American Society of Mechanical Engineering (ASME) [Schwer *et al.*, 2006]. A general understanding of validation and the basic concepts of calibration are laid out by them. However, a scope of improvement is identified for laying out benchmark cases and validation experiments. In particular, the following broad points necessary for the validation procedure are identified from the ASME guide [Schwer, 2007]:

- Extensive code verification must be carried out before undertaking validation and all bugs removed.
- Initial and boundary condition must be clearly laid out as a part of the validation process.
- Component–wise validation must be carried out before moving to a complex system validation.
- It should be noted that the validation procedure is specific for a computational tool to capture a bounded realm of physics that the equations are meant to be solving.
- The capability of the model can only be assessed in the realm of physics in which model is validated. For beyond the limits of validation experiments, uncertainty quantification of predictions is still not clear. These are often referred to as *predictions*.
- Uncertainties arising from both the simulation results and experimental data should be clearly laid out for a meaningful comparison.

In the DEM community, there is a lack of validation experimental data and predictive capability of DEM is not well established. In order to asses how different research groups around the world would solve well defined geo-mechanics problems, an interesting study was conducted by Holst *et al.* [1999] and Sanad *et al.* [2001]. A computational modelling challenge was given to groups across world for blind predictions on silo and hopper flows. The reported discrepancies between these predictions ranged up to 10 times between themselves. This study highlighted a need of well established validation practices, so as to gain confidence on the predictions by DEM simulations. Since then, progress in establishing general guidelines in application of DEM to solve physical problems have been slow, but steady. Recently, benchmarking studies for DEM were laid out by Chung and Ooi [2011]. Eight benchmarking cases followed component wise particle level impact tests for verification of DEM codes. Validation procedures in complex granular flows still remain a significant challenge [Ooi, 2013].

The literature review section pointed out different multi-scale strategies to model dense multiphase flows. In the multiphase community, there are very few attempts to address verification and validation procedures for any of these strategies. Grace and Taghipour [2004] provided a rough pathway for the application of validation and verification procedures to dense multiphase system with suggested guidelines on the comparison of simulations with the experiments. Table 3 in Grace and Taghipour [2004] gives verification and validation claims, related to CFD codes and fluidized beds, made in literature prior to 2004. This study is critical on the loose usage of the terms "verification" and "validation" in the multiphase community and even concluded by saying:

> *Exaggerated claims of validation can create a false sense of the prowess of models, ultimately leading to disillusionment that could delay the development of models that could be of major benefit. Similar principles apply to efforts to confirm the validity of scaling based on dynamic similarity principles*

In more recent efforts to quantify uncertainty of predictions, National Energy Technology Labs (NETL) introduced computational challenge problems in dense phase flows which were called the NETL challenge problems [Li *et al.*, 2012*a*]. These are well defined with initial & boundary conditions and particle & fluid parameters provided. Blind predictions of certain quantities such as voidage and particle velocities using any numerical method are invited. Experimental data is published after the challenge deadline. Such efforts would close the gap between researchers working on similar problems and would help to create confidence in the multiphase tools. Grace and Taghipour [2004] identified need for close collaborations between experimentalists and simulation scientists for a more meaningful comparison between the experiments and simulation predictions. Garg *et al.* [2012] and Li *et al.* [2012*b*] laid out benchmark problems for verification and validation of the DEM-CFD code MFIX-DEM [Garg *et al.*, 2010]. These studies were extensive and covered many relevant problems but failed to address discrepancies between the simulation and experimental results. Gel *et al.* [2013] applied and demonstrated validation and uncertainty quantification methodology to multiphase computational fluid dynamics modelling of a pilot-scale circulating fluidized bed. These studies are promising route for any future modeller or tool developer in the multiphase community.

2.5 Forces acting on fluidized granular particles

Hydrodynamics of a fluidized bed system are very complex and numerically modelling each phenomenon will not only add complications to the multi-scale modelling strategy but add significant computational time. An identification of the key forces arising due to the fluid-particle and inter-particle interactions related to dense phase gas-solid fluidization process is very necessary. This section reviews the force estimations on granular assemblies.

2.5.1 Hydrodynamic forces

Fluid-particle interactions form the governing dynamics of the fluidization process. Hence, the role of these must be carefully considered and modelled for an accurate description. In the literature, hydrodynamic interactions have been described by accounting for drag forces, effect of buoyancy and unsteady terms such as virtual mass, Basset and lift forces [Kenning and Crowe, 1997]. Hydrodynamic forces and their relevance to the gas-solid fluidization processes are enlisted here:

- Fluid-particle drag (F_d): This is considered as the driving force of fluidization [Zhu *et al.*, 2007]. A theoretical understanding of fluid particle drag on a single isolated particle in creeping flows was first given by Stokes [1851]. The understanding has not been satisfactorily generalized for particulate systems and increased flow rates. The problem being that the neighbouring particles reduce the fluid flow unpredictably, resulting in shear stresses around the particle. It is well established that the drag forces are of great importance in the fluidization process and will be discussed in detail in Chapter 3.

- Pressure-gradient forces: These forces are given as $\Delta P V_p$. In a single phase steady state flow, the pressure gradient is equivalent to the $\rho_f g$, where ρ_f is the fluid density. In the multiphase flow, such an approximation can not be made and the pressure field is solved with the multiphase equations. This contribution is very important and estimated force can be given as F_d/ϵ [van der Hoef *et al.*, 2005].

- Virtual Mass (F_{vm}) and Basset forces (F_B): F_{vm} is the force required to accelerate the surrounding fluid and can be interpreted as the addition of the displaced fluid mass to the particle. F_B accounts for viscous effects on particles due to surrounding fluid and is added to account for changes in the relative velocity between the phases, leading to the boundary layer development. F_B and F_{vm} are only meaningful in fluids with high accelerations and a comparable density to the particles and these are safely neglected in literature [Hjelmfelt Jr and Mockros, 1966].

- Lift forces: These include Saffman lift forces and Magnus lift forces, and account for lift or upward force due to particle rotations. Saffman and Magnus lift forces are caused by the gradient in the velocity magnitude and due to particle rotation. In dense gas-solid fluidized beds, the effects of these forces have been shown to be minimal [Di Renzo and Di Maio, 2007].

- Turbulence: Agrawal *et al.* [2001] argued that for dense gas-solid flows, when the inertial particle forces are much greater than that of the gas, the deviatoric term in the fluid-phase stress momentum term can be safely neglected. This leads to a conclusion that the viscous terms for both laminar and turbulent phase are not important. It should be noted that for single or lean phase flows, turbulence plays an important role.

It has recently been pointed out by Di Renzo and Di Maio [2007] that there is a need for strong assessment to quantify the errors due to neglecting some of these terms.

2.5.2 Inter-particle forces

Fluidization processes are applied to a wide range of particle sizes and densities. Agglomeration and clump formation are common due to forces arising between the particles. These forces are usually attractive and are measured in the relation to the weight of a single particle. This quantification is called the granular Bond number (Bo_g) [Castellanos, 2005]. A higher granular Bond number indicates more attractive forces. A distinction between cohesion and adhesion is a mere representational one. Adhesion is defined as attraction between two different type of material whereas cohesion is defined for the same material [Kinloch, 1987]. It should be noted that, in relation to the DEM modelling, both adhesion and cohesion are used almost interchangeably. The adhesion forces can originate from different means and total attractive forces are calculated by superposition of each force. However, it is very difficult to identify the origin of adhesion. Some of the sources as reviewed from the literature are enlisted here:

- Solid bridges: common situations are: sintering, exothermic chemical reactions and recrystallization of the material. In the present context, focus is on hydrodynamics at room temperature and solid bridges are not accounted for.

- Mechanical adhesion: adhesion resulting from interlocking of surface irregularities from different shape and size particles. Typically, these are not the dominant source of adhesion. From a modelling point of view, these are extremely difficult to take account of.

- Electrostatic adhesion: occurs between charged particles due to transfer of electrons. For dry and neutrally charged powders, effects are negligible [Rietema and Piepers, 1990].

- van der Waals forces: dominant attractive forces arising from the dipole-dipole interaction and London dispersion forces. These are long range intermolecular forces which have significant effects at nanometer distances between the particles. The most simplified expression is given by equation 2.12 [Israelachvili, 2011], where A is the Hamaker constant; s is the separation distance between the surfaces; r_p and r_l are the radii of particles p and l. The equation 2.11 can be simplified to equation 2.12 for limiting condition $s << min(r_p, r_l)$ and r_{pl} is the average particle radius.

$$F_{vdw} = \frac{A}{3} \frac{2r_p r_l (r_p + r_l + s)}{s^2 (2r_p + 2r_l + s)^2} \left[\frac{s(2r_p + 2r_l + s)}{(r_p + r_l + s)^2 - (r_p - r_l)^2} - 1 \right]^2 \tag{2.11}$$

$$F_{vdwl} = \frac{A r_{pl}}{6 s^2} \tag{2.12}$$

The Hamaker constant is a function of surface chemical properties and can be estimated in the order of 10^{-20} J for most materials. F_{vdwl} decreases almost linearly with the particle size of the same material, but decrease in weight is much more in comparison with F_{vdwl}. Furthermore, F_{vdw} is inversely proportional to the square of the distance and reduces to 2 orders of magnitude by a change in separation of a few nanometers. The equation 2.11 is not a very accurate representation, as there is a singularity when the particles collide ($s = 0$). In order to avoid this, F_{vdw} is taken as constant after a minimum distance, at which it attains the maximum value. In the most strict sense, Hamaker approximated the inter-particle forces in a vacuum and the results might not be readily extended in a medium. However, the expression is readily used in literature to model inter-particle van der Waals forces [Hamaker, 1937]. To account for effects of surface asperities, the Hamaker model was modified by Rumpf [1990]. The model was developed with a single hemispherical asperity interacting with a much larger particle given by equation 2.13, where r_{asp} is the radius of asperity.

$$F_{vdw} = \frac{A r_{pl}}{12 s^2} \left(\frac{1}{1 + r_{pl}/r_{asp}} + \frac{1}{(1 + r_{pl}/r_{asp})^2} \right) \tag{2.13}$$

The equation suggests an increase in cohesion with increased asperity sizes. More modifications to the equation were given by Forsyth and Rhodes [2000] to improve the quantification of surface effects. The equations presented here to represent cohesion force are a little too complex to model, as the systematic quantification of model parameters is difficult and not readily available. Chapter 3 will provide the van der Waals equation incorporated in the DEM-CFD model.

- Liquid bridges: The forces relate to liquid fluidization when a liquid bridge is formed between the interacting particles. The forces are calculated as a function of the volume of liquid bridge. Since, the focus of this work is gas-solid fluidization, these forces are not relevant.
- Magnetic forces: These forces can exist between the metallic industrial raw material but are unlikely to develop naturally. In the scope of this work, magnetic forces will not be considered, but readers are referred to Hristov [2007]; Zhu and Li [1996] for more details on fluidization studies dominated by magnetism phenomena.

2.5.3 Other forces

Apart from hydrodynamic forces and the inter-particle forces, a fluidized particle experience contact forces from the collisions with other particles and the gravitational force. Contact force modelling will be presented in more detail in chapter 3 of this thesis.

2.6 Geldart A fluidization

2.6.1 Introduction

This section will briefly review studies of Geldart A fluidization from over five decades of research. Later sections will review state of the art for simulation studies of Geldart A regimes.

2.6.2 Notable studies from 1960-80

Before the 1950's, behaviour of fluidized powders in a disorderly and agitated manner seemed a very counter-intuitive phenomenon to the scientific community, as opposed to ordered uniform suspension [Gibilaro, 2001]. But in the 1960's, fluidization behaviour was explained theoretically as an unstable and transient phenomenon by Jackson [1963]. Work on the theoretical framework, laying out the fundamental equations and linear instability analysis of the fluidization systems was started way back in the early 1960's. This was a decade before the work by Geldart [1973] on the identification of different fluidization regimes. The first insights into stability of fluidized

beds was attributed to an unpublished work of Prof. Robert Pigford during a sabbatical at University of Cambridge [Gibilaro, 2001]. However, an independent research from Jackson [1963] was the first major published theoretical attempt into explaining why fluidized beds are intrinsically unstable. The results from Prof. Pigford were published two years later [Pigford and Baron, 1965]. As accounted by Gibilaro [2001], another interesting but unpublished work by Wallis started before Jackson [1963]. This work included terms into momentum equations to answer both the stable and unstable behaviour of fluidized beds. During the 1970's, earlier studies claiming that the "*fluidized beds are intrinsically unstable*", were refuted by many experimentalists who produced evidence of stable bed expansion [El-Kaissy and Homsy, 1976; Rietema, 1973; Verloop and Heertjes, 1970]. In particular, Geldart [1973], explicitly pointed out the uniform expansion regime. Due to these advancements many fundamental questions on the fluidization process emerged, that remain unanswered.

2.6.3 Overview of controversies and debates on Geldart A fluidization

The Geldart chart (2.1) distinguishes between type A and B particles by estimating particle diameters and densities when the window of uniform expansion tends to be very small ($U_{mf} \sim U_{mb}$) [Geldart, 1973]. This relationship was empirical and reasonably predictive, but lacked a fundamental basis to address this smooth transition. Fluidization regimes of Geldart A, especially homogeneous expansion, is notoriously intriguing and its origins are still debated in literature. Opinions on the microscopic origins of uniform expansion are divided into (1) purely hydrodynamic (2) non-hydrodnyamic yield stresses from particle-particle interactions.

2.6.3.1 Pure hydrodynamic origins

There is a gradual change of fluidization properties as the particle size decreases across the A–B transition [Geldart, 1973]. This suggested to many that such a behaviour can be explained from only accounting for the fluid-particle interactions and no inclusion of solid stresses are required in the momentum equation. Garg and Pritchett [1975] suggested that a force proportional to the gradient of particle concentration should be added to the momentum equation to adequately explain stable bed expansion. Foscolo and Gibilaro [1984] had a similar idea but argued that such a term should be added to the fluid-particle drag closure instead. Batchelor [1988] disregarded these arguments and questioned the fundamental basis of this term and argued that the fluctuations of the particle velocity leading to hydrodynamic diffusion should be incorporated into the momentum equation. This idea was further supported by the acoustic noise experiments by Cody *et al.* [1996], which quantified particle granular temperature. However, Loezos *et al.* [2002] argued that the bed studied in these experiments might not have

been in Geldart A uniform bed expansion regime but a gentle bubbling regime. Foscolo and Gibilaro [1987] extended the work of Foscolo and Gibilaro [1984] and proposed the particle bed model (PBM) to explain stable bed expansion. This work has been the cornerstone of many recent works: Mazzei and Lettieri [2008] and Di Renzo and Di Maio [2007].

2.6.3.2 Inter-particle forces responsible

On the contrary to the purely hydrodynamic origins theory, early studies in the 1960's by Anderson and Jackson [1967] and Jackson [1963] suggested that the particle phase stresses in the momentum equation are essential for the formation of an expanded bed. Researchers believe that the inter-particle contacts are responsible for stability and expansion of Geldart A beds and solid stresses should be included in the momentum equation [Sundaresan, 2003]. It has been pointed out that it is the generation of yield stresses associated with enduring particle contacts that are responsible for homogeneous expansion [Loezos *et al.*, 2002; Sundaresan, 2003]. Experimental evidence leading to this conclusion are given by Loezos *et al.* [2002]; Menon and Durian [1997*b*]; Mutsers and Rietema [1977]; Rietema [1973] and Rietema and Piepers [1990] to indicate the presence of non-hydrodynamic stresses in such a fluidized state. However, the underlying mechanism of yield stress generation is another point of debate [Hou *et al.*, 2012]. Yield stress generation can either be attributed to the adhesive interactions between the particles [Mutsers and Rietema, 1977; Rietema, 1973; Rietema and Piepers, 1990] or the compressive yield strength arising from inter-particle and particle-wall friction can be sufficient to explain homogeneous expansion [Loezos *et al.*, 2002; Sundaresan, 2003]. Such questions are far from being resolved.

2.6.4 Fluidization studies of Geldart A particles

These controversial questions are difficult to addressed with experimental studies due to lack of data at the particle scale. Multi-scale modelling strategies for Geldart A fluidization have emerged by incorporating a fundamental understanding of physics arising from previous research. As opposed to gas-solid, liquid-solid fluidization is more stable and homogeneous as the instabilities develop much slower than the gas fluidization, however the underlying mechanisms can differ significantly due to the forces associated with the fluids. It is again emphasized that the present work only concerned with gas-solid fluidization.

2.6.4.1 TFM studies

Early TFM studies to predict the hydrodynamics of Geldart A particles have over-predicted bed expansion in the risers [Agrawal *et al.*, 2001; Andrews IV *et al.*, 2005;

Yang *et al.*, 2003]. These studies pointed out that an ad-hoc application of drag models to the heterogeneous fluidization is a major cause of this discrepancy. This led to the inception of modified or filtered drag models that could account for sub-grid structures [Igci and Sundaresan, 2011; Yang *et al.*, 2004]. Others studies pointed out that the issues related to particle level physics cannot be resolved in the continuum modelling framework [Wang *et al.*, 2009]. Recently, Wang *et al.* [2011*b*] pointed out that the resolution of the spatial length scale might be responsible for severe over-prediction of bed expansion by TFM. It should be noted that these continuum studies are mostly based on the view-point of purely hydrodynamic origins of the uniformly expanded bed. The studies do not include the effect of inter-particle forces in the constitutive relations of solid stresses. TFM studies by Mazzei and Lettieri [2008] added elastic terms to the momentum equations, which were similar to what was suggested by Foscolo and Gibilaro [1984], to predict stable expansion of Geldart A particles. A state of the art review of TFM modelling of Geldart A particles can be found in Wang *et al.* [2009].

2.6.4.2 DEM-CFD studies

DEM-CFD studies have given more promising results for simulations of Geldart A fluidization, mostly due to the ability to resolve forces at the particle scale [Zhu *et al.*, 2007]. The model requires a constitutive model to approximate hydrodynamic forces at the particle scale and it is not a fully resolved fluid-particle model. The strength of this model lies in fully capturing the inter–particle physics and yet improving computational tractability by not describing the fluid field completely. The earliest successful attempt to reproduce an expanded bed regime through DEM-CFD was reported by Rhodes *et al.* [2001*a*,*b*] on a 2D bed. Emphasis was laid on the importance of including inter-particle cohesion forces for stable bed expansion. Similar 2D studies by Yu and Xu [2003] showed that the mechanism of the bed expansion was a complex interplay between hydrodynamic and non-hydrodynamic forces. Ye *et al.* [2004, 2005] and Pandit *et al.* [2005, 2006] presented studies of different gas and particle parameters that influence the formation of an expanded bed. It was found that increasing the cohesive strength at the contact level leads to a transition from Geldart B to C. These studies were based on a 2D bed and lacked a direct comparisons with the experiments.

Based on these earlier studies, Hou *et al.* [2012] presented a micro-mechanical study of Geldart A fluidization regimes. The emphasis was laid on correlating micro-structural quantities coordination number and porosity. Several issues relating to the stability and formation of an expanded bed were addressed but no definite conclusions were reached. However, this study stated that the reproduction of the Geldart A phenomenon was sensitive to all the model parameters, yet no details were presented on the permissible range. Recently, 2D DEM-CFD studies by Yang *et al.* [2013] investigated the

effect of surface energy on the transition from fixed to bubbling gas-fluidised beds by employing an adhesive contact model developed by Thornton and Ning [1998]. The study was qualitative and concluded that the expanded bed window (U_{mb}-U_{mf}) increases with increasing cohesive strength, but could not point out transition from Geldart A to C regimes. The most recent DEM-CFD studies are conducted by Kobayashi *et al.* [2013] employing a dynamic adhesion force model. They investigated the role of contact model parameters influencing the fluidization behaviour of weakly cohesive powders.

All DEM-CFD studies presented until now, focussed mainly on adding an inter-particle force term modelled via different adhesion models to reproduce uniform expansion [Hou *et al.*, 2012; Kobayashi *et al.*, 2013; Yang *et al.*, 2013; Ye *et al.*, 2004, 2005]. However, a noteworthy mention is the DEM-CFD study conducted by Di Renzo and Di Maio [2007] who without including cohesion terms and demonstrated that bed expansion rate was captured quantitatively. Chapters 6, 7 and 8 of this thesis will attempt to address several issues related with the Geldart A fluidization regimes in the DEM-CFD framework.

Chapter 3

DEM-CFD Methodology

3.1 Introduction

DEM-CFD simulations have been employed extensively to study the dynamics of dense gas-solid fluidization process. Even though the methodology is well established, there is still no unanimous consensus on the exact underlying fluid equations and the numerical treatment of certain terms [Di Renzo and Di Maio, 2007]. This chapter presents the DEM-CFD methodology, implemented by coupling two popular open-source codes. The code was originally developed from collaborative work by at Princenton [Xiao and Sun, 2011]. In this study, the code has been further developed with new capabilities like bi-disperse drag models and post processing tools added. An extensive verification and validation of this code is presented in chapters 3 and 4.

Specifically, the field operational library OpenFOAM is used to construct upon a fluid solver, which is based on an existing TFM multiphase model there within [Rusche, 2003]. The Molecular Dynamics (MD) code LAMMPS is used to solve the DEM equations [Plimpton, 1995]. Some of the key features of the hybrid DEM-CFD code include:

- Open-source C++ based libraries providing an open architecture are coupled together using MPI libraries.
- BubbleFOAM, a TFM model based in OpenFOAM library [Rusche, 2003], is modified to couple with the DEM equations. The solver employs the finite volume method for discretization. The momentum transfer terms are treated implicitly leading to an improved numerical stability.
- Unstructured meshes and complex geometries are within the capabilities of the OpenFOAM environment but not so straightforward in LAMMPS.

- A soft sphere approach employing various visco-elastic contact models is used to resolve particle collisions with a highly efficient DEM solver.

3.2 Gas phase equations

The fluid velocity at each point in space is replaced by its average, taken over a spatial domain large enough to contain many particles but still small compared to the whole region occupied by the flowing mixture. The locally averaged incompressible continuity and momentum equations for the gas phase are given by [Anderson and Jackson, 1967; Jackson, 1997]:

$$\frac{\partial \epsilon}{\partial t} + \boldsymbol{\nabla} \cdot (\epsilon \mathbf{u}_f) = 0, \tag{3.1}$$

and

$$\rho_f \frac{\partial \epsilon \mathbf{u}_f}{\partial t} + \rho_f \nabla \cdot (\epsilon \mathbf{u}_f \mathbf{u}_f) = -\boldsymbol{\nabla} P + \boldsymbol{\nabla} \cdot \tau_f + \epsilon \rho_f \mathbf{g} - \mathbf{I}_f, \tag{3.2}$$

where ϵ is porosity, $\mathbf{u}_f$, P, ρ_f and τ_f are the fluid velocity, pressure, density and viscous stress tensor, respectively; $\mathbf{g}$ is the gravitational acceleration; and $\mathbf{I}_f$ is the inter-phase momentum transfer term arising due to fluid–particle interactions.

These equations are based on Model B as distinguished by Feng and Yu [2004] and reviewed in section 2.3.4.2. The deviatoric stress tensor τ_f include the viscous stresses also. The porosity term ϵ is calculated from the particle positions supplied by the DEM solver. An exact procedure for the porosity calculations will be presented at a later section. The fluid momentum equations are discretized and solved on an Eulerian grid by a finite volume method. The PISO solution procedure is followed to solve the fluid momentum equation and can be summarized as follows:

- Momentum prediction: solve the equation using the pressure field and the external forcing (like the interphase momentum term), available from the previous time step
- Pressure solution: solve the pressure equation, and update the pressure field.
- Velocity correction: correct the velocity field using the updated pressure field.
- Repeat step 2 and 3 until convergence.

The inter-phase momentum equation terms are treated semi-implicitly to improve numerical stability (details can be found at Xiao and Sun [2011]). The convection and diffusion terms are discretized with a blend of central difference (with second-order

accuracy) and upwind difference (with first order accuracy), respectively. An implicit first-order Euler scheme is used for the time integration of the momentum equation.

3.3 Discrete element method

The Newtonian equations of motion are solved for each particle in a Lagrangian framework [Cundall and Strack, 1979]. The equations for the translational and rotational movement given by:

$$m_i \frac{d}{dt}\mathbf{v}_i = \mathbf{f}_{\mathrm{c}i} + \mathbf{f}_{\mathrm{fp}i} + m_i\mathbf{g} + \mathbf{f}_{\mathrm{vdw}i} \tag{3.3}$$

and

$$I_i \frac{d}{dt}\boldsymbol{\omega}_i = \mathbf{T}_i, \tag{3.4}$$

The mass, moment of inertia, velocity, rotational velocity, force and torque of particle i are denoted by m_i, I_i, $\mathbf{x_i}$, $\boldsymbol{\omega}_i$, $\mathbf{f_i}$ and $\mathbf{T_i}$, respectively. It is pointed here that bold symbols indicate vectors and $\mathbf{v_i}$ implies $[v_{xi}, v_{yi}, v_{zi}]$.

The total force acting on a particle is calculated as the sum of total contact, cohesion, gravitational and fluid interaction forces. The contact force ($\mathbf{f}_c$) is calculated as a sum of all the forces due to collisions with neighbouring particles. The cohesion force ($\mathbf{f}_{vdw}$) is calculated as a sum of all pair-wise cohesive forces due to the other particles in the vicinity. The fluid-particle interaction force ($\mathbf{f}_{\mathrm{fp}}$) is obtained from a drag model, which is based on coarse grained fluid and particle variables. The total torque $\mathbf{T}_i$ results from a vector summation of the torque at each particle–particle contact. It is assumed that the fluid-particle interaction does not contribute to the rotational motion.

The $\mathbf{f}_{vdw}$ term is only added when simulating cohesive interactions. These forces are non-contacting long range forces and are implemented with a cut off distance (beyond which they are not important). Contact and cohesion forces are pair wise and in totality Newton's third law is followed when implementing these forces. Collisions of the particle with the physical walls are resolved by assuming the wall as an infinite mass particle. Following steps are enlisted to solve the dynamics of fluidized granular particle motion by the DEM equations:

- Neighbour list building: Identify the neighbouring particles that are in actual contact or in the vicinity of the adhesion sphere of influence, using the particle positions information.

- Contact Model: Calculate the forces due to the inter-particle collisions and the energy dissipation due to the frictional and viscous damping.
- Cohesion Model: Calculate the inter-particle adhesive forces.
- Time-step calculations: Estimate the particle-particle time-step based on the contact model employed and its parameters.
- Drag Model: Calculate the fluid-particle interaction force from the coarse-grained quantities. These calculations are done at the fluid time step which is much greater than the particle time step.
- Time integration: Evolve the particle positions and velocities to the next particle time-step using the forces calculated from above steps.

These steps would be briefly discussed in following subsections. A detailed explanation and implementation of each step can be found at Plimpton [2005].

3.3.1 Neighbour lists

DEM time-step is typically of the order of 10^{-7} s. In order to calculate the forces by contact models on each particle, one has to loop over each particle twice per time step. This makes the DEM computations very expensive. The computational load can be reduced by maintaining neighbour lists to keep a track of only the neighbouring particles of each particles in the system. Efforts are done to minimize the neighbour list size without omitting any force pair: contact or cohesion. In literature, three such algorithms are employed to the build neighbour lists:

- Verlet Neighbour List (VNL): A maximum search radius is supplied as an input parameter, which is more than the cohesion influence of sphere. This radius is decided by: (1) the dynamics of the system (2) the particle time-step. A lower search radius can decrease computational times drastically, but there is a risk of omitting some force pairs. A conservative search radius would be around 2-2.5 times diameter of the average particle size in the domain. It should be noted that the neighbour list is updated only so often and not at every particle time step.
- Link Cells: The simulation domain is divided into a number of sub-domains with a bin size around 2-3 diameter of particle. A list of all the particles is maintained for every sub-domain and the contacts are only checked within the sub-domain. Computational costs of this method is slightly more than the VNL method due to extra costs associated with keeping a track of all the contacts across the boundaries. However, this algorithm can be employed more efficiently if the code is parallelized. LAMMPS employs a link cell algorithm for contact detection.

- Lattices: Lattice points are defined within the domain. Each particle is indexed in relation to a lattice point and a neighbour list is created for all cells within a particle diameter d.

3.3.2 Contact model

Contact models are used to determine forces on the particles based on the particle's colliding velocities and material properties. Consider two contacting particles (i, j), with radii (a_i, a_j), at positions ($\mathbf{r}_i$, $\mathbf{r}_j$), with velocities ($\mathbf{v}_i$, $\mathbf{v}_j$) and angular velocities $\boldsymbol{\omega}_i$, $\boldsymbol{\omega}_j$ (as shown in the figure 3.1).

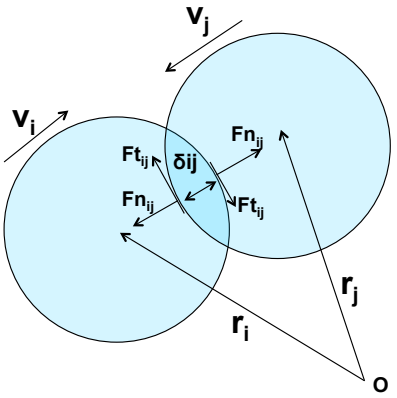

Figure 3.1: Schematic of two particles i and j in contact and position vectors $\mathbf{r}_i$, $\mathbf{r}_j$, respectively, with overlap δ_{ij}. Resultant normal and tangential forces acting on each particle are shown here.

The normal compression δ_{ij}, relative normal velocity $\mathbf{v}_{\mathrm{n}_{ij}}$, and relative tangential velocity $\mathbf{v}_{\mathrm{t}_{ij}}$ can be given as follows:

$$\delta_{ij} = d - r_{ij}, \tag{3.5}$$

$$\mathbf{v}_{\mathrm{n}_{ij}} = (\mathbf{v}_{ij} \cdot \mathbf{n}_{ij})\mathbf{n}_{ij}, \tag{3.6}$$

$$\mathbf{v}_{\mathrm{t}_{ij}} = \mathbf{v}_{ij} - \mathbf{v}_{n_{ij}} - (a_i\boldsymbol{\omega}_i + a_j\boldsymbol{\omega}_j) \times \mathbf{n}_{ij}, \tag{3.7}$$

where $d = a_i + a_j$, $\mathbf{r}_{ij} = \mathbf{r}_i - \mathbf{r}_j$, $\mathbf{n}_{ij} = \mathbf{r}_{ij}/r_{ij}$, with $r_{ij} = |\mathbf{r}_{ij}|$ and $\mathbf{v}_{ij} = \mathbf{v}_i - \mathbf{v}_j$. The rate of change of the elastic tangential displacement $\mathbf{u}_{\mathrm{t}_{ij}}$, set to zero at the initiation of a contact is:

$$\frac{\mathrm{d}\mathbf{u}_{\mathrm{t}_{ij}}}{\mathrm{d}t} = \mathbf{v}_{\mathrm{t}_{ij}} - \frac{(\mathbf{u}_{\mathrm{t}_{ij}} \cdot \mathbf{v}_{ij})\mathbf{r}_{ij}}{r_{ij}^2}. \tag{3.8}$$

The last term in equation (3.8) arise from the rigid body rotation around the contact point and ensures that $\mathbf{u}_{\mathrm{t}_{ij}}$ always lies in the local tangent plane of contact. Popular

contact models that are employed in the literature are a combination of spring, slider and a dash-pot. This assembly is used to estimate the normal and tangential contact forces [Cundall and Strack, 1979]. The capability of the model to capture collisional behaviour depends upon the force-displacement ($\mathbf{F}_{\mathrm{n}_{ij}} - \delta_{ij}$) relationships. A brief listing of different contact models is provided here. For a more comprehensive details on each model, readers are referred to LAMMPS user manual [Plimpton, 2005].

- Cohesion-less normal contact models: Common examples of these are linear spring dash-pot (first used by Cundall and Strack [1979]). Hertz-midillin contact model [Tsuji *et al.*, 1992], hysteretic spring models that dissipates energy [Walton and Braun, 1986] and models accounting for plastic deformations [Thornton, 1997].

- Elastic adhesive contact models: These model include effect of adhesive forces to simulate fine powders. Commonly used models are JKR [Johnson *et al.*, 1971], DMT [Derjaguin *et al.*, 1980] and models accounting for both adhesion and plasticity [Thornton and Ning, 1998],[Luding, 2008],[Thakur *et al.*, 2014].

In the present work, a linear spring-dashpot model is employed for the contact force model with the static friction between the particles, modelled according to the Coulomb's law (given below).

$$\mathbf{F}_{\mathrm{n}_{ij}} = f(\delta_{ij}/d)(k_{\mathrm{n}}\delta_{ij}\mathbf{n}_{ij} - \gamma_{\mathrm{n}} m_{\mathrm{eff}}\mathbf{v}_{\mathrm{n}_{ij}}), \tag{3.9}$$

$$\mathbf{F}_{\mathrm{t}_{ij}} = f(\delta_{ij}/d)(-k_{\mathrm{t}}\mathbf{u}_{\mathrm{t}_{ij}} - \gamma_{\mathrm{t}} m_{\mathrm{eff}}\mathbf{v}_{\mathrm{t}_{ij}}), \tag{3.10}$$

where $k_{\mathrm{n,t}}$ and $\gamma_{\mathrm{n,t}}$ are the spring stiffness and viscoelastic constants, respectively, and $m_{\mathrm{eff}} = m_i m_j/(m_i + m_j)$ is the effective mass of spheres with masses m_i and m_j. The corresponding contact force on particle j is simply given by Newton's third law, i.e., $\mathbf{F}_{ji} = -\mathbf{F}_{ij}$. The function $f(\delta_{ij}/d) = 1$ is for the linear spring-dashpot model, and $f(\delta_{ij}/d) = \sqrt{\delta_{ij}/d}$ is for Hertzian contacts with viscoelastic damping between spheres.

3.3.3 Cohesion Model

The cohesion forces are modelled as long range, van der Waals forces acting between two particles. The attractive forces $\mathbf{F_{vdw}}$ act in a direction of the normal vector which joins the centre of interacting particles.

$$\mathbf{F_{ij}^{vdw}} = -\frac{Ad^6}{6s^2(s+d)^3(s+2d)^2}\mathbf{n_{ij}} \tag{3.11}$$

Here A is the Hamaker constant; d is the diameter of the particles; s is the separation between the particle surfaces and $\mathbf{n_{ij}}$ is the normal contact vector between the particles i and j. For separations which are much smaller than the diameter of the particles ($s <<<< d$), the equation reduces to:

$$\mathbf{F_{ij}^{max}} = -\frac{Ad}{24s^2}\mathbf{n_{ij}} \tag{3.12}$$

According to the equation 3.12, a particle collision will lead to a singularity. A minimum cut off separation, s_{min} is used beyond which the cohesion force is treated as a constant, with force equal to its value at s_{min}. The present simulations employ $s_{min} = 4$ nm, which is in the order of typical intermolecular distances. van der Waals forces reduce significantly at the long distances. In order to speed up the simulations, a maximum cut-off separation between the particle surfaces is set equal to $d/4$, beyond which the cohesive forces are not calculated. A dimensionless quantity called granular Bond number (Bo_g) is defined as the ratio of $\mathbf{F_{ij}^{max}}$ and weight of the particle mg. This quantity would be used as a measure of cohesive strength of the bed.

3.4 Interphase momentum transfer

The coupling between the gas phase and particle motion is implemented through a volume averaged fluid–particle interaction term ($\mathbf{I}_\mathrm{f}$) in the gas momentum equation. According to the Newton's third law, negative of a similar term is added to the particle equation of motion ($\mathbf{f}_{\mathrm{fp}i}$):

$$\mathbf{f}_{\mathrm{fp}i} = -V_{\mathrm{p}i}\boldsymbol{\nabla} p + \frac{\beta_i V_{\mathrm{p}i}}{\phi}\left(\mathbf{u}_{\mathrm{f}i} - \mathbf{v}_i\right), \tag{3.13}$$

Here $V_{\mathrm{p}i}$ is the volume of particle i; $\phi = (1-\epsilon)$ is the solid volume fraction; $\mathbf{u}_{\mathrm{f}i}$ is the fluid velocity extrapolated to the particle i position and β_i is the particle based drag coefficient. The total interaction $\mathbf{I}_f$ in a fluid cell is calculated by adding all particle–fluid interaction forces in the cell as

$$\mathbf{I}_f = \frac{1}{V_{\mathrm{cell}}}\sum_{i=1}^{n}\mathbf{f}_{\mathrm{fp}i}W_i, \tag{3.14}$$

where V_{cell} is the volume of the fluid cell and W is the weighting function accounting for the contribution of a particle. The weights are calculated according to a Box-car or a Gaussian function [Xiao and Sun, 2011]. The drag force is first calculated on each individual particle and then volume averaged to give it back to the fluid cell. In order

to calculate β_i, many different correlations derived in limited conditions are employed in ad-hoc ways, to dynamic conditions present in a fluidized bed.

3.4.1 Drag model closures

The drag coefficient used in the Eq. 3.13 can be written as

$$\beta = 18\mu\phi(1-\phi)\frac{F}{d^2}, \tag{3.15}$$

where F is the drag force, non-dimensionalized by the Stokes–Einstein drag force ($3\pi\mu d\left(\mathbf{u}_{\mathrm{f}i} - \mathbf{v}_i\right)(1-\phi)$); and μ is the fluid viscosity. This dimensionless drag force can be expressed as a function of solid fraction (ϕ) and the particle Reynolds number ($Re = \epsilon\rho_f d_i \left|\mathbf{u}_{\mathrm{f}i} - v_i\right| / \mu$), for a particle of diameter d.

3.4.1.1 Traditional drag models

Drag models correlations were traditionally deduced from the experiments [Di Felice, 1994; Ergun, 1952; Wen and Yu, 1966]:

- Measuring pressure drop across a fixed bed [Ergun, 1952], fluidized with different inlet fluid velocities. The pressure drop was related to the particle and fluid properties along with the operational conditions.
- Sedimentation of small particles in a very dilute regime [Richardson and Zaki, 1954] and correlating the drag forces to the terminal velocity and voidage function (form ϵ^n).
- Wen and Yu [1966] used experimental data of Richardson and Zaki [1954] and correlated drag forces by a different function with a slightly better fit.
- Sedimentation of mono-disperse particles in a dense phase regime [Di Felice, 1994], and introducing an explicit function of voidage to take into account of restricted flow around many particles.

For a list of more drag models, readers are referred to the fluidization hand book by Yang [2003]. A combinations of these drag models also been used to cover a wide range of solid fractions and flow conditions found in a fluidized bed. The most popular of these models are by Gidaspow [1994] which combines the Ergun [1952] and the Wen and Yu [1966] drag models, given by equation 3.16.

$$F_{\mathrm{EWY}}(\phi, Re) = \begin{cases} (1 + 0.15Re^{0.687})(1-\phi)^{-3.65} & \phi \leq 0.2 \\ \frac{150}{18}\frac{\phi}{(1-\phi)^2} + \frac{1.75}{18}\frac{Re}{(1-\phi)^2} & \phi > 0.2 \end{cases}, \tag{3.16}$$

Modifications to the Richardson and Zaki [1954] correlations were done by Syamlal and O'Brien [1987] to get a better drag model applicable at high solid fractions and extended to cover particle Re numbers upto 10. To account for non-spherical particles, drag coefficient expression was developed by Haider and Levenspiel Haider and Levenspiel [1989], based on the Di Felice [1994] equations:

$$F_{\mathrm{HL}}(\phi, Re) = \left[(1 + A(Re)^B) + \frac{C}{1 + \frac{D}{Re}}\right](1-\phi)^{-\chi}, \tag{3.17}$$

where

$$\chi = 4.7 - 0.65\exp(-(1.5 - \log_{10} Re)^2/2),$$
$$A = \exp(2.3288 - 6.4581\alpha + 2.4486\alpha^2),$$
$$B = 0.0964 + 0.5565\alpha,$$
$$C = \exp(4.905 - 13.8944\alpha + 18.4222\alpha^2 - 10.2599\alpha^3),$$
$$D = \exp(1.4681 + 12.2584\alpha - 20.7322\alpha^2 + 15.8855\alpha^3),$$

α is the particle sphericity which is defined as the ratio of the surface areas between a spherical particle with an equivalent volume and the irregular particle.

3.4.1.2 Drag models derived from LB simulations: Monodisperse

To capture physics of the system accurately, constitutive laws should be derived from the first principle. However, due to complexity of fluid-particle systems, these derivations were not possible until early 2000's. DNS simulations were employed to calculate the drag exerted by a fluid flow on a bed of randomly distributed monodisperse particles, at low Re numbers. First of these calculations were done by Hill *et al.* [2001*b*] and Hill *et al.* [2001*a*] to cover a wide range of Re and solid fractions (ϕ). The drag model was presented in a functional form with a good fit of the data. Later, similar studies by van der Hoef *et al.* [2005] based on the permeability data were presented with a much complex function, but only limited to low Re numbers. Major hurdles in the derivations of these drag models were:

- Computational times: particle numbers as low as 500 were used with a periodic domain.
- Difficulty in finding correlated functions: Karman-Cozeny type correlation was employed for a low Re number. But for higher Re number, a best fit is difficult to get with a highly scattered data. This leads to considerable approximations and errors.

These studies were extended to a moderate or intermediate Re number regime by Benyahia *et al.* [2006] and Beetstra *et al.* [2007*a*]. Equation for the Beetstra *et al.* [2007*a*] drag model is given by:

$$F_{\mathrm{BT}}(\phi, Re) = \frac{10\phi}{(1-\phi)^2} + (1-\phi)^2(1+1.5\phi^{1/2}) + \frac{0.413Re}{24(1-\phi)^2}\left[\frac{(1-\phi)^{-1} + 3\phi(1-\phi) + 8.4Re^{-0.343}}{1+10^{3\phi}Re^{-(1+4\phi)/2)}}\right]. \tag{3.18}$$

3.4.1.3 Drag models derived from LB simulations: Bidisperse

In spite of industrial raw materials showing wide distribution in sizes, it was only until mid 2000's that considerable research efforts were put into the development of drag models applicable for poly-disperse systems. Beetstra *et al.* [2007*a*] fluidized 150 different combinations of Re and ϕ with diameter ratio varying from 1:1.5 to 1:4 at different compositions. It should be noted that Beetstra *et al.* [2007*a*] drag model was derived for accuracy and simplicity, but not completely from theoretical considerations.

Let d_i, N_i, ϕ_i be the diameter, number and packing fraction of $i = 1, 2$ individual species and dimensional less drag force for each species be F_i, Beetstra *et al.* [2007*a*] defined these parameters in the dimensionless forms as:

$$x_i = \frac{\phi_i}{\phi} \tag{3.19}$$

$$y_i = \frac{d_i}{< d >} \tag{3.20}$$

Here, $< d >$ is the Sauter mean diameter, given by:

$$< d >= \frac{\sum_{i=1}^{c} N_i d_i^3}{\sum_{i=1}^{c} N_i d_i^2} \tag{3.21}$$

Here, c is the number of species present in the system. The dimensionless drag for species i is given by a similar equation defined earlier for a monodisperse system as $F_i = F_{d,i}/(3\pi\mu d_i U)$. A final equation for F_i in terms of dimensionless quantities and the dimensionless drag (defined for monodisperse systems) is given by equation 3.18:

$$F_i = ((1-\phi_i)y_i + \phi y_i^2 + 0.064(1-\phi)y_i^3)F(\phi, < Re >) \tag{3.22}$$

Here, $< Re >$ indicates that the Re number calculations are based on the averaged Sauter diameter $< d >$. This expression will be used in segregation studies for predicting segregation rates in a bidisperse fluidized bed. The expression is based on the fact that the particle with a smaller diameter should have lower drag than estimated by monodisperse expression. And similarly, particles with a higher diameter should have a higher drag. In the equation 3.22, the expression in front of $F(\phi, < Re >)$ can be seen as a correction for bidispersity. Yin and Sundaresan [2008] further extended the drag model expression to include effects of particle hydrodynamics. It was argued that, hydrodynamics of the bidisperse system is affected by (1) difference in the solid fractions of each species and (2) difference in the relative velocity of the species.

Modifications were made by Yin and Sundaresan [2008] based on several inconsistencies from theoretical point of view. The drag form at low Re numbers, to account for bidispersity only, is given by equation 3.23. A polynomial function based on ϕ is given by 3.24. Here $F_{Di-fixed}$ is the drag acting on per particle of species i on a fixed bed and $F^*_{D-fixed}$ is given by equation 3.22.

$$F^*_{Di-fixed} = \frac{1}{1-\phi} + \left(F^*_{D-fixed} - \frac{1}{1-\phi} \right) [a y_i + (1-a) y_i^2] \tag{3.23}$$

$$a(\phi) = 1 - 2.66\phi + 9.096\phi^2 - 11.338\phi^3 \tag{3.24}$$

Later Holloway *et al.* [2010] extended the drag model to include the effect of species based hydrodynamics and changed the working form, given by equation 3.25. The dimensionless drag form was expressed as a function of the relative velocity of both the species 1 and 2 with the fluid:

$$f_{Di} = -\beta_{ii} \Delta U_i - \beta_{ij} \Delta U_j \tag{3.25}$$

Here, f_{Di} is the average drag force per unit volume of type i, and β_{ij} is the volume friction coefficient. The influence on the drag of particle phase i due to the motion of particle phase j is reflected in the off-diagonal components of the matrix [Holloway *et al.*, 2010]. The final expression for average fluid-particle drag per particle of species i (F^*_{Di}) was given by 3.26. This drag model will be referred to as HYS 2010 model.

An expression for $F^*_{Di-fixed}$ is given by equation 3.23. α_{ij} is a logarithmic function of the ratio between the lubrication cut-off λ and the size of the smaller particle species of the two, given by equation 3.27.

$$F^*_{Di} = -3\pi(1-\phi)\left[y_i \Delta Re_i F^*_{Di-fixed} + \sum_{j\neq i} \frac{2\alpha_{ij}\phi_j y_i^3(\Delta Re_i - \Delta Re_j)}{y_i^2/F^*_{Di-fixed} + y_j^2/F^*_{Dj-fixed}}\right] \quad \textbf{(3.26)}$$

$$\alpha_{ij} = 1.313 log_{10}(min(d_i, d_j)/\lambda) - 1.249 \quad \textbf{(3.27)}$$

Hydrodynamics of the fluidized bed depends heavily upon the drag model applied. It should be noted that there is no single drag model derived explicitly for a full scale fluidized bed in heterogeneous conditions.

3.4.2 Algorithm for inter-phase momentum exchange

The overall algorithm for fluid-particle interaction used in the open-source DEM-CFD code can be summed up in the following way manner:

1. Calculate the inter-phase momentum term from the previous time step velocity fields (u_f^{n-1}, P_f^{n-1}).
2. Substitute the drag terms in the momentum equation and solve iteratively the momentum equation using PISO alogithm described earlier. Update the pressure and velocities field to current time step: (u_f^{n-1}, P_f^{n-1}) to (u_f^n, P_f^n)
3. Calculate the inter-phase momentum term based on (u_f^n, P_f^n).
4. Compute the fluid particle drag on each particle based on (u_f^n, P_f^n) and evolve particle position using DEM simulator.
5. Obtain the voidage (ϵ) and the coarse grained particle velocity fields via averaging from DEM particle positions and velocity.
6. Give these field back to the fluid momentum equation as an input for (n+1) time step.

3.5 Numerical methods

DEM-CFD code works on two time scales: (1) inter-particle (2) fluid-particle interaction. Inter-particle contact time for the collisions is estimated from the contact force model employed. For a linear spring dash-pot model, a maximum contact time can be calculated in terms of spring coefficient, effective mass of particles, and the damping coefficient for collision between the particles m and n (equation 3.28). The time step

for DEM integration is typically kept fairly low, around 2% of the contact time. For fluid-particle interaction, the particle relaxation times τ_p is used to quantify the time scales of the interactions. For a stationary particle released in a fluid, relaxation times can be calculated with a constant slip velocity assumption (defined as $u_{ri} = u_{pi} - u_{fi}$) by the equation 3.29.

$$t_{mn}^{col} = \pi \left(\frac{k_{mn}}{m_e} - \frac{\eta_{mn}^2}{4m_e} \right)^{-1/2} \tag{3.28}$$

$$\tau_p = \frac{U_e m_i}{\epsilon_f f_{di}} \tag{3.29}$$

where ϵ_f is the void fraction; f_{di} is the drag force acting on particle; U_e is the slip velocity and m_i is the mass of the particle i. Another important consideration for the fluid time step is the Courant-Friedrichs-Lewy (CFL) conditions based upon the mesh size employed [Xiao and Sun, 2011]. Particle time steps are decided by the minimum of the two time scales, whereas fluid time step is decided by the CFL conditions. Furthermore, turbulent length scales can be important especially in case of high Re number and lean phase cases such as pneumatic conveying Sommerfeld and Kussin [2003]. tau_p and t_{mn}^{col} governs the fluid and particle time steps. For gas-solid interactions, the particle time steps are 2-3 order of magnitude more than the fluid time steps.

3.6 Post processing of DEM data

3.6.1 Introduction

Post processing and visualization of particle discrete data is challenging for industries, as the meaningful information is hidden in the enormous amount of DEM data. For this reason, it is desired to find a continuum or an averaged description of the solid flow. Following challenges are identified for post processing DEM data of the fluidized beds:

- Presence of mesoscopic organized structures such as bubbles, makes the spatial averaging length scale dependent. This essentially means that the continuum picture would be a function of averaging parameters.
- Particle force data are represented as a continua, challenge is to average the data consistently and conserving momentum at each continuum cell.
- Temporal averaging of such a dynamic process might not be representative of the process itself and information might not be very useful for design or optimization

purposes. However, post-processing of DEM data is important for the correct comparison between the experimental and the simulation results. For exampple, spatial-temporal average of the MR data was performed to obtain the voidage, particle velocity and granular temperature profiles in the experiments [Holland *et al.*, 2008]. In order to have a direct comparison between DEM data and MR measurement, compatible post-processing techniques should be used.

In order to tackle these challenges, a coarse graining method is presented here which is based on the procedures by Goldenberg and Goldhirsch [2004]; Goldhirsch and Goldenberg [2002]. Coarse-graining particle position and velocity data provide a continuum solid fraction and velocity field (equation 3.30).

$$< \psi(\mathbf{r}, t) >= \sum_{p} \psi(\mathbf{x_p}) w(\mathbf{x} - \mathbf{x_p}(t)) \tag{3.30}$$

Specifically, the spatial averaged solid volume fraction ϕ at the location $\mathbf{r}$ is calculated as:

$$\rho(\mathbf{r}, t) = \sum_{i} m_i \phi(\mathbf{r} - \mathbf{r_i}(t)) \tag{3.31}$$

By substituting momentum P, instead of $\psi(x_p)$ in equation 3.31, a coarse grained $P(x_p)$ can be found. The coarse graining schematic is shown in the figure 3.2. The weighting function used in this study are Gaussian and Heavi-side, given by equations 3.30 and 3.31, respectively. The weights related to certain particles are calculated according to their distances from the centre of the coarse graining volume (shown in the figure 3.2). Every weight function have a property that the area under the curve is 1. Similar concept can be extended to the temporal averaging.

$$\psi_G(x) = \frac{1}{\sqrt{2\pi} w^3} e^{-\frac{|x - x_p|^2}{w^2}} \tag{3.32}$$

$$\psi_H(x) = \frac{1}{(4/3)\pi w^3} H(w - |x - x_p|) \tag{3.33}$$

3.6.2 Contact based force information to the stress calculations

The microscopic force equation for a single particle i could be presented as:

$$\sum_{j \neq i} \mathbf{f}_{ij} + \mathbf{b}_i = m_i \dot{\mathbf{v}}_i \tag{3.34}$$

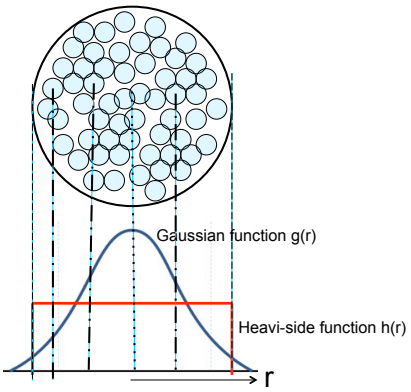

Figure 3.2: Schematic of spatial averaging at a point r situated at the centre of the sphere with radius a enclosing the particles. Two weighting function: Gaussian (equation 3.32) and Heavi-side (equation 3.33) function are shown, with weights of certain particles indicated by the the intersection of the vertical line with the weighting functions.

where $\mathbf{f}_{ij}$ is the total interaction force (cohesion and contact) between particles i and j, $\mathbf{b_i}$ is the total body force vector, m_i and v_i are mass and velocity of particle i, respectively.

A corresponding coarse-grained equation could be derived by weighted spatial averaging. The wieght function is given by:

$$\mathbf{f}_w(\mathbf{x},t)\mathbf{b}_w(\mathbf{x},t) = \sum_{i=1}^{N} m_i \dot{\mathbf{v}}_i w(\mathbf{x}_i - \mathbf{x}) \tag{3.35}$$

where,

$$\mathbf{f}_w(\mathbf{x},t) = \sum_i \sum_{j \neq i} \mathbf{f}_{ij}(t) w(\mathbf{x}_i - \mathbf{x}) \tag{3.36}$$

and,

$$\mathbf{b}_w = \sum_i \mathbf{b}_i(t) w(\mathbf{x}_i - \mathbf{x}) \tag{3.37}$$

$w(x_i - x)$ is a weighting or coarse graining function, which can be Heavi-side or Gaussian function. Coarse grained equation could be identified with the Cauchy equations.

$$\boldsymbol{\nabla} \cdot \underline{\sigma} + \mathbf{b} = \rho \mathbf{a} \tag{3.38}$$

where,

$$\mathbf{a} = (\boldsymbol{\nabla} \cdot \mathbf{v})\mathbf{v} + \frac{\partial \mathbf{v}}{\partial t} \tag{3.39}$$

The equation 3.40 could be rearranged to:

$$-\boldsymbol{\nabla}\cdot\sum_i m_i\mathbf{v}_i'\mathbf{v}_i' w(\mathbf{x}_i-\mathbf{x})+\mathbf{f}_w+\mathbf{b}_w=\rho_w\mathbf{a}_w \tag{3.40}$$

where,

$$\mathbf{a}_w=(\boldsymbol{\nabla}\cdot\mathbf{v}_w)\mathbf{v}_w+\frac{\partial\mathbf{v}_w}{\partial t} \tag{3.41}$$

$$\mathbf{v}_i'=\mathbf{v}_i-\mathbf{v}_w \tag{3.42}$$

$$\mathbf{v}_w=\frac{\sum m_i\mathbf{v}_i w}{m_i w} \tag{3.43}$$

The equation 3.40 could be identified with,

$$\boldsymbol{\nabla}\cdot\underline{\sigma}=\boldsymbol{\nabla}\cdot\sum_i m_i\mathbf{v}_i'\mathbf{v}_i' w+\mathbf{f}_w \tag{3.44}$$

The stress tensor could be further decomposed into:

$$\underline{\sigma}=\underline{\sigma}^k+\underline{\sigma}^c \tag{3.45}$$

where $\underline{\sigma}^k$ is kinetic stress that can be identified as $\sum_i m_i\mathbf{v}_i'\mathbf{v}_i' w$. The σ^c is referred to as interaction stress: a sum of cohesion and contact stresses.

$$\boldsymbol{\nabla}\cdot\underline{\sigma_c}=\mathbf{f}_w==\sum_i\sum_{j\neq i} f_{ij}w(\mathbf{x}_i-\mathbf{x}) \tag{3.46}$$

This relation poses a certain restriction on the form of the stress calculation using f_w. The form for pair-wise balanced forces $\mathbf{f}_{ij}=-\mathbf{f}_{ji}$ can given by:

$$\underline{\sigma_c}=\sum_i\sum_{j\neq i}\mathbf{f}_{ij}\otimes\mathbf{b}_{ij}(\mathbf{x},t) \tag{3.47}$$

where,

$$\boldsymbol{\nabla}\cdot\mathbf{b}_{ij}=\frac{1}{2}[w(\mathbf{x}_i-\mathbf{x})-w(\mathbf{x}_j-\mathbf{x})] \tag{3.48}$$

One choice for $\mathbf{b_{ij}}$, given by Goldenberg *et al.* [2006]:

$$\mathbf{b}_{ij}=\mathbf{b}_{ij}(\mathbf{x})=\frac{1}{2}\hat{b_{ij}}(\mathbf{x})(\mathbf{x}_j-\mathbf{x}_i) \tag{3.49}$$

A solution to equation 3.49 is the Hardy's Bond function:

$$\hat{b}_{ij}^{H}(\mathbf{x}) = \int_0^1 w(\lambda(\mathbf{x}_j - \mathbf{x}_i) + (\mathbf{x}_i - \mathbf{x}))d\lambda \tag{3.50}$$

$$\underline{\sigma}^c = \frac{1}{2}\sum_i \sum_{j \neq i} \mathbf{f}_{ij} \otimes \hat{\mathbf{b}}_{ij}^{H}(\mathbf{x})(\mathbf{x}_j - \mathbf{x}_i) \tag{3.51}$$

Consequently, solution to σ^c could be given as:

$$\underline{\sigma}^c = \frac{1}{2}\sum_i \sum_{j \neq i} \mathbf{f}_{ij} \otimes (\mathbf{x}_j - \mathbf{x}_i) \int_0^1 w(\lambda(\mathbf{x}_j - \mathbf{x}_i) + (\mathbf{x}_i - \mathbf{x}))d\lambda \tag{3.52}$$

Subsequently, $\underline{\sigma}^c$ could be written as a sum of cohesion stress ($\underline{\sigma}^{cohe}$) and contact stress ($\underline{\sigma}^{cont}$). Each of the stresses $\underline{\sigma}^{cohe}$ and $\underline{\sigma}^{cont}$ can be calculated according to equation from contact and cohesion forces and the branch vectors between the particles i and j. The stress implementations are done inside MATLAB employing different weight functions and representative volumes.

3.6.3 Coordination numbers

The coordination number is the most local measure of the packing density. It is defined as the number of contacts per particle. In this study, two kinds of coordination number (Z) would be discussed (1) mechanical coordination number (MCN) (2) cohesion coordination number (CCN). When the particles are in actual or mechanical contact i.e. when the distance between the centres of the particle is less than or equal to the sum of their radii, contact is considered as MCN. When the particles are in each others cohesion influence i.e. distance between the spheres is less than twice the maximum cohesion cut-off, the particles are considered in cohesion contacts. In meso-scopically homogeneous conditions, higher MCN would imply higher packing fraction or density.

3.6.4 Implementation of the post-processing tools

Following particle data at high temporal frequency was obtained from LAMMPS using the dump custom commands:

1. Data stored on particle centre: ID, diameter, density, position X, position Y, position Z, velocity X, velocity Y, velocity Z, total force X, total force Y, total force Z, Voronoii volume V.

2. Contact pair data: contact ID, Particle ID1, Particle ID2, Contact force FX, Contact force FY, Contact force FZ
3. Wall contact data: contact ID, Particle ID, Wall contact force FX, Wall contact force FY, Wall contact force FZ
4. Cohesion pair data: cohesion contact ID, Particle ID1, Particle ID2, Cohesion Force FY, Cohesion Force FZ, Cohesion force FZ.
5. Geometry: xlo, xhi, ylo, yhi, zlo, zhi
6. User input: Maximum coordinates for region to be meshed, number of cells in each direction X,Y,Z and coarse graining parameters: band width or the radius of coarse graining volume.

Following procedure was used to calculate the continuum data from the discrete data at each time step.

- Building Eulerian grid points, according to the input coordinates of the area to be meshed and the bin sizes.
- Based on the position of the particles, the location and weight function of each particle with respect to the Eulerian grid points is calculated.
- Porosity and momentum is calculated using the coarse graining function according to number of particles present in the coarse graining volume, momentum is divided by the porosity field to find solid velocity. In case there is no particle present in the fluid mesh, solid velocity is taken as zero.
- Solid velocity is subtracted from the instantaneous velocity of the particles to find the fluctuating velocity components. The fluctuating velocity components are again coarse grained using the weighted function to find the kinetic stresses components and the granular temperatures.
- Averaged Voronoii volume is calculated using same procedure as finding the solid velocity.

For the contact based data:

- For stress fields, contact and cohesion contact data is used.
- Each particle position is accessed from the particle data to calculate the contact or the branch vector of the particles in contact or in cohesion contact.

- For the situation when one particle is inside the coarse graining volume and other is outside, a correction length of contact vector has to be calculated as laid out by the coarse graining procedure earlier. Since the surface equation is known and the equation of line can be obtained from the branch vector, exact length and contribution can be calculated.
- Branch vector, contact or cohesion forces and the correction (if applicable) are multiplied for each contact pair added and divided by the coarse graining volume to find the contact or cohesion stress.
- Coordination numbers (Z) are calculated by keeping a counter on each mechanical or cohesion contact.

Chapter 4

Verification of the DEM-CFD model

4.1 Introduction

Multiphase flows are prevalent in many processes in the pharmaceutical, food and agricultural industries. Thanks to recent computational advancements, multi-scale modelling has become a widespread tool for furthering the fundamental understanding of multiphase flows [Deen *et al.*, 2007]. Optimization and scale up of multiphase industrial processes requires an accurate description of the hydrodynamics [Li *et al.*, 2012*b*]. Modelling of momentum exchange between the fluid and particle phases is one significant challenge in this area. In the DEM-CFD framework, fluid-particle interactions are modelled at a coarser scale and require constitutive models to close the equation. These models are referred to as drag models. A major challenge in the drag model implementation is that they are highly non-linear and algorithms to solve them are often complex. Numerous open-source and commercial codes capable of multiphase modelling at both continuum and discrete particle level have been developed recently, for example Barracuda, MP-PIC, STARCCM+, EDEM-Fluent, MFIX-DEM, CFDEM. Each of these codes have slightly different implementation of the drag models than each other. Even though, these tools have showed great capabilities, there is a general lacking of rigorous verification, validation and benchmarking. Solving complex physics of rapidly evolving gas-solid interactions by computer simulation requires sophisticated mathematical modelling and programming. An outline of this process is given here:

- First, the physics of the problem is conceptualized into a mathematical model by general observation and analysis.Key variables affecting the physics of the problem are identified, and a function found that is applicable at all the possible conditions. For example, constitutive modelling for fluid-particle interactions in dense

granular flows involves highly non-linear relation between mesoscopic solid fraction, particle Reynolds number and relative fluid-particle velocity [Beetstra *et al.*, 2007*a*].

- Mathematical sub-models that are employed to describe physics of different aspects of system are then linked together into a computer code. For example, fluid-particle interaction, particle-particle interaction, evolution of particle trajectory, influence of particles on fluid flow and vice versa, are all modelled differently and linked together in the DEM-CFD code.

- Verification of implementation is necessary to check for computer coding errors, such as poorly initialized variables taking nonsensical values, unintended variable assignment and so on. These errors might be hidden and not show up during compilation or as run time errors, but will effect the predictive capability of the tool. Such errors can lead to convergence to an erroneous solution. Verification assessment should be conducted, using relatively simple cases which are targeted to check only one or two sub-models. For example, testing particle-wall interaction by a ball dropping test in a DEM code [Chung and Ooi, 2011]. These should be relatively simple cases with well-established analytical solutions. Any errors found during the verification activity should be removed before moving onto next step.

- Assessing the predictive capability and the ability of mathematical models to reproduce physical phenomena is referred to as the **validation process**. Validation is typically conducted by comparisons against experimental measurements. Experimental results will include a full range of hydrodynamic conditions from dilute to dense and low to high Reynold number flows, and conditions are often not idealized. Mathematical modelling therefore becomes very complex if it is desired to include non-idealized parameters such as the sphericity and orientation of particles. Multiphase experimental measurements are often non-intrusive and can only capture hydrodynamics near the boundaries [Goldschmidt *et al.*, 2003], making the validation process even more difficult. The level of discrepancy between experiments and model is established and where possible, key discrepancies are attributed to different areas of the code.

- Benchmarking is referred to as a summary of validation and verification studies. A benchmarking report can be referred back to, and test cases repeated whenever new capabilities are added to the code [Chung and Ooi, 2011].

This framework of verification, validation and benchmarking forms the cornerstone of development of any multi-scale modelling tool. These procedures are well established

in the CFD [Oberkampf and Trucano, 2002] and computational solid mechanics community [Schwer, 2006], but similar considerable efforts are lacking [Ooi, 2013] in the field of multiphase flow. Validation and verification of the open source code MFIX-DEM ([Garg *et al.*, 2010]) has been done recently, pointing out some test cases that can be employed to test coupling implementation and solvers [Garg *et al.*, 2012; Li *et al.*, 2012*b*]. This study covers a wide range of applications but is not sufficiently comprehensive to address the level of discrepancy with the analytical or experimental results based on mesh dependency, interpolation algorithms, fluid-particle time step ratio and various other known numerical issues.

This chapter presents cases for testing the fluid-particle coupling terms in a multiphase DEM-CFD model. Verification test cases are used to ascertain numerical errors in the solution algorithms and solver. Two sedimentation test cases are studied here: single particle sedimentation (SPS) and constant porosity block (CPB). Single particle sedimentation checks the drag force implementation (calculation and integration) for a single particle falling through different fluid media. These results can be compared to analytical results from single particle creeping flow approximations in the Stokesian regime. The CPB checks the drag model implementation for both phases at a constant porosity field and a simple velocity field. The fixed bed test case employs a constant porosity, fixed granular bed subjected to increasing inlet fluid velocity. An analytical force balance across the bed can be used to obtain the pressure drop according to the drag model employed, and this value can be compared with the pressure drop predicted by the DEM-CFD simulation. Each of the test cases checks interphase coupling term implementation in the coarse grained fluid momentum equation. It should be noted that open-source codes LAMMPS and OpenFOAM coupled in this thesis are heavily verified codes with a very large user base. This exercise is mostly to check the coupling between them.

4.2 Single particle sedimentation (SPS)

4.2.1 Introduction

Sedimentation is the tendency of a particle to settle under gravity in a fluid with density less than its own. A single particle is allowed to fall under gravity with resistance given by the drag force and buoyancy. When the velocity dependent drag force is equal to the weight of the particle, the particle is at its constant terminal velocity.

SPS test case is often employed to determine the hydrodynamic radius of irregular particles, for particles as big as rocks in geology [Paola and Voller, 2005] or in chemistry labs to determine size of large molecules, where the force of gravity is augmented

with centrifugal force in an ultracentrifuge [Schuck, 2000]. SPS has also been used as a validation experiment for capturing fluid-particle interactions in a very dilute regime using immersed boundary-lattice Boltzmann method (LBM) simulations [Feng and Michaelides, 2004; Ten Cate *et al.*, 2002]. Recently, an SPH-DEM code used SPS as a test case [Robinson *et al.*, 2014], with parameters similar to those presented in this chapter. SPS is a well established benchmark case for checking time integration and fluid-particle interaction terms.

This section employs the DEM-CFD code to simulate SPS. Even though our DEM-CFD code is developed to describe multiphase hydrodynamics in the dense regime, it is still essential that single particle hydrodynamics can be captured accurately with careful selection of DEM and CFD parameters. The choice of meshing and statistical averaging strategy used to calculate coarse-grained solid fraction and particle velocity are very important parameters when solving the locally averaged Navier-stokes fluid momentum equation [Anderson and Jackson, 1967]. The dependence of solid fraction calculation on meshing will be discussed. Fluids with varying density and viscosity are used to check the code in different flow conditions.

4.2.2 Simulation set up and methodology

Figure 4.1 shows a schematic diagram of a particle falling through the column. Table **??** gives the geometrical parameters and particle properties. The domain comprises of fluid in a column under gravity (in the negative y direction) with full-slip boundary conditions employed at the side and front/back walls. The domain size is chosen to be large enough to avoid boundary effects, and the fluid is described by 3D CFD equations. The fluid-particle interaction is modelled by the Stokes drag model, applicable at low Re number. The modelled drag force is independent of the solid fraction, but the dependence of solid fraction on the locally averaged momentum equation cannot be avoided. Three different fluids, namely air, water and a 10% solution of water-glycerol are used. Water-glycerol is the most dense and viscous of the three fluid. The fluid-particle relaxation time is shown in **??**, which provides a time-scale for the response of the particle to the fluid. The time-step for the fluid phase is set to an order of magnitude much lower than the relaxation time.

The particle Reynolds number is defined using the superficial velocity (relative velocity of the particle with respect to the surrounding fluid, divided by the porosity) and the diameter of the particle (used as the characteristic length). Different fluid properties and Stokes drag models are tested. In the Stokesian or creeping flow regime an analytical equation is solved to calculate the terminal velocity (figure 4.1).

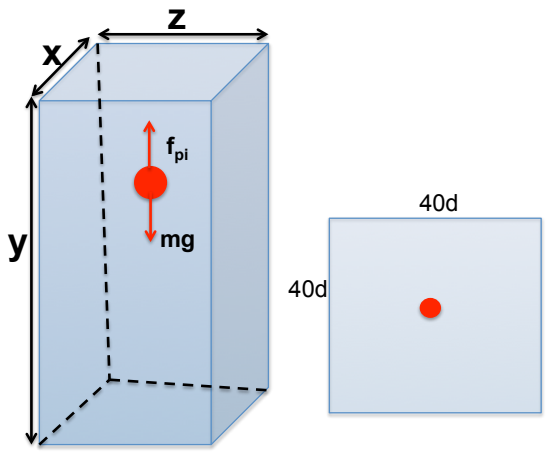

Figure 4.1: Schematic diagram and force balance for single particle sedimentation in a vertical column. d is the particle diameter and width of the box is 40 times the diameter.

Table 4.1: Simulation domain and particle properties.

Parameters	Value
Box width (m)	4e-3
Box height (m)	6e-3
Particle diameter (m)	1e-4
Particle Density (kg/m^3)	2500

Table 4.2: Fluid properties.

Parameters	Air	Water	Water-Glycerol
Fluid density (kg/m^3)	1.1839	1000	1150
Fluid viscosity (Pa.s)	1.86e-5	8.9e-4	8.9e-3
Porosity	0.6-1	0.6-1	0.6-1
Calculated terminal velocity (m/s)	0.0102-0.5	1.3-7.6e-3	1.3-8.4e-4
Fluid CFL conditions (s)	1.4-4.5e-5	1.4-4.5e-5	1.4-4.5e-5
Particle Reynolds number	0.65-3.19	0.15-0.85	0.002-0.011
Relaxation time (s)	7.47e-2	1.56e-3	1.56e-4

$$v(t) = \frac{(\rho_p - \rho)Vg}{b}\left(1 - e^{-bt/m}\right) \tag{4.1}$$

$$b = 3\pi\mu d \tag{4.2}$$

Here μ is the dynamic viscosity of the fluid, d is the diameter of the particle, V is the particle volume and $\rho_p - \rho$ denotes the density difference between solid and fluid media.

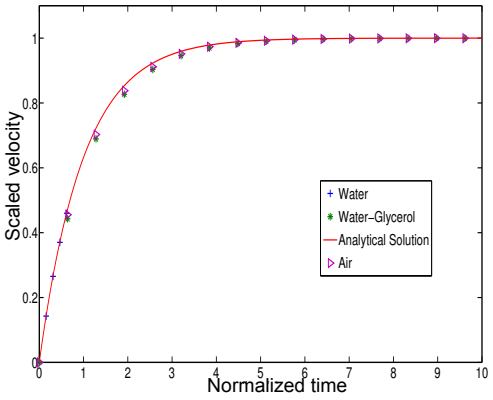

Figure 4.2: Normalized sedimentation velocity as a function of scaled time, for a single particle sedimentation in air, water and water-glycerol using DEM-CFD. Velocity is scaled by the terminal velocity from the analytical solution and time by the drag relaxation time. This Figure shows comparisons with analytical solution from Stokes law. The red solid line shows the analytical solution.

4.2.3 Results and discussion

Figure 4.2 gives DEM-CFD simulation results for single particle sedimentation in air, water and water-glycerol solution using the Stokes drag model. The DEM-CFD model is able to capture single particle sedimentation results quite accurately. The vertical velocity was normalized with the steady state terminal velocity and time was normalized with the time taken to reach a steady state, according to the analytical solution 4.1. For comparison purposes, the DEM-CFD simulations are run with a coarse mesh, in order to have a negligible effect on porosity calculation (discussed later in the section). DEM-CFD results for the normalized terminal velocity are within 1 percent of the analytical solution, for vast majority of simulations. These results verify that the buoyancy calculations are done accurately by the gradient in the pressure field, indicating that the pressure gradient balances out the drag force at the correct terminal velocity. It should be noted that falling DEM particles do not reach the terminal velocity for air before reaching bottom of the domain. DEM-CFD results are quite accurate from the very start of the simulation, which indicates good convergence and pressure-velocity decoupling scheme. For the water-glycerol case, the drag force on the particle is much higher than for water and the particle reaches terminal velocity very quickly. However, simulation time-steps for particle and fluid are reduced in comparison to the water case in order to resolve the drag force relaxation time t_d as per Eq. (4.1). Errors are within 1 percent, relative to the analytical solution.

In summary, the results indicate that the DEM-CFD simulations for all reference fluids are very accurate and reproduce the analytical velocity curve within 1% error. All data scale using u_t and t_d for velocity and time, respectively. Analytical solutions are based

on the premise that the surrounding fluid is not affected by the fluid motion, however DEM-CFD is a two-way coupled simulation in which both fluid and particles are solved. It should be further noted that a possible source of error is the convergence of the momentum equation. The porosity of a single particle in a vast domain is negligible, but DEM-CFD calculates the porosity locally by dividing the particle volume by the mesh volume used. A particle is considered inside a fluid mesh cell if the particle centre lies within the cell. To obtain suitable statistics for the porosity calculation, a fluid mesh cell requires around 30-40 particles to be present, In a dense phase regime, this calculation is fairly accurate due to the presence of many particles, but in a single particle case, the porosity fluctuation can effect the solution of momentum equation.

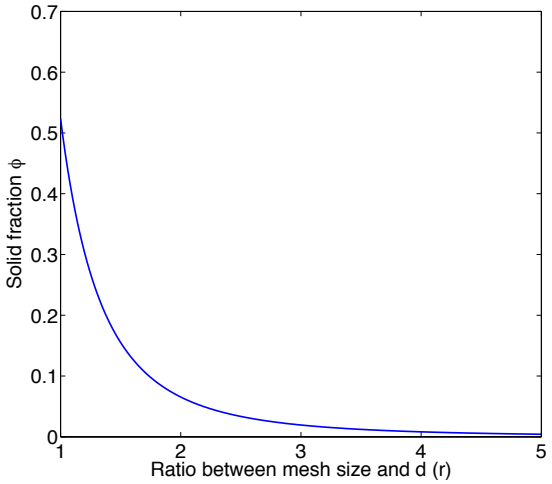

Figure 4.3: Calculated solid fraction (ϕ) plotted with mesh discretization ratio (r), with particle diameter. For a dense phase flow, ratio r is decided according to a mesoscopic length scale appropriate to the physical phenomenon. The solid fraction of a single isolated particle in a vast domain should ideally tend to zero, and not depend upon the mesh used. The plot shows mesh dependence for a coupled DEM-CFD simulation.

Consider particle diameter as d and mesh discretization size as $r \times d$ with $r >> 1$ in all three directions. Solid fraction is calculated by the DEM-CFD code as equation 4.3. Such a calculation is seemingly meaningless, since theoretically single isolated particle would have solid-fraction almost equal to zero. Figure 4.3 plots solid fraction with ratio r. Even with mesh discretization greater than 3 times the particle diameter, the solid fraction is finite and effects the momentum calculations. Conversely, a ratio close to 1 is desirable to resolve flow around the particle. This problem poses a considerable dilemma to model dilute phase flows in the DEM-CFD framework. It is suggested by works of Feng and Michaelides [2004] that more resolved LBM is feasible and accurate for dilute flows at a wide range of Re numbers. One-way DEM-CFD coupling can be another possible way to model lean phase flows [Chaumeil and Crapper, 2013].

$$\phi = \frac{pi}{6r^3} \tag{4.3}$$

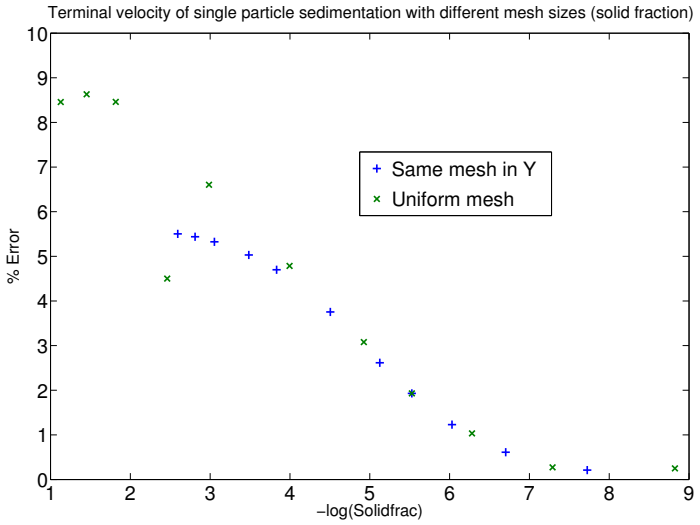

Figure 4.4: Error in the terminal velocity calculated with respect to the analytical solution plotted with the logarithm of the solidfraction. 'X' indicates that the mesh size is same in all the directions, whereas '+' are the errors when the vertical mesh size is kept constant and mesh size in x and z directions are varied. The Figure demonstrates the meshing errors in single particle sedimentation.

Figure 4.4 plots the error calculated in the terminal velocity with the negative of the log of the solid fraction calculated from the code. Errors are much higher for finer meshes (up to 10 %) compared to coarse meshes (1 %). Figure 4.5 plots the normalized terminal velocity with the scaled time for different mesh sizes. The legend shows the solid fraction experienced by the particle according to the mesh size (given by equation (4.3)). The drag and the buoyancy field is updated every fluid time step, but the particle force balance is solved every particle time-step. This difference in the fluid and particle time-step could be problematic when the particle is at the edge of a mesh cell boundary and is crossing over to another fluid mesh cell. Recursions of this can be seen as fluctuations in the terminal velocity. It should be noted that as mesh discretization size is increased and ϕ is decreased, the terminal velocity reaches the value calculated when the coarse mesh was employed. This aspect of DEM-CFD is very counter-intuitive for the CFD community, as more accurate solutions are expected for a fine mesh discretization.

It is identified that errors in the mesh discretization studies (figure 4.4) could be due to 1) fluctuations in the terminal velocity 2) "artificial" porosity due to mesh-discretization,

felt by the particle effecting the solution of the momentum equation. In order to distinguish between the errors, mesh discretization studies were conducted by keeping the vertical discretization constant. Figure 4.4 shows the terminal velocity errors while keeping the vertical discretization constant, in comparison with the same mesh discretization in all directions. The two errors are similar, leading to the conclusion that the errors in the terminal velocity are due to the artificial porosity arising from the mesh discretization.

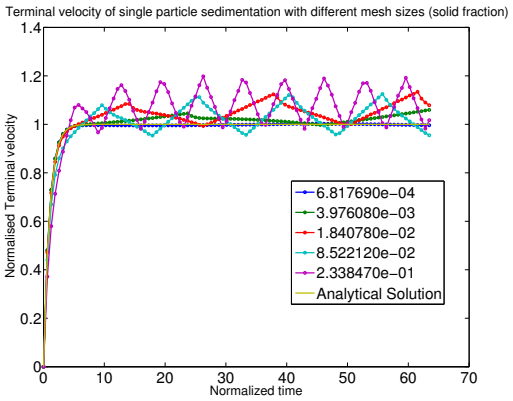

Figure 4.5: Normalized terminal velocity plotted with scaled time for different fluid mesh sizes. The legend shows the solid fraction experienced by the particle according to mesh size. Fluctuations in the velocity are due to the crossing of the particle in between cells.

4.3 Constant porosity block sedimentation

In the last section, SPS was simulated and constraints in modelling the dilute phase with fully coupled DEM-CFD model were realized and quantified. The drag model had no dependence on the local solid fraction. This section deals with a more complex case of dense phase sedimentation under a controlled environment. A constant porosity block (CPB) is generated with equally spaced non-interacting particles and allowed to fall under gravity in water. Particles are constrained to not to move relative to each other. This case can be seen as similar to numerous single particles falling under resistance of fluid with the neighbouring particles influencing flow field around them.

The CPB is created using a regular grid of DEM particles that are separated by a constant distance $\Delta r = \left(\frac{V}{1-\epsilon}\right)^{1/3}$ (V is the particle volume and ϵ is the desired porosity). The DEM particle positions are fixed relative to each other during the simulation. To implement this for the CPB tests, the drag force calculated for each particle is summed over the CPB and then divided equally among all its component particles, thus ensuring each particle experiences the same drag force. For the CFD simulation of the CPB, the fluid mesh is created with respect to the distance between the particles, giving 8

particles placed symmetrically in each fluid cell. The simulation domain is identical to that used in the SPS test case.

A drag force model accounting for the effect of both particle Reynolds number and local porosity is employed [Di Felice, 1994], as opposed to the more simple drag model used in SPS case. Since the porosity is held constant in this case, the drag model can be simplified considerably and the force balance equation on the constant porosity block can be given as equation 4.4 at equilibrium. This equation is solved to obtain the terminal velocity. DEM-CFD simulations are conducted using the same drag relation and boundary condition, for physical walls with full slip conditions. Five different assemblies of CPB are generated by varying the spacing between the particles, using water as a reference fluid. Each of the CPB blocks of varying porosities attained an equilibrium terminal velocity with the net force equalling zero. The terminal velocity was calculated and normalized based on the terminal velocity of a single isolated particle with porosity 1.

$$0.392Re^2 + 6.048Re^{1.5} + 23.04Re - \frac{4}{3}Ar\epsilon^{1+\xi} = 0 \qquad \textbf{(4.4)}$$

where $Ar = d^3\rho(\rho_p - \rho)g/\mu_2$ is the Archimedes number.

Figure 4.6 shows the scaled average terminal velocity plotted with the porosity calculated from DEM-CFD simulations. Results are compared with the solution of equation 4.4. In general, DEM-CFD simulations are fairly accurate in reproducing CPB sedimentation. High porosity cases tend to have lower error compared to low porosity cases. This trend is consistent with the SPS results at varying porosities using DEM-CFD (4.4).

On average, 5 % error can be seen in comparison with the analytical solution. The analytical solution employed to calculate terminal velocities does not consider the effect of interstitial fluid velocity, and the porosity is assumed to be constant throughout the block (the DEM particles at the edge of the block experience a lower porosity). Simulations are coupled two-way, however, so the interstitial fluid is effected by the particle assembly. Interstitial fluid flow (which affects the particle velocity) is effected by porosity and Reynolds number, contributing to the errors reported. Studies by Robinson *et al.* [2014] using meshless SPH-DEM method simulated CPB and reported a similar order of discrepancy.

This case tests the implementation of the drag model at finite solid fractions and low Reynolds number. Drag models implemented in the DEM-CFD code include Gidaspow [1994], Syamlal and O'Brien [1987], Beetstra *et al.* [2007*a*], Yin and Sundaresan [2008] and Di Felice [1994].

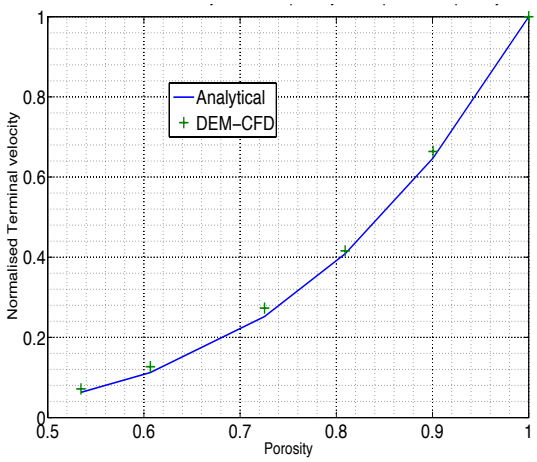

Figure 4.6: Average scaled terminal velocity of the constant porosity block (CPB) with porosity, using DEM-CFD. The velocity is averaged over 0.5 seconds of simulation time.

4.4 Pressure drop across fixed bed

Table 4.3: Domain size and DEM-CFD simulation parameters.

DEM Parameter	**Value**
Number of Particles	64000
Diameter, m	1e-4
Contact model	Linear spring dash-pot
Particle Density, ρ (kg/m^3)	2540
Particle time step, (s)	$1e-6$
Gas Phase	
Gas density, ρ_f (kg/m^3)	1.225
Gas viscosity, μ_f Pa.s	1.8e-5
Boundary conditions (side,front and back walls)	full-slip
Boundary conditions (inlet)	Uniform air inlet
Boundary conditions (Outlet)	Pressure, 10^5 Pa
Fluid timestep (s)	$1e-4$
Drag model	[Gidaspow, 1994]
inlet velocity, m/s	0.0-1.0
Geometry	
Bed width (x), m	4e-3
Bed height (y), m	8e-3
Bed thickness (z), m	4e-3
Discretization length (dx), m	5e-4
Discretization length (dy), m	5e-4
Discretization length (dz), m	5e-4

The previous two sections deal with sedimentation cases at low Reynolds number and fluid velocity, and tested drag model implementation and numerical convergence of

fluid fields. Dense granular flows, however, are often subjected to high fluid inlet velocity e.g. during fluidization. A fixed granular bed of constant porosity subjected to high inlet velocity is simulated. The case employs a similar set up as the constant porosity blocks, except that the particles are not moved at all and are fixed at the bottom of the domain. The simulation domain and particle parameters are similar to CPB case. This case tests the implementation of the drag model and pressure-velocity convergence at high Reynolds number and high solid fraction.

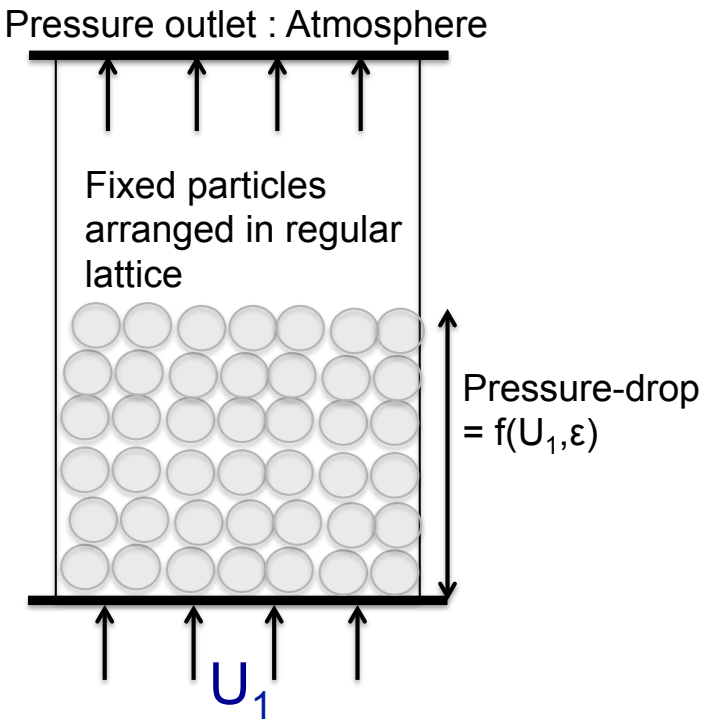

Figure 4.7: Set up for pressure-drop simulation of a constant porosity block set up.

The constant porosity block is treated as a fixed fluidized bed, and subjected to an increasing high inlet air velocity. In general, with increasing in air velocity, the pressure drop across the bed increases until a minimum fluidization velocity (U_{mf}) [Ergun and Orning, 1949] is reached, after which the fixed bed transcends to a bubbling or uniformly expanded bed. In this case, particle positions are removed from the DEM time-integration and particle remain fixed with time. Boundary conditions are important for the pressure drop case, as the wall-particle friction can lead to an increased pressure drop. 1D model of solution of fluidization curves for frictional assemblies was given by Loezos *et al.* [2002].

Figure 4.7 shows a schematic diagram for the pressure drop simulation set up. The bed

is surrounded by physical walls with full-slip boundary conditions for the fluid. Particle-wall interactions are smooth and no friction is applied, in order to accurately match the analytical solution. All the simulation parameters are summarized in Table 4.3. Three different porosity blocks used here cover the typical range of porosities experienced in dense phase flows (0.52-0.63).

The Ergun drag model is employed to measure the pressure drop across the bed, and compared against an analytical force balance given by equation 4.5. The empirical solution of the pressure drop gives a quadratic dependence on inlet velocity, if porosity is kept constant.

$$\frac{\Delta P}{L} = \frac{P_o}{\bar{p}}\left[150\frac{(1-\epsilon)^2}{\epsilon}\frac{\mu U}{d^2} + 1.75\frac{1-\epsilon}{\epsilon^3}\frac{\rho U^2}{d}\right] \tag{4.5}$$

where U is the superficial velocity at the bed inlet, μ and ρ gas viscosity and density respectively, P_o and $\bar{p}$ inlet pressure and average bed pressure.

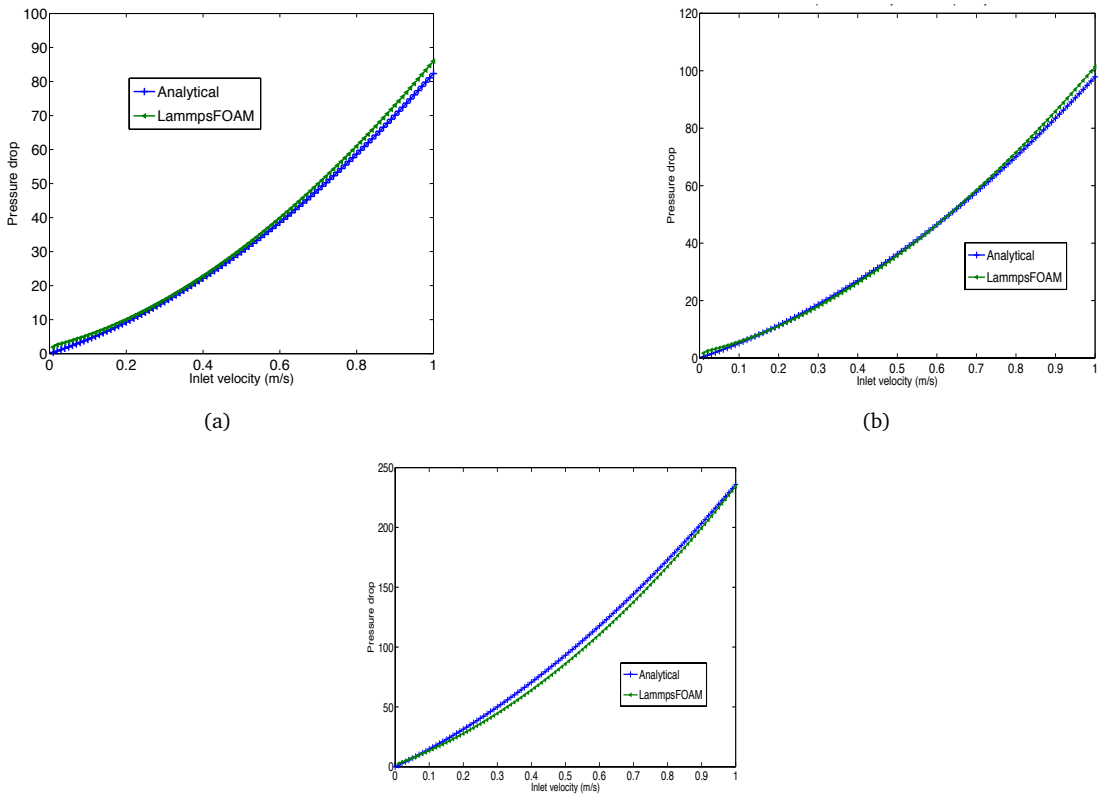

Figure 4.8: Pressure drop across the bed plotted with the increasing inlet velocity, with Ergun and Wen Yu drag model, at constant porosity of (a) 0.63 (b) 0.58 (d) 0.52

Figures 4.8 compare the pressure drop across the bed obtained through DEM-CFD simulations with the analytical solutions obtained from equation 4.5 at different porosities

ranging from 0.52 to 0.63. The results show that the pressure drop across the bed is adequately captured with maximum error 0.5% . These results demonstrate that drag model and buoyancy are implemented correctly with no coding errors.

4.5 Conclusion

DEM-CFD code is tested by employing verification cases with increasing order of complexity. The aim was to test any coding errors that might have got missed in the debugging process. This could include uninitiated variables taking garbage values and ultimately leading to a wrong convergence. The importance of verification is highlighted by specifically testing different aspects of the code with the three test cases implemented in this study. It should be noted that the open-source codes to solve particle phase (LAMMPS) and for fluid phase (OpenFOAM) are already well established tools with a high user base and support and this exersice was mostly mean to check interface between the two. Following conclusions are reached from the three test cases proposed here.

- Single particle sedimentation (SPS): SPS tested the DEM-CFD code implementation of fluid-particle coupling term in very lean phase at low Re number. Velocity of the sediment particle was plotted as a function of time analytically and compared against DEM particle velocities. Maximum errors of 1-5% were reported for all three fluids used: air, water, water-glycerol. Analytical solution is based on assumption that the fluid flow is not disturbed by the particle motion (one–way coupling) where as DEM-CFD simulations are fully coupled, a source of error. Furthermore, issues of meshing, boundaries and statistical issues were addressed in DEM-CFD framework. A fake porosity as a numerical artefact is felt by the particle in case of a fine mesh, which resulted in errors upto 10% .

- Constant porosity Block (CPB): CPB tested the open-source code implementation of fluid-particle coupling at finite solid fraction and the complex drag model implementation. A constant porosity block was created by placing equally spaced DEM particles in a regular lattice and fixed relatively to each other. CPB was allowed to sediment into a tank of water and analytical solution of the terminal velocity was calculated based on the drag model employed [Di Felice, 1994]. A maximum error of 5 % is reported and can be explained by the fact that analytical solutions do not account for motion of interstitial fluid.

- Pressure drop across a fixed CPB: This verification case tested the fluid particle interaction implementation at high solid fraction and Re number. A fixed porosity

bed was fluidized with increasing inlet velocity. Analytical solution for pressure drop across the bed can be found by solving the force balance, with drag forces calculated at constant porosity. The pressure drop versus inlet velocity curve compared for the analytical solutions and the DEM-CFD simulations were in excellent agreement.

Chapter 5

Validation of the DEM-CFD model

5.1 Introduction

The previous chapter presented a detailed verification of the DEM-CFD code. The code was checked for any coding errors and the coupling code between CFD and DEM solvers was found to be bug-free. This chapter is in continuation of work from the previous chapter and focuses on answering a question: *Are we solving the right equations?* This question is answered by a methodology called validation. Validation was described as *The process of determining the degree to which a model is an accurate representation of the real world from the perspective of the intended uses of the model* by Oberkampf and Trucano [2002]. An extensive literature on the validation of numerical techniques and especially multiphase solvers is given in the section 2.4. This chapter will present a series of validation cases to assess the capability of the DEM-CFD code to reproduce different fluidization phenomenon. Following test cases are chosen:

- Bubbling/slugging fludized beds
- Spouted fludized beds
- Bi-disperse fluidized beds.

DEM-CFD solver will be validated in the dense and highly mobile particle regimes and intended to capture the hydrodynamics of Geldart A regimes. The rest of the chapter is organized as follows. Next section will lay out a systematic procedure for validation of DEM-CFD model, based on the literature review of other numerical techniques and section 5.3, 5.4 and 5.5 will present validation studies for each of three cases listed above.

5.2 Validation procedure for DEM-CFD

Based on the literature from different numerical methods communities, the following key components are identified for a DEM-CFD model validation:

- Breaking model into sub-models responsible for different physics e.g. DEM modelling of inter-particle interactions and drag force modelling for fluid-particle terms.
- Identifying sub-model parameters that govern the dynamics at the sub-model level. For example DEM modelling parameters like static friction, Hamaker constant, coefficient of restitution, spring stiffness, particle density. These parameters are determined by separate characterization experiments such as particle drop tests and angle of repose tests.
- Calibration of the sub-model parameters: Calibration is defined as: *The process of adjusting numerical or physical modelling parameters in the computational model for the purpose of improving agreement with experimental data* [Oberkampf and Blottner, 1998]. Calibration experiments are often employed to find free parameters in the sub-models. For example drag model parameters are determine by pressure drop experiments across a fixed bed. Calibration experiments should be kept as different as possible from the validation experiments. In order to avoid extra costs of building experimental set-ups, most of the studies employ the same experiments conducted in different regimes for both calibration and validation purposes.
- Model conceptualization: Mathematical models are based on simplified assumptions. For example, particles are modelled as perfect spherical shapes due to inherent assumptions of DEM modelling. Almost all the drag models found in literature are derived for spherical mono-disperse particles. However, it is difficult to define the experimental conditions and materials used in terms of model parameters. It is a considerable challenge for the modellers to bridge this gap and separate the model simplification errors from its predictive capability.
- Quantifying spatial discretization and time-stepping effects: Optimized mesh sizes and fluid time-steps are decided based on preliminary DEM-CFD simulations. In any other mesh-based method, a usual rule of thumb is " the higher the mesh-resolution, the better the results". However, DEM-CFD requires discretization of spatially averaged fluid equations at a length scale which is much greater than particle size but much less than the largest governing scale of the system. This provides a considerable challenge to find a optimized and solution independent

mesh. Another major road-block in the DEM-CFD simulation is the optimization of particle time-step which is considerably smaller than the fluid time-step.

- Validation experiment set-up conditions: DEM-CFD simulations are set up according to sub-model parameters supplied from characterization experiments, operating conditions of the validation experiment and the model conceptualization. Important considerations are given to initial and boundary conditions. For example, initial packing density and composition of the bed are critical to the granular flow.

- Examining model uncertainty: This refer to quantification of differences between the simulation results and the experimental measurements. Errors can be due to (1) Inaccurate description of the physics by the underlying equations (2) Sub-model simplification and assumptions made (3) Uncertainty in the experimental measurements (4) Lack of calibration experiments for the sub-models.

It is noted that, validation of entire DEM-CFD code is not possible due to inter-play of many different fundamental interactions that govern the physics of the problem. However, a significant effort is to be put into covering a wide variety of flow regimes. Application of the code to the problems beyond the region of validation experiments is termed as prediction.

5.2.1 Validation experiments and measurement techniques

Fluidization experiments for validation purposes are designed according to the measurement techniques employed. Pseudo 2D beds are commonly used to capture and measure flow around the walls. Even if laboratory experiments are controlled, measurements are difficult to obtain and often certain phenomenon are missed in the data acquisition due to variety of reasons. Different measurement techniques employed in the literature for multiphase flows are:

- Particle Image Velocimetry (PIV) and Digital image analysis (DIA) to capture 2-D macroscopic bulk phenomenon [Chaouki *et al.*, 1997; Dijkhuizen *et al.*, 2007; Goldschmidt *et al.*, 2003; Laverman *et al.*, 2008]. Wall effects hinder such studies and the phenomenon could only be captured at the front wall.

- Magnetic Resonance (MR) [Holland *et al.*, 2008; Müller *et al.*, 2008]: Non intrusive 3-D technique with high spatial resolution of voidge and particle velocity but only temporally averaged phenomenon is available.

- Positron Emission Particle Tracking (PEPT) [Link *et al.*, 2008]: Non intrusive 3-D technique, single radioactive particle within fluidization experiment is tracked

for long hours until it has covered all the phase space domain. Data is temporally averaged.

- Diffusion Wave Spectroscopy (DWS) [Menon and Durian, 1997*a*,*b*]: Non intrusive technique to obtain voidage, particle velocity and granular temperature profiles. Low spatial and temporal resolution.

- Electrical Capacitance Tomography (ECT) [Liu *et al.*, 2005]: Use in the flow measurements, but low spatial resolution.

5.2.2 Challenges in the validation procedure

- Inability to separate sub-models as the physics is convoluted together: Validation has to be followed in a hierarchical manner. Component models are joined together to form a system model. In a multi-physics process such as fluidization, separation of these components is very complex as governing dynamics is formed as an interplay between these models. Even if components are tested separately, joint interplay can not be tested rigorously.

- Inability to perform controlled experiments: Fluidization phenomenon are sensitive to the small changes in certain operating conditions. An uneven distribution of the air through the distributor plate is one problem area. Small leaks can cause a preferential fluid flow and instabilities formed in the bed can be very different from what is expected. Experiments conducted can never guarantee a perfectly uniform distribution, unlike the boundary conditions in the simulations.

- Measurement techniques listed in the previous section are very expensive and very few research groups in the world have successfully generated meaningful data for validation purposes.

- Meaningful comparison between experiments and simulations: Due to expensive experimental procedure and measurements, repeatability of the experiments is often compromised. The same is often true for simulations, computationally expensive DEM-CFD computations makes it difficult to repeat simulations with different initial canonical granular beds. This leads to error limits not being established with a considerable confidence interval for both simulations and experiments. Also, post processing of data from experiments and simulations follow different procedures and interpretation can be very difficult for a meaningful comparison.

- Lack of proper particle characterization: DEM-CFD simulations require parameters based on material properties which are obtained by particle impact tests in isolated environments. A direct applicability of these parameters in a multiple

contact and dense regime is highly questionable. Often data on material characterization is missed while providing the validation data and the modellers rely on empirical relations or literature on the same or similar material to get their input parameters.

- Some of the DEM-CFD model parameters are free parameters and need to be calibrated based on bulk properties by experiments. This data is essential but is often missing alongside validation experimental data. These calibration experiments are often not carried out and modellers rely on sensitivity studies to fix these.

5.3 Bubbling bed case

5.3.1 Introduction

Bubbling or slugging gas-solid fluidization processes are critical to many chemical and pharmaceutical industries, owing to the high rates of mass and heat transfer that can be generated between interacting phases. In these regimes, it has been demonstrated that the gas-particle interaction governs the fluidization dynamics, and particle-particle interactions are of lesser importance [Sundaresan, 2003]. In this section, the ability of the DEM-CFD code will be validated for the intended use for capturing bubbling/slugging fluidization dynamics. The bubbling bed experiments were carried out by Müller *et al.* [2009] and characterized by MR techniques [Holland *et al.*, 2008]. Spatially and temporally averaged voidage, particle velocity and granular temperature obtained from the experiments are compared with the post-processed data from the DEM-CFD simulations. In these simulations, kidney shaped poppy seeds with averaged particle size of 1.2 mm and density of 1000 kg/m^3 were fluidized with air at ambient temperature and pressure. If mapped to the Geldart chart, these particles lie on the Geldart B/D boundary.

Previously, the MR experimental data obtained by Müller *et al.* [2008] has been employed as a validation case for different DEM-CFD validation codes [Li *et al.*, 2012*b*; Müller *et al.*, 2008, 2009]. Large discrepancies in the solid circulation pattern and hydrodynamics around the wall boundaries were evident from the temporally averaged solid velocity, voidage and the granular temperature data at various heights above the distributor plate. DEM-CFD parametric studies by Müller *et al.* [2009] found that coefficient of restitution (0.49-0.97) and different drag models closures had minimal effects on the temporally averaged hydrodynamics. Even though discrepancies were identified and attributed to inability to correctly model hydrodynamics of the kidney-shaped particles used in experiments, these numerical studies failed to address these discrepancies [Li *et al.*, 2012*b*; Müller *et al.*, 2009] adequately. Similar DEM-CFD validation

studies using MFIX-DEM were conducted by Li *et al.* [2012*b*], simulation results were similar to those found by Müller *et al.* [2009] quantitatively. Even though, hydrodynamics of non-spherical poppy seeds was accounted partially account by particle shape factor used in Ergun and Wen Yu drag correlation [Gidaspow, 1994], studies did not address the discrepancies completely. Studies by Li *et al.* [2012*b*] also investigated rolling friction effects but limited effects on bubbling bed hydrodynamics were found. Continuum TFM modelling of the same problem was also attempted by a second-order moment method [Dan *et al.*, 2009] and issues with inter-phase momentum exchange terms were pointed out.

A meaningful comparison between the experiment and simulation results highlighting discrepancies between the simulations and the experiments is presented here. Hydrodynamics around the walls and at the middle section of the bed will be carefully addressed. Discrepancies arisen due to model simplifications[Li *et al.*, 2012*b*; Müller *et al.*, 2008, 2009] will be assessed quantitatively. Modelling of wall-particle interactions will be emphasized in order to address retarding particle velocities around the walls which was observed in the experiments [Müller *et al.*, 2008]. Inter-phase drag model by [Haider and Levenspiel, 1989] will be employed to partially account for particle shape. Furthermore, particle size would be varied from 1.1-1.3 mm to quantify differences in the particle hydrodynamics and bed expansion for same bed height and weight.

5.3.2 Simulation details and post-processing techniques

5.3.2.1 Experimental measurements and simulation details

The fluidized bed was a pseudo 2-dimensional perspex apparatus with dimensions of 44, 1000 and 10 mm in the width, height and depth, respectively. A 30 mm high granular bed consisting of kidney-shaped poppy seeds was fluidized by uniform air flowing through a porous distributor plate at the bottom. Time and spatially averaged granular temperature, solid velocity and voidage distributions were obtained using MR spectroscopy. Details of reconstructing MR data signals to obtain the data at sub-particle size resolution can be found in [Holland *et al.*, 2008]. The MR pixel size, which limits the spatial resolutions, was 1.88^2 mm^2 for granular temperature, and 0.94^2 mm^2 for velocity and voidage measurements [Müller *et al.*, 2008].

The full-scale bed was simulated with parameters for the geometry, fluid properties and contact model summarised in table 5.1. The fluid flow was modelled as 2D, since the thickness was comparatively small to other dimensions of the bed. The particles were modelled as spheres moving in 3D. The distributor plate was simulated using 4 layers of fixed particles of 1 mm diameter which covered two fluid cells exactly.

Table 5.1: Domain size and DEM-CFD simulation parameters

DEM Parameter	**Value**
Number of Particles	9240
Diameter, mm	1.2
Particle Density, ρ (kg/m^3)	1000
Spring Stiffness, k (N/m)	200
Coefficient of restitution, e (N/m)	0.98
Inter-particle friction coefficient, μ (N/m)	0.1
Particle-wall friction coefficient, μ (N/m)	0.1
Gas Phase	
Gas density, ρ_f (kg/m^3)	1.225
Gas viscosity, μ_f (Pa $\cdot$ s)	1.8e-5
Inlet velocity, v_f (m/s)	0.6,0.9
Wall boundary condition	No-slip
Inlet boundary condition	Uniform inflow
Outlet boundary condition	Pressure outlet, 10^5 Pa
Geometry	
Bed width (x), m	0.044
Bed height (y), m	0.12
Bed thickness (z), m	0.01
Discretization length (Δx), m	0.004
Discretization length (Δy), m	0.003
Discretization length (Δz), m	0.01

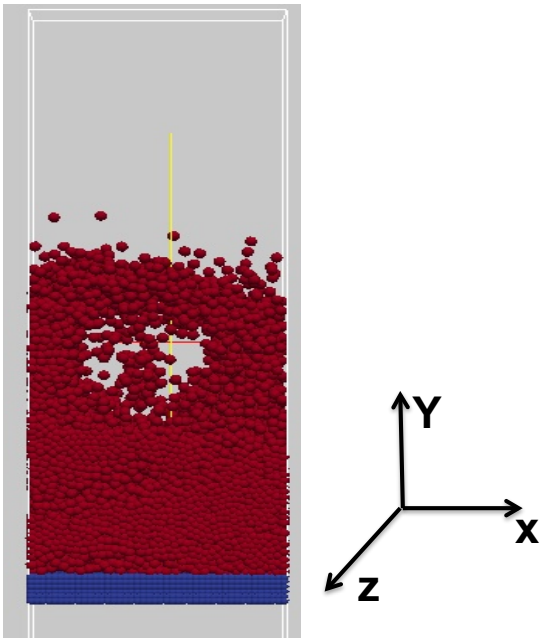

Figure 5.1: Typical snapshot of DEM-CFD simualtion of gas-solid fluidized bed with particle size 1.2 mm and density 1000 kg/m^3 at inlet velocity 0.9 m/s

The particle–wall interaction is modelled as either with a flat surface or with a wall consisting of solid particles, whose details will be given in section 5.3.3.3. The no-slip boundary condition was applied between fluid and all the walls. The coefficient of friction between particles and the walls was set to 0.1. A typical snap shot of the DEM-CFD simulation at a superficial velocity of 0.9 m/s can be seen in figure 5.1.

5.3.2.2 Post-processing of DEM data

Post-processing of DEM data is important for the correct comparison between the experimental and the simulation results. Spatial-temporal average of the MR data was performed to obtain the voidage, particle velocity and granular temperature profiles in the experiments [Holland *et al.*, 2008]. In order to have a direct comparison between DEM data and the MR measurement compatible post-processing techniques are employed. The spatial-temporal averaged solid volume fraction ϕ and velocity $\mathbf{V}$, at the location $\mathbf{r}$, are calculated respectively using

$$\phi(\mathbf{r}) = \frac{\pi}{6N_f} \sum_{j=1}^{N_f} \sum_{i=1}^{N_p} d_{i,j}^3 W(\mathbf{r} - \mathbf{r}_{i,j}), \tag{5.1}$$

and

$$\mathbf{V}(\mathbf{r}) = \frac{\sum_{j=1}^{N_f} \sum_{i=1}^{N_p} \mathbf{v}_{i,j} W(\mathbf{r} - \mathbf{r}_{i,j})}{\sum_{j=1}^{N_f} \sum_{i=1}^{N_p} W(\mathbf{r} - \mathbf{r}_{i,j})}, \tag{5.2}$$

where $\mathrm{d}_{i,j}$ and $v_{i,j}$ are the diameter and instantaneous velocity of a particle at a location $\mathbf{r}_i$ and a time instant j, respectively, N_p is the number of particles in the domain, N_f is the number of time steps used in the time averaging and $W(\mathbf{r} - \mathbf{r}_i)$ is a weighting function. We used $W(\mathbf{x}) = \frac{1}{\Omega(w)} H(w - ||\mathbf{x}||)$, where H represents the Heaviside function and $\Omega(w)$ is the volume of the averaging sphere of radius w. The averaging results were found not sensitive to the forms of the weighting function. The calculation of solid velocity in eq. 5.2 is consistent with the so-called “particle based averaging" used in [Boyce *et al.*, 2013], which was found to yield better agreement between DEM and experimental analysis than using the “frame based averaging" approach, in which the spatially averaged solid velocity at every time instant is averaged over time with equal weightings.

Since the MR measurements are time-averaged measurements of the mean and variance of the velocity, the MR measured variance of the velocity is a combination of both the local fluctuations about the mean velocity, and the time-averaged fluctuations of the mean velocity [Müller *et al.*, 2008]. It is not possible to separate these contributions to granular temperature in the MR measurements. The “bubble granular temperature" is

calculated, which was shown to lead to closer agreement [Holland *et al.*, 2008], given by

$$\theta_{bubble}(\mathbf{r}) = \frac{1}{3}\left(\overline{V_x'V_x'} + \overline{V_y'V_y'} + \overline{V_z'V_z'}\right), \tag{5.3}$$

where the variance of the velocity is defined as

$$\overline{V_i'V_j'}(\mathbf{r}) = \frac{1}{N_f}\sum_{k=1}^{N_f}\left[\overline{V}_{i,k}(\mathbf{r},t) - V_i(\mathbf{r})\right]\left[\overline{V}_{j,k}(\mathbf{r},t) - V_j(\mathbf{r})\right]. \tag{5.4}$$

The spatially averaged velocity $\overline{\mathbf{V}}(\mathbf{r},t)$ is calculated by

$$\overline{\mathbf{V}}(\mathbf{r},t) = \frac{\sum_{i=1}^{N_p}\mathbf{v}_i W(\mathbf{r}-\mathbf{r}_i)}{\sum_{i=1}^{N_p} W(\mathbf{r}-\mathbf{r}_i)}. \tag{5.5}$$

The averaged voidage, solid velocity and granular temperature are dependent on the spatial and temporal scales used for the averaging. The scales were found to be functions of number of particles, averaging time, sampling frequency and dynamics of the system. Sensitivity studies have been carried out to determine the length and time scales at which the results are insensitive to the scales. It was found that a length scale of 2.5 times of particle diameters, a sampling frequency of 100 Hz and an averaging time of 45 seconds yield such scale insensitive results. The time average for DEM data has been found invariant with longer time periods although the experimental data acquisition time was much longer at about 30 minutes. Attention is now turned to the simulation results and the comparison with the experimental results.

5.3.3 Results and discussions

5.3.3.1 Bed pressure drop analysis

The fluidization curve for the bed was determined by simulations with the inlet velocity linearly increased from 0.0 to 0.6 m/s. The initial packed bed porosity was around 0.328, close to experimental value of 0.33 [Müller *et al.*, 2009]. The total pressure drop across the bed is plotted against the superficial inlet velocity in figure 5.2, where the pressure drop is normalised by the bed weight per unit cross section area and the velocity is normalised by the minimum fluidization velocity U_{mf} determined in the experiments (0.3 m/s) [Müller *et al.*, 2009]. It is demonstrated that the basic fluidization phenomena can be correctly captured, i.e. the pressure drop plateaus out at a level supporting the total weight of bed at around the U_{mf}. The different drag models tested show little effect on the fluidization curve with the predicted U_{mf} values, listed in Table 5.2, within 10 percent of the experimental value.

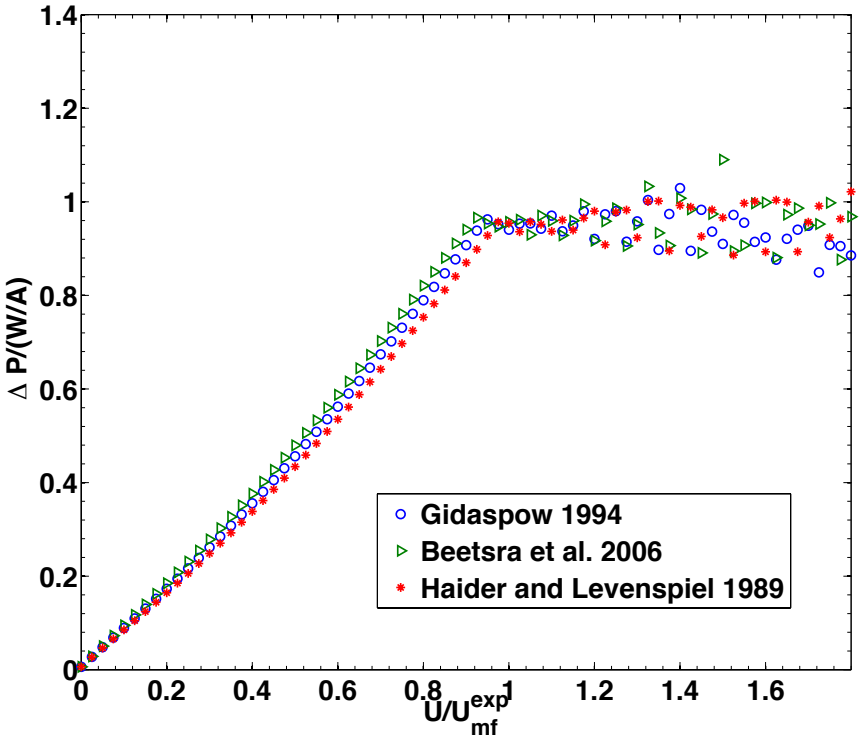

Figure 5.2: Pressure drop (ΔP) across the bed (normalised with the bed weight (W) divided by distributor plate area (A)) plotted against inlet velocity (normalised by experimental $U_{\mathrm{mf}}^{exp} = 0.3\ m/s$ for different drag models shown in the legend.

Table 5.2: Minimum fluidization velocity U_{mf} for particle size $d = 1.2mm$ and density $1000\ \mathrm{kg/m^3}$ with different drag models

Drag model	U_{mf} (m/s)
Gidaspow [1994]	0.281
Syamlal and O'Brien [1987]	0.315
Beetstra *et al.* [2007*a*]	0.275
Di Felice [1994]	0.285
Haider and Levenspiel [1989]	0.29

The absolute pressure drop calculated immediately above the distributor plate is plotted as a function of time at the inlet velocity of 0.6 m/s, around 2 times U_{mf}, in figure 5.3a. Periodic fluctuations in the pressure drops can be observed, which are usually linked with the instabilities, such as bubbles, arising at the distributor plate. Fast Fourier Transformation (FFT) analysis of pressure drop fluctuations have been previously used to identify the fluidization regimes, e.g. bubbling or slugging [Bai *et al.*, 1999; Felipe and Rocha, 2004; Kage *et al.*, 2000]. The power spectrum obtained using the same technique is shown in figure 5.3b. The spectrum has multiple small peaks in the range of 0–10 Hz, and one prominent peak at 7 Hz. These results are in a quantitative match with the pressure drop and FFT results obtained from DEM-CFD simulations by Boyce

et al. [2014], of a 3-D cylindrical fluidized bed with the same particles. The bubble formation frequency at the distributor plate in the experiment was found to be also around 7 Hz [Boyce *et al.*, 2014], implying a link with the large pressure fluctuations. To ensure the dynamic process of bubble formation can be fully recorded, the data sampling frequency is chosen to be much higher at 100 Hz.

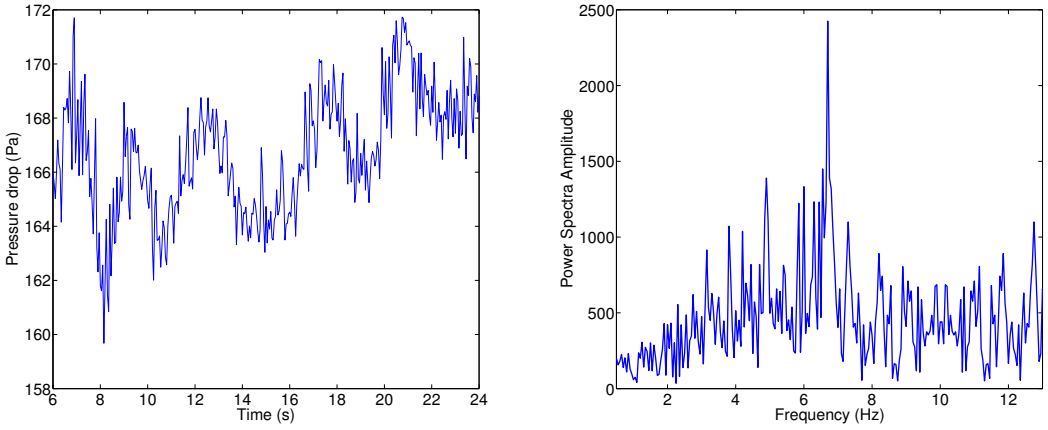

(a) (b)

Figure 5.3: (a) Pressure drop across the bed plotted against time at fluidizing velocity 0.6 m/s (b) Power-spectra versus frequency (Hz) by FFT transformation of pressure drop data.

5.3.3.2 Voidage, solid velocity and granular temperature comparison

In this section, simulation results are compared with the MR measurements of voidage, solid velocity and granular temperature for the cases with superficial fluidization velocities of 0.6 and 0.9 m/s. The base simulation case employs the drag model developed by Beetstra *et al.* [2007*a*], has particle–wall interaction as with a flat surface, and uses the parameters as specified in table 5.1. It is noted that the simulation results presented here are not sensitive to particle properties, such as stiffness, coefficient of restitution and static friction coefficient, which have been tested in our parametric studies. It is first demonstrated that the simulation is able to capture the solid circulation pattern observed in the experiment, as shown by the 2-D contour plots of solid velocity components in figure 5.4 for the case with 0.6 m/s inlet velocity. The experimental data was obtained for a x-y cross section at the middle in the depth direction [Holland *et al.*, 2008]. The vertical (V_y) velocity is negative close to the side walls and positive otherwise with the maximum in the center; the lateral V_x velocity has opposite signs symmetric to the vertical center line. Together the velocities show that the solid particles are transported upwards in the center of the bed and downwards close to the wall on average in time, which is a robust feature of dense bubbling beds. The location and

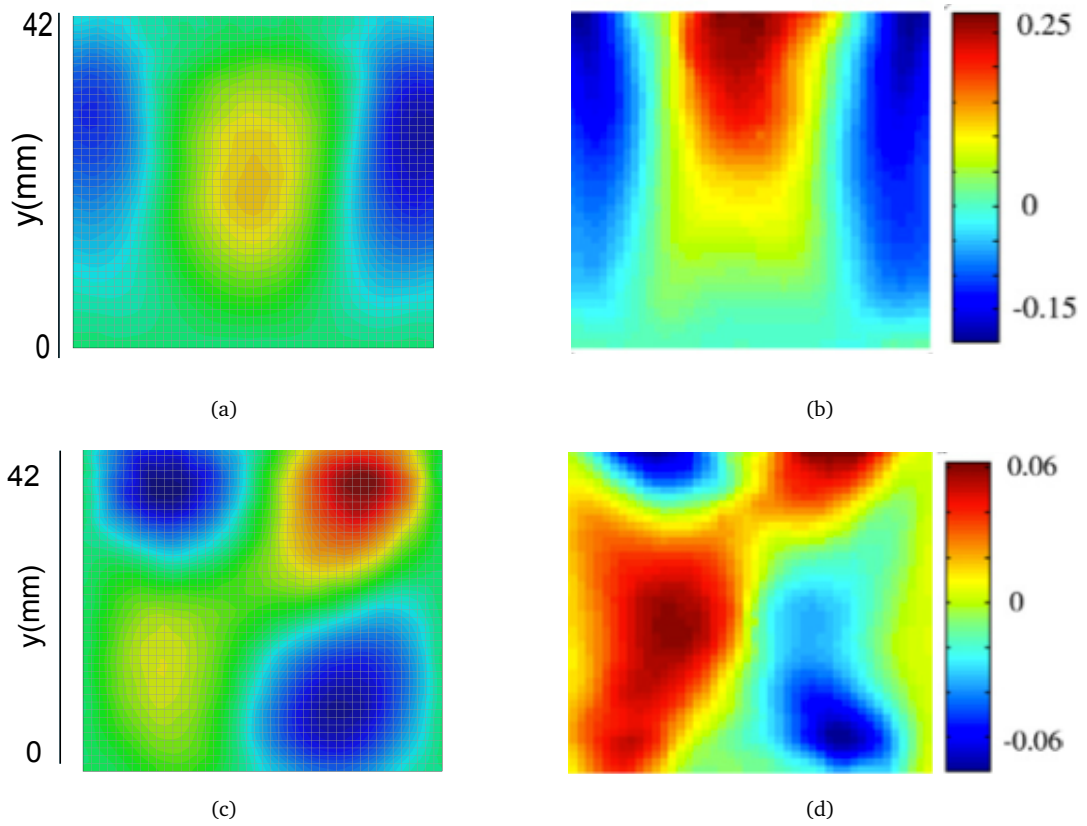

Figure 5.4: Contour plots of solid velocity component (a) V_y and (c) V_x obtained from DEM-CFD simulations compared with the corresponding MR measurment in (b) and d (reproduced from [Holland *et al.*, 2008]) for the case with superficial fluidization velocity of 0.6 m/s.

magnitude of the maximum velocities, however, do not agree, which are affected by the particle shape and size as discussed in section 5.3.3.4.

The solid velocity for the case with inlet velocity of 0.9 m/s indicates a similar solid circulation pattern. To more quantitatively compare to the experimental results, the vertical velocities, V_y, at the heights of 15, 25 and 35 mm above the distributor plate are plotted with respect to the x-coordinates across the bed width in figures 5.5(a), (b) and (c), respectively. Although general agreement with the experimental data is still observed for these velocity profiles, significant mismatches are found in the boundary layers of about 5 particle diameters from the side walls ($x = 0$ or 44 mm). The simulation velocities are consistently higher (more negative) than the experimental values, i.e., particles move downwards faster in the simulation, independently of the bed heights. The difference in dynamics is also reflected in the granular temperature profiles as shown in figure 5.6. The experimental data suggests that granular temperature decreases considerably toward the walls from the central region (around $x = 22$

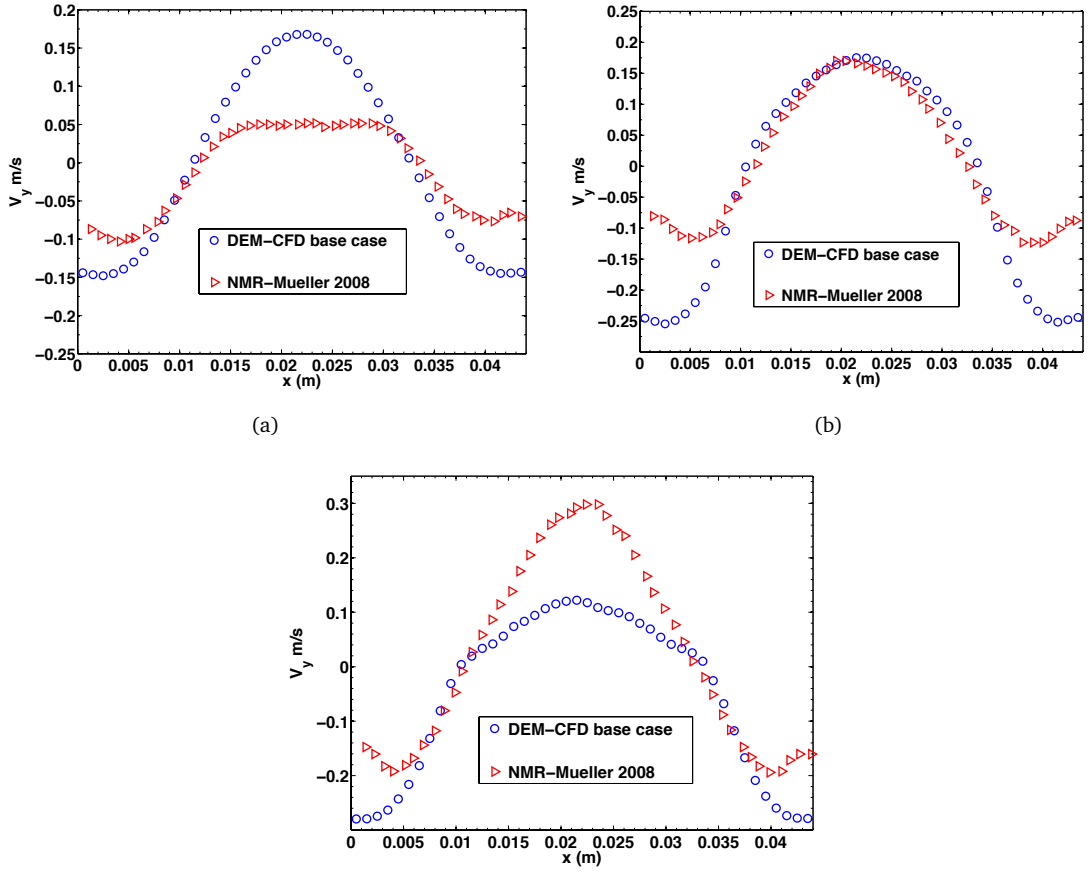

Figure 5.5: DEM-CFD simulation results for lateral vertical velocity profiles at height (a) 15 mm (b) 25 mm (c) 35 mm above distributor plate for superficial velocity 0.9 m/s, compared with experimental results by Muller et al. 2008

mm), whereas the simulation results show an opposite trend of increasing granular temperature for all three profiles. This qualitative difference in granular temperature suggests that velocity fluctuation is a more sensitive measure to reveal the dynamic state than the mean velocity for which only quantitative difference was observed. The simulation predicts higher granular temperature, indicating larger velocity fluctuations than in the experiments in the wall boundary layers. Such discrepancies at the wall have been investigated and attributed to the particle–wall interaction models used in the simulation, discussed in section 5.3.3.3.

The simulation also over-predicts (under-predicts) the velocity in the central region at the height of 15 mm (35mm) although also has good match at the height of 25 mm. The time averaged voidage contours are plotted in figure 5.7(a), showing a gulf-like pattern with higher voidage (more dilute) in the middle of and lower (denser) close to the walls. This general variation can also be seen from the voidage profile at the heights

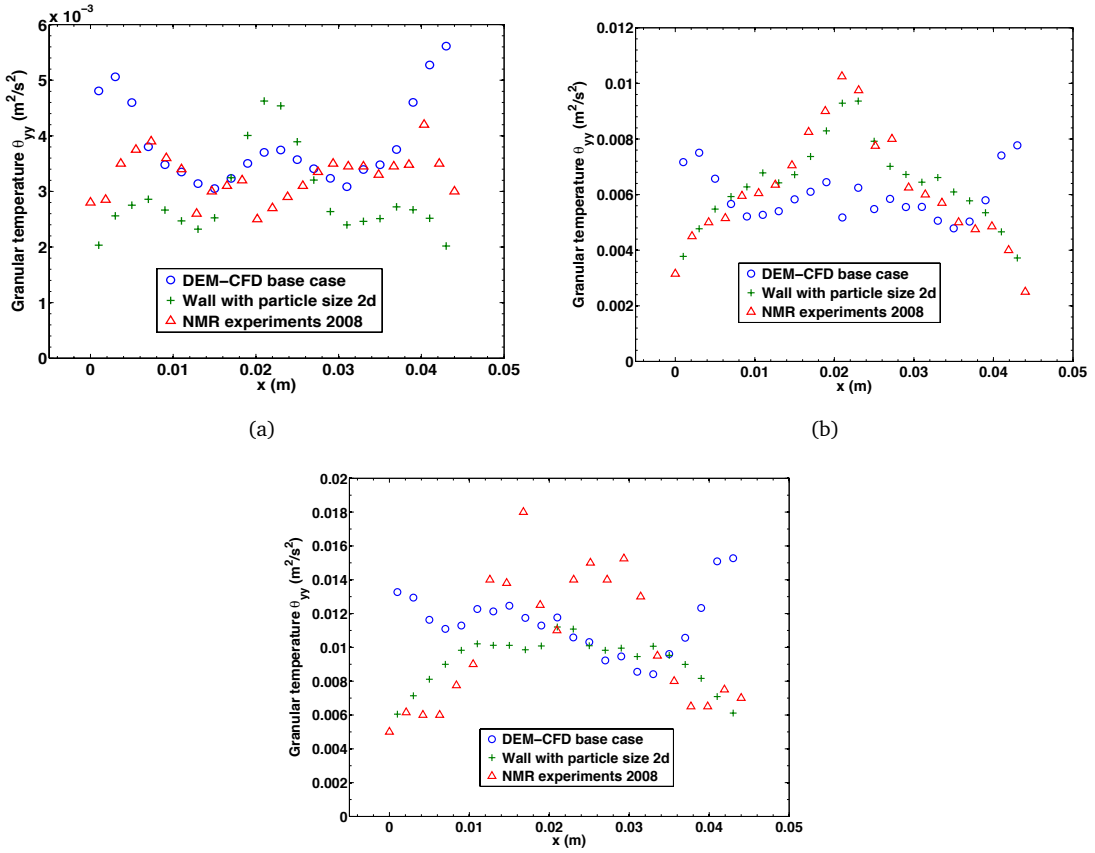

Figure 5.6: DEM-CFD simulation results for granular temperature (vertical direction) profiles at height (a) 7.5 mm (b) 20 mm (c) 35 mm above distributor plate for superficial velocity 0.9 m/s with wall particle effects, compared with experimental results by Muller et al. 2008 and the base case

of height 16.4 (figure 5.7(b)) and 31.4 mm (figure 5.7(c)). The voidage near the walls at 31.4 mm is over-predicted by 40 percent, whereas a good match is obtained at 16.4 mm. These mismatches are related to the bed expansion and the velocity variation along the bed height (as seen in the velocity contour plots in figure 5.4), which will be shown to be sensitive to particle size and shape in section 5.3.3.4.

5.3.3.3 Wall boundary effect on solid velocity and voidage

The comparison in the previous section indicated that the particle motion is retarded more in the experiments than in the simulation in the wall boundary layers. The fluid–wall interaction could form a viscous layer in the near-wall region and indirectly slow down the particle dynamics. Recent Direct Numerical Simulation (DNS) [Tsuji *et al.*, 2013] found that wall friction affect the fluid flow only within one particle diameter of the wall. Furthermore, the pressure drops predicted by the Beetstra drag model were very close to the DNS results outside of this one-diameter zone. Thus, the fluid-wall

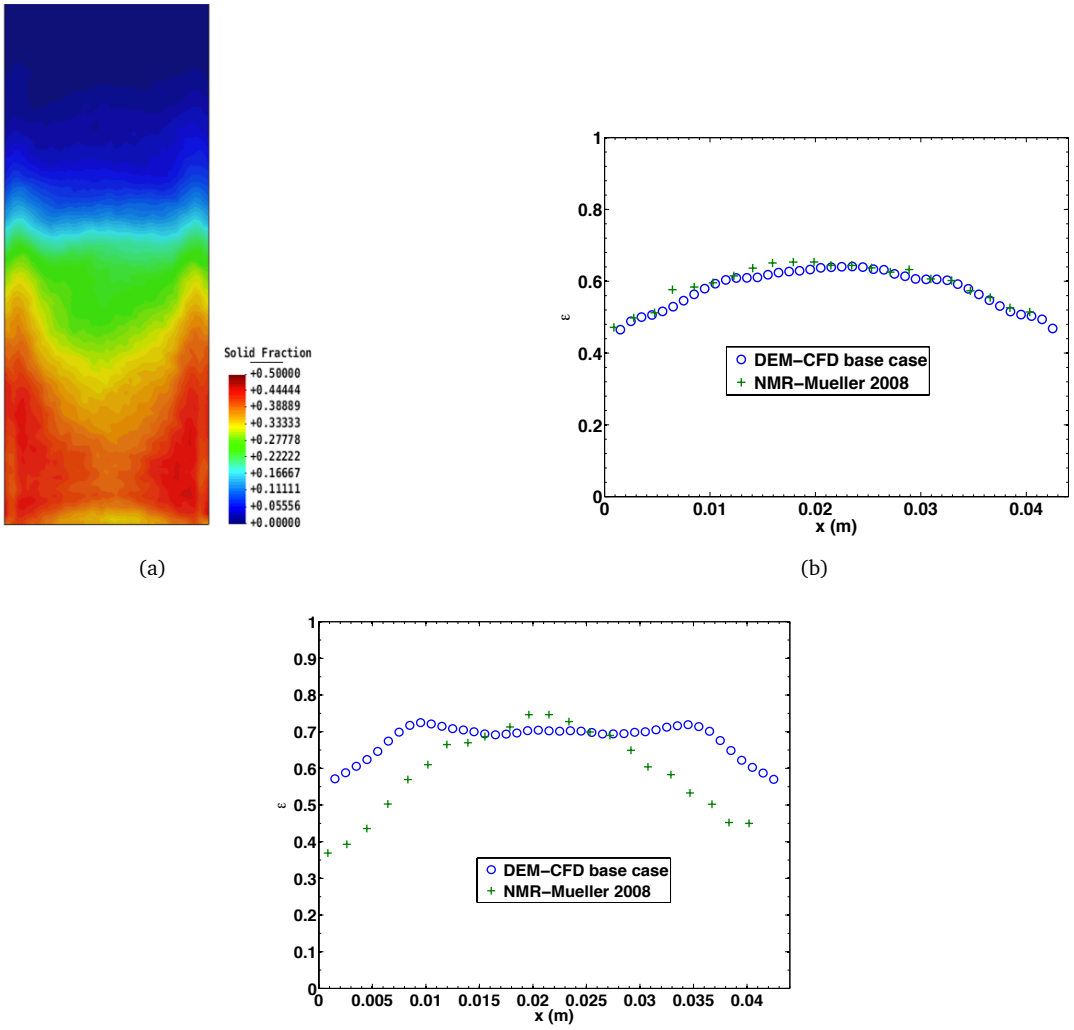

Figure 5.7: DEM-CFD simulation voiadage results: (a) 2D contour plot (b) lateral voidage profiles at height 16.4 mm (c) lateral voidage profiles at height 31.2 mm above distributor plate compared with experimental results by Muller et al. 2008. Superficial inlet velocity for simulations and experimental data is 0.9 m/s.

interaction seems unlikely to account for the solid velocity discrepancy observed in the 5-diameter boundary layer. The fluid-wall boundary effect is further tested by changing the boundary condition from the no-slip to the full-slip one, which should exert a larger effect beyond the one-diameter zone since the current simulation employs a fluid cell of about 3 particle diameters. No discernible effect was found on the solid velocity, which corroborates the point that the fluid–wall effect is not significant in determining the solid velocity in the wall boundary layers.

Attention is now diverted to the particle–wall interaction. In the base simulation case, particles interact with wall via the same force model as the particle–particle interaction

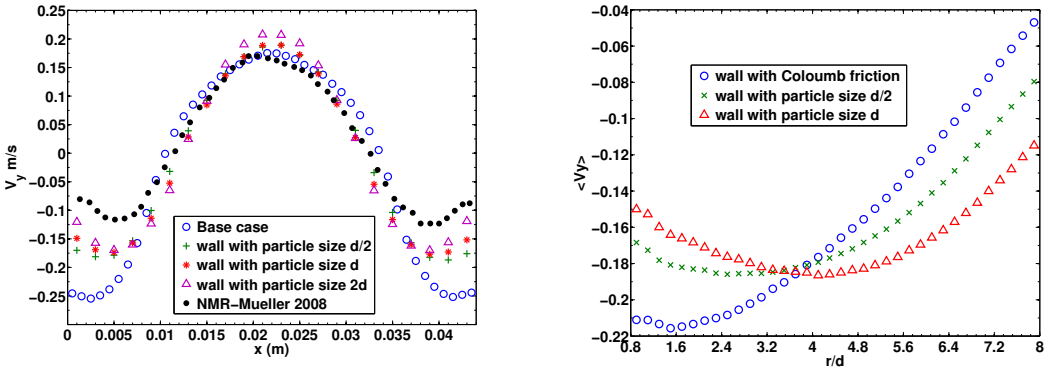

(a) (b)

Figure 5.8: (a) Lateral vertical velocity profiles at height 25 mm at superficial velocity 0.9 m/s in comparison with experimental results by Muller et al. 2008 with rough wall modelled as fixed particle wall made of different diameter of particles (b) Zoomed-in view of the averaged particle velocity around the walls, post-processing with higher time and spatial resolution

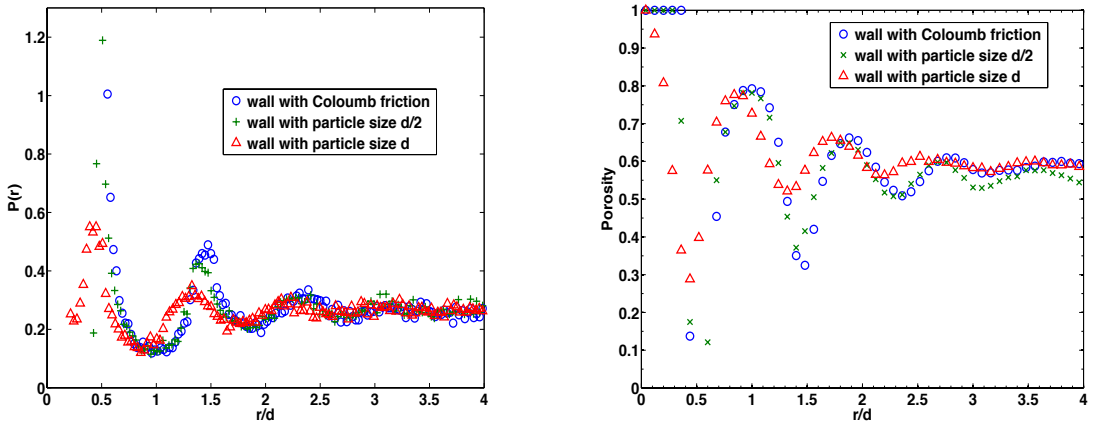

(a) (b)

Figure 5.9: (a) Distribution function of the particle locations (b) Time averaged voidage plotted with distance from the wall (normalised with particle diameter) for different particle-wall conditions

while taking the wall being a flat surface. The only way to change the resistance to particles in this model is to change the particle–wall friction coefficient which limits the tangential force according to the Coulomb's friction law. The coefficient of friction parameter was varied from 0.1 to 0.98 and no significant difference was found in the resulting solid velocity profiles, indicating the wall resistance offered in this model is not sensitive to the friction coefficient. It is noted that the rolling friction between particle and wall was found to have no significant impact on particle dynamics either in another study conducted by Li *et al.* [2012*b*].

Another approach to model solid walls is employed by using closely packed particles,

which would provide additional resistance due to geometric effects, consistent with that from the asperities on a rough wall. The wall particles and inner particles interact with the spring-dashpot model. The former, however, do not move, which is realised in the simulation by either setting their velocities to zero every time step, or not performing the time integration for them. The wall particles are arranged in a regular lattice with no spacing or overlap between them. Two layers of wall particles were added to both the side walls. Since the pattern and spacing are fixed, the particle diameter is the only variable used to tune the "roughness" of the walls. Three different diameters of 0.5, 1 and 2 times of the inner particle diameter were used to test the roughness effect. It should be noted that particle-wall boundaries are employed only for the DEM calculation while the fluid–wall boundary condition remains as flat walls with no slip. Figure 5.8(a) show the effect of particle-walls on the solid velocity for the profile at the height of 25 mm, where there exist largest discrepancies at walls between the base simulation and the experimental results. Similar results for solid velocities have been found for other heights at 15 and 35 mm, but not shown here. It can be seen that the magnitudes of the velocities in the wall boundary layers are reduced by 40–60% compared to the base case and closer to the experimental data for all three particle-wall conditions. Figure 5.8(b) shows the zoomed-in profiles in the near wall region at a higher spatial resolution. It can also be seen that increasing the wall particle diameter results in a greater reduction of solid velocity in the wall boundary layers. The particle-wall also affects the velocities outside of the boundary layers, albeit to a much smaller extent, which also increasing with larger wall particles. At the diameter equal to $2d$, there are appreciable differences from the experimental values in the central region. More interestingly, the granular temperature variation reverses the trend from increasing to decreasing toward the walls when the particle-wall boundary is employed, as demonstrated in figure 5.6. The magnitudes also agree well with the MR measurement.

Examining the particle packing structure more closely, oscillations are found in the particle (Figure 5.9(a)) and voidage (figure 5.9(b)) distributions close to the wall and converge to the bulk values after about 5 particle diameters. The particle distribution function is defined as the ratio of number of particles at a certain distance to the total number of particles which are counted in a region of 20–30 mm above distributor plate and averaged over 40 seconds of simulation. The zero x-coordinate in figure 5.9 is set to the position of either the flat surface or the center of wall particles. Such oscillations in voidage have been reported for particle packing probed by NMR spectroscopy [Sederman *et al.*, 2001]. The particle-wall leads to important difference in the distributions, particularly for those within 0.5 diameter from the wall. Particles are

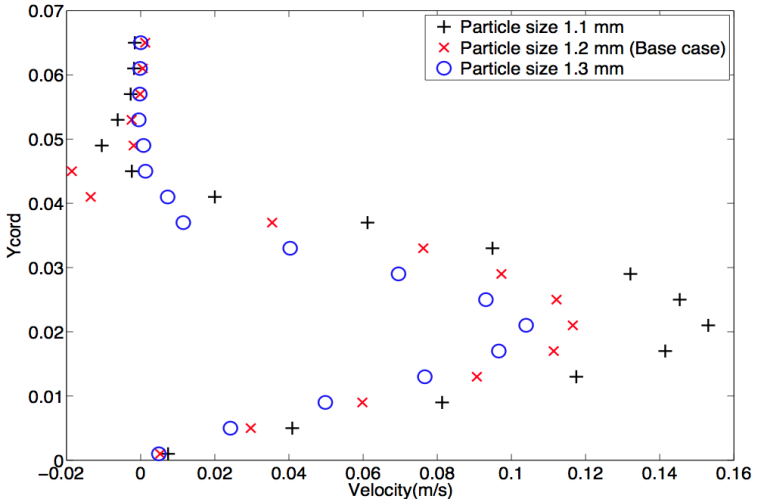

Figure 5.10: Axial profile of time averaged coarse grained vertical velocity for bubbling bed dynamics for particle sizes 1.1,1.2 and 1.3 mm at superficial velocity 0.6 m/s

all excluded from the flat wall by their own volumes and have the highest probability located 0.5 diameter away, where the voidage is correspondingly lowest. This dense layer of particles slide along the wall. On the contrary, there are more particles distributed within the $0.5d$ region when the particle-wall is present, which contributes to greater resistance to the particle flow.

The wall boundary analysis shows that the particle–wall interaction dominate the particle dynamics in the boundary layers of about 5 particle diameters. The wall model with roughness offers more resistance to the particle flow than a smooth frictional wall.

5.3.3.4 Particle shape and size effects

Apart from the dynamics close to the wall, mismatch has also been observed in the middle region especially for the heights at 15 and 35 mm, for example see figure 5.5. This type of mismatch is related to how bed dynamics varies along the bed height direction, which is sensitive to the particle shape and size as demonstrated next.

Kidney-shaped poppy seeds, which naturally have variations in size and shape, were used in the MR fluidization experiments [Müller *et al.*, 2009]. Such size and shape distribution are neglected in the simulation, for which monodisperse spheres with diameter of 1.2 mm were used as described in section 5.3.2. Without performing extensive parametric studies using poly-disperse non-spherical particles, we used a set of simplified simulations to probe the sensitivity to particle size and shape. Simulations of monodisperse spheres are performed at different diameters, namely 1.1 and 1.3 mm, maintaining roughly the same initial bed height and weight as those of the 1.2 mm diameter particles. The simulated minimum fluidization velocity was thus kept in the

range of 0.28–0.32 m/s, close to the experimental value, 0.3 m/s. The variation of velocity V_y along the bed height is plotted in figure 5.10 for the three different particle diameters at a fluidization velocity equal to 0.6 m/s. These profiles are significantly different from each other with the maximum velocity magnitude increased by 50% for a 18% decrease in the particle size. Such a change in magnitude is close to the mismatch between the base simulation and the experimental results (refer to the contour plots in figure 5.4). The velocity is higher for smaller particles at all the positions below 40 mm, above which negative velocities for 1.1 and 1.2 mm particles appear, indicating higher bed expansion. This velocity variation combined with the segregation tendency of a fluidized bed could qualitatively explain the mismatches observed in the middle region at the heights of 15 and 35 mm. Imagining the poppy seeds have larger and smaller particles, the former would tend to concentrate toward the lower part of the bed and the latter to the upper. As particles of a mean size are chosen in the simulation, it would over-predict in the lower and under-predict in the upper part, the same as observed in figure 5.5.

The particle shape effect is somewhat more difficult to quantify, and closely related to the size effect. Here, only the effect on fluid–particle interaction using an empirical drag force correlation [Haider and Levenspiel, 1989] is examined, leaving non-spherical particle-particle contacts for future studies. The drag force model was developed by Haider and Levenspiel [Haider and Levenspiel, 1989] and uses a sphericity index, defined by the ratio of the surface area of a sphere to that of the irregular particle having the same volume. The velocity profiles obtained from the simulations using a sphericity of 0.72 are compared with the base case results in figure 5.11, which shows closer agreement with the experimental results. Specifically, the over-prediction at the center of the bed at 15 mm is reduced from 0.18 to 0.12 m/s (experimental value of 0.05 m/s); the under-prediction is increased from 0.1 to 0.17 m/s (experimental value of 0.3 m/s). The results from the size and shape effect studies suggests that a combination of the two is likely to significantly change the bed dynamics prediction.

5.3.3.5 Effect of bed height

The 2D velocity contour plots suggested that there is a mismatch between the bed expansion predicted by the DEM-CFD simulations, which makes it difficult to capture the hydrodynamics of the bubbling bed by the parametric studies. Particle size effects showed previously that perhaps using a lower particle size than 1.2 mm might be helpful in understanding the differences in the magnitude of the time averaged vertical velocities, but interestingly changing the particle size had no effect on the bed expansion. This could be due to the same bed height used for all the same size particles. Figure 5.12 shows an axial profile of time averaged coarse grained vertical velocity for

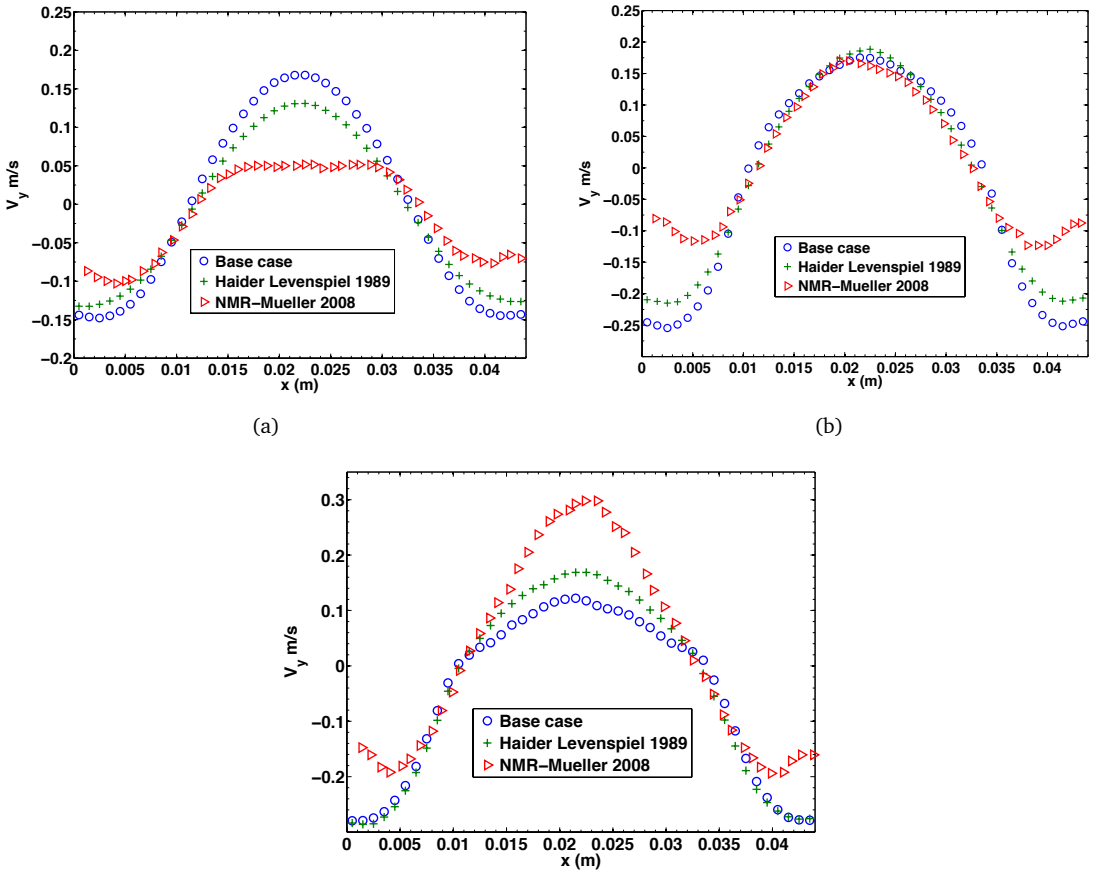

Figure 5.11: DEM-CFD simulation results for lateral vertical velocity profiles at height (a) 15 mm (b) 25 mm (c) 35 mm above distributor plate for superficial velocity 0.9 m/s with Haider and Levenspiel drag model accounting for non-spherical particles, compared with experimental results by Mueller et al. 2008

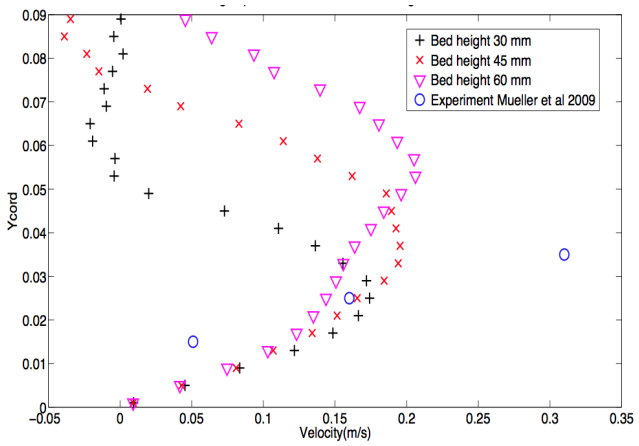

Figure 5.12: Axial profile of time averaged coarse grained vertical velocity for bubbling bed dynamics for different bed heights at superficial velocity 0.9 m/s and particle diameter 1.2 mm.

different initial bed heights at superficial velocity 0.9 m/s and particle diameter 1.2 mm. The trend indicates that changing bed height from 30 mm to 45 mm corrected the contour position of maximum vertical velocity and even the discrepancy in the magnitude of vertical velocity is reduced when compared to the experimental results. These result indicates that bed height is an important parameter in fluidized bed study even a slight error in the experimental measurement can cause discrepancies in the results. Müller *et al.* [2009] did not give details on how the bed height was measured. It would be interesting to simulate different bed heights with different particle sizes and shapes to check if a closer match in the bed hydrodynamics can be reached, these are kept for the future studies. It should be noted that these studies would best serve the interest of validation studies, as every attempt should be made to replicate the experimental conditions while running simulations.

5.3.3.6 Conclusion for bubbling bed validation study

Validation and model sensitivity studies of DEM-CFD to capture bubbling fluidized bed dynamics are presented. DEM-CFD code is validated against fluidization experiments by Müller *et al.* [2009]. The simulations are able to accurately capture the minimum fluidization velocity, pressure drop fluctuations and its major frequency measured in the experiments. Further comparison of the spatial-temporally averaged solid velocity shows that the solid circulation pattern can also be reproduced qualitatively, but robustly independent of the model parameters. There, however, exist quantitative discrepancies in the spatial-temporally averaged voidage, solid velocity and granular temperature profiles, most noticeably in the near wall regions, and in the middle at the upper or lower bed. The level of the differences is largely in line with that previously discovered by other DEM-CFD simulations.

Although such discrepancies are intricately related to various model simplifications and may not be fully addressed in the DEM-CFD framework, it is important to identify how the physical models employed affect the simulation predictions and how sensitive these effects to model parameters. To this end, it is found that the particle–wall interaction dominates the particle dynamics over the fluid–wall interaction in a wall boundary layer of about 5 particle diameter wide. Using a solid wall consisting of particles provides more resistance to the particle motion than using a smooth frictional wall, reducing the mean and variance of particle velocities and leading to closer agreement with the experimental data. This finding shows the importance of the wall boundary for DEM-CFD simulation and leads to the interesting question of how to model such wall boundary layers in a continuum two-fluid model framework, for which proper boundary conditions are essential for correct prediction of large-scale flow behaviour. The data here

suggests that models of effective wall boundary conditions for solid velocity and granular temperature in a two-fluid model could be constructed using the particle dynamics data in such boundary layers.

The bed expansion and dynamics have been found to be sensitive to the particle size, shape and initial bed height. Smaller particles have higher vertical velocities throughout the bed, which implies that size segregation could be a factor contributing to the over-(under-)prediction of velocities at the lower (upper) parts of the bed. The shape effect on fluid–particle interaction investigated through using a modified drag model led to appreciably closer agreement with the experimental solid velocities. These findings also point to some problems warranting further studies. It would be interesting to conduct DEM-CFD simulations using spherical particles with a size distribution which has the mean of 1.2 mm and a small variance to test if such size distributions contribute to the velocity discrepancies observed in the lower and upper bed. In the same spirit, DEM-CFD simulations of non-spherical particles together with the modified drag force model could further quantify the effect of the particle–particle interaction in this condition.

5.4 Spouted bed fluidization

5.4.1 Introduction

This section will deal with another type of fluidization process called the spouted fluidization. The process differs from the conventional procedure and supplies a jet inlet velocity at the centre of the bed instead of uniform distribution. When inlet velocity is uniformly distributed throughout the distributor plate, instabilities develop all across. In a spouted fluidization, a jet of very high inlet velocity (U_{sp}) is forced through a very small area in the middle of the distributor plate and rest of the distributor plate is subjected to a background inlet velocity (U_{bg}) which is greater than the U_{mf}. For bubbling bed dynamics, it was observed that the instantaneous bed behaviour is very random and chaotic, but the time averaged profile brought out a regular solid recirculation pattern which was not at all representative of transient behaviour. The particles in a spouted beds are always in circulating motion, leading to a better mixing and maximizes heat and mass transfer rates. Pharmaceutical tablet coating, drying and granulation processes have all benefited vastly through spouted bed hydrodynamics. An understanding of the spouted bed phenomenon is crucial for their successful application and optimization of operating conditions. Recent advancements in the spouting bed technology is summarized in a review by Sutkar *et al.* [2013].

Spout bed experiments by Link *et al.* [2008] have served as an excellent study for validation purposes of DEM-CFD codes [Li *et al.*, 2012*b*; Link *et al.*, 2008]. These experiments are conducted in different spouted bed fluidization regimes: (a) Intermediate/spout-fluidization (b) Spouting-with-aeration (c) Jet-in-fluidized-bed. Further details on these regimes can be found in Link *et al.* [2005] and Zhang and Tang [2004]. The present study does not delve into the spouted bed phenomenon, but use it for extensive validation of DEM-CFD code. This validation study tests capabilities of the code in several different ways as opposed to the earlier bubbling bed case, apart from application to a different fluidization process.

- The magnitude of U_{sp} in this study can escalate as high as 60 times U_{mf} and tests numerical convergence of the code in dense regions with very high Re numbers as opposed to the bubbling bed case where maximum inlet velocity was only $3U_{mf}$.
- Large number of particles (around 44K), a significant increase to test codes capability to handle large data in a reasonable computational time.
- Well rounded glass beads are modelled and contact mechanics parameters are well studied and reported by Goldschmidt *et al.* [2003].
- The apparatus is a 3D bed with a considerable depth, hence 3D CFD is modelled to describe the fluid motion as opposed to pseudo 2D in the bubbling bed case.

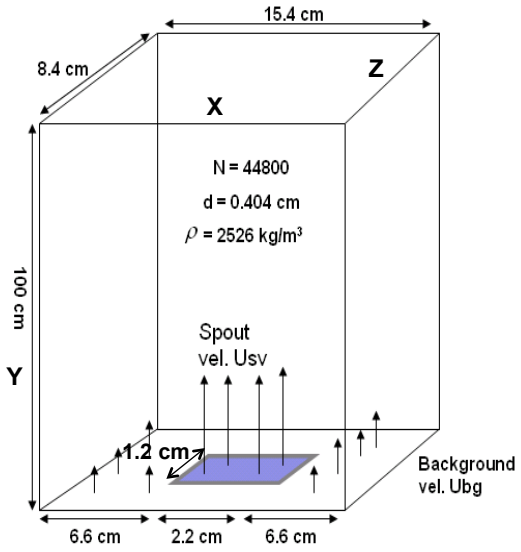

Figure 5.13: Schematic diagram of the 3D spouted bed showing geometry and inlet for spouted velocity (U_{sp}) and background velocity (U_{bg}). Dimensions are in cm.

5.4.2 Simulation set-up

The fluidized bed set-up is a three-dimensional apparatus with side wall made of aluminium, where as the front and back walls are made of poly-carbonate. A schematic diagram of the 3D bed with dimensions can be seen in the figure 5.13 with regions for U_{sp} and U_{bg} well indicated. A bed height of around 47 cm containing, glass beads of diameter 4.04 mm and density 2526 kg/m^3, was fluidized with a spout region of dimension 1.2 cm in the depth direction (z) and 2.2 cm in the axial direction (x). The rest of the inlet region was fluidized with background velocity U_{bg} to avoid stagnant zones. The experimental U_{mf} was found to be around 1.77 m/s. A non intrusive experimental measurement technique called Positron Emission Particle Tracking (PEPT) was employed to find temporally averaged particle velocities. The PEPT technique is based on the principles of radio-isotopes decaying continuously [Link *et al.*, 2008]. The particle trajectory and velocity of a single radio-active particle inside the spouted bed is tracked by PEPT for several hours. The details of obtaining the temporally averaged data at various points by in fluidized bed can be found in Link *et al.* [2008].

Table 5.3: Domain size and DEM-CFD simulation parameters for spouted bed case

DEM Parameter	**Value**
Number of Particles	44800
Diameter, mm	4.04
Sphericity	1
Particle Density, ρ (kg/m^3)	2526
Spring Stiffness, k (N/m)	800
Coefficient of restitution, e (N/m)	0.97
Inter-particle friction coefficient, μ (N/m)	0.1
Particle-wall friction coefficient, μ (N/m)	0.1
Particle time-step, t_p (s)	10^{-7}
Gas Phase	
Gas density, ρ_f (kg/m^3)	1.225
Gas viscosity, μ_f (Pa $\cdot$ s)	1.8e-5
Wall boundary condition	No-slip
Inlet boundary condition	Inlet velocity profile
Outlet boundary condition	Pressure outlet, 10^5 Pa
Fluid time-step, t_f (s)	10^{-5}
Geometry	
Bed width (x), m	0.154
Bed height (y), m	1.0
Bed thickness (z), m	0.084
Number of cells (N_x)	8
Number of cells (N_y)	80
Number of cells (N_z)	5

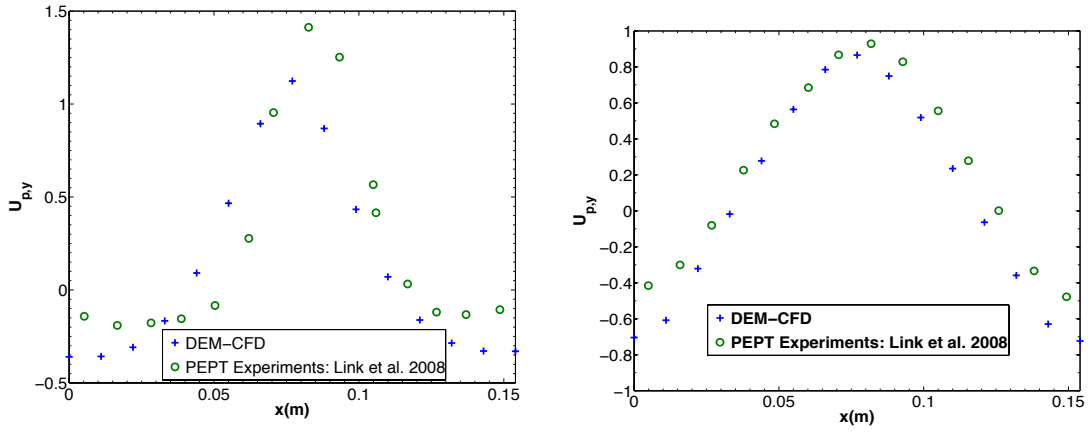

(a) (b)

Figure 5.14: Lateral profile of the time-averaged vertical particle velocity in the central x-z plane for case B1 at different heights (a) 15 mm (b) 25 mm. Velocities are measured in m/s

The full-scale bed was simulated with parameters for the geometry, fluid properties and contact model summarised in table 5.3. The fluid flow was modelled as 3D, even though the the thickness of the bed was comparatively small to height. The no-slip boundary condition was applied between fluid and all the walls. The coefficient of friction between particles and the walls was set to 0.1. The inlet velocity conditions for different cases is summarized in table 5.4. These operating conditions were carefully selected for the experiments and simulations by Link *et al.* [2008] to cover spout bed fluidization regime map given by Zhang and Tang [2004].

Table 5.4: Operating conditions for different simulations for spouted bed

Case	Background velocity (U_{bg}), m/s	Spouting velocity (U_{sp}), m/s
A	2.5	60
B	2.5	90
C	3.5	65

The present study employed a drag model by Syamlal and O'Brien [1987] to model hydrodynamics, while studies by Link *et al.* [2008] employed drag model by Koch and Hill [2001]. Li *et al.* [2012*b*] did not report the drag model used. As the inlet jet velocity is very high, a low fluid time step of 10^{-5} s was used to achieve a stable numerical convergence. A total of 30 seconds of simulation were run with DEM data recorded at 100 Hz frequency. The first 5 seconds of the data was discarded as start-up phase. Numerical studies by Link *et al.* [2008] and Li *et al.* [2012*b*] ran simulations for 20 and 25 seconds respectively as opposed to 1 hour of PEPT experiments.

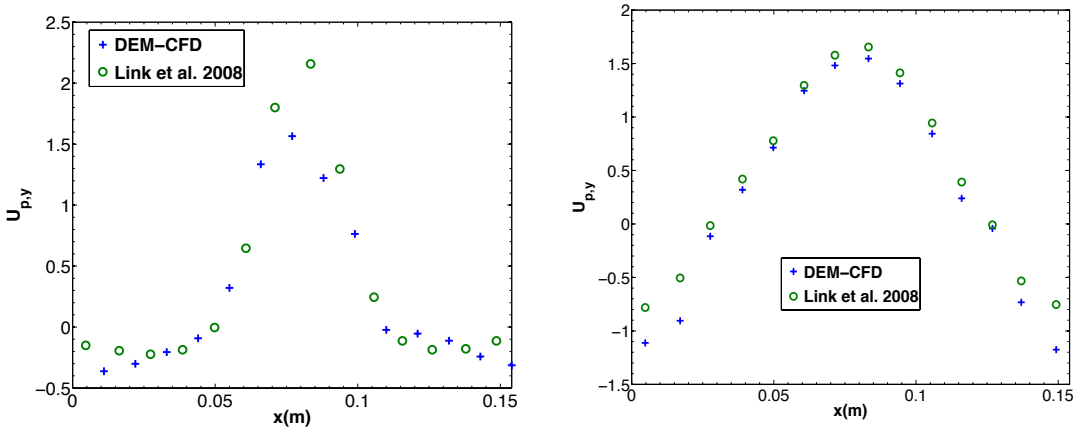

(a) (b)

Figure 5.15: Lateral profile of the time-averaged vertical particle velocity in the central x-z plane for case B2 at different heights (a) 15 mm (b) 25 mm. Velocities are measured in m/s

5.4.3 Comparison with experiments

This section will present the results of time-averaged vertical velocity compared with PEPT experimental measurements. The PEPT measurements comprises of the particle trajectory at different times, which is used to derive the instantaneous particle velocity [Link *et al.*, 2008] at the particle position. The time averaged particle velocity is derived by collocating data at longer times. A similar averaging method is applied to the DEM data to obtain the averaged particle velocity. This averaging is the same as the point-based averaging technique used in the NMR case. The data in the central x-y plane is recorded with $0.036 < z < 0.048$ m for experiments and DEM-CFD simulations. A key difference between the experiments and simulation data post processing is the difference in the resolution of the data. PEPT records a single particle data over 1 hr which gives recording data of 1 hr/particle $\times$ 1 particle $\sim$ 1 hour, where as in DEM-CFD simulations data for 44K particles is recorded over 20 s/per particle which gives data of $\sim$ 220 hours. A key assumption in extracting data from PEPT is that the fluidization process is ergodic and the time averaging is same as the ensemble averaging. This assumption has not been rigorously tested and it is further assumed that the experiments have run long enough that the tracer particle has been through all the phase space possible.

Case A in the table 5.4 shows an intermediate spout regime in which the spouting channel is interrupted periodically from the annulus region. Figure 5.14 shows comparison for time averaged plots of velocities between the experiments and at heights 0.15 m and 0.25 m above the distributor plate for case A (table 5.4). There is a good agreement between the DEM-CFD data and the experiments for both the heights. Quantitatively,

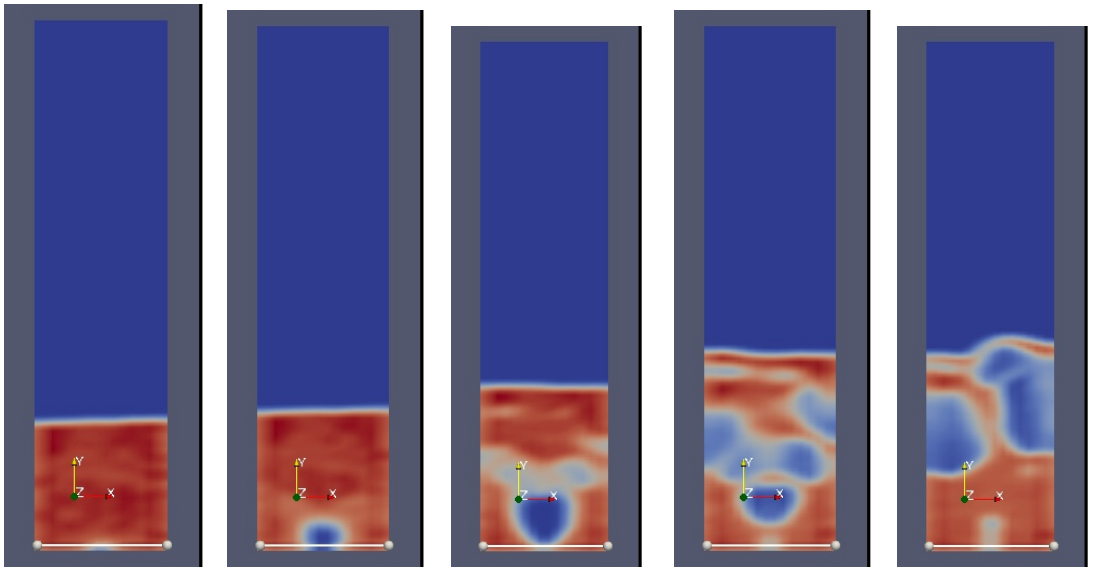

(a) (b) (c) (d) (e)

Figure 5.16: [Snapshots of DEM-CFD simulations for Case B spouting bed simulation]. The figure shows the coarse grained solid fraction at a central x-z cross-section, red is the dense region ($\phi = 0.65$) and blue is the dilute region ($\phi = 0$) at different times (a) 0.0 s (b) 0.5 s (c) 1 s (d) 1.5 s (e) 2 s.

at height 0.15 m (figure 5.14a), the spouting section of the bed (mid region) has a maximum discrepancy of around 20%. Around the walls, there is a similar discrepancy as seen from the bubbling bed section, though the severity of the mismatch is lower. Link *et al.* [2008] observed that the tracer particle had a tendency to be around spouting section than to be around the walls. This lead to poor resolution data around the walls and experiments were repeated by introducing the tracer close to the wall.

Case B presents a spouting-with-aeration regime, in which the spout channel is stable and penetrates the bed continuously. Figure 5.15 shows that the comparison for time averaged plots of velocities between the experiments and at heights 0.15 and 0.25 m which for this case gives a fine agreement. Quantitative disagreement around the walls and the mid sections are around 18% and 23% respectively. Case C represents a jet-in-fluidized bed regime, in which both the spout channel and the bubbles are in close interaction with each other. Figure 5.17 shows the comparison between the experiments and DEM-CFD simulations which show a good match. Quantitative disagreements are similar to the previous two regime cases. A similar analysis between the experimental and DEM-CFD simulations in the spouted bed fluidization for these regimes was reported by Li *et al.* [2012*b*] and Link *et al.* [2008]. A evolution of the jet in the spouting bed is shown in the figure 5.16. The figure shows the coarse grained solid fraction at a central x-z cross-section, red is the dense region ($\phi = 0.65$) and blue is the dilute region ($\phi = 0$) at different times (a) 0.0 s (b) 0.5 s (c) 1 s (d) 1.5 s (e) 2 s.

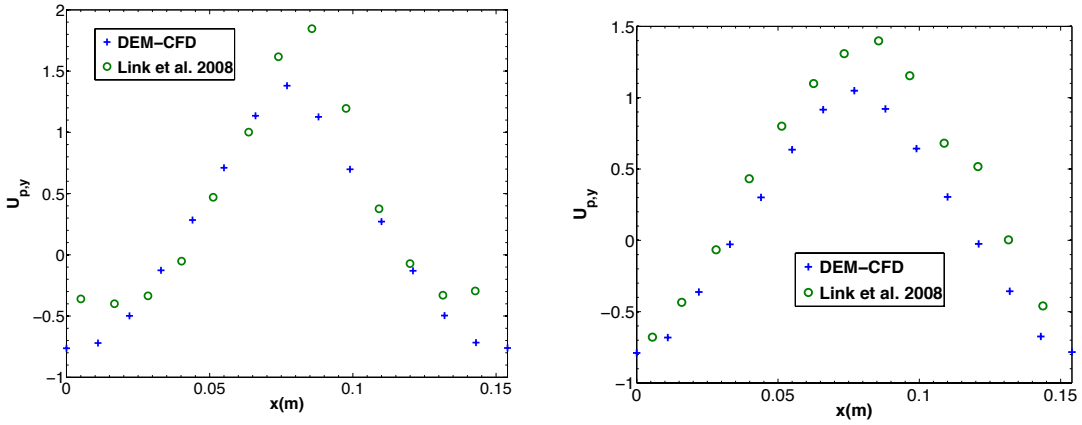

(a) (b)

Figure 5.17: Lateral profile of the time-averaged vertical particle velocity in the central x-z plane for case B3 at different heights (a) 15 mm (b) 25 mm. Velocities are measured in m/s.

5.4.4 Discussion and conclusions

The capabilities of DEM-CFD code to reproduce the complex hydrodynamics of different regimes of spouting fluidization is assessed. For all three regimes studied, the predictions on the averaged particle velocities are in good agreement with the experiments. Quantitatively, differences in between the experiments and simulations were much smaller than observed from the bubbling bed case. This could be mainly due to the fact that, the particle used in this study were spherical, monodispersed glass beads in the experiment whose hydrodynamics are easier to model by drag models presented in literature [Di Felice, 1994; Syamlal and O'Brien, 1987]. The spout bed regimes presented here cover both dense and dilute phase at high Reynolds number, which is the intended usage of the DEM-CFD model later. The realm or the limit of validation is increased from the previous bubbling bed case with higher inlet velocities. Also, it is noted that, given the accurate particle shape representation of spherical glass beads, a better agreement can be reached between the numerical simulations and experiments. Statistical averaging issues are apparent while using the PEPT technique to characterize the fluidized bed hydrodynamics and subsequent comparisons with DEM-CFD simulations. It is further suggested that, similar to the PEPT characterization, instead of taking all the DEM particle data, a few hundred tracer particles can be tracked at different places for post processing with simulations recorded at a higher frequency and running a longer time. It should be further noted that, even though the averaged hydrodynamics predicted by the DEM-CFD code is in close agreement with experiments, it does not guarantee that the physics has been fully captured at a local time scale. Fluid-particle drag can be a major cause of the discrepancies between the numerical

and experimental data. It is emphasized that drag models used here are beyond their region of validity and employed in an ad-hoc manner. Such practices are quite prevelant in literature due to the lack of drag model which is applicable in a wide range of Reynolds number and solid fractions present in a typical fluidized system.

5.5 Bidisperse bed: Segregation

Particles with different properties, such as size and density, are encountered in many industrial processes. Industrial raw materials have narrow or wide particle size distributions largely affecting bulk macroscopic behaviour of the system. Hydrodynamics effects at different length scales are very evident from the span of the Geldart chart covering sizes from 10^{-6} to 10 mm. A better understanding of these processes is required to either optimize segregation or enhance mixing, depending upon the application.

This study employs the DEM-CFD code to model segregation in beds with 2 different particle sizes or densities. Consider two kinds of particles, denoted as p_1 and p_2, with number, size, density,mass and minimum fluidization velocities of homogeneous packed beds as (n_1,d_1,ρ_1,m_1,U_{mf1}) and (n_2,d_2,ρ_2,m_2,U_{mf2}) with $m_1 < m_2$. According to Ergun's equation [Ergun, 1952], U$_{mf}$ for heavier particles (U_{mf2}) will be greater than U_{mf1}. If a uniformly mixed granular packed bed of p_1 and p_2 is fluidized with inlet velocity U such that U_{mf1} < U < U_{mf2}, then segregation would occur due to different fluidization characteristics of the two species. Since U_{mf1} < U, particle species p_1 are fully fluidized and the weight of these particles is countered by hydrodynamic forces and they have a tendency to go up. By similar logic, particle species p_2 will tend to sink down due to their own weight. The particles p_1 and p_2 are referred to as flotsam and jetsam particles respectively. Segregation experiments were conducted by Goldschmidt *et al.* [2003] on a pseudo 2D bed to quantify the rate of segregation and will be used as validation data for testing capabilities of the DEM-CFD model to capture hydrodynamics of the bi-disperse bed. Since segregation is driven by the hydrodynamics, drag model closures are critical and will be addressed more carefully in this study.

5.5.1 Simulation set-up

The fluidized bed set-up is a pseudo two-dimensional apparatus with perspex walls. Particle properties used in the experiments are summarized in the table 5.5. Experimental fluidization velocities for homogeneous beds of these particles were measured from pressure drop versus inlet velocity curves as U_{mf1} = 0.78 m/s and U_{mf2} = 1.25 m/s. Different mass ratio of particles p_1 and p_2 ranging from 0-1 were prepared and U$_{mf}$ measured.

Table 5.5: Bed dimensions and particle numbers for segregation rate experiment.

Rig dimensions	15 X 70 X 1.5 cm
Total mass of the particles	247 g
Number of p_1	27710
Number of p_2	5980
Bed height	7.5 cm

To measure segregation rates, 50% by mass ratio of particles p_1 and p_2 were uniformly mixed with a bed height of 75 mm (around half the width of the bed) and fluidized at inlet velocity of 1.2 m/s. More detailed tables on the rig apparatus can be found in Goldschmidt *et al.* [2003]. U_{mf} of this bed was measured around 0.93 m/s. Digital image analysis of the segregation phenomenon was conducted at the front wall to measure relative segregation rates. In order to enhance the image contrast, glass beads of the 2 different particle types were coated with yellow and blue colours respectively. A detailed calibration of measurement technique details can be found at Goldschmidt *et al.* [2003].

The front wall of the experiment was discretized for calculation of relative segregation index (s)[Goldschmidt *et al.*, 2003], given by equation 5.6:

$$s = \frac{S-1}{S_{max}-1} \tag{5.6}$$

Where S,the ratio of average heights of the small and large particles, is given by equation 5.7:

$$S = \frac{< h_{small} >}{< h_{large} >} \tag{5.7}$$

Averaged height of the particle species per time step is a porosity weighted average of discretized cells, given by equation 5.8. Here, k is the time step and $\epsilon_{k,cell}$ is the porosity of a cell at time step k. S_{max} is the maximum segregation that could occur in a bed with mass fraction of smaller particle (x_{small}), given by equation 5.9.

$$< h_k >= \frac{\sum \epsilon_{k,cell} h_{cell}}{\sum \epsilon_{k,cell}} \tag{5.8}$$

$$S_{max} = \frac{2 - x_{small}}{1 - x_{small}} \tag{5.9}$$

The simulated fluidized bed in this study is at the same scale as the experimental bed along with the number of particles and the bed weight. It should be noted that the

segregation rate depends upon both the bed composition and bed heights [Goldschmidt *et al.*, 2003]. The distributor plate is simulated by arranging particles of size 500 μm in a regular lattice array of spanning 2 fluid mesh cells in the height direction. Table 5.6 presents the simulation parameters for the DEM-CFD simulations. The simulation bed was prepared by the rainfall method with a mixture of particles p_1 and p_2 particles settling under gravity. The assembly was fluidized at a much higher velocity than U_{mf2} for 10 seconds. The gas inlet supply was suddenly stopped and particles were allowed to settled down resulting in a well-mixed bidisperse bed. The particles p_1 and p_2 are represented by blue and red colour respectively. s calculations are done on the DEM particle data, except the whole domain is meshed in pseudo 2D with only one cell in the depth direction, as opposed to the experimental calculations done only on the data taken on the front wall. It is attempted to keep the initial composition and the spatial distribution of lighter and heavier particles, which is quantified by s for simulation and experiments as close as possible for a fair comparison.

Table 5.6: Simulation Parameters for DEM-CFD modelling of bidisperse bed

DEM Parameter	**Value**
Diameter, mm	1,1.5, 2.5
Small particle volume fraction	0-1
Sphericity	1
Particle Density, ρ (kg/m^3)	2523
Spring Stiffness, k (N/m)	200
Coefficient of restitution, e (N/m)	0.98
Static friction, μ (N/m)	0.1
Gas Phase	
Gas density, ρ_f (kg/m^3)	1.225
Gas viscosity, μ_f Pa.s	1.8e-5
Inlet velocity, v_f m/s	0.8-1.3
Geometry	
Bed width, m	0.15
Bed height, m	1
Bed thickness, m	0.015

5.5.2 Result and discussion

5.5.2.1 Packing density and minimum fluidization velocity

An optimization of random packing is necessary for maximum efficiency of processes that employ packed or fixed beds [Yang *et al.*, 2000]. In particular, fluidization characteristics depend not only on the bed composition but also on spatial distribution of widely distributed particle sizes. Bidisperse bed of different mass ratios of particle p_1

and p_2 were prepared to capture both the experimental trends of bed packing and compare minimum fluidization velocities (U_{mf}).

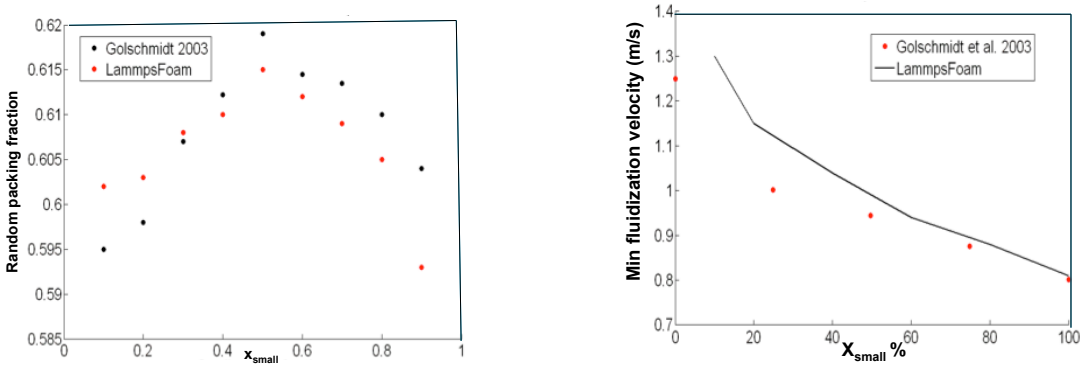

(a) (b)

Figure 5.18: Comparison plots between experiment and DEM-CFD simulation for (a) solid fraction at different mixture by mass for larger and smaller particles and (b) Minimum fluidization plot at different volume mixture contents

Figure 5.18a compares the packing density of DEM simulated bed with experimental results by Goldschmidt *et al.* [2003] as a function of bed composition. Here x_{small} denotes the ratio between the total mass of particle p_1 and p_2. There is a close agreement between the experimental data [Goldschmidt *et al.*, 2003] and DEM simulation results presented here. Robust trends of higher packing density for 50% bed composition evident in the experiments was captured by the simulations as well. Similar conclusions were reached by Li *et al.* [2012*b*] employing DEM simulations of random packing assemblies. It should be pointed out that simulations and experiments are conducted in a pseudo 2D bed and these results suffer from wall effects and cannot be readily compared to solutions given by Fedors and Landel [1979] and Yu and Standish [1987], which are derived in homogeneous conditions.

Figure 5.18b compares experimental U_{mf} for different bed compositions with the U_{mf} results from the DEM-CFD simulations employing the Gidaspow [1994] drag model. U_{mf} trends are captured accurately for most of the assemblies with an average error of 8%. Since U_{mf} depends upon the hydrodynamics and initial packing fraction, a series of simulations were run with different drag models from literature for bed composition x_{small}=0.5. Static or fixed bidisperse bed was fluidized with inlet velocity varying linearly with time from 0.0 to 1.8 m/s to 0.0 in 12 seconds. Figure 5.19 demonstrates the fluidization and defluidization curves. U_{mfa} was calculated by finding minimum inlet velocity at which pressure drop does not increase linearly but fluctuates around a mean for the fluidizing branch. U_{mfb} was calculated similarly from defluidizing branch. U_{mf} for the assembly is taken as average of U_{mfa} and U_{mfb}.

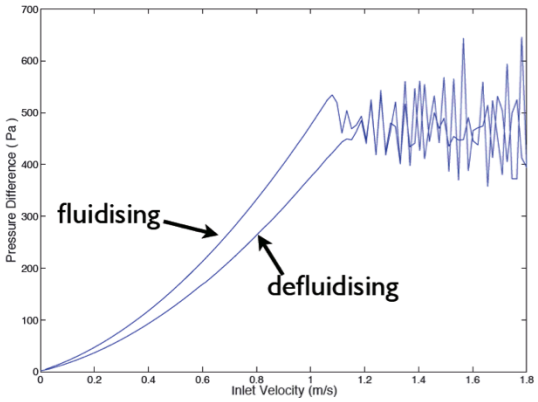

Figure 5.19: Plot between pressure drop and varying inlet velocity, average between fluidising and defluidising curve gives the minimum fluidisation velocity

Table 5.7: Minimum fluidization values for 50% by volume fraction of bidisperse bed for different drag laws. HYS 2010a drag model means that only bidisperse corrections are taken while HYS2010b means corrections for hydrodynamic interactions are also accounted for.

Drag Models	Umf (m/s)
Gidaspow [1994]	1.075
Syamlal and O'Brien [1987]	1.01
Beetstra *et al.* [2007*a*]	1.04
HYS 2010a (Holloway *et al.* [2010])	1.045
HYS 2010b (Holloway *et al.* [2010])	1.05
Experimental [Goldschmidt *et al.*, 2003]	0.98

A substantial amount of research have been put into developing drag models for bidisperse systems in past decade. The drag models used in this study can be broadly classified into three categories. Equations, theory and implementation of these drag models in the DEM-CFD code can be studied from section 3.4.1.

- C1: Drag models derived for monodisperse systems but employed in an ad-hoc manner (Gidaspow [1994],Syamlal and O'Brien [1987].Beetstra *et al.* [2007*a*]).
- C2: Drag models derived by LB simulations of polydisperse particles accounting for bidispersity effects in fixed bed conditions [Beetstra *et al.*, 2007*b*] or flow at intermediate Reynolds number [Holloway *et al.*, 2010]. The drag forces acting on smaller and larger particles calculated from monodisperse drag models were re-weighted. The larger and smaller particles were given more and less drag forces respectively ([Beetstra *et al.*, 2007*a*]).
- C3: C2 drag model by Holloway *et al.* [2010] accounting for effect of hydrodynamic interactions between 2 solid species present in the system.

Values of U_{mf} as calculated from DEM-CFD simulations with different drag models are summarized in table 5.7. The experimental U_{mf} by Goldschmidt *et al.* [2003] was measured as 0.98 m/s. All the drag models predict U_{mf} within 8% of the experimental value. The pressure drop and packing studies indicate that macroscopic features of bidisperse fluidized beds are well captured by DEM-CFD simulations. Attention is now turned to study mesoscopic and more robust phenomenon: segregation.

5.5.2.2 Segregation rates

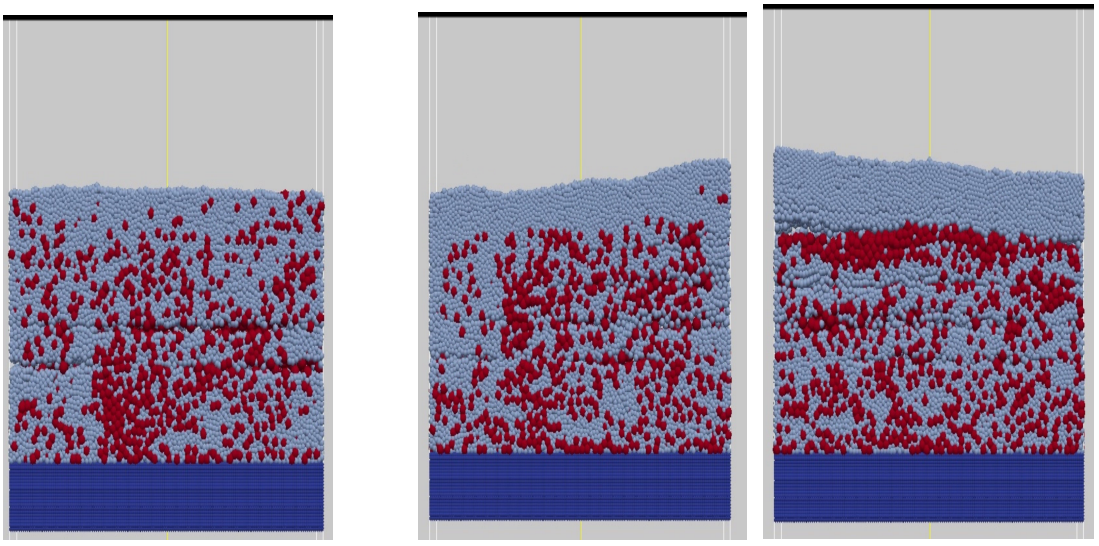

(a) (b) (c)

Figure 5.20: Snapshots of DEM-CFD simulations of bi-disperse bed at time (a) 0.1 s (b) 3 s (d) 10. Particle size 1.5 mm (blue) and 2.5 mm (red) fluidized at $1.1U_{mf}$ velocity using Gidaspow [1994] drag model. (a) shows a well mixed bed bidispese bed while (b) and (c) have high concentration of small and large particles at the top and bottom of the bed respectively.

Relative segregation rate (s) of a bidisperse bed with 50% by mas ratio of particle size 1.5 and 2.5 mm, was obtained from Goldschmidt *et al.* [2003] at 1.1 m/s ($1.12U_{mf,e}$). In this section, the DEM-CFD simulation results will be presented for the same case with different drag models. Since, U_{mf} is different for drag models presented in table 5.7, it is only fair to compare segregation rates from DEM-CFD simulations at normalized inlet velocities i.e. $1.12U_{mf}$ instead of absolute velocity of 1.1 m/s. Figure 5.20 presents snapshots of DEM-CFD simulations of bi-disperse bed at time (a) 0.1 s (b) 3 s (d) 10 s. Particles of size 1.5 mm (blue) and 2.5 mm (red) are fluidized at $1.1U_{mf}$ velocity using Gidaspow [1994] drag model. Figure 5.20(a) shows a well mixed bed bidisperse bed while 5.20(b) and 5.20(c) have high concentration of small and large particles at the top and bottom of the bed respectively indicating segregation.

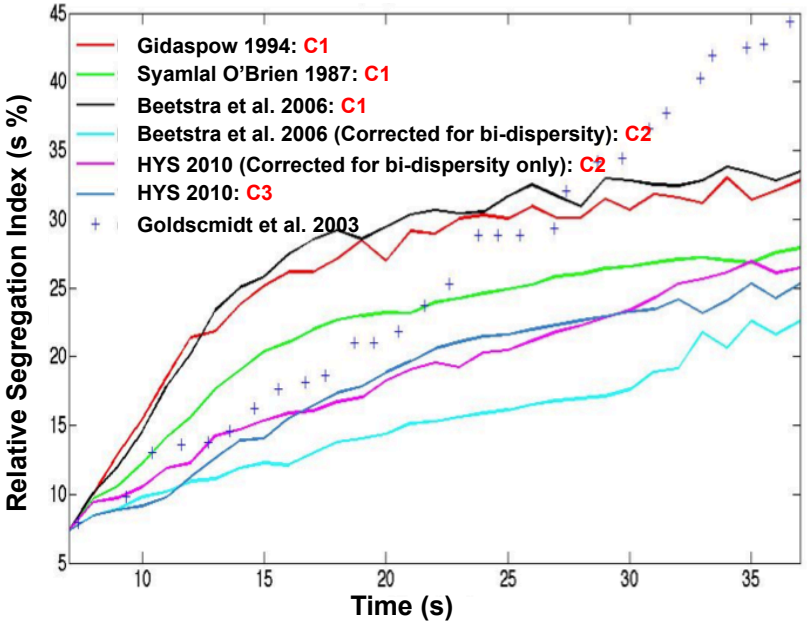

Figure 5.21: Relative segregation rate (s %) plotted with time for different drag models.

The figure 5.21 shows a comparison of segregation rates by different drag models, amongst themselves and the experimental results by Goldschmidt *et al.* [2003]. The DEM-CFD simulations can capture features of bidisperse bed segregation and linear trends are captured qualitatively by the model. The two-fluid model was employed to compare with Goldschmidt *et al.* [2003] experimental data and shown to have large over-estimation of segregation rates by Sun and Battaglia [2006]. The segregation rates predicted by C1 drag models are much higher than by C2 and C3 drag models. In comparisons with the experimental data, C2 and C3 predictions are better than C1 drag models. Experiments suggest that segregation rates are linear with time throughout the run, but DEM-CFD simulation predictions, in general, plateau on after initial 20 seconds when the bed is segregated. In particular, drag model C3 captures experimental behaviour until 20 sec, but under predicts at later times. This segregation rate under-prediction at the later times might be due to higher concentration of larger particles at the bottom of the bed. When the larger particles settle down, they experience more drag due to higher volume fraction according to the correction factor of bidisperse drag laws. This promotes mixing when the bed is highly segregated at the later times and mono disperse drag laws are more applicable in segregated beds. The limitation of C3 drag model for applicability in highly segregated bed can be reflected by a constraint on it of $1 < (\phi_1/\phi_2) < 3$, where ϕ_1 and ϕ_2 are the solid fraction of lighter and heavier particles respectively [Holloway *et al.*, 2010].

Table 5.8: Particle properties for 50% by number study.

	p_1	p_2	Ratio (p_1/p_2)
Number	10527	10527	1
Diameter (mm)	1.5	2.5	0.6
U_{mf}(m/s)	0.78	1.25	0.625
Density (kg/m$\hat{3}$)	2523	2526	1
Total mass (g)	47	217	0.21

In line with present findings, a multifluid model study of bidisperse bed by van Sint Annaland *et al.* [2009] also reported that simulations with Gidaspow [1994] predicted high segregation rates than the experimental rates measured by Goldschmidt *et al.* [2003]. Li *et al.* [2012*b*] employed the Gidaspow [1994] with poly-disperse correction and found a good match with experiments, however, such a treatment of drag models is questionable. Though, it is noted that segregation rates are difficult to model by just one drag model and perhaps a combination of these are required. Furthermore, it is identified that a careful study of calibrating certain parameters of HYS 2010 models is needed. There is no clear distinction between C2 and C3 drag models in this study due to following points.

- The particle sizes used in this study 1.5 and 2.5 mm were similar, and hence differences in the relative velocities of each species with the fluid were similar. Fluid particle drag is a function of the projected surface area of the particles. The effect of hydrodynamic interactions will be more profound at larger particle size ratios.
- The number of large particles were far less than the smaller particles. The drag model is constrained by volume fraction ratios ($1 < (\phi_1/\phi_2) < 3$).

A preliminary study to investigate effect of particle hydrodynamics is proposed with 2 modifications to current set of particle properties. 1) Instead of mass ratio = 1, Number ratio of each particle species is equal to 1. 2) Increase the particle diameter ratio from 1.66 to 2.5, particle size 1 and 2.5 mm respectively. The C3 drag model is applicable in the range: $1 < d_1/d_2 < 2.5$ [Holloway *et al.*, 2010]. The particle properties for first study with number ratio 1, are summarized in table 5.8. U_{mf} for this bidisperse bed was calculated from the pressure drop versus inlet velocity curve is summarized in the table 5.9.

The figure 5.22a plots segregation rates with time for bidisperse bed with equal number of particles at fluidizing velocity of $1.1U_{mf}$. The legend indicates the drag models employed from different categories C1, C2 and C3. In the 50% by number study, a higher number of larger particles are being corrected for poly-dispersity as compared

Table 5.9: Minimum fluidization values for 50% by volume fraction of bidisperse bed for different drag laws. HYS 2010a drag model means that only bidisperse corrections are taken while HYS2010b means corrections for hydrodynamic interactions are also accounted for.

Drag Models	Umf (m/s)
Gidaspow [1994]	0.84
Syamlal and O'Brien [1987]	0.83
Beetstra *et al.* [2007*a*]	0.85
HYS 2010a (Holloway *et al.* [2010])	0.865
HYS 2010b (Holloway *et al.* [2010])	0.87

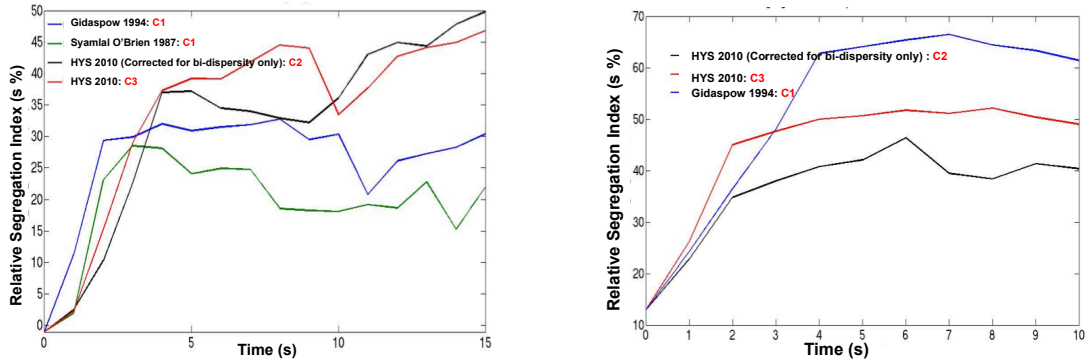

(a) (b)

Figure 5.22: Segregation rates

to the case with 50% mass ratio. The segregation rates for 50% by number case are significantly higher than the 50% by mass study. The C1 drag models plateau after 5 seconds of simulation and segregation of around 30%, but the C2 and C3 drag models are increasing linearly. The trends of C2 and C3 drag models are similar, but differences can be seen after 35% segregation.

Table 5.10: Particle properties for higher particle diameter ratio study.

	Small particles	Large particles
Number	28648	1464
Diameter (mm)	1.0	2.5
U_{mf}(m/s)	0.68	1.25
Density (kg/m$\hat{3}$)	2523	2526
Total mass (g)	47	217

Table 5.10 summarizes bidisperse study with a higher particle size ratio at 50% by mass ratio. U_{mf} for this bidisperse bed was calculated from the pressure drop versus inlet velocity curve and summarized in the table 5.11. Figure 5.22b shows the segregation rates with time for bidisperse bed with these particles properties at fluidizing velocity of $1.21U_{mf}$. The segregation rates are very high in comparison with the previous two

Table 5.11: U_{mf} for 50% by mass fraction bidisperse bed with particle sizes 1 and 2.5 mm. HYS 2010a drag model means that only bidisperse corrections are taken while HYS2010b means corrections for hydrodynamic interactions are also accounted for.

Drag Models	Umf (m/s)
Gidaspow [1994]	0.93
Syamlal and O'Brien [1987]	0.925
Beetstra *et al.* [2007*a*]	0.94
HYS 2010a (Holloway *et al.* [2010])	0.955
HYS 2010b (Holloway *et al.* [2010])	0.97

study cases of 50% by mass and number using 1.5 and 2.5 mm particles respectively. The segregation rates are found to be much higher than the previous studies.

The C1 drag model estimates the segregation rates higher than C2 and C3 which is consistent with the results of previous 50% by mass study with lower particle diameter ratio. This study bring out the differences in the slope of the segregation curves using the drag model of categories C2 and C3. The fluidizing velocity employed is far less than the U_{mf} for bulkier particles of size 2.5 mm but much greater than U_{mf} of the lighter particles. The differences in the relative velocities for two particle types will be much greater and this is reflected in the C3 model predictions. A systematic study with different mass and number ratios with different particle diameter ratios can bring out a pathway for drag models suitability in different scenarios. This knowledge can be further used to develop a new drag model which could be applicable at wide range of these parameters to predict robust features such as segregation rates.

5.5.3 Conclusions for bidisperse fluidized bed study

DEM-CFD capabilities to capture robust features of bidisperse fluidization were tested both qualitatively and quantitatively. Simulation results matched experimental data of random packing fraction and U_{mf} for different mass % composition bed, quite accurately. Segregation rates were captured by DEM-CFD qualitatively by employing drag models which were for bidispersity and for relative hydrodynamic interactions between the solid species [Holloway *et al.*, 2010]. Different drag models from literature were identified and categorized according to their usage in capturing bidisperse bed phenomenon. It is noted that no single drag model is able to capture segregation rates accurately but a combination of them can be employed. A systematic study is required by varying mass fraction, particle diameter ratio and inlet velocities to establish a strategy on drag model usage in bidisperse modelling with DEM-CFD. In conclusion, DEM-CFD with accurate drag-model closures can capture segregation rates in bidisperse fluidization.

5.6 Conclusion to the chapter

Open-source DEM-CFD code is validated for different fluidization processes: bubbling/slugging, spouted and bidisperse beds. The exercise of validation was to bring out and highlight the discrepancies which will serve a greater cause towards development of better models. It should be noted that the DEM-CFD code was first verified for any implementation errors before proceeding to the validation studies. An intended usage of the DEM-CFD code was pointed as to study hydrodynamics of the fluidized bed processes and in that spirit, a conscious effort was put to select the validation test cases covering a great range of operating condition, solid fraction and Reynolds number and bed conditions. Together with hydrodynamics, basis of choosing test cases were high quality validation data obtained from well established experimental measurements [Müller *et al.*, 2009], [Link *et al.*, 2008] and [Goldschmidt *et al.*, 2003]). Following note-worthy points came out from each of the three studies.

- Bubbling bed study: DEM-CFD simulations were able to accurately capture the minimum fluidization velocity, pressure drop fluctuations and its major frequency measured in the experiments. Mesoscopic time averaged phenomeon like solid circulation pattern can also be reproduced qualitatively. Quantitative discrepancies in the spatial-temporally averaged voidage, solid velocity and granular temperature profiles were noticeable near the wall regions and in the middle at the upper or lower bed. The discrepancies are intricately related to various model simplifications and may not be fully addressed in the DEM-CFD framework. It was found that the particle–wall interaction dominated the particle dynamics over the fluid–wall interaction in a wall boundary layer of about 5 particle diameter wide. Using a solid wall consisting of particles provides more resistance to the particle motion than using a smooth frictional wall, reducing the mean and variance of particle velocities and leading to closer agreement with the experimental data. The data suggested that the models of effective wall boundary conditions for solid velocity and granular temperature in a two-fluid model could be constructed using the particle dynamics data around the walls. The bed expansion and dynamics were found to be sensitive to the particle size, shape and initial bed height. Smaller particles have higher vertical velocities throughout the bed, which implies that size segregation could be a factor contributing to the over-(under-)prediction of velocities at the lower (upper) parts of the bed. The shape effect on fluid–particle interaction investigated through using a modified drag model led to appreciably closer agreement with the experimental solid velocities.

- Spouted bed study: fluidization behaviour was well captured by DEM-CFD simulations for all the three regimes studies. The predictions on the time averaged particle velocities were in good agreement with the PEPT characterization of the experimental spouted bed by Link *et al.* [2008]. Qaunaitatively, in comparison with bubbling bed case, there was a much better agreement with the experiments. The spout bed regimes covered both dense and dilute phase at high Reynolds number increasing the realm or the limit of validation. Statistical averaging issues are apparent while using PEPT technique to characterize the fluidized bed hydrodynamics and subsequent comparisons with DEM-CFD simulations. Assumptions of ergodicity while calculating the time-averaged profiles and tracer particles covering whole phase space of the fluidization process were made in PEPT but not rigorously tested against. Fluid-particle drag formulation was identified as a major cause of the discrepancies between numerical and the experimental data and emphasized that drag models used in the study were beyond their region of validity and employed in ad-hoc manner

- Bidisperse bed study: DEM-CFD simulation results matched experimental data of random packing fraction and U_{mf} of different mass % composition bed by Goldschmidt *et al.* [2003], quite accurately. Segregation rates were captured by DEM-CFD qualitatively, by employing drag models which were corrected for bidispersity and for relative hydrodynamic interactions between the solid species [Holloway *et al.*, 2010] instead of using traditional monon disperse drag models. Different drag models from literature were identified and categorized according to their usage in capturing bidisperse bed phenomenon. It was noted that no single drag model was able to capture segregation rates accurately and suggested that a combination of drag models can be employed. With the advent of LBM-DEM fully resolved simulations lately, better characterizaion can be done and generalized to provide a drag model covering a wider range. Furthermore, a systematic study is required by varying mass fraction, particle diameter ratio and inlet velocities to establish a strategy on drag model usage in bidisperse modelling with DEM-CFD.

The bubbling bed and the spouted bed study compared spatially and temporally averaged dynamics, but bidisperse bed study measured the transient phenomenon which is much more difficult to capture. All of the three test cases highlighted the importance of model conceptualization and the errors added due to sub-model simplification. In totality, the three studies covered a wide range of solid fractions, inlet velocities and the bed conditions. These validation studies are useful to asses the tools capability in studying fluidization behaviour of Geldart A particles later in the thesis. Furthermore,

looking at the validation experiments in a little more critical light a few guidelines for multiphase experiments for validation purposes are noted here:

- Characterize the particle used for their mechanical properties and data on the particle shape and size like particle size distribution. Define the geometry, or if possible provide SEM or TEM images of the particles if not spherical. Even though sub-models are not sophisticated enough to capture every fine detail, but this will provide a better understanding and approximations that would be used at the sub-model level.

- Calibration data for DEM parameters such as results on the particle drop tests, so as to provide modeller a better estimate on the particle properties.

- Provide information on the wall materials and the particle wall interaction parameters. Information on the distributor plate is very useful for a modeller to mention the boundary conditions. If possible, run an empty bed experiment to judge if uniform inlet velocity distribution was achieved.

- Preliminary validation data such as pressure drop versus inlet velocity tests. This will help in calibrating the drag model and understanding its ability to capture the macro-scopic trends such as U_{mf}. Bed expansion data can be highly useful, even without capturing the mesoscopic bubble etc.

- Provide a complete set of validation data covering most of the bed. For example, time averaged contour plots provided by MR experiments in the bubbling bed case. This would help in assessing mismatch much better than comparing quantities at different heights.

- Spatial and temporal resolution of the experimental measurements used and relevance of the actual run of experiments. Also, a clear methodology on the post-processing of the experimental measurements to obtain the meaningful validation data should be provided along with a sensitivity assessment of any parameters involved.

Chapter 6

DEM-CFD Simulation of Geldart A particles

6.1 Introduction

Gas-solid fluidization of Geldart A particles is of great importance to process industries. The associated fluidization regimes offer several advantages such as homogeneous heat, mass transfer and efficient gas-solid contacts. As reviewed in chapter 2, Geldart A fluidization can be classified into 3 regimes with increasing inlet velocity. A schematic diagram of these regimes are presented in figure 6.1. As indicated in the figure, U_{mf} signifies onset of fluidization, i.e. when weight of the bed is just counterbalanced by the hydrodynamic forces. U_{mb} indicates onset of bubbling i.e. appearance of bubbles and slugs and transition from homogeneous to heterogeneous fluidization. The stable bed expansion regime (6.1b) is a marked feature of Geldart A fluidization. It lies in the velocity range between the fixed and bubbling phase. The bed expands homogeneously and particles are apparently homogeneously distributed in the carrier phase without any large voidage spaces. This regime has garnered industrial attention, where uniform fluidized conditions are desirable as it is more energy efficient than fixed or bubbling regime and offers uniform hydrodynamic contacts between the fluid and solid phase. Experimental and simulation studies of Geldart A fluidization reviewed in the section 2.6 indicated that many outstanding question related to stability, microstructure and formation of the homogeneous regime are still unanswered [Hou *et al.*, 2012].

Numerical studies provide an alternative route to study the Geldart A regimes. Any numerical model is based on a fundamental understanding of the physics from the physical systems. In order to study Geldart A regime, modellers suffer a considerable

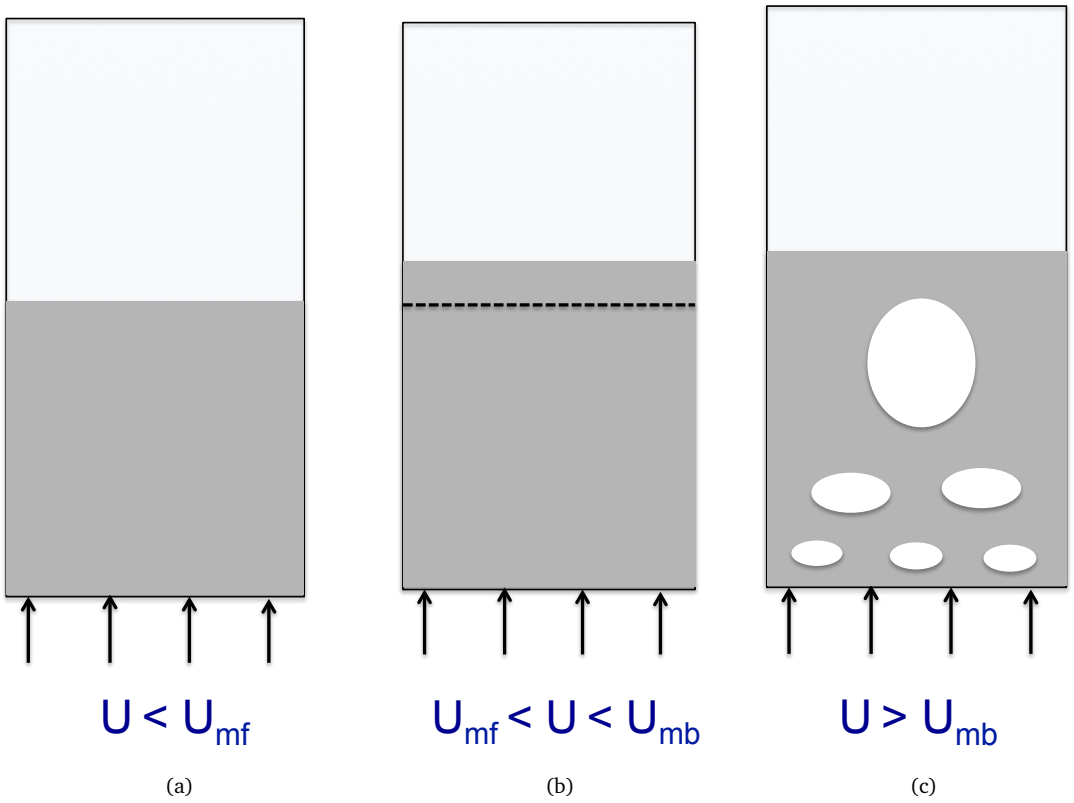

Figure 6.1: Geldart A regimes

dilemma because of uncertainty in the underlying phenomenon (section 2.6). The phenomenon reproduced numerically by the models is just a mere reflection of the physics given to sub-models. An ad-hoc approach is usually followed in literature to model Geldart A fluidization. Based on the physics described at the sub-models, key phenomenon related to Geldart A regimes is checked and results inferred accordingly. Proponents of the theory that expanded bed is formed by purely hydrodynamic forces, employ two-fluid model (TFM). These approaches describe solid phase as a high density and viscous fluid interacting with the fluid phase. A major hurdle in this regard is faced due to issues related to constitutive modelling of solid phase, required to close the solution. A review on failed two-fluid simulations (TFM) of Geldart A fluidization is summarised by Wang [2009]. Poor resolution of scale or mesh-grid choice has been identified as one tentative reason for TFM failure to capture macroscopic behavior Wang *et al.* [2009]. These TFM studies does not include cohesion stresses in the solid phase tensor.

Researchers believing in importance of inter-particle forces employ more sophisticated models that could capture particle contacts. DEM-CFD is a popular numerical technique in literature, because of advantages of solving particle phase accurately but yet maintaining computational tractability by solving fluid-particle interactions at a coarser

scale. DEM-CFD simulations of Geldart A regimes has been reported in the literature by including inter-particle forces in DEM equations [Hou *et al.*, 2012; Kobayashi *et al.*, 2013; Pandit *et al.*, 2006; Ye *et al.*, 2004]. Physical phenomena like pressure drop overshoot and uniform bed expansion ($U_{mb} > U_{mf}$) were captured with different cohesion models. Some the challenges in reproducing Geldart A fluidization within DEM-CFD framework are identified from these studies:

- Sensitivity of numerical methods and discretization on the fluidization phenomenon
- Identification of expanded bed regime and the onset of fluidization remains another open question in the literature.
- Wall effects or geometry effects (2D or 3D) on the expanded bed regime.
- Segregating the effects of sliding friction, wall friction and cohesion influencing the phenomenon.

This chapter focus on DEM-CFD simulations of Geldart A fluidization and ability of these to capture realistic expanded bed behaviour. Adhesive interactions between the particles are modelled by van der Waals type model. Bond number (Bo_g) would be used as an measure of cohesive forces in the system and its effect will be studied on fluidization regimes and quantified. From the literature reviewed in chapter 2, following questions are identified in relation to homogeneous expansion in Geldart A gas-solid fluidization.

- Can DEM-CFD simulations capture robust features of Geldart A fluidization regimes? if yes, how can these simulations help in improving continuum modelling of solid phase.
- What is the role of inter-particle adhesion forces and contact stresses in the formation of uniformly expanded bed?
- How stable is uniformly expanded bed and what is the criterion for onset of bubbling?
- What is the microstructural state of expanded bed?
- What is the mechanical state of the uniformly expanded bed: solid like or fluid like?

This chapter will address first two questions while next questions will be addressed in subsequent two chapters.

6.2 Simulation methodology and modelling set-up

6.2.1 DEM-CFD methodology

DEM-CFD methodology is employed to simulate Geladart A particles (d_p = 100 μm and ρ_p = 1440 kg/m^3). According to particle size and density, fluidization behaviour can be mapped to Geldart A/B border. Adhesive forces between particles are modelled by pair wise van der Waals forces . The idea is to reproduce Geldart B, A and C behaviour by not changing particle size but the inter-particle cohesive properties. In reality, inter-particle adhesive forces should increase with decrease in particle sizes [Israelachvili, 2011]. The fluid-particle interaction depends non-linearly on particle sizes [Deen *et al.*, 2007]. The governing dynamics of Geldart A fludization is an interplay between both of these complex interactions. Full-slip boundary conditions were employed for fluid boundary conditions and rough flat walls with Coloumbic friction were employed for the particle-wall boundaries.

Hydrodynamic interaction force (f_d) is a function of particle diameter (d_p), density (ρ_p), coarse grained particle volume fraction (ϕ) , relative velocity of averaged particle velocity ($< u_p >$) with respect to fluid (V_f) and particle Reynold number (Re_p). f_d has a very strong dependence on d_p and ρ_p and is instrumental in the prediction of macroscopic trends like U_{mf}. It should be pointed out that the fluid-particle interactions are unresolved in the DEM-CFD framework. An attempt has been made to minimize the hydrodynamic force variations across different cohesive fluidization regimes by keeping d_p and ρ_p constant. However, as f_d is affected by the local bed conditions ϕ, u_p and V_f, it is impossible to keep f_d invariable across all the cohesive simulations.

6.2.2 Bed preparation

Physical, geometrical and model parameters are enlisted in table 6.1. Rigid walls are employed for side and front and back, DEM parameters are similar for particle-wall interaction and the particle-particle interactions. Bed thickness was identified as an important criterion affecting the mesoscopic results. 2D beds have been previously employed with various bed thickness varying from 4-8 particle diameter thickness with and without periodic boundaries [Feng and Yu, 2004; Hou *et al.*, 2012; Kafui *et al.*, 2002; Yu and Xu, 2003]. Present study employs 3D bed with bed thickness equal to the bed width and 3-D CFD is used to accurately describe the gas flow.

3D granular static cohesion-less bed of 8000 particles in a closed domain of size 20d $\times$ 20d $\times$ 60d (d is the particle diameter) was prepared using the rainfall method. The particles are allowed to settle down and supported by the rigid walls, forming a dense granular bed. The simulation was run up to a point until averaged particle translation

and rotational velocity are 5 orders of magnitude less than the terminal velocity of an isolated particle in air. This critical velocity value was in order of 10^{-5} m/s. For all numerical purposes, such a assembly of the particles can be considered as a static state. It is checked that using a lower value of critical velocity value would not change the results but only increase the computational times.

van der Waals model is used to capture the adhesive behaviour between the particles. The equations, governing parameters and the definition of Bond number are described in the section 2.5.2. This packed bed was used as a starting point to prepare cohesive bed with varying Bond numbers (0.1-5). Hamaker constant (A) was increased keeping other model parameters same. In reality, the Hamaker constant depends upon physical and chemical properties of the particles like particle diameter, surface roughness and asperity [Israelachvili, 2011]. A sudden change in the force balance by the addition of van der Waals force destabilizes the assemblies. For this reason, the cohesive assemblies were allowed to equilibrate for 1 sec to reach a quasi-static state according to criterion on the average particle velocities used before. For any fluidization simulations done in this thesis, these cohesive beds with varying Bond numbers will be used as initial states.

6.2.3 Fluidization procedure

The rate at which the fluidizing gas is introduced can effect the Geldart A fluidization mesoscopic behaviour. In literature, the gas has been introduced either in a slow linearly increasing manner, increasing in steps or sudden constant gas supply. These fluidization procedures are briefly described here:

- Procedure 1: Increasing superficial gas inlet velocity linearly in time, given as equation 6.1.

$$U = Kt \tag{6.1}$$

  Here K is the slope of the fluidization curve. Variation of K results in a very slow or fast fluidization process. Studies by Ye *et al.* [2005] have employed this procedure with K=0.02-0.03 m^2/s. In these studies, K was chosen in a way to increase inlet velocity very slowly and avoiding adding any sudden voidage shocks to the bed. This procedure is numerically efficient to study tranitions of the fluidization regimes. However, a major drawback is that the steady state behaviour is not reached before change in hydrodynamic conditions so it can not be used to characterize expanded bed microscopic quantities.

Table 6.1: Domain size and DEM-CFD simulation parameters.

DEM Parameter	**Value**
Number of Particles	8000
Diameter, m	1e-4
Contact model	Linear spring dash-pot
Particle Density, ρ (kg/m^3)	1440
Spring Stiffness, k (N/m)	2000
Coefficient of restitution, e (N/m)	0.98
Inter-particle Static friction, μ (N/m)	0.1
Particle Static friction, μ (N/m)	0.1
Particle time step, (s)	$1e-7$
Cohesion model : van der Waals	
Hamaker constant, A (m^{-6})	(0.284-14.4) e-20
s_{max} (m)	1.25e-4
s_{min} (m)	4e-9
Bond number, Bo	0.1-5
Gas Phase	
Gas density, ρ_f (kg/m^3)	1.225
Gas viscosity, μ_f Pa.s	1.8e-5
Boundary conditions (side,front and back walls)	No-slip
Boundary conditions (inlet)	Uniform air inlet
Boundary conditions (Outlet)	Pressure, 10^5 Pa
Fluid timestep (s)	$1e-4$
Drag model	Beetstra *et al.* [2007*a*]
Minimum fluidization velocity, U$_{mf}$ m/s	0.0058
Normalized inlet velocity, U/U$_{mf}$ m/s	0.1-3
Geometry	
Bed width (x), m	2e-3
Bed height (y), m	6e-3
Bed thickness (z), m	2e-3
Discretization length (dx), m	2e-4
Discretization length (dy), m	4e-4
Discretization length (dz), m	2e-4

- Procedure 2: Simulations at constant inlet velocities U in the range 0-2U$_{mb}$ spanning a time until a steady state is reached. For $0 < U < U_{mf}$, bed is in fixed bed range hence simulation is run till a few seconds and DEM data is recorded at a lower frequency. For U$_{mf}$<U<U$_{mb}$, a start up or transient incipient phase can be discarded and data is recorded for few seconds after the steady state is reached. In the range $U > U_{mb}$, transient phase is discarded as first few seconds and data is sampled at a high frequency for further time. This procedure has been followed by Hou *et al.* [2012] to study micromechanics of Geldart A fluidization.

- Procedure 3: Rhodes *et al.* [2001*a*] and Ye *et al.* [2004] used a step-wise increase

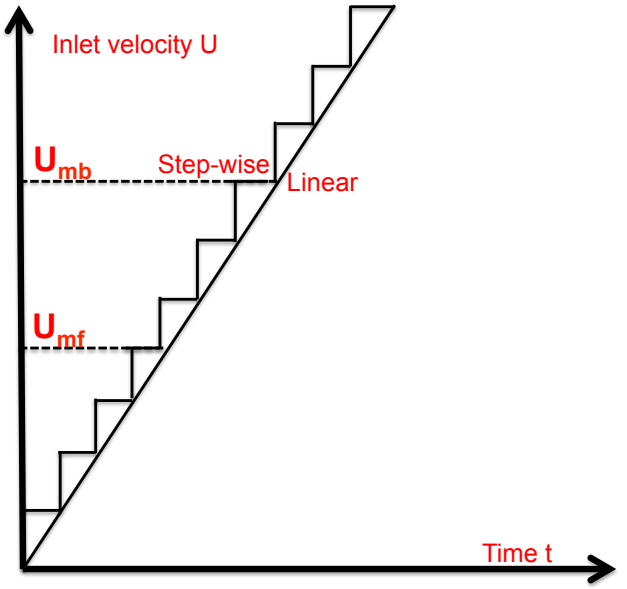

Figure 6.2: Schematic difference between fluidization procedural difference between linear progression and step-wise increase of inlet velocity.

of inlet velocity. The gas velocity is increased step by step from 0 to 2 U_{mb} instead of linear progression as in procedure 1 (see figure 6.2). Time interval between the step change is kept sufficiently long enough for bed to a reach steady state. A caution is taken so as not to give a big jump to the inlet velocity, so as to prevent a voidage shock.

The choice of procedure depends upon spatial and temporal scale of interest. Procedure 3 can be seen as a hybrid of procedure 1 and 2, but borrowing disadvantages of poor quality temporal data at a particular inlet velocity from procedure 1 and high computational times by procedure 2. Decisions on time interval length and magnitude of inlet velocity are not straightforward and should be adaptive based on dynamics of the bed. Procedure 3 can be useful but does not save computational time as these decisions are taken mostly conservatively.

Procedure 1 is useful in studying the macroscopic trends such as identification of U_{mb} and pressure drop analysis for U_{mf} identification. Procedure 2 and 3 would provide high resolution spatial and temporal data but only at a few inlet velocities. A disadvantage of using procedure 2 is insufficient data to resolve the transition between the regimes. The present study employs procedure 1 for U_{mb} and U_{mf} identification and studying macroscopic trends and Procedure 2 for the microstructural and stability studies in chapter 7 and 8.

6.3 Minimum fluidization velocity

Minimum fluidization velocity (U_{mf}) is defined as the superficial velocity at which incipient fluidization is achieved. In more physical sense, at U_{mf}, weight of the bed is fully supported by the hydrodynamic forces (quantified by pressure drop ΔP). This can be expressed mathematically by equation 6.2 which equates the pressure drop gradient with sum of gas and particle bed weight.

$$\frac{\Delta P}{H} = \epsilon \rho_g g + (1-\epsilon)\rho_p g \tag{6.2}$$

Here, ϵ is the bed porosity, ρ_p and ρ_g are densities of particle and gas. Empirical relation for U_{mf} was given by [Abrahamsen and Geldart, 1980] by equation 6.3. For particle diameter d_p = 100 μm and density 1440 kg/m^3 fluidized by air, U_{mf} is estimated as 0.0048 m/s using equation 6.3.

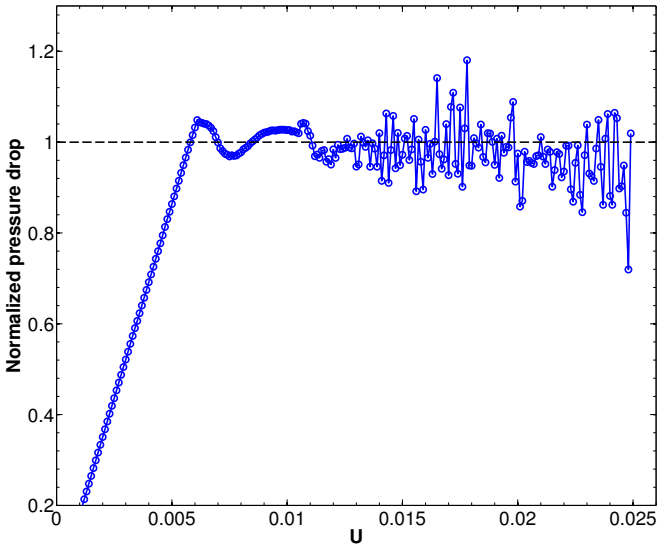

Figure 6.3: Pressure drop across the bed, normalized by weight of the bed devided by cross section area, is plotted against increasing inlet velocity for 3D DEM-CFD simulation of particle size d = 100 μ m, density 1440 kg/m^3 with inter-particle cohesive forces quantified by Bond number = 2. Black dotted line represents normalized pressure drop = 1 and intersection with pressure drop curve provides U_{mf}.

$$U_{mf} = \frac{9.0X10^{-4} d_p^{1.8}[(\rho_p - \rho_g g)]^{0.934}}{\rho_g^{0.066}\mu_g^{0.87}} \tag{6.3}$$

In literature, U_{mf} is derived theoretically by equating bed weight to hydrodynamic forces, which are estimated by drag models proposed by many researchers e.g. Ergun [1952],Syamlal and O'Brien [1987] and Di Felice and Rotondi [2012]. U_{mf} is

determined by the experiments and simulations by plotting pressure drop versus inlet velocity using procedure 1 described in the section 6.2.3 and calculated as the velocity at which pressure drop first counterbalances weight of the bed.

6.3.1 Prediction of minimum bubbling velocity (U_{mb})

Bubbles in the gas-solid fluidization terminology are defined as sharp gradients in the porosity field. These large voidage spaces are clearly visible in Geldart B fluidization process with increase in inlet velocity beyond minimum fluidization velocity (U_{mf}). Geldart A fluidization is characterized by a stable expansion with smooth fluidization appearance and onset of the bubbling occurs much beyond U_{mf}. Minimum bubbling velocity (U_{mb}) is defined as the superficial inlet velocity which marks the onset of bubbling. The definition, in itself is little obscure and philosophical as to pin-point exactly when did this departure of the stable smooth like appearance occur? The practice of visual inspection of the first bubble while increasing the inlet velocity has been prevalent for last many years [Wang *et al.*, 2011*a*]. This method is not very accurate as visual inspection can only point out bubbles at the walls. Several attempts have been made to relate U_{mb} to particle and gas properties. In fact, boundary of Gedart A and B behaviour in the Geldart classification was a result of equating these empirically determined U_{mf} and U_{mb} (Geldart [1973]). Abrahamsen and Geldart [1980] used 23 different powders ranging from diameter (d_p) 20-72 μ m and density (ρ_p) 1100-4600 kg/m^3 and 5 different fluids (viscosity μ_g) to relate U_{mb} to the particle and gas properties (equation 6.4).

$$U_{mb} = \frac{2.07 d_p \rho_g^{0.06}}{\mu_g^{0.347}} exp(0.716 F_{45}) \tag{6.4}$$

where F_{45} is the mass fraction of particles having a diameter less than 45 μ m. Experimental data by Lettieri *et al.* [2002]; Simone and Harriott [1980]; Xie and Geldart [1995] are shown to have been in reasonable agreement with the equation 6.4. Numerical simulations of Geldart A fluidization behaviour are far less found in literature in comparison to Geldart B and D. This is mostly due to inability to capture physics of homogeneous expansion and subsequent prediction of U_{mb}. DEM-CFD have been employed to 2D bed to some success by incorporating inter-particle cohesion to simulate uniform expansion by Hou *et al.* [2012]; Ye *et al.* [2005]. However, U_{mb} predicted in these studies are only accurate to the extent of order of magnitude. On the contrast, prediction of U_{mb} through continuum CFD modelling (two-fluid model) have been largely unsuccessful (Mazzei and Lettieri [2008]; Mckeen and Pugsley [2003]). These studies fail to predict even order of magnitude for U_{mb}. Wang *et al.* [2011*a*]

attributed failure of two-fluid model (TFM) to predict U_{mb} to lack of scale resolution rather than incorporation of solid stresses due to inter-particle effects.

As indicated earlier, key issue of identifying onset of bubbling and further estimating U_{mb} still remains to be answered [Wang *et al.*, 2011*a*]. Different statistical tools have been employed in literature to identify U_{mb} in experiments and simulations:

- Observation of first bubble by visual inspection from either the experiments or snapshots from numerical studies (Abrahamsen and Geldart [1980]; Colafigli *et al.* [2009]; Di Renzo and Di Maio [2007]; Donsi and Massimilla [1973]; Geldart [1973]; Mazzei [2008]; Mazzei and Lettieri [2008]; Molerus [1982]).
- By studying bed expansion and contraction characteristics and estimating local maximum of bed height with increasing inlet velocity [Simone and Harriott, 1980; Valverde *et al.*, 2003].
- Identification of microscopic variable for abrupt change in magnitudes at the onset of bubbling: standard deviation of pressure drop [Rhodes *et al.*, 2001*c*], standard deviation of apparent bed elasticity [Kono *et al.*, 2002] and local porosity fluctuations [Ye *et al.*, 2005]. Definition of local porosity fluctuation function is given by equation 6.5, where ϵ_k is the porosity of a grid cell k

$$\Delta\epsilon = \sqrt{\frac{1}{N_{sub}-1}\left[\sum_{k=1}^{N_{sub}}\epsilon_k^2 - \frac{1}{N_{sub}}\sum_{k=1}^{N_{sub}}\epsilon_k\sum_{k=1}^{N_{sub}}\epsilon_k\right]} \tag{6.5}$$

- Global granular temperature or measure of averaged fluctuating velocity as an indicator of onset of bubbling (Wang *et al.* [2013]). Effect of sub-grid structures affecting the granular temperature are included in this definition and given by equation 6.6.

$$\theta = \frac{1}{3}\left(\theta_x + \theta_y + \theta_z\right) \tag{6.6}$$

where θ_k and averaged velocity v_k, is defined as

$$\theta_k = \frac{\sum_{i=1}^{N_p}(v_{k,i} - v_k)^2}{N_p} \tag{6.7}$$

$$v_k = \frac{\sum_{i=1}^{N_p} v_{k,i}}{N_p} \tag{6.8}$$

Here N_p is the total number of particles in the system.

In the present study, 3D DEM-CFD simulation are conducted with particle size d = 100 μm and density ρ_p = 1440 kg/m^3. Bond number, a measure of cohesive strength, for a bed of this sized particles can be approximated as between 1 and 2 [Seville *et al.*, 2000]. Simulations are run using procedure 1 with inlet velocity increasing from 0-4 U_{mf} in 20 seconds. U_{mf} is approximated as 0.0048 m/s for these particles [Abrahamsen and Geldart, 1980].

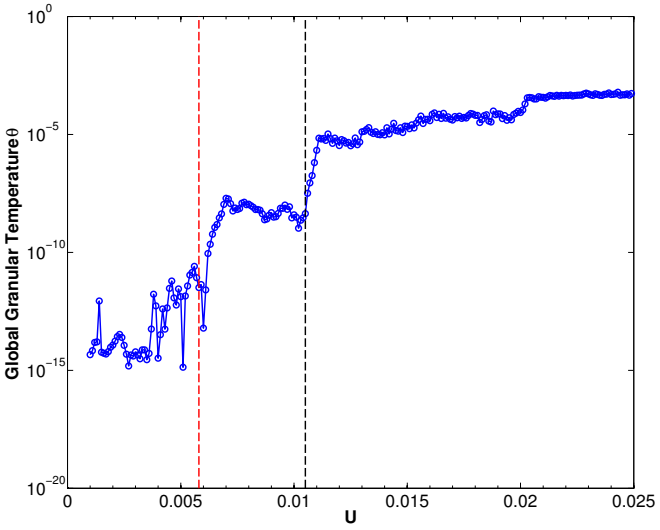

Figure 6.4: Global granular temperature, calculated with equation 6.6 [Wang *et al.*, 2013] with increasing inlet velocity. Clear jumps of 2 orders of magnitude at U_{mf} and at velocity U ($U > U_{mf}$). This velocity is identified as U_{mb}.Transition lines dotted red and black lines indicate U_{mf} and U_{mb}. Uniform bed expansion window is identified between U_{mf} and U_{mb}. Data is from 3D DEM-CFD simulations of particle size d =100 μ m and density 1440 kg/m^3 is conducted with cohesive interactions quantified as Bond number =2

It has been reported that the θ changes order of magnitude by 2 at the onset of fluidization (U_{mf}) and remains constant during bed expansion phase. A sudden jump of 2 order of magnitude is noticed at the onset of bubbling (U_{mb}) [Wang *et al.*, 2013]. Figure 6.4 plots the global granular temperature (calculated according to equation 6.6) with increasing inlet velocity [Wang *et al.*, 2013]. Clear jumps of 2 orders of magnitude at U_{mf} and at a velocity U ($U > U_{mf}$) is noticed. This velocity is identified as U_{mb}. Dotted red and black lines indicate these transition. Uniform bed expansion window is identified between U_{mf} and U_{mb}. The present study will employ θ as an indicator of onset of bubbling throughout the thesis.

The literature review pointed out that the pressure drop fluctuations and local porosity fluctuations can also be used as U_{mb} indicators. To validate the quantification of U_{mb}, the nature of these curves at $U = U_{mb}$ will be probed further around the transition identified. Figure 6.3 shows pressure drop versus inlet velocity plot for these simulations. Start of fluctuations in the pressure drop can be seen at U_{mb}, the velocity

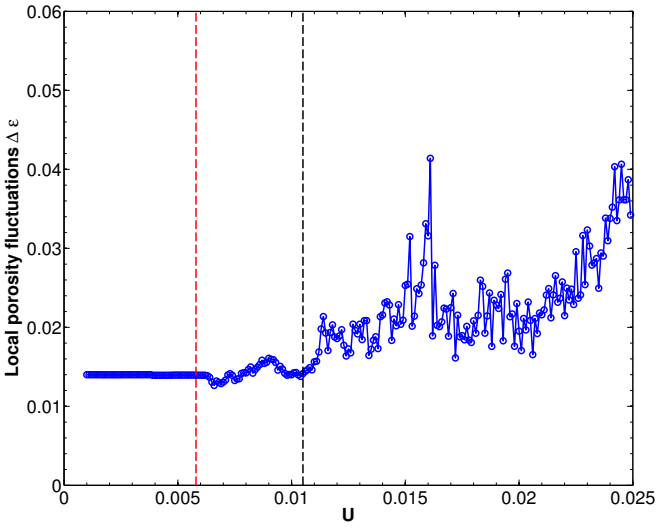

Figure 6.5: Local porosity fluctuations calculated with equation 6.5 [Ye *et al.*, 2005] with increasing inlet velocity. Transition lines dotted red and black lines indicate U_{mf} and U_{mb}. Uniform bed expansion window is identified between U_{mf} and U_{mb}. Data is from 3D DEM-CFD simulations of particle size d =100 μ m and density 1440 kg/m^3 is conducted with cohesive interactions quantified as Bond number =2

identified from θ versus inlet velocity plot. Figure 6.5 plots local porosity fluctuations against rising inlet velocity. A clear transition at U_{mf} and U_{mb} is apparent in the figure. It is concluded that the three indicators mentioned here are consistent with each other and DEM-CFD simulations can capture transition from expanded to the bubbling bed in a robust manner.

6.4 Parametric study

Discrete particle methodology (DPM) studies of Geldart A particles are not as common in literature as Geldart B or D studies. In early 2000's, Rhodes *et al.* [2001*a*] and Kobayashi *et al.* [2002] used DPM to study influence of cohesive inter-particle forces on a 2D fluidized bed. Particle sizes used were 1 mm and densities of the order 1590-2650 kg/m^3 which mapped them to Geldart B fluidization behaviour. Window for uniform expansion and delay in the onset of bubbling due to cohesive interaction were identified in these simulations. Even though the parameters used in the studies were not physical, this work opened up a promising route to study effects of certain particle and gas parameters that influence U_{mb} prediction [Ye *et al.*, 2005]. Ye *et al.* [2005] studied effects of DEM contact model parameters such as coefficient of restitution (e), spring stiffness (k) and gas viscosity effects. The pressure overshoot phenomenon was found to be increasing with inter-particle cohesive forces. But a clear explanation of its origins and quantification was lacking.

Recently DEM-CFD studies by Hou *et al.* [2012] and Yang *et al.* [2013] have successfully reproduced Geldart A behaviour and have attempted to characterize expanded bed regime in a 2D bed. Studies byHou *et al.* [2012] were reported as sensitive to any of the parameter changes given by them.Wang *et al.* [2009] identified that the coefficient of restitution have minimal effect on the fluidization characteristics of Geldart A particles and was contrary to the conclusion with Geldart B particles (Goldschmidt *et al.* [2001]). A systematic understanding of model parameters is essential for robust reproduction of Geldart A fluidization within DEM-CFD framework.

Following parameters are identified to have significant effect on Geldart A simulation characteristics from the literature:

- Effect of cohesion was identified to delay onset of bubbling but a proper incorporation of cohesive interaction and explanation of underlying mechanism of stable bed expansion is still lacking.
- Mesh-size effects were first identified by Wang *et al.* [2011*b*] to effect U_{mb} in a TFM study. Drag models gives different estimation of hydrodynamic forces on an assembly leading to differences in prediction of U_{mb} and U_{mf}.
- Fluidization procedure 1 parameter K (section 6.2.3) can be one of the parameter influencing U_{mb} [Ye *et al.*, 2005].
- Drag models are seen to have a significant effect in modelling hydrodynamics of the fluidized beds.

6.4.1 Effect of cohesion

Yang *et al.* [2013] studied effect of surface adhesion forces and varied Bond numbers from 0 to 5. However, the wall effects in these studies were profound and role of cohesive parameters was neither clear nor quantified. The present study employs the DEM-CFD methodology on a 3D granular bed with varying Bond numbers 0.1-5 and effect on U_{mb} and U_{mf} is quantified. Granular beds are fluidized by inlet velocity varying linearly with time (figure 6.11). Figure 6.6 plots the pressure drop across the bed against the inlet velocity Inlet velocity is normalized with U_{mf} of the base case (no cohesion, calculated as 0.0058 m/s). The plot shows that U_{mf} is not a function of Bond number. This result is expected as U_{mf} is a macroscopic quantity dependent only on the weight of the bed and not the microscopic inter-particle interactions. For Bond numbers 0 and 0.1, pressure drop fluctuations are observed after the onset of fluidization itself. But such fluctuation are seen only after a certain $U > U_{mf}$ for Bond numbers 1,2 and 5. Bond 10 have no pressure fluctuation which is expected in

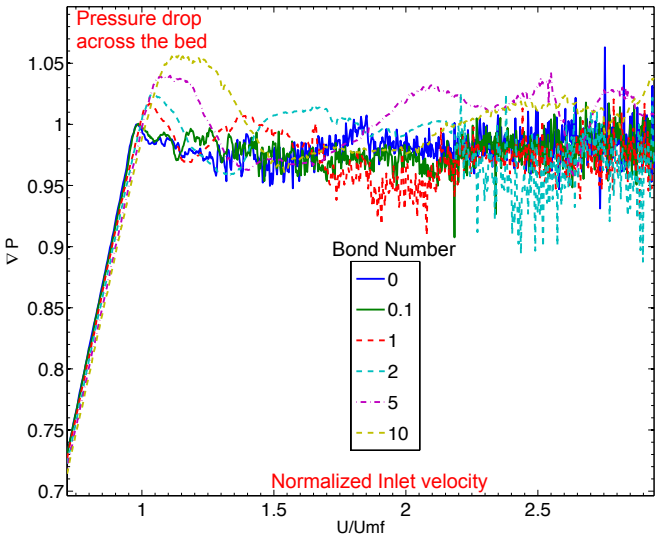

Figure 6.6: Pressure drop across the bed, normalized by weight of the bed devided by cross section area, is plotted against increasing inlet velocity for 3D DEM-CFD simulation of particle size d = 100 μ m, density 1440 kg/m^3 with inter-particle cohesive forces quantified by Bond numbers mentioned in the legend.

Geldart C fluidization [Hartman *et al.*, 2009]. U_{mf} is defined as the velocity at which the pressure drop (ΔP) is equal to the pressure exerted by the granular bed on the distributor plate ($P_o = W/A$). For inlet velocities greater than U_{mf}, it is expected that the mean of ΔP is equal to P_o. The pressure drop (ΔP) is expected to fluctuate around the mean as P_o at the commencement of bubbling. An interesting feature can be seen in Geldart A fluidization when around U_{mf}, the pressure drop ΔP keeps increasing beyond P_o. This phenomenon is known as pressure overshoot. An increase in excess pressure ($\Delta P - P_o$) can be observed with increasing cohesive strength (figure 6.6). This phenomenon would be addressed at a later section in the chapter and will be linked to the internal solid stresses.

Figure 6.7 plots the global granular temperature θ, calculated with equation 6.6 [Wang *et al.*, 2013] with increasing inlet velocity. Clear jumps of 2 orders of magnitude for θ can be observed at inlet velocities identified as U_{mf} and U_{mb}. U_{mb} for different Bond numbers (1, 2 and 3), are indicated by dotted lines in the plot. In contrast, Bond number 0.1 plot shows an increase in θ value, even before the onset of fluidization. This indicates that bubbling commenced at around U_{mf} and Geldart B behaviour can be inferred for Bond number 0.1 simulations ($U_{mb} \sim U_{mf}$. Table 6.2 gives ratio of U_{mb}/U_{mf} with Bond number calculated from θ versus inlet velocity plot. Experimental value of U_{mb}/U_{mf} for gas fluidization of these particles (d = 100 μ m and ρ_p) is calculated as 1.6 (Abrahamsen and Geldart [1980]), which is corresponding to a Bond number around 1.5.

Table 6.2: Cohesive interactions quantified by Bond number and ratio of U_{mb}/U_{mf} as calculated from the graph between θ and inlet velocity U.

Bond Number	U_{mb}/U_{mf}
0.1	1
1	1.4
1.5	1.5
2	1.65
2.5	1.95
3	2.05

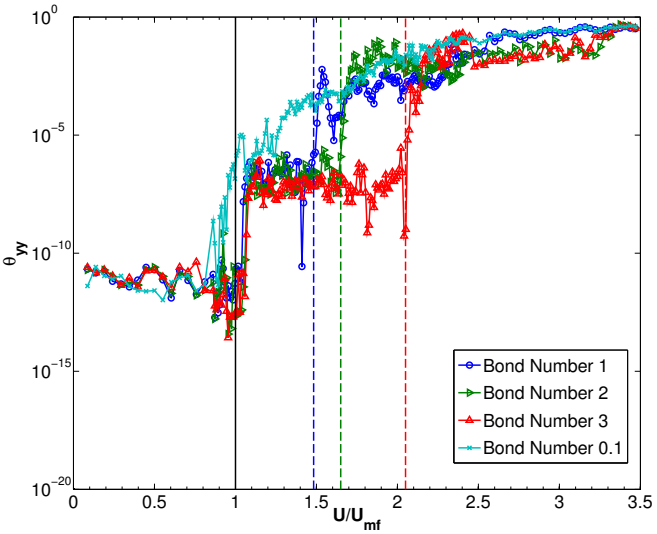

Figure 6.7: Kinetic Stresses in different fluidization regimes with increasing inlet velocity and Bond numbers

6.4.2 Effect of mesh-size

Effect of spatial length resolution has been extensively studied by Wang *et al.* [2011*b*] in two-fluid model study of Geldart A simulation. This study summarizes all the failed attempts by TFM to simulate homogeneous expansion and attributes the mis-match to unresolved mesh sizes. Similar studies in DEM-CFD framework are lacking, so as to quantify the effect of unresolved mesostructures on macroscopic bulk behaviour. Statistical averaging constraints a minimum number of particles in a fluid mesh cell as around 100. This means that the fluid is resolved at a coarser scale. The local averaging procedure on which the fluid equations are based [Anderson and Jackson, 1967] are derived on an assumption that mesh discretization is chosen at a mesoscale which is much greater than particle size but much smaller than overall macroscopic length scale. The accuracy of hydrodynamic interactions between the particle and fluid interaction is severely compromised during the coarse-graining procedure. In the spirit of multi-scale modelling, it is suggested that the constitutive laws should be derived from the first

principle rather than resorting to the empirical correlations as applicable with the drag models. This pose a fundamental problem to the physics of the problem, hence the role of mesh-size is extremely important. To address this problem until very recently, filtered drag models capturing sub-grid structures have been introduced[Igci and Sundaresan, 2011]. As a side note, it is noted that there is a clear need to differentiate the solid meshing from the fluid meshing in DEM-CFD framework. Though it is further noted that it would require an efficient algorithm to tranfer informations between the meshes, so as to not increase any computational costs.

Present study checks effect of mesh-size on the macroscopic trends of pressure drop, granular temperature determination of U_{mf} and U_{mb}. 3 different mesh sizes employed are enlisted in table 6.3. It should be noted that for averaging purposes, Gaussian kernel is employed with band width equal to 1.5 the cell size for all the meshes [Xiao and Sun, 2011].

Table 6.3: Mesh size discretization for different mesh numbers.

Mesh	Δ x	Δ y	Δ z
1	4d	4d	4d
2	2d	2d	2d
3	4d	2d	4d

Figure 6.8(a) plots global granular temperature θ and normalized pressure drop ΔP with increasing inlet velocity at different mesh sizes for Bond number 2 simulation. Mesh 1 and 2 are coarse and fine mesh respectively. Mesh 3 is a coarser mesh in the depth and width direction but finer in the height direction and should be able to resolve atleast the gravitational instabilities. Figure 6.8(b) indicates that the meshing have almost no effects on U_{mf} since total drag and weight of the bed is independent on the grid size. It should be noted that the pressure drop is inherently linked to the drag model employed employed. The drag models are derived on a mesoscopic mesh and based on the coarse-grained variables. This makes calculations of U_{mf} consistent in the DEM-CFD framework without even resolving the fluid fields. However, the fluctuations in the pressure drop indicates that the meshing have strong effect on the mesoscopic bubbling phenomenon. Figure 6.8(a) indicates strong meshing effects on U_{mb}. Onset of bubbling is significantly delayed in coarser mesh simulations as opposed to the finer mesh simulations. This can be explained by the fact that bubbling is a mesoscopic phenomenon and resolution of mesostructures is dependent on the length scale of averaging. U_{mb} is found to be $2.5U_{mf}$ and $1.65U_{mf}$ for coarse and fine mesh simulation. Mesh 3 simulation results are close to Mesh 1 result with U_{mb} estimated as $1.8U_{mf}$. These results indicates that instabilities are more effected by resolution in the gravity

directions. It should be further pointed that variations in U_{mb} with mesh effects in DEM-CFD is far less than meshing effects in TFM model pointed out by Wang *et al.* [2011*b*]. Studies by them pointed out that U_{mb} can be over-predicted by 10 times if coarser mesh is used in TFM. This further highlights need of better constitutive modelling of solid stresses in continuum modelling. Finer meshes are computationally expensive for two-fluid modelling and defies its advantage of better run times over DEM-CFD. For future simulations and results, mesh 2 would be employed and treated as a base case.

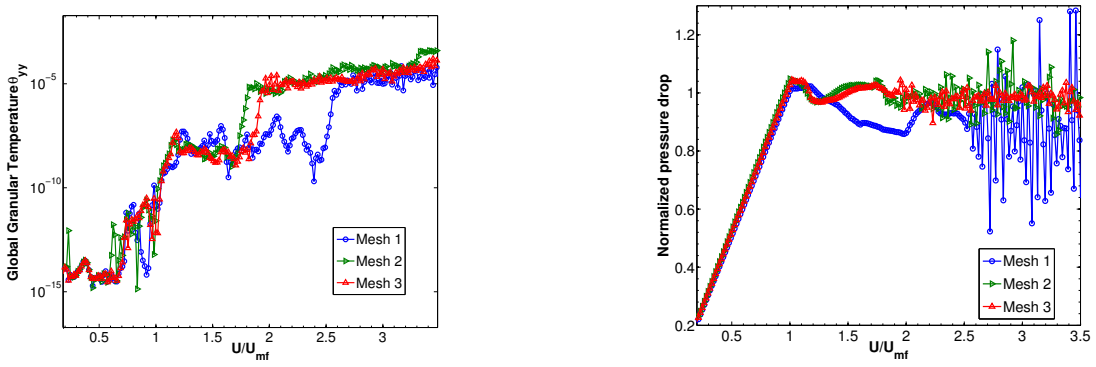

(a) (b)

Figure 6.8: Meshing effects on (a) global granular temperature and (b) pressure drop versus inlet velocity. Resolution of meshes indicated in the legend are given in table 6.3. Mesh 1 and 2 are coarse and fine meshes respectively.

6.4.3 Effect of drag models

Fluid-particle interaction defines the physics of any fluidization regimes. Realistically, accurate description of these hydrodynamic interactions is very necessary at microscopic level. But, due to the averaging procedures followed in DEM-CFD, the interaction remains unresolved at the microscopic scale and the solution is closed at mesoscopic length scale by drag models. The averaging procedure, drag models and implementation in the momentum equation can be found in methodology section (section 3.4.1). The drag force is modelled as a function of mesoscopically coarse grained porosity and particle velocities and unresolved fluid velocity. The effect of different drag closures can be seen at both macroscopic and microscopic quantities. The present study employs three different drag models by Beetstra *et al.* [2007*a*], Syamlal and O'Brien [1987] and Gidaspow [1994]. Gidaspow [1994] drag model is a combination of Ergun drag model [Ergun, 1952] and Wen Yu drag model [Wen and Yu, 1966] employed in dense and dilute regimes respectively.

Figure 6.9 presents θ and ΔP plots with increasing velocity for different drag models. U_{mf} and U_{mb} evaluated from these figures are summarized in table 6.4. The drag model by Beetstra *et al.* [2007*a*] predicts U_{mf} as 0.0058 m/s which is fairly close to

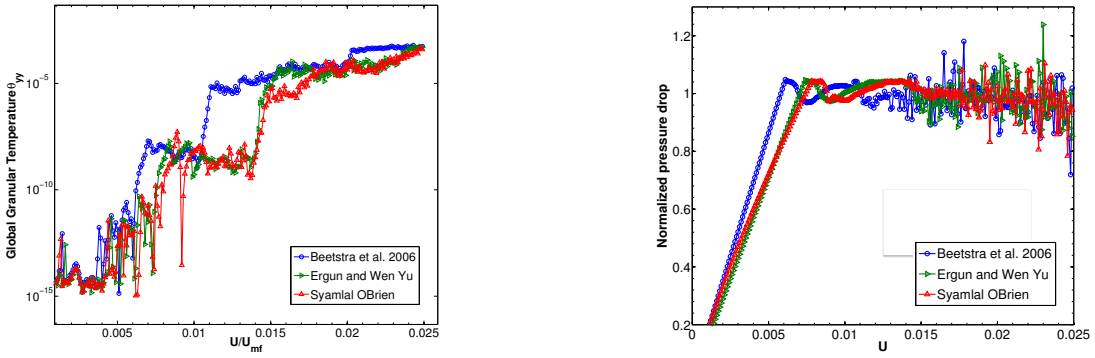

(a) (b)

Figure 6.9: Drag model effects on (a)global granular temperature and (b) pressure drop versus inlet velocity. Drag models are indicated in the legends as [Beetstra *et al.*, 2007*b*], [Syamlal and O'Brien, 1987] and [Gidaspow, 1994].

the $U_{mfe} = 0.0048m/s$ predicted by empirical correlation by Abrahamsen and Geldart [1980]. Syamlal and O'Brien [1987] and Gidaspow [1994] drag models predict U_{mf} as 0.0068 and 0.007 m/s respectively for the given powder (d = 100 μm and ρ_p = 1440 kg/m^3). Similar DEM-CFD studies for 2D bed was conducted by Hou *et al.* [2012] employing Gidaspow [1994] drag model and U_{mf} was predicted at 0.0072 m/s, which is fairly close to the value predicted here.

Table 6.4: U_{mb}, U_{mf} and expanded bed window for different drag models with Bond number 2 simulations.

Drag model	U_{mf} (m/s)	U_{mb} (m/s)	$U_{mb} - U_{mf}$ (m/s)
Beetstra *et al.* [2007*a*]	0.0058	0.0102	0.0044
Syamlal and O'Brien [1987]	0.0068	0.0135	0.0067
Gidaspow [1994]	0.007	0.0138	0.0068

U_{mb} predicted by Beetstra *et al.* [2007*a*] drag model for Bond number 2 is calculated as 0.0102 m/s. This is very close to U_{mb} prediction of 0.0096 m/s by Abrahamsen and Geldart [1980]. For the drag models by Syamlal and O'Brien [1987] and Gidaspow [1994], U_{mb} is predicted as 0.0135 m/s and 0.0138 m/s respectively. The window of uniform expansion can quantified as difference of U_{mb} and U_{mf} and presented in the table 6.4. It is interesting to note that this window is similar for Syamlal and O'Brien [1987] and Gidaspow [1994], but Beetstra *et al.* [2007*a*] predicts U_{mf} and U_{mb} closer to the experimental correlations. For rest of this thesis, Beetstra *et al.* [2007*a*] drag model would be used as a base case parameter.

6.4.4 Effect of path dependence

Three fluidization procedures indicated in earlier sections (section 6.2.3) may or may not result in same mesoscopic trends. If inlet velocity is introduced very gradually i.e.

K tends to 0, then the mesoscopic trends obtained from procedure 1 may coincide with those obtained using procedure 2. Hence, simulation procedure 1 is tested here with varying values of K in the equation 6.1. The final inlet velocity is kept around 3 U_{mf}. The simulations are run for different maximum times to achieve same end velocity. A wide range of K value from 0.001 to 0.03 m^2/s is tested to optimize simulations. Previously U_{mb} is found out to be a function of K upto a certain extent Ye *et al.* [2005].

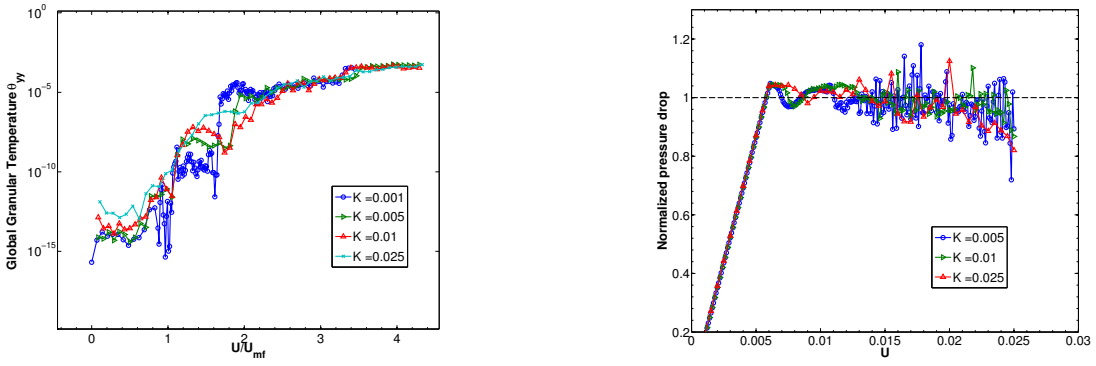

(a) (b)

Figure 6.10: Effect of path dependence parameter K on global granular temperature and pressure drop versus inlet velocity to find U_{mb} and U_{mf}. A cohesive bed with Bond number 2 is used for this study.

Figure 6.10a and b plots θ and ΔP for different values of K respectively. A cohesive bed with Bond number 2 is used for this study. A lower value of K indicates that a longer time is required to reach final inlet velocity. Figure 6.10b indicates that variation of K seems to have almost no effect on U_{mf} and pressure overshoot. This can be explained by the fact that the U_{mf} only indicates if the bed weight is counted balanced by the fluid-drag forces which are just a function of final inlet velocity and the bed properties.

Figure 6.10a plots θ with an increasing inlet velocity. For a high value of K = 0.03 m^2/s. θ is seen to be increasing gradually from the onset of fluidization $U = U_{mf}$ indicating that there is no clear window of uniform expansion. For K = 0.01 m^2/s curve, jump of order of 2 order of magnitude is not clear at U_{mb} but identified as 1.78 U_{mf}. For K = 0.005 and 0.001 m^2/s, a clear distinction between U_{mf} and U_{mb} can be made. U_{mb} is predicted for K = 0.005 and 0.001 m^2/s as 1.73 and 1.65 U_{mf} respectively.

Decreasing K results beyond 0.001 m^2/s, can increase in the computational time with not so much gain in U_{mb} prediction. A change in K from 0.01 to 0.001 m^2/s decreases U_{mb} predictions by 7%. For further studies K = 0.001 m^2/s is employed to capture the expanded regime.

Based on the path dependence studies, in any future DEM-CFD studies, superficial inlet velocity will be varied with the time 6.11. Different values of K has been used

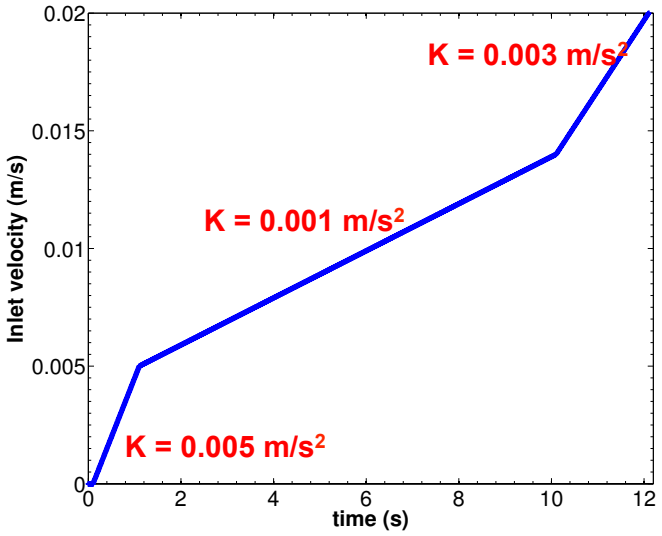

Figure 6.11: Inlet velocity versus time plot employed by DEM-CFD using simulation procedure 1

to optimize the computational time in different regimes. Transitions from fixed to expanded regime and expanded to bubbling regime will be optimally captured form this variation of inlet velocity. A higher value of K = 0.005 m^2/s is employed in the fixed bed region $U < U_{mf}$ and a significantly low value of K = 0.001 m^2/s is used for expanded bed region $U_{mb} > U > U_{mf}$. In order to cover a broad range of inlet velocity, K is increased to 0.003 m^2/s in the region $U > U_{mb}$. By employing such low values of K, it is expected that these studies can be even used to study trends of microscopic quantities with some level of confidence in chapter 7. Based on path dependence studies, it is concluded that procedure 2 (sec 6.2.3) must be employed for microstructure quantification and studying steady and unsteady characterization of expanded bed. Microstructural quantities from these simulations can be ensemble averaged over steady state.

In summary of all the parametric studies: effects of cohesion, mesh-size, drag model and fluidization path on the macroscopic trends have been ascertained. The simulation conditions, mesh size and path of fluidization have been optimized for a reasonable run time. Physical phenomenon related to Geldart A fluidization such as stable bed expansion and pressure overshoot have been captured by DEM-CFD simulations. Increasing cohesion delays onset of bubbling and Beetstra *et al.* [2007*a*] drag model captures U_{mf} and U_{mb} to a reasonable extent.

At this point, it is established that the Geldart A stable expanded bed phenomenon is adequately captured by DEM-CFD simulations by incorporating inter-particle forces.

Key phenomenon can be identified but a formal characterization of expanded bed is still pending.

6.5 Expanded bed regime characteristics

Experimental evidences have suggested a smooth like stable expansion for expanded bed. Previous stability studies have employed 2 criterion to establish hydrodynamic state of expanded bed [Busciglio *et al.*, 2010]. These equilibrium conditions are given as:

- Ensemble averaged macroscopic particle velocity ($< u_p >$) tends to zero in the stable expansion window.

$$< u_p >= 0 \tag{6.9}$$

- Inlet velocity U is related to bulk porosity ϵ by a linear logarithmic relation over a full range of expanded bed window. This relation (equation 6.10) was first extensively investigated experimentally by Richardson and Zaki [1954] and from here on referred to as Richardson–Zaki (R–Z) correlation.

$$U = u_t \epsilon^n \tag{6.10}$$

  Here, n is the Richardson-Zaki correlation coefficient (6.11) and u_t is the terminal velocity of free falling isolated particle given by equation 6.13. ρ_p is the particle density, μ is the fluid viscosity, g is the gravitation constant, d_p is the particle diameter. u_t is correlated with n and Archimedes number Ar and is given by equations 6.12 and 6.11.

$$n = \frac{4.8 + 0.1032 Ar^{0.57}}{1 + 0.043 Ar^{0.57}} \tag{6.11}$$

$$Ar = \frac{g d_p^3 (\rho_p - \rho_f)}{\mu_f^2} \tag{6.12}$$

$$u_t = [-3.809 + (3.809^2 + 1.832 Ar^{0.5})^{0.5}]^2 \mu_f / (d_p / \rho_f) \tag{6.13}$$

These 2 criterion will now be tested on the expanded bed regime reproduced through DEM-CFD simulations in the present study.

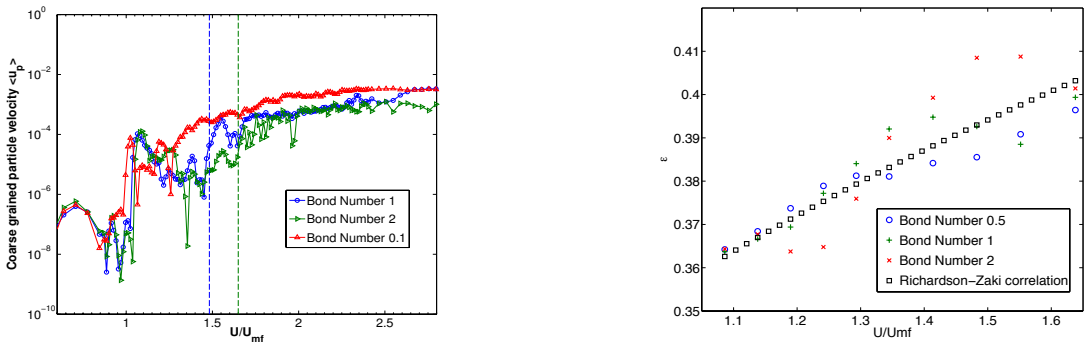

(a) (b)

Figure 6.12: Expanded bed characteristics tested by plots (a) Coarse grained particle velocity $< v_p >$ versus normalized inlet velocity (b) Bulk porosity ϵ plotted with inlet velocity U for different Bond numbers (in the legend) in the region of expanded bed regime and compared with Richardson-Zaki correlation.

Figure 6.12a plots coarse grained particle velocity $< u_p >$ with inlet velocity U. The dotted lines shows U_{mb} identified from previous sections for Bond number 1 and 2. In the expanded bed window, magnitude of $< u_p >$ for both of the Bond number plots is seen to less than 10^{-5} m/s. In comparison to a typical bubbling bed, $< u_p >$ magnitude of 10^{-2} m/s is observed. On the other hand, v_p magnitude for Bond number 0.1 is seen to be gradually increasing after onset of fluidization with no expanded bed regime window identified.

Figure 6.12b plots bulk porosity ϵ with the inlet velocity U for different Bond numbers in the expanded bed regime window. ϵ is calculated from the steady state simulations of expanded bed using simulation procedure 2. These relations are compared with empirically calculated Richardson-Zaki correlation [Richardson and Zaki, 1954] fitted with n=3.93. Experiments have identified n to be in the broad range of 3.4 to 4.8. The relation of n with terminal velocity is given by equations 6.11, 6.12 and 6.13 respectively [Rowe, 1987]. A calculated value of n = 4.13 from these expressions are fairly close to 3.93 used here to fit the simulation data.

6.6 Stress state of analysis of a stable expanded bed

Mechanical state of expanded bed has been a focal point of long standing debate. It is widely believed that both the solid and fluid like state is possible and there is a gradual transition within the window of stable expansion from solid-like to fluid-like bed [Valverde *et al.*, 2003; Valverde and Castellanos, 2007*b*]. Internal solid stresses can reveal the mechanical state of the fluidized regimes. Valverde and Castellanos [2007*b*]

concluded that the particle-particle enduring contacts are eminent in the solid-like behaviour where as for fluid-like behaviour bed acts as a low viscosity fluid exhibiting fluid properties.

6.6.1 Stress profiles

In order to study the role of solid stresses during fluidization/defluidization process, a 1D model was first proposed by Jackson [2000]. A minor modification to this analysis was proposed by Srivastava and Sundaresan [2002] and implemented by Loezos *et al.* [2002]. Equation 6.14 presents the 1D model:

$$\frac{d\sigma_{yy}}{dy} \pm \frac{4}{D}\mu j \sigma_{yy} = \rho_p g \phi - \frac{dp}{dy} \tag{6.14}$$

Here σ_{yy} is the yy-component of total stress in the gravity direction; y is the coordinate in the gravity direction and measured from the top surface of the bed; D is the bed diameter; μ is the coefficient of wall friction; j is the Janssen's coefficient (assumed to be constant); $\frac{dp}{dy}$ is the fluid pressure gradient; ρ_p is the particle density and ϕ is the solid fraction. Uniform bed expansion was explained by this model by examining the nature of fluidization and defluidization curves. The model was able to capture the bed height and pressure overshoot when compared with the experimental data. It was further noted that the σ_{yy} are the total solid stresses and no distinction between the contact or cohesion stresses were made. Even though, it was largely concluded that the wall friction is responsible for bed expansion [Loezos *et al.*, 2002].

In the present study, internal stresses are calculated by post processing of the DEM data (section 3.6.2). In particular, distinction is made between the cohesion, contact and kinetic stresses to bring out the role of cohesion. The stresses are calculated on a 2D slab across the x-z direction at different heights in the y direction. Figure 6.13 explains the geometry and mesh grid used for stress calculations. 10 different heights are from height 2d to 16d height and overlapping slabs with centre at these height and size 4d are employed. Steady state simulations using simulation procedure 2 are used for these studies. At each superficial velocity, simulations are run for 2 seconds and first 0.5 seconds are removed as transient phase. The stresses are calculated at each height and then ensemble averaged over next 1.5 seconds.

From 1D model, term $\frac{4}{D}\mu j \sigma_{yy}$ can be neglected as 3D bed dimensions are taken. This means that the sum of $\frac{d\sigma_{yy}}{dy}$ and $\frac{dp}{dy}$ should be roughly constant in the fixed bed regime as solid fraction ϕ is constant. From the pressure drop curves, it is known that the term $\frac{dp}{dy}$ is decreasing non-linearly as the inlet velocity is increased in the fixed bed

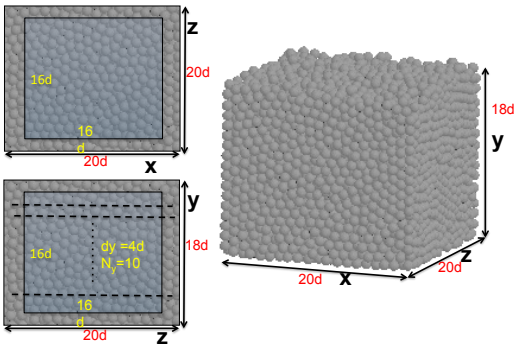

Figure 6.13: Geometry and discretization used for Stress calculations from DEM contact data. There is no discretization in x and z direction and slab width 14d is used. 10 overlapping slabs of size 4d is employed in the height direction. d is the particle diameter = 100 μm

regime, up until $U_U mf$. This indicate a similar drop in the internal stresses. Figure 6.14a plots the stress profiles for Bond number 0.1. At low inlet velocities (U/U_{mf} = 0.167,0.33,0.5,0.83 and 1), σ_{yy} gradient decreases with increase in inlet velocity and similar trends are observed for Bond number 2 and 3. Positive stresses means compressive stresses and negative stresses are tensile. This observation confirms that the DEM-CFD model predictions are in line with the 1D model proposed by Loezos *et al.* [2002].

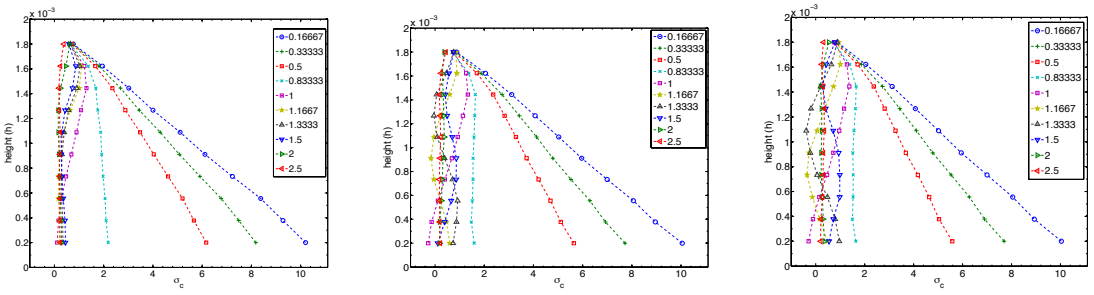

(a) (b) (c)

Figure 6.14: Stress profile (x-axis) with different height (y-axis) at different normalized superficial velocity (in the legend) for Bond numbers (a) 0.1 (b) 2 (c) 3. At each superficial velocity, simulations are run for 2 seconds and first 0.5 seconds are removed as transient phase. Stresses are calculated at each height and then ensemble averaged over next 1.5 seconds.Height and stress units are m and Pa respectively.

Furthermore from figure 6.14 and the region $U > U_{mf}$, stress profile shows a clear transition from the fixed to fluidized states. Low compressive stresses observed in the region $U > U_{mf}$ indicates binary short time contacts in the bubbling regime. At U/U_{mf} = 2.5, stresses tends to zero throughout the bed indicating that the role of stresses in this regime is negligible. Fluid-particle drag governs the hydrodynamics of the fluidized system in the bubbling bed regimes.

For Bond number 2 and 3, this transition from fixed to expanded bed is not so straightforward. Negative tensile stresses and change in gradient of stresses are observed for the inlet velocity $U > U_{mf}$. The stress profiles at a particular inlet velocity can be looked more closely in the figure 6.15.

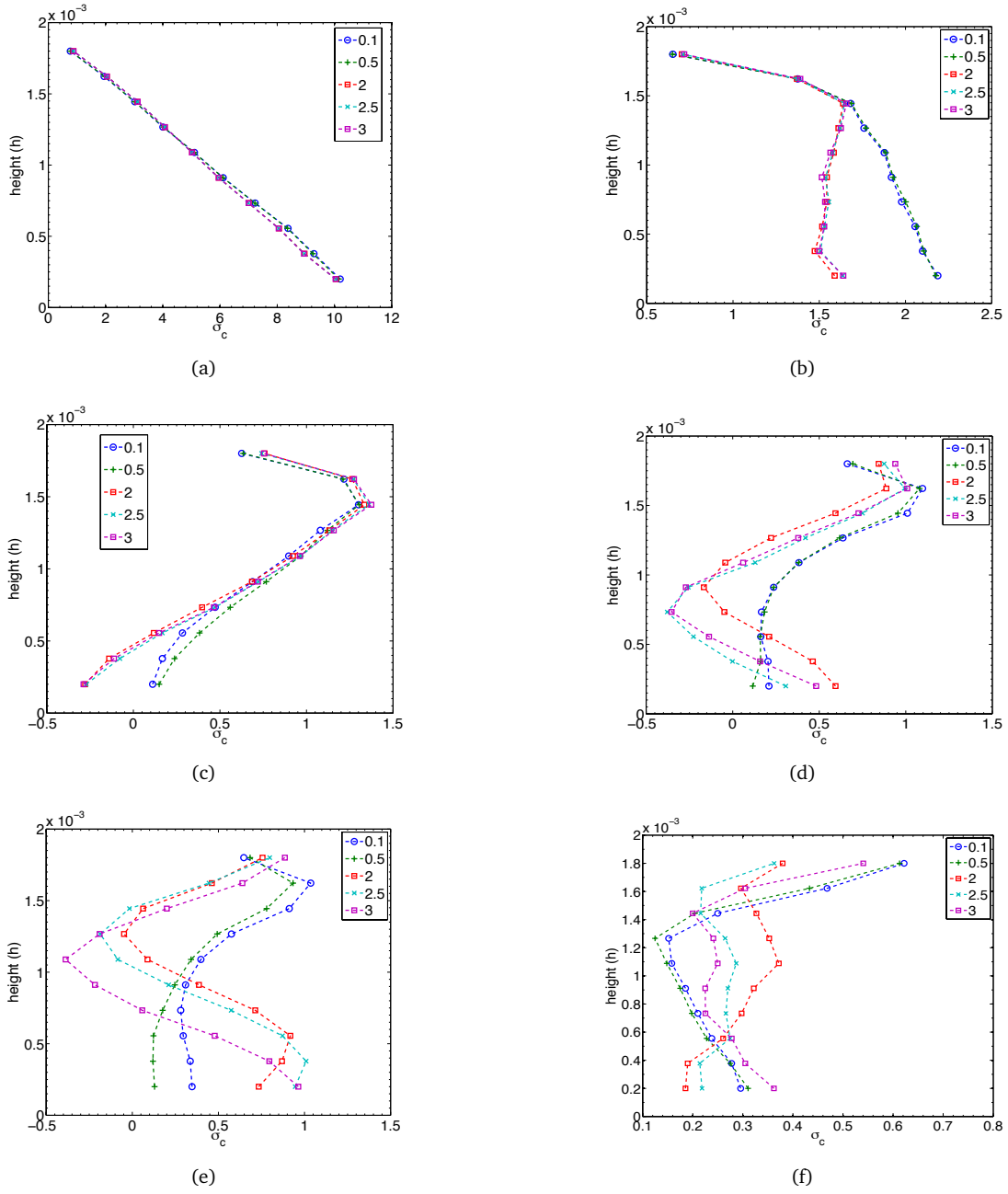

Figure 6.15: Stress profile (x-axis) with different height (y-axis) at different Bond numbers (in the legend) at (a) $U/U_{mf} = 0.167$ (b) $U/U_{mf} = 0.833$ (c) $U/U_{mf} = 1$ (d) $U/U_{mf} = 1.3$ (e) $U/U_{mf} = 1.5$ (f) $U/U_{mf} = 2$.Height and stress units are m and Pa respectively.

Figure 6.15 shows stress profiles at 6 different inlet velocities for different Bond numbers. Figure 6.15a shows stress profiles at $U/U_{mf} = 0.167$. The plot indicates a linearly

varying stress profile from bed bottom to the bed surface for all the Bond numbers. Figure 6.15b plots the stress profiles at a velocity close to the onset of fluidization ($U/U_{mf} = 0.83$). The magnitude and trend of the stresses change significantly from $U/U_{mf} = 0.167$ plot. For higher Bond numbers ($Bo_g > 1$), the gradient of the stresses is different for $Bo_g < 1$ highlighting the role of cohesion.

At the onset of fluidization $U/U_{mf} = 1$, stresses gradient are seen to be reversed for Bond numbers 1-3 and negative tensile stresses are apparent at the bottom of the bed. Whereas for Bond numbers 0.1 and 0.5, stresses are almost close to zero but compressive. The presence of negative stresses at the onset of fluidization was identified as a sufficient condition for the uniform bed expansion by Sundaresan [2003]. Furthermore, tensile stresses at the bottom of the bed can lead to the pressure overshoot phenomenon observed from the figure 6.6. The extra pressure observed can be expalined by additional hydrodynamic forces required to break the inter-particle adhesive forces in addition to the weight of the bed [Espin *et al.*, 2011]. The magnitude of tensile stress at the bottom of the bed for Bond number 2 is close to 3.5% of the total stress applied by the self weight of the bed on the distributor plate. Figure 6.3 shows the pressure overshoot to be around 4% for Bond number 2 fluidization curve. These observations indicates that fluidization experiments and simulations can provide a clear way to measure tensile strength of a cohesive powder.

Figure 6.15d and e shows stress profiles for $U/U_{mf} = 1.3$ and $U/U_{mf} = 1.5$. These inlet velocities can form stable expanded beds for Bond numbers 1-3. The stress profiles show a rather curious picture as the tensile stresses are present in the middle of the bed at different heights for expanded bed state. The tensile stresses indicates sustained enduring particle contact. These would in turn curb bubbling and increase in hydrodynamic forces by the inlet velocity is instead manifested into an expanded bed. Alternatively, for the Bond number 0.1 and 0.5, these stresses are compressive and fluidization behaviour is aggregative or bubbling. A point to note is the upward shift of the location of tensile stresses with increase in the inlet velocity for a particular Bond number. The tensile stresses present at the bottom of the bed at onset of fluidization shift to the top of the bed at the onset of bubbling. This shift is delayed by increasing cohesive strength of the bed leading to a delay of onset of bubbling. These observations clearly brings out the role of cohesion to suppress bubbling and aid the formation of expanded bed instead. Figure 6.15f show stress profiles for $U/U_{mf} = 2$, which is bubbling regime for all the Bond numbers. The stresses are compressive and tend to zero at all the heights. As expected for bubbling bed, inter-particle contacts are binary as the cohesive bonds which hold them together are broken.

6.6.2 Cohesion Stress

Previous section indicated presence of negative stresses in the expanded fluidized bed. Origin of these negative stresses are the cohesive interactions between the particles. Figure 6.16 plots the cohesion stress profiles for different inlet velocities in fixed (6.16a), expanded (6.16b) and the bubbling bed (6.16c) regime. Cohesion stress profile for the fixed bed regime is almost constant with height and does not vary linearly, as found in the total stress profiles seen in figure 6.15a. This indicates that the linear variation should come from the contact stress profiles. In the expanded regime for Bond numbers 1-3, magnitude of cohesion stresses (figure 6.16b) is more negative in the middle of the bed than the positive magnitude of contact stresses (see figure 6.17b) leading to a total net negative tensile stresses as seen from plot 6.15d.

In the bubbling bed regime, magnitudes of both the cohesion (figure 6.16c) and the contact stresses (figure 6.17c) are close to zero. Bond number 0.1 and 0.5 exhibit a very low cohesive and contact stresses in the region $U > U_{mf}$ as the contacts are binary and not enduring.

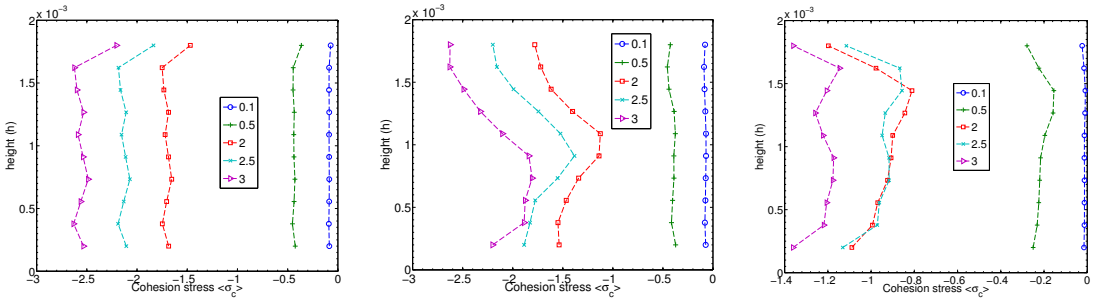

(a) (b) (c)

Figure 6.16: Cohesion stress profile (x-axis) with different height (y-axis) at different Bond numbers (in the legend) at (a) $U/U_{mf} = 0.167$ (b) $U/U_{mf} = 1.33$ (c) $U/U_{mf} = 2.5$. Height and stress units are m and Pa respectively.

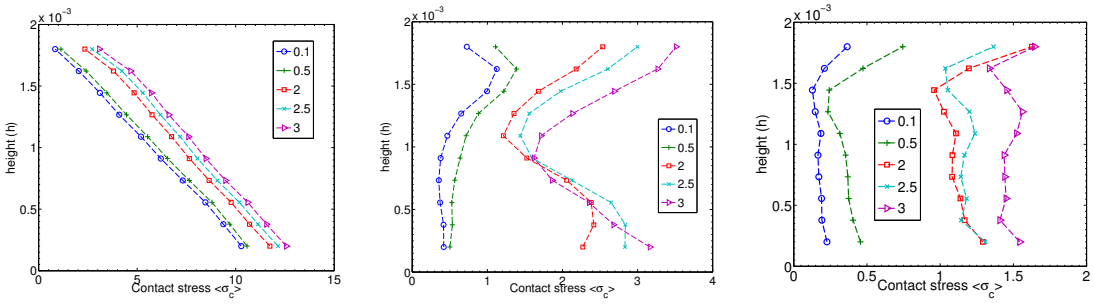

(a) (b) (c)

Figure 6.17: Contact stress profile (x-axis) with different height (y-axis) at different Bond numbers (in the legend) at (a) $U/U_{mf} = 0.167$ (b) $U/U_{mf} = 1.33$ (c) $U/U_{mf} = 2.5$

In order to study evolution with increasing inlet velocity in the expanded bed regime, cohesion stresses are averaged throughout the bed height and plotted in figure 6.18a with different Bond numbers (1-3) indicated in the legend. Dotted line indicates U_{mb} for each of the Bond numbers. In the fixed bed region $U < U_{mf}$, cohesion stresses are constant with an increase in inlet velocity. It should be noted that, with increasing inlet velocity in the fixed bed region, total stress gradient should decrease according to the 1D model. This decrease in the gradient is apparent for the contact stresses but not for cohesion stresses. While increasing the inlet velocity, the overlaps between the particles decrease due to increase in the hydrodynamic forces but the cohesion forces remains constant as it does not vary with the overlap.

It should be further noted that with an increasing Bond number, initial cohesion stresses in the bed vary. To provide a meaningful comparison, figure 6.18b plots cohesion stresses normalized by the averaged cohesion stresses present in the static bed. At the onset of the fluidization, magnitude of cohesion stresses decreases gradually for each of Bond numbers and suddenly drops at the onset of bubbling. For Bond number 1 curve, there is only 10 % decrease in the cohesive stresses till the onset of bubbling. During the bubbling regime, the cohesion stresses drop significantly upto 10% of the initial cohesion stresses in the bed. This sudden drop in the cohesion stresses indicate that the cohesive bonds have been broken and any cohesive stress contribution would be due to binary collisions. These graphs further clarifies the extent of role played by cohesive stresses on delaying onset of bubbling.

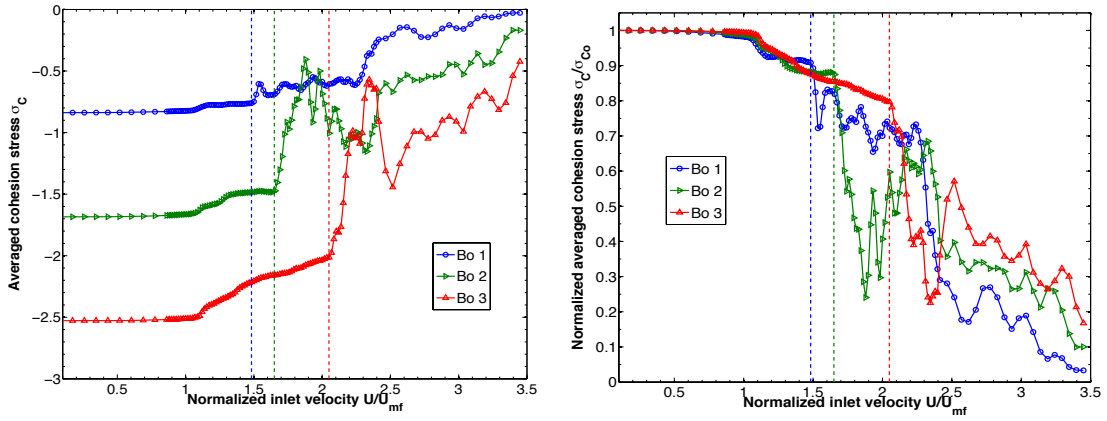

(a) (b)

Figure 6.18: Cohesion Stresses in different fluidization regimes with increasing inlet velocity and Bond numbers

6.7 Conclusion

DEM-CFD simulations of Geldart A fluidization was undertaken in this chapter and following conclusions can be drawn:

- Open-source DEM-CFD code with van der Waals cohesion model was able to capture robust feature of Geldart A fluidization. Some of the key phenomeon captured in the study are: pressure over-shoot phenomenon, macroscopic U_{mf} predictions, uniform stable bed expansion and delay in the onset of bubbling. A quantitative assessment of U_{mf} reveal a closer match with the experiments and theoretical predictions.

- Cohesive strength of the bed was measured by the Bond number. The methodolody applied to study the role of cohesion was to keeping the particle diameter and density constant and varying the Bond number and studying the fluidization behaviour of these beds. A transition between A/B was noted for $Bo_g = 0.5$ and between A/C for $Bo_g = 3$.

- Global granular temperature (θ), local porosity fluctuations and the pressure drop fluctuations were identified as indicators to determine onset of bubbling (U_{mb}). In particular, θ was used extensively for this purposes as a clear jump of 2 orders of magnitude were noticed at the onset of bubbling.

- U_{mb} was found to be an increasing function of the cohesive strength of the bed. Pressure overshoot magnitude also increased with the Bond number, but the U_{mf} was found to be constant.

- Discretization of the domain was found to be a key parameter for determination of U_{mb}. It was noted that U_{mb} increased with employment of a coarser mesh. These mesh were not able to resolve bubbles which are of typically order of few particle diameters. U_{mf} was largely unaffected by meshing, as it is a macroscopic quantity determined by overall force balance of the assembly. U_{mb} is a mesoscopic phenomenon and is affected by meshing. An optimized mesh size was identified as 2.5-3 times particle size.

- Fluidization path, meaning rate at which the fluid introduced in the system, played an important role in U_{mb} determination. An optimized path was decided by these decided to be employed in future studies of microstructure characterization.

- Different drag models were tested and both U_{mb} and U_{mf} are seen to be sensitive to them. Beetstra *et al.* [2007*a*] drag model was seen to be in closest agreement with empirical relations and was employed for further studies.

- Expanded bed was rigorously characterized by satisfying two criterion: (1) macroscopic averaged particle velocity tending to be almost zero ($< u_p >= 0$) and (2) bed bulk porosity related to the inlet velocity by Richardson–Zaki correlation. These criterion are popularly checked in the literature before for the same purpose.

- Stress analysis of the expanded bed revealed presence of tensile stresses at the bottom of the bed during onset of fluidization. As the inlet velocity is increased with $U < U_{mb}$, a longitudinal shift of these negative stresses is observed until it reaches the top of the bed. Negative stresses were seen at the bed surface at the onset of bubbling. The role of cohesion stresses in the formation of expanded bed and suppressing of bubbling was highlighted.

- At the minimum fluidization velocity, the negative tensile stresses at the bottom the bed can be linked to the pressure overshoot phenomenon. The magnitude of the pressure overshoot and tensile stresses were close and both were found to be increasing function of cohesion.

- Role of cohesion stresses was further highlighted in the expanded bed regime as an abrupt decrease in its magnitude was noticed at the onset of bubbling.

Chapter 7

Microstructure Characterisation

7.1 Introduction

The transition from particulate to aggregative fluidization, with increasing fluid velocity, is a unique feature of Geldart A fluidization. Geldart A particles are characterised as weakly cohesive and exhibit a window of stable expansion before the appearance of bubbles. Uniform expansion is a classical liquid fluidization feature, when the instabilities grow from the distributor plate to the bed surface as a wave at a much slower speed. However, experimental evidences of uniform gas-solid fluidization has also been reported for last few decades. More on these studies can be found in the literature review chapter of this thesis. In the previous chapter, it was demonstrated that DEM-CFD simulations are capable of capturing robust features of bed expansion. The expanded bed was characterized with highly immobile particles and checking experimental R–Z correlation to be satisfied. It is noted that throughout the literature, uniform expansion has been referred to as *homogeneous fluidization* [Abrahamsen and Geldart, 1980; Lettieri *et al.*, 2002; Mutsers and Rietema, 1977]. It is a general understanding that the term *homogeneous* simply means absence of bubbling and a smooth appearance in bed expansion as opposed to heterogeneous aggregative fluidization with large voidage spaces and agitated appearance. However, in the most strict sense, homogeneity would imply an even particle concentration through out the domain. It is therefore pointed here that the homogeneous macroscopic appearance does not imply homogeneity at lower spatial length scales as well. Industrial processes are mostly driven by the microstructure interactions but are designed on phenomenological studies based on macroscopic behaviour. It is therefore essential to study the microstructure of the bed. These studies can be beneficial in different ways:

- The studies will lead to better design, scale-up procedures and optimization of industrial processes. A knowledge on the inter-particle interactions and local arrangement of particles can potentially save millions of pounds by improving contact energy transfer efficiency.

- The studies are useful in providing a fundamental understanding of the fluidization phenomenon itself. The microstructure can be linked to the mesostructures such as bubbles and eventually to the macroscopic bulk behaviour. This will be helpful to devise better multi-scale modelling strategies by providing a route to better constitutive laws based on microstructural evolution [Sun and Sundaresan, 2011].

- Microstructural studies can provide information on the smallest length scales governing the dynamics of the system. Recently, nano particle (NP) fluidization is shown to be governed by low-density agglomerates than the individual particles themselves [Hakim *et al.*, 2005; van Ommen *et al.*, 2012]. Formation of these agglomerates alters the passing fluid behaviour resulting in a heterogeneous distribution, which results in channelling and inefficient gas-solid contact [Valverde, 2013].

Previously, experimental techniques such as scanning electron microscopy (SEM), X-ray CRT or LASER imaging systems have been employed on the granular systems to characterize microstructure [Hakim *et al.*, 2005; Yao *et al.*, 2002]. However, dynamic processes such as fluidization systems are difficult to characterize through these techniques due to significant delay in data acquisition. In addition to this, experimental techniques are expensive and highly non-portable. Numerical simulations, capable of capturing micro-level physics and reproduce robust features of fluidization regimes, could provide an alternative route and give the required information at the particle level. To this end, DEM-CFD methodology provide an opportunity to study the microstructure of fluidized regimes for its ability to resolve inter-particle collisions and maintaining computational tractability. Recently, Hou *et al.* [2012] employed DEM-CFD to link mechanical coordination number (MCN) to the local porosity (ϵ) and identified it as a measure of local structure in an expanded bed regime. MCN is defined as the average number of contact per particle (definition would be discussed in more detail in the later section). A phase diagram based on the MCN-ϵ relationship was also developed to represent the microscopy of expanded and bubbling beds. However, such a criterion did not take account of agglomerate formation (mesoscopic structure). It fails to establish a link between microscale interactions and mesostructures which can be agglomerates or cavities. A similar recent study by Yang *et al.* [2013] employed DEM-CFD

to study the effect of surface energy on the transition from a fixed to expanded bed on a 2D bed. The inter-particle surface energy was modelled via an adhesive elastic-plastic contact model by Thornton and Ning [1998]. It was concluded that the expanded bed regime is not homogeneous, but didnot delve into details of heterogeneity.

7.2 Objectives of the chapter

This chapter aims to characterize microstructure of different fluidization regimes identified for Geldart A particles: Fixed bed ($U < U_{mf}$), expanded bed ($U_{mf} < U < U_{mb}$) and bubbling bed ($U > U_{mb}$). Statistical tools will be employed on the DEM data of contact and cohesion force networks, to characterize the microstructure of fluidization regimes at different local length scales. Force networks refers to the list of particle pairs either in the mechanical contact or the cohesion contact, and the forces between them. In the previous chapter, presence of cavities or agglomerates were inferred. This chapter builds onto this information and quantify these inhomogeneities. Coordination numbers providing a measure of local contact information, are employed along with coarse-grained solid fraction to provide information at a mesoscale.

It is already established that there is a presence of strong force networks in the static fixed granular bed which carries bulk of the assembly. The rest of the contact pairs mostly form a support network [Silbert *et al.*, 2002]. It is therefore, natural to check for such distinction in the rest of fluidization regimes and in particular solid-like expanded bed. This would also reveal information on the mechanical states of the bed. In the present study, distinction between the strong and weak force pairs is made by pre-processing the force networks and filtering out all the pairs with forces less than a pre-decided limit (mostly average contact force). The interest lies in microstructural studies of particle belonging to the strong force network. Major focus of this part of the study would be to check how particles belonging to strong force networks coordinated for different fluidized regimes. Furthermore, Voronoi tessellation are employed to study microstructure distribution and quantify clustering based on standard deviations as outlined in Tagawa *et al.* [2012]. Voronoi volumes are often used to quantify the local arrangement of particles and provide a picture that coarse grained solid fractions or coordination numbers fail to provide.

7.3 Definition of the microstructural quantities

This section presents the definition and relevance of different microstructural quantities that would be employed in this chapter.

1. Mechanical coordination number (MCN): This is defined as averaged number of mechanical contacts per particle per time step. A mechanical contact is deduced if the modulus of the contact vector between the particles is less than the sum of their radii. The number of total contacts per particles are counted and then averaged over each particle having atleast one contact. A list of all the particles that are in contact with each other, is outputted from the DEM-CFD simulations at a sampling rate of 200 Hz. The contact pair information includes: Particle ID's, contact force in each direction calculated as a function of overlap (present study employs linear spring dash-pot model) and the normal contact vector defined as vector joining the centre of each particle. MCN has been employed and measured previously to quantify the microstructure and reveal information on the momentum transfer through contacts and heat transfer models [Majmudar and Behringer, 2005; Zhou *et al.*, 2009]. It is the most local information on the microstructure of a granular system. Nevertheless, MCN takes into account all the contacts regardless of the forces transmitted through it. In this study, first the force data over all the contacts is averaged to find an average contact force magnitude per particle (f_{av}) and then a cut off force (F_C) will be decided based on f_{av}, the contact list will be filtered for contact force per pair less than F_C. The strong force network MCN will be calculated on the new force contact data list.

2. Cohesion coordination number (CCN): It is defined as the average number of neighbouring particles in the cohesion sphere of influence of a particle. CCN definition is similar to MCN except that the cohesion force network is considered instead of mechanical contact network. A list of all the cohesion pairs is prepared with information on the particle ID's, cohesion forces and the contact vector. Unlike contact forces which have both normal and tangential components, cohesion forces act only along the normal contact vector. The cohesion force can be non-contacting and decreases with the separation distance between the particles. By definition, they are long range forces but most of the cohesion models employs a parameter called maximum cut-off distance (S_{max}) beyond which cohesion forces are taken as zero. This study employs van der Waals model and figure 7.1 gives a plot between inter-surface distance (s) and the cohesion force magnitude F_{vdw}. S_{max} = 1.25d, where d is the particle diameter is used throughout the study. S_{max} is a useful parameter to reduce the neighbour list build for cohesive interaction.

   The cohesion sphere of influence of a particle is equal to volume of the sphere with centre as particle centre and radius equalling S_{max}. All the particles within this cohesion sphere are counted to give a local CCN and then averaged over number of particles over the domain to give a averaged CCN. If particles are in

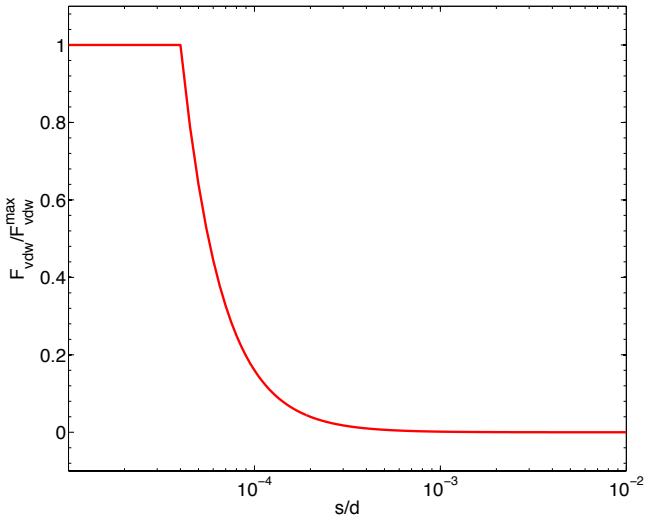

Figure 7.1: Variation of van der Waals forces between a pair of particles (F_{vdw}) with the separation of the surfaces (s). van der Waals forces are normalised by maximum cohesion forces between particles when particle surfaces are separated by a minimum distance (S_{min} (beyond which van der Waals forces are constant). Seperation between the surfaces (s) are normalized by the particle diameter (d). Typical S_{min} value is taken here as $4e-5d$ = 4.0e-9 m.

mechanical contact, the cohesion forces are taken as constant and does not vary with the overlap. It is here pointed out that, all the mechanical contact pairs are the subset of cohesion force network. As noted for the MCN calculations, the definition of CCN does not include any distinction based on the magnitude of the cohesion force between the particle pair. This will be dealt by including a cut off force based on averaged cohesion forces between the particles.

3. Coarse-grained solid fraction (ϕ_m): This is defined as weighted average of volume of all the particles occupying a certain mesoscopic volume, generally of the order of 2-4 times the particle diameter. Unlike MCN and CCN defined before, ϕ_m is a continuum quantity and a measure of particle occupancy. An Eulerian mesh is defined on the full 3D domain to generate lattice points. Alternatively, unstructured mesh can also be defined. Taking each lattice point as centre, a representative symmetric coarse-graining volume is defined (this could be a cube or a sphere). The coarse-graining volume is decided according to the mesoscopic phenonmenon. A list of particles with centre inside this coarse graining volume is prepared. The volume of particles are weighted averaged and divided by the volume of representative volume. This is expressed as the coarse-grained solid fraction at the lattice point. In this chapter, a spherical coarse-graining volume of radius 2.5 times particle diameter will be employed on a $8 \times 8 \times 8$ lattice. It should be noted here that ϕ_m is defined and averaged over a mesoscopic phenomenon

and can-not provide the microscopic information. However, linking MCN and CCN to ϕ_m can be useful in providing information on the governing dynamics at the particle level itself.

4. Local solid fraction based on Voronoi tessellations: Voronoi diagram is a spatial discretization subjected to the condition that each point on the Voronoi cell is closest to the particle it encloses than any other particle [Tagawa *et al.*, 2012]. The domain walls and surfaces form the boundaries of the cells if they are closer. The volume of the Voronoi volume (V_v) can be seen as free volume for a single particle. Particle volume divided by the Voronoii volume provides a local solid fraction (ϕ_l). Unlike ϕ_m, it is a discrete quantity calculated on a Lagrangian framework. More details on the construction of Voronoi diagram can be found at Okabe *et al.* [2009]. This study employs Voronoii compute and package based in open source DEM code LAMMPS [Plimpton, 1995] to calculate the tessellations on the fly. ϕ_l holds a certain advantage over the averaged ϕ_m, as it does not depend upon any mesoscopic length scale [Tagawa *et al.*, 2012]. Even though the information provided by ϕ_l is less local then MCN or CCN, it provides an opportunity to link a significant gap of length scales between ϕ_m, CCN and MCN. Vornoi volume analysis would be particularly helpful in studying the mesostructures such as cavities and agglomerates, if present in the expanded bed regime.

Figure 7.2 provides a graphical description of the length scales of these statistical tools. These length scales of interaction or calculations are given as the radius from the centre of the particle. Here d is the particle diameter. MCN is based on the particle surfaces, typically at a distance d/2 from centre. Overlaps are fairly small in comparison with the diamter of the particle. CCN is based on the cohesion network and is calculated for all particles within $S_{max} = 1.25d$ distance from the particle. ϕ_m is calculated at a mesoscopic length scale of 2.5 d according to coarse graining procedure. ϕ_l is calculated according to the Voronoi volume. It is shown in dotted line and typically varies from 1.2 to 1.45 in a dense fluidized system.

In this chapter, all four of these statistical tool would be employed to study and quantify inhomogeneities present in different fluidized regimes of Geldart A particles. In particular, it will be interesting to compare expanded bed and the fixed bed regime.

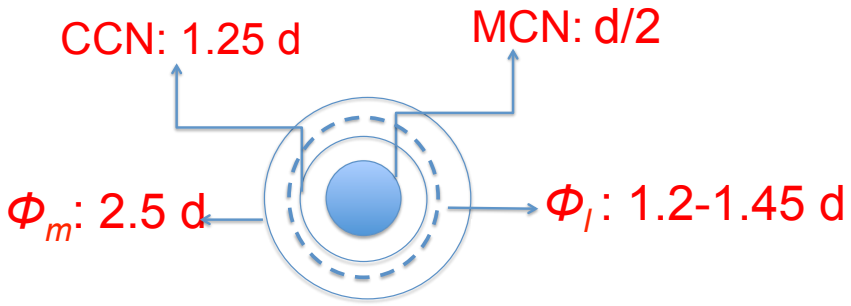

Figure 7.2: Description of relevant length scales of microstructure characterisation. Here, the length scales of interaction or calculations are given by the radius from the centre of the particle. d is the particle diameter

7.4 Simulation Set up

The physical, geometrical and contact parameters for used are similar to those used in the last chapter. These are enlisted in table 6.1. In the last chapter, distinction between the fixed, expanded and bubbling bed was made based upon the normalized inlet velocity (U/U_{mf}) and the granular Bond number (Bo_g). In order to study microstructure of these regimes, two kind of simulations will be post-processed based on procedure laid out in the section 6.2.3.

- Procedure 1 simulations: Inlet velocity is varied linearly with time from 0.0 to 3.0 U_{mf} in 20 seconds. These would be post-processed to study general trend of the averaged microstructural quantities (MCN, CCN, ϕ_m). However, these would not be used for statistical evaluation due to insufficient temporal information.

- Procedure 2 simulations: Granular bed is subjected to a constant inlet velocity in time. Each of weakly cohesive beds (0.5,1,1.5,2,2.5 and 3) will be subjected to 15 different inlet velocities in the range 0-3.0 U_{mf} (5 values each in the 3 different fluidization regimes). This makes a total of 90 (15×6) simulations and are run for 2 seconds each at high sampling rate. Before post-processing, initial transient phase time (variable, but mostly less than 0.5 seconds) is removed for both bubbling and expanded bed state.

7.5 Results and discussion

In this section, four statistical tools described earlier will be employed on the fluidization regimes of Geldart A particles.

7.5.1 Variation of averaged ϕ_m with inlet velocity

Granular bed with different cohesive strengths were subjected to inlet velocities linearly increasing with time from 0.0 to 3.0 U_{mf} in 20 seconds. DEM data at every time-step was post processed to calculated mesoscopic solid fraction (ϕ_m) by coarse graining particle positions over a volume with radius 2.5d on an $8 \times 8 \times 8$ Eulerian grid. The solid fraction, ϕ_m, is further averaged over all the grid points to find ϕ_{av}. Figure 7.3 shows variation of averaged solid fraction (ϕ_{av}) with increasing normalized inlet velocity for different cohesive strength bed (indicated by Bond numbers in the legend). As already indicated, these simulations are not very useful to characterize micros-structure but provide a general trend and are beneficial to study transition between the regimes. At $U/U_{mf} = 1$, the bed is fully fluidized and hydrodynamic interactions have just outbalanced the weight of the bed. In the last chapter it was concluded that the U_{mf} is not effected by the cohesive strength of the bed but U_{mb} increases with the Bond number. Two vertical lines in the figure 7.3 indicates U_{mb} for Bond numbers 1 and 2. For the region $U/U_{mf} > 1$ and $U/U_{mb} < 1$, bed is homogeneously expanding without any bubbling for Bond numbers 1-3. It is noted that ϕ_{av} decreases at a slower rate with decreasing Bond number. This might be due to fact that as the Bond number is increased, particles are forming agglomerates leading to an increase in fluid-particle drag. Nevertheless, ϕ_{av} is a coarse-grained quantity and can not reveal information at a sub-particle spatial resolution scale. After $U/U_{mb} > 1$, bubbling commences and fluctuations in the averaged local solid fraction are seen for cohesive assemblies with $Bo_g < 3$. A sudden drop in ϕ_{av} is observed in the transition from non-bubbling to bubbling regime for each of Bond number plots. These sudden drops are reflected on the mesoscopic scale as the bubble sizes are usually few particle diameters in size. For Bond number 5, ϕ_{av} decreases constantly in the expanded bed regime and U_{mb} is beyond $U/U_{mf} > 2.5$, and thus, is not shown in the plot. It should be noted that the bed is in the Geldart C regime. For this regime, a rapid decrease in solid fraction can be attributed to bed cracking and ratholing and not due to the bed expansion.

7.5.2 Variation of coordination numbers with inlet velocity

Averaged coordination numbers (MCN and CCN) are calculated from the DEM data at different Bond numbers with increasing inlet velocity. Coordination number is a more local microstructural quantity than the solid fraction calculations (ϕ_{av}). As the MCN is calculated from particle contacts and the cohesion coordination number (CCN) is calculated according to criterion $s < S_{max}$. These microstructural quantities are expected to be related to the coarse grained solid fraction (ϕ_m). A hydrodynamic disturbance at the particle contact should propagate to the different length scales in the domain.

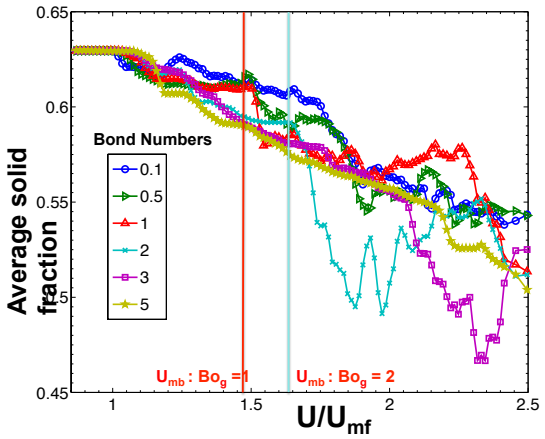

Figure 7.3: Variation of averaged solid fraction (ϕ_{av}) with increasing normalized inlet velocity for different cohesive strength bed (indicated by Bond numbers in the legend)

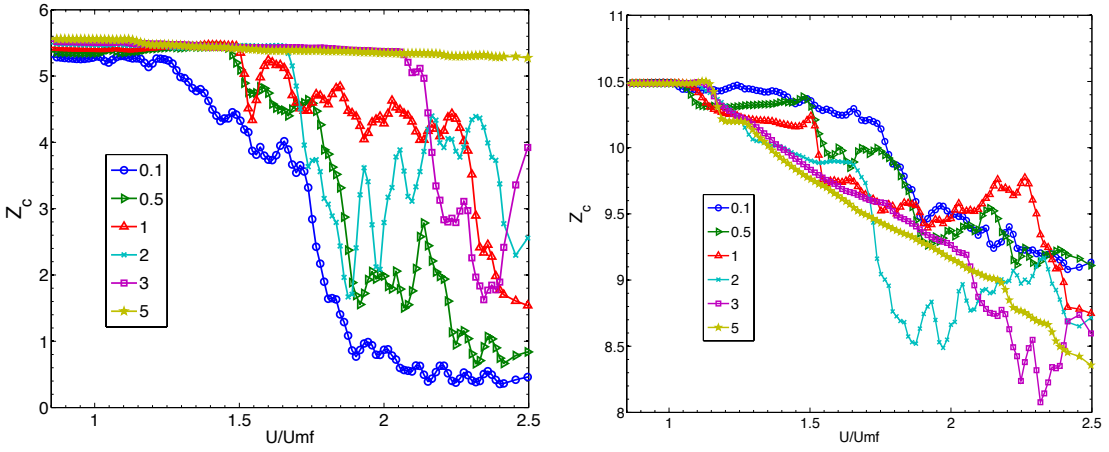

(a) (b)

Figure 7.4: Variation of coordination numbers for different Bo numbers with increasing normalised inlet velocity (a) Mechanical Coordination Number (MCN) (b) Cohesion Coordination Number (CCN)

Figure 7.4a shows variation of averaged MCN in different fluidization regimes. Averaged MCN remains constant for $U_{mf} < U < U_{mb}$ during homogeneous bed expansion. This indicates that microstructure at the most local sub-particle scale is not disturbed by the homogeneous expansion and hydrodynamic forces are not large enough to break adhesive inter-particle bonds. These trends are consistent for case the fluidization behaviour across all the expanded bed regimes characterized ($1 < Bo_g < 3$) . This finding explains the increasing trend of U_{mb} with Bond numbers. A greater adhesion forces between particles would require greater hydrodynamic forces or inlet velocity to break the adhesive bonds for bed to transcend to aggregative behaviour. For lower Bond number cases ($Bo_g < 0.5$), cohesive forces are not large enough hold particles together in a

fully fluidized regime ($U > U_{mf}$). This leads to a condition when bubbling commences directly after minimum fluidization is reached ($U_{mb} \approx U_{mf}$), reminiscent of Geldart B fluidization behaviour. It should be noted that, for much high Bond numbers ($Bo_g > 3$), weaker cohesive bonds (contacts which are only cohesional but not mechanical) break first and instead of bubbling behaviour, cohesive Geldart C behaviour of bed cracking, channeling and ratholing can be observed after ($U > U_{mb}$). Figure 7.4b shows that during homogeneous bed expansion, CCN shows similar decreasing variations as seen for ϕ_{av}. This behaviour is different from the MCN plots shown in 7.4a. This trend is rather counter-intuitive, it is expected that microstructure changes would vary from most local microstructural quantity (MCN) to the coarse-grained mesoscopic quantities (ϕ_{av}). Refer to figure 7.2 that gives the relevant length scales for each of these microstructural quantities. CCN plots indicate that microstructural changes at inter-particle contacts might not be governing the expanded bed dynamics and particles tend to act as agglomerates with strong adhesive contacts with neighbours. A similar observation was drawn for NP fluidization [van Ommen *et al.*, 2012]. Figure 7.5a gives a scenario when agglomerates are in mechanical contact, while figure 7.5b shows particle are only in cohesion contacts and mechanical bonds are broken. A complete breakage of cohesion and contact network could occur if hydrodynamic forces are stronger than the cohesion and contact forces at $U > U_{mb}$, transiting from particulate to aggregative fluidization regimes. Next sections would further investigate microstructure quantities CCN and MCN, differentiating between the weak and strong contact and cohesion networks to probe the clustering and agglomeration in the expanded bed regimes.

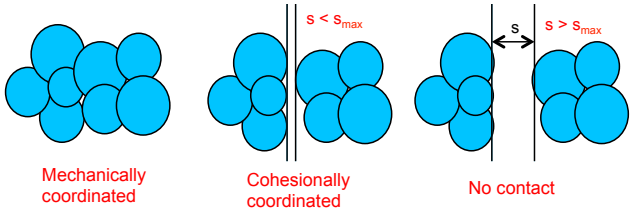

Figure 7.5: Pictorial description of contacts a particle can be in (a) Mechanical contact (which implies MCN+CCN) (b) Cohesion contact but not mechanical contact (c) No contact

7.6 Interplay between cohesion and hydrodynamic forces

Typical forces acting on a gas fluidized particle in Geldart A regime are shown in the figure 7.6. Geldart A fluidization is governed by interplay between inter-particle and hydrodynamic interactions [Yu and Xu, 2003]. An analysis of these forces is crucial to a basic understanding of the phenomenon and to link these interactions to macroscopic bulk behaviour. 2D DEM-CFD study of expanded bed by Yu and Xu [2003] found that

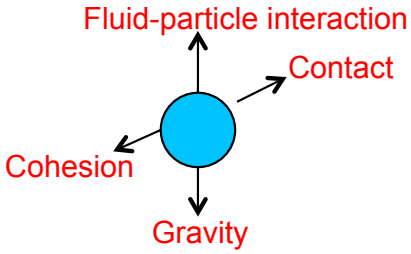

Figure 7.6: Typical free body diagram of a Geldart A particle.

the interaction forces between particles balances each other and hydrodynamic forces are balanced by gravity. Similar conclusion was found for a 3-D bed by Hou *et al.* [2012]. Two force balance modes: Simple and complicated, were identified in the study [Hou *et al.*, 2012].

Hou *et al.* [2012] calculated effective contact forces (f_{ec}) as $f_{ec} =< |\bar{f}_c| > - < |\bar{f}_v| >$ to quantify interplay between the cohesion and contact forces interplay at the minimum fluidization velocity. Here $< |\bar{f}_c| >$ and $< |\bar{f}_v| >$ are the time and ensemble averaged contact force and van der Waals force respectively. $f_{ec}/(mg)$ variation with increasing inlet velocity was plotted and trend showed decrease of forces in the fixed bed regime and constant in the expanded bed regime by Hou *et al.* [2012]. In the present study, fluidization simulations on cohesive assembly (Bo_g = 1) are run for 2 seconds for different inlet velocities. Initial 0.5 seconds are discarded as unsteady states, contact and cohesion force pairs are extracted for steady state at 100 Hz and post processed to calculate time and assembled $< |\bar{f}_c| >$ and $< |\bar{f}_v| >$. For a particular time-step, vector sum of all the contact forces on each particle is added and magnitude calculated as $f = \sqrt{f_x^2 + f_y^2 + f_z^2}$. This force is averaged over all the particles. Time and ensemble average on particle is defined as $< \bar{f}_i > = (\int_{t_1}^{t_2} \sum_{i=1}^{N} f_i/N dt)/(t_2 - t_1)$. Figure 7.7 plots time and ensemble averaged contact and cohesion forces for Bond number 1 case. Similar trends were found for other Bond number cases and not shown here. In the fixed bed regime, with increasing velocity contact force $< \bar{f}_c >/mg$ is observed to be decreasing until $U = U_{mf}$. This prediction is consistent with the 2D DEM-CFD studies by Yu and Xu [2003] and pseudo 2D studies by Hou *et al.* [2012]. In the expanded bed regime $U_{mf} < U < U_{mb}$, contact force $< \bar{f}_c >/mg$ is constant but is reduced considerably from fixed to expanded bed. However, time and ensemble averaged cohesion force $< \bar{f}_v >/mg$ is constant in the fixed and expanded bed regime (figure 7.7). During the bed expansion, the particles are coordinated due to adhesive forces holding them together. Reduced $< \bar{f}_c >/Mg$ in the expanded regimes suggests that particles are in mechanical contact but with a minimum overlap. Ratio of $< \bar{f}_c >/mg$ and $< \bar{f}_v >/mg$

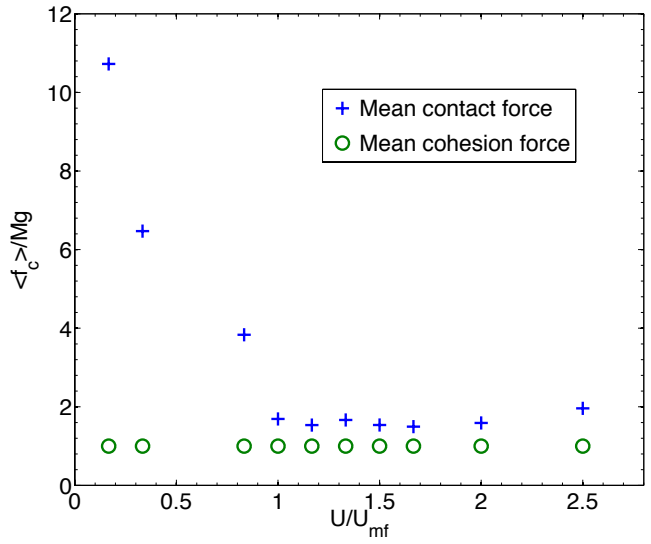

Figure 7.7: Mean cohesion and contact forces plotted for different normalised inlet velocities for Bond number 1. For cohesion plots, forces belonging to only strong cohesion network are averaged.

is almost 1 in the expanded bed regime. This is consistent with previous findings of Yu and Xu [2003] suggesting that expanded bed regime is formed according to an interplay between cohesion and contact forces. Next sections will discuss distribution of these forces that would provide further insights into contact and cohesion networks and force transmission through them.

7.7 Force distribution in weakly cohesive fluidization regimes

Force analysis of weakly cohesive fluidization regimes in the previous studies [Hou *et al.*, 2012; Yu and Xu, 2003] were done at bulk level and failed to address more complex force balance played at the particle level. A careful investigation is required by distinguishing between strong and weak force networks and identifying role played them in the force transmission that leads to expanded bed stability. Experimental evidences by analysing stable expansion by diffusion wave spectroscopy (DWS) have indicated that the forces are transmitted through enduring particle contacts [Menon and Durian, 1997*b*]. In a fixed bed, particles are under stress owing to their own weight. The contact forces decay exponentially and only a fraction of particles take the whole bed weight Mueth *et al.* [1998]; Peters *et al.* [2005]. It is interesting to study the force distribution in the expanded bed regime which gives similar solid like appearance as a fixed bed.

Aim of this section is to investigate contact and cohesion force distribution in weakly cohesive fluidization regimes. The force magnitude distribution can give a better insight

into complicated force transmission through contacts. In totality, macroscopic force distribution trends would be studied in a better light by distinguishing weak and strong force networks and analysing their contribution to the fluidization dynamics.

7.7.1 Force magnitude distribution

Force distribution in static and quasi-static cohesionless granular systems is well studied and understood [Antony, 2000; Blair *et al.*, 2001; Mueth *et al.*, 1998; Radjai *et al.*, 1999; Silbert *et al.*, 2002]. Weak force network can be identified with criterion on normalised contact force f. Here f is defined as F/F_{avg}; F_{avg} is the bulk averaged force for the assembly and F is the interaction force between a pair. A pair is considered in a weak force network by criterion: $f < 1$ and in strong force network otherwise. Alternatively, f_{cut} is defined as a threshold to differentiate between the strong and the weak force contacts for analysis purposes in later sections. It should be noted that contact network is a sub-set of cohesion network as all the particles in mechanical contact are also in cohesion network with maximum van der Waals force. In a fixed granular bed, contact force magnitude distribution have a exponential decrease for larger contact forces [Silbert *et al.*, 2002]. Force contact network is complex and it is known that in static granular assemblies, bulk of the assembly is only carried by 20% of the contacts present [Mueth *et al.*, 1998]. The rest of the contacts forms just a support network. Present study aim to understand coordination of the strong force network in different fluidization regimes.

Figure 7.9a plots the distribution of contact force magnitude $P(f)$ for different fluidization regimes at $Bo_g = 1$. X-axis plots the contact force magnitude normalised by the bulk average contact force magnitude, while Y axis plots the distribution. DEM data is filtered for initial 0.5 seconds is discarded as a transient phase. After 0.5 s of simulation run, all the time steps accumulated for the fluidization simulations of U/U_{mf}= 0.1, 1.4 and 2.5, The inlet velocities represent fixed, expanded and bubbling bed respectively. Fixed granular bed shows a typical granular media contact force distribution with tailed exponential decay of forces. These findings are consistent with previous experimental and simulations studies by Mueth *et al.* [1998]. The distribution function $P(f)$ can be fitted according to equation $P(f) = a(1 - be^{-f^2})e^{-\beta f}$, with $a = 2.9$, $b = 0.75$ and $\beta = 1.8$. Figure 7.9b shows a peak around the $f = 1$ in the expanded bed contact force distribution indicating that the contact forces are very evenly distributed. This trend is significantly different from the fixed bed distribution function which shows an exponential decay. It should be further noted that averaged contact force (F_{avg}) is very different for a fixed and an expanded bed (figure 7.7). The difference between the distribution of contact forces is very counter-intuitive as the averaged MCN was found to

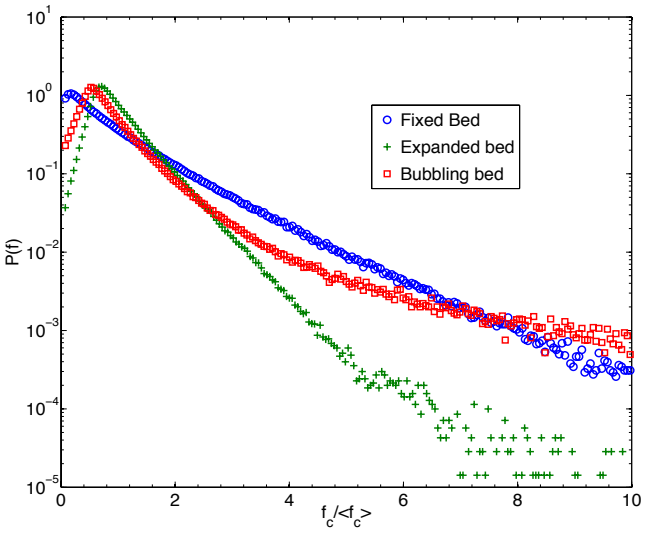

Figure 7.8: Distribution of contact forces P(f) at bond number 1 and different normalised inlet velocities U/U_{mf}: 0.1 (Fixed bed), 1.4 (Expanded bed) and 2.5 (Bubbling bed).

be similar for fixed and expanded bed (figure 7.4a). In appearance, both the fixed and the expanded bed looks static with immobile particles. An even distribution of contact forces around a mean implies that a clear distinction between strong and weak force network might not be readily distinguishable.

Bubbling bed contact force distribution is very similar to the expanded bed except that the larger forces decays at a much slower rate. Similar distribution of cohesion force was plotted and it was found that just more than half of the cohesion contacts (53%) have maximum possible van der Waals force. These cohesion contacts are mechanical contacts with maximum van der Waals forces (not a function of overlap). It should be noted that the cohesion forces decrease fairly rapidly with an increase in separation when particles are not in contact. In fact, these 53% of cohesion contacts carries 99% of total cohesive forces present in the system. Rest of the 47% cohesion contacts contribute just 1% to the cohesive interactions. This essentially means that cohesion forces between non=contacting particles can be safely neglected to save storage and computational time.

Figure 7.9 plots contact force distribution with different Bond number assemblies. Increasing cohesive strength increases the magnitude of contact forces (figure 7.7) but does not change the distribution trend for f. Since no variation in contact force distribution plots is observed with an increasing Bond number, from now on expanded characterisation would be based on post processing of fluidization regimes with $Bo_g = 1$.

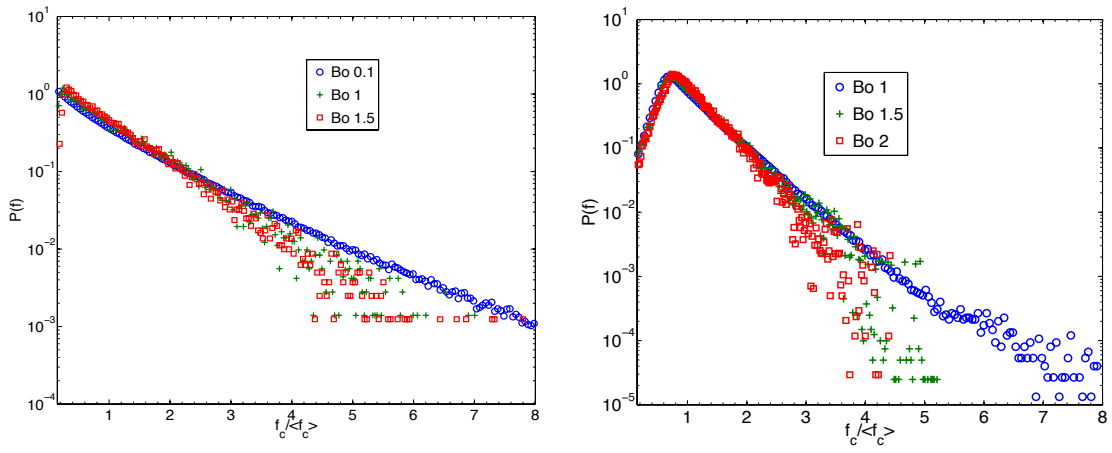

(a) (b)

Figure 7.9: Distribution of contact forces $P(f)$ for (a) Fixed bed regime ($U/U_{mf} = 0.1$) (b) Expanded bed regime ($U/U_{mf} = 1.4$). The legend indicates different Bond numbers varying from 0.1-2. Fixed bed regime corresponds to effect of cohesion in a static granular bed assembly and Expanded bed regime plots indicates that contact forces decay more rapidly and are skewed around the mean.

7.7.2 Contact Networks for fluidization regimes

Distinction between strong and weak forces is important for understanding complex network of granular materials. Such an understanding lead to a previous idea that the bulk of the particles carry weaker forces and act just a support network [Socolar *et al.*, 2002] in a static granular bed. However, Silbert *et al.* [2002] showed for a frictional granular packings that 50% of contacts carry 80% of the forces in the system. It was argued that although strong contact force network is apparent but its not very safe to neglect weak forces as a support network. This section will investigate a similar contribution percentages of the weak and strong contact forces in different fluidization regimes. Figure 7.10 plots the fraction of the bonds with the contact force greater than the threshold cut off f_{cut} and the percent of the forces carried by those contacts.

Left Y axis is the percentage of the contacts with the contact forces (f) greater than the f_{cut}. For example for a fixed bed plot (7.10a), 1% of the contacts can be inferred to have contact forces greater than 5 times the average contact force present. Right Y axis plots the force contribution of these pairs bearing contact forces greater than the threshold limit f_{cut}. For example for a fixed bed plot (7.10a), $f_{cut} > 5$ means that all the pairs carrying force greater than the 5 times the bulk average bear around 10% of the total forces. Figure 7.10a corresponds to the fixed bed regime for $Bo_g = 1$ and $U/U_{mf} = 0.1$. The decay in the fraction of bonds is very rapid with 85% of the contacts corresponding to $f_{cut} = 2$. This is set as the distinction limit for strong and weak forces for the fixed bed regime. It is noted that in the fixed bed regime, less than 1% contact

contain $f > 5$ contact strength and 50% or more have contact strength $f < 1$. These statistics indicates that DEM-CFD simulations are able to capture the presence of strong and weak forces within static and quasi-static granular systems as previously inferred by Silbert *et al.* [2002]. This further serves as a validation of DEM-CFD simulations to reproduce Geldart A regimes.

As already pointed out from last section, the contact forces are more distributed in the expanded regime. Figure 7.10b points out that the percentage of contacts with $f > 1$ is much greater than the corresponding plot for the fixed bed number of contact distribution (7.10a). In an expanded bed, almost 50% of contacts carry similar percentage (60%) of the contact forces as opposed 85% observed in the fixed bed regime. The curve indicates that a distinction between weak and strong forces is not very clear for the expanded bed regime. Even though expanded bed gives a solid-like appearance, the force network is very different from the fixed bed and similar to a bubbling bed. This indicates that the mechanical state of the bed is more fluid-like than the solid-like.

Recalling plots for coordination number v/s inlet velocity indicated that MCN is similar for fixed and expanded bed regimes (figure 7.4. This means that for in expanded bed, particles are still in contact, with lesser overlaps than the fixed bed regimes. The particles are just bind together by the adhesion forces with minimum overlap which explains why coordination number does not change but the contact force distribution and magnitude changes significantly. These bonds are kept together by the adhesive cohesion forces between particles until $U > U_{mb}$. Hence, the average cohesion magnitude (figure 7.7) remains same with increasing inlet velocity transcending from fixed to expanded regimes. A change in cohesion coordination number with increasing velocity could be due to weak cohesion bonds that are between non-contacting particles within the sphere of cohesion influence. These non-mechanical cohesive bonds exhibit a very weak attraction and gets broken easily by the hydrodynamic interactions even in the regime $U < U_{mb}$. This is well reflected in the plots for averaged CCN with increasing inlet velocity (figure 7.4b). Results from figure 7.10 and figure 7.9 further adds to the conclusion that the particles were in clusters and held together by cohesion forces with very low contact forces between them. Any break in the structure (as seen from cohesion and solid fraction plots) due to hydrodynamic interaction would at weak cohesion bond. Next section would try to re-interpret coordination numbers based on understanding of weak and strong forces in the fluidization regimes.

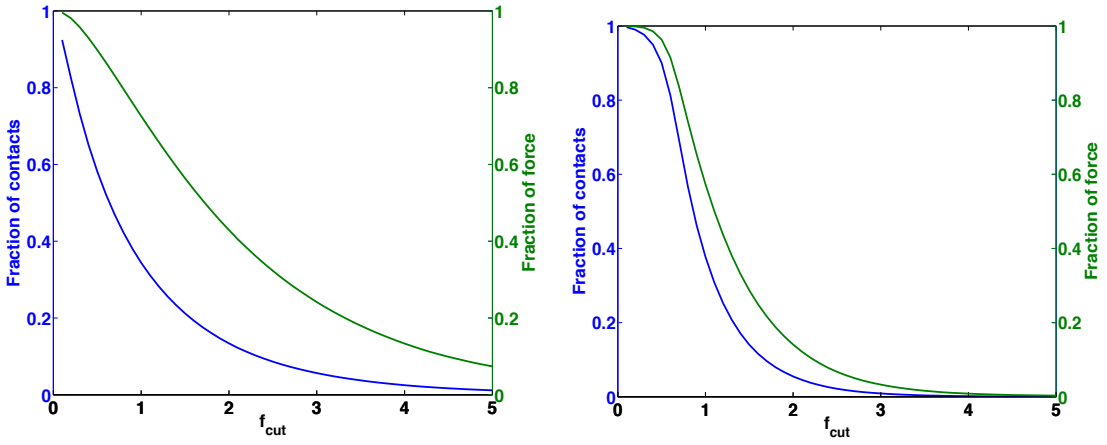

(a) (b)

Figure 7.10: Contribution to the average contact force and the fraction of contacts accounting for those forces, plotted versus threshold force for (a) Fixed bed regime (Bond number 1, $U/U_{mf} = 0.1$) (b) Expanded bed regime (Bond number 1, $U/U_{mf} = 1.5$), Blue line is the number of contacts with forces greater than the average

7.7.3 Coordination Numbers for particles with strong force contact network

Previously it has been shown that in granular systems, particles in the strong contact force network are minimally coordinated [Cates *et al.*, 1998]. Figure 7.11 shows the coordination numbers of particles which are within the strong force contact network determined by $f > f_{cut}$. Force networks are pre-processed according to criterion $f > f_{cut}$ and then post processed to calculate coordination numbers. For a contact force network, f magnitude varied from 0-10 but with different distributions for fixed and expanded bed regime. However, for a cohesion force network, it was noted that the 53% of the contact have maximum van der Waals force. Rest of the normalized cohesion forces varied from O(-1) to O(-6). For this reason, the cohesion F_{cut} is plotted on an logarithmic scale.

For the fixed bed regime, particles with contact network $f > 2$ are coordinated strongly with averaged MCN around 2.2. Expanded bed statistics earlier suggested that particles are clustered with contact forces distributed and there is no clear distinction between the strong and weak networks. Expanded bed plot is similar to the fixed plots with MCN rapidly decreasing with increasing f_{cut}. For $f_{cut} = 4$, which have contact fractions of less than 1% is seen to have MCN = 1. This indicates that the particles are minimally coordinated mechanically in the strong force network.

CCN plots are shown in figure 7.11b. scale for f_{cut} varies from O(-6) to O(1). CCN rapidly decreased from around 9 to 5.3 for weak cohesion contacts. Weak cohesion

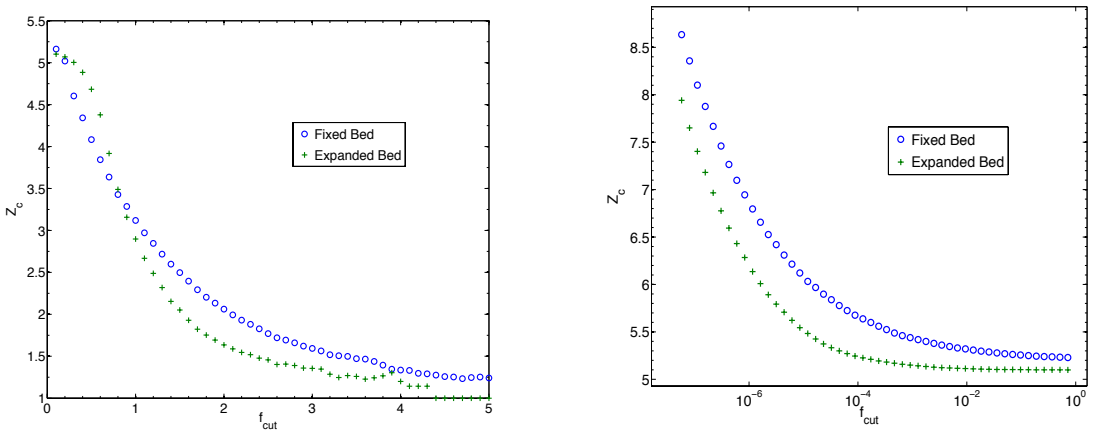

(a) (b)

Figure 7.11: Coordination number for fixed and expanded bed fluidization regimes as a function of f_{cut} for (a) Mechanical contact network (b) Cohesion force network. Pairs with $f > f_{cut}$ are considered in the calculations of the coordination numbers.

contacts are the contacts which are not in mechanical contacts. It is here pointed out that after the cohesion coordination number for $f_{cut} = 1$ is same as MCN with $f_{cut} = 0$ (5.3). This is consistent for both the fixed and expanded regimes. This means that the mechanical contacts, irrespective of the strong or weak network (indicated by $f_{cut} = 0$), are same as cohesion contacts carrying bulk of the cohesion forces. Furthermore, figure 7.11b indicates that $S_{max} = 1.25d$ can be significantly reduced for modelling purposes, without affecting the dynamics of the system and saving computation time with hard disk space for storing cohesion contact data.

7.7.4 Voronoi volume analysis

Microstructural studies at different length scales (CCN, MCN and ϕ_m) identified agglomeration of particles in the expanded bed regime. This section would employ another statistical tool: Voronoi cell volume analysis to quantify the local structure. As defined in the section 7.3, Voronoi diagram is a spatial discretization subjected to the condition that each point on the Voronoi cell is closest to the particle it encloses than any other particle [Tagawa *et al.*, 2012]. Three-dimensional Lagrangian Voronoi analysis for clustering of particles and bubbles have been previously employed in lean turbulent multiphase flows to study preferential flows of heavier or lighter particles [Mercado *et al.*, 2012; Nilsen *et al.*, 2013; Tagawa *et al.*, 2012]. The solid fraction (ϕ_{av}) of the domain was as low as 10^{-4}. The probability density functions (p.d.f.s) of the Voronoi cell volumes were compared with randomly distributed particles to quantify clustering. The standard deviation of the p.d.f. normalized by that of randomly distributed particles was used as a parameter to study deviation from randomly distributed assembly.

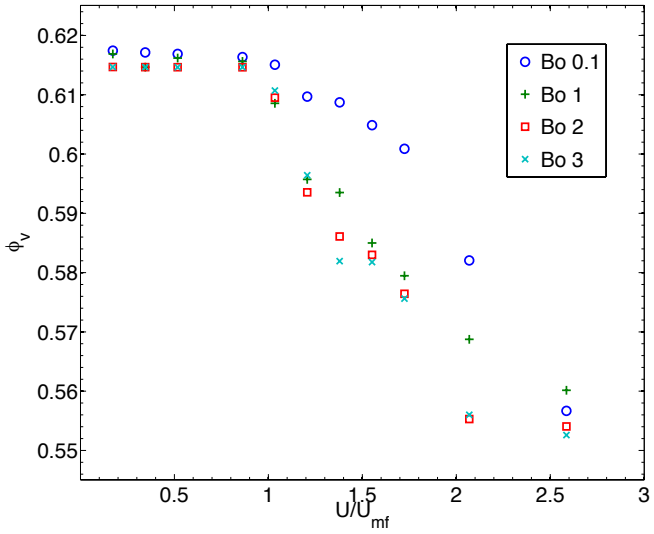

Figure 7.12: Averaged local concentration (calculated from as particle volume divided by the Voronoi cell volume) plotted with increasing inlet velocity at different bond numbers

Γ distribution function was found to fit Voronoi cell volume distribution almost perfectly for simulated data in a lean phase flow [Tagawa *et al.*, 2012]. Voronoi volumes ranged over 3 orders of magnitude in these studies. However, dense granular flows with high-volume fraction (0.60) are more difficult to quantify by Voronoi volume distribution method. Voronoi volumes are expected to be very narrowly distributed as particles are closely packed. kGamma distribution for Voronoi cell volume was proposed for dense granular flow by Aste *et al.* [2010]. It was concluded that distribution with a scaling parameter, which is dependent on the variance of the data, fits remarkably well to experiment and simulation data and no adjustment of parameters was required. This distribution was based on the hypothesis that there is a degree of freedom 'k' (which was found to be around 11-13) associated with Voronoi volumes and force transmission could be related to k. Such a hypothesis lacked a fundamental framework to explain a very complicated force transmission. In the present study, Γ distribution function will be employed to fit the simulated data.

Objective of the present study is to quantify clustering with respect to randomly generated cohesion less static geometry of particles. The effects of cohesion on clustering in fixed, expanded and bubbling fluidized bed would be studied. This study would give direct evidence of clustering at microscopic level examined with microstructural quantities such as CCN and MCN before.

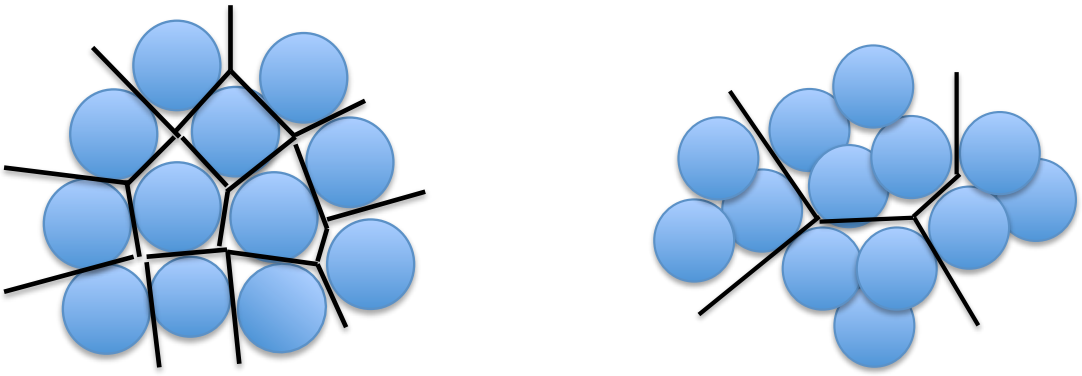

(a) (b)

Figure 7.13: Illustration of Voronoi tessellation for a fixed bed narrow distribution for Voronoi cell volumes and for a wider distribution for expanded bed when clusters have formed. Figures are only for demonstration purposes and not actual Voronoi tessellation.

7.7.5 Local concentration (ϕ_v) plotted with inlet velocity

Local concentration (ϕ_l) is calculated as particle volume divided by the volume of the Voronoi cell enclosing it. ϕ_l is the most local microscopic concentration for particle, as it is calculated on the free volume of a single particle. DEM-CFD Simulations are run by fluidization procedure 2, as mentioned in the section 6.2.3. For each inlet velocity and Bond number, 2 seconds of simulations are run and initial 0.5 seconds removed. Voronoi volume for each particle is calculated for every time step outputted and then averaged over number of particle and time to calculated ϕ_v. Figure 7.12 plots ϕ_v calculated for different cohesive strength bed (quantified by the Bond number) at different inlet velocities. Voronoi calculations for particles on open surfaces are ill-defined and are removed from the calculations beforehand. Figure 7.12 indicates decreasing ϕ_v in the expanded bed regime (U/U_mf >1). The spatial resolution of Voronoi calculation can be calculated as $(V_v/V_p)^{1/3}$, where V_v is the averaged Voronoi volume and V_p is the particle volume. A typical value is calculated in a dense regime as 1.17 times diameter of particle. It is noted that ϕ_v is more local calculation than CCN, which was calculated on 1.25 times diameter of particle. The Voronoi volume plot shows same qualitative trends as CCN and ϕ_{av} but different trends from MCN. This evidence further suggests that the inter-particle contacts are not broken and instead agglomerates are breaking into forming cavities during the expansion phase. A further conclusion can be made that agglomerate chain is upto the neighbouring contact and doesn't extend beyond it.

7.7.5.1 Density functions

Local concentration distribution function for different fluidization regimes is plotted in the figure 7.14. Fixed bed regime has a very narrow distribution around the mean

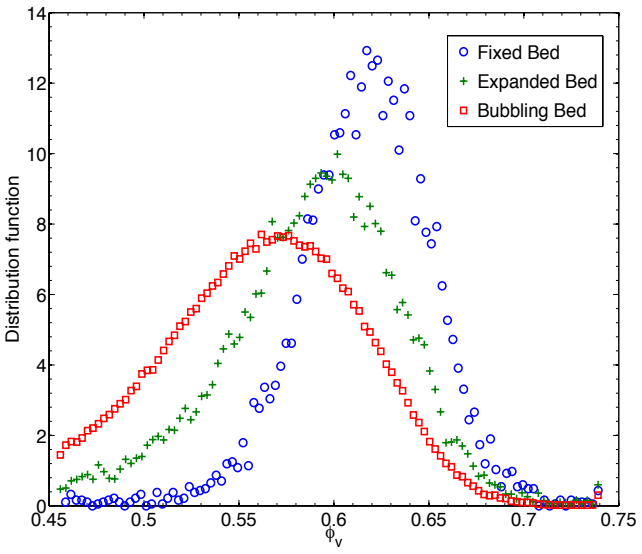

Figure 7.14: Distribution of local concentration (ϕ_l) in different fluidization regimes. DEM-CFD simulations are conducted for Bond number 1 and U/U_{mf} = 0.1,1.4 and 2.5 for fixed, expanded and bubbling bed respectively. Expanded bed regimes indicates that, even though magnitude of the peaks are similar, but the Voronoi volumes are quite widely distributed than the static or the fixed bed

packing fraction of a static cohesive granular assembly. Expanded and bubbling bed distribution is distributed widely across a lower local concentration. This is expected for expanded bed to have a lower mean local concentration than the fixed bed. Wider distribution is indicative of particle agglomeration and clustering, as smaller and higher Voronoi volumes are more probable in a clustered solid-like bed. This preferential clustering is clearer in an expanded bed regime where hydrodynamic interaction breaks the weaker cohesion contacts. However, fluid forces are not able to penetrate stronger cohesive contacts forming a cluster. Figure 7.13 demonstrates that the clustering of particles leading to a wider distribution of Voronoi volumes in expanded bed.

Figure 7.15 fits a Γ distribution function to the Voronoi distribution of different fluidization regimes with a variable $V = (V_v - V_{min})/(< V_v > - V_{min})$ normalised by its mean. Here, V_{min} is the smallest possible volume that a Voronoi cell could have, estimated as $0.693d^3$ and $< V_v >$ is the averaged Voronoi volume [Aste *et al.*, 2010]. Standard deviation (σ_o) for a cohesion less static geometry is calculated as a base case where clustering effects are not due to cohesion and hydrodynamic interactions. σ is calculated for Γ distribution for different fluidization regimes with increasing inlet velocities. Figure 7.16 plots the normalised standard deviation (σ/σ_o) with inlet velocities at different Bond numbers. The plot indicates that the normalised standard deviation is 1.2-1.4 times more for expanded bed regimes than the fixed bed regimes which quantifies agglomerate formation and cavities as evident from the local concentration plots.

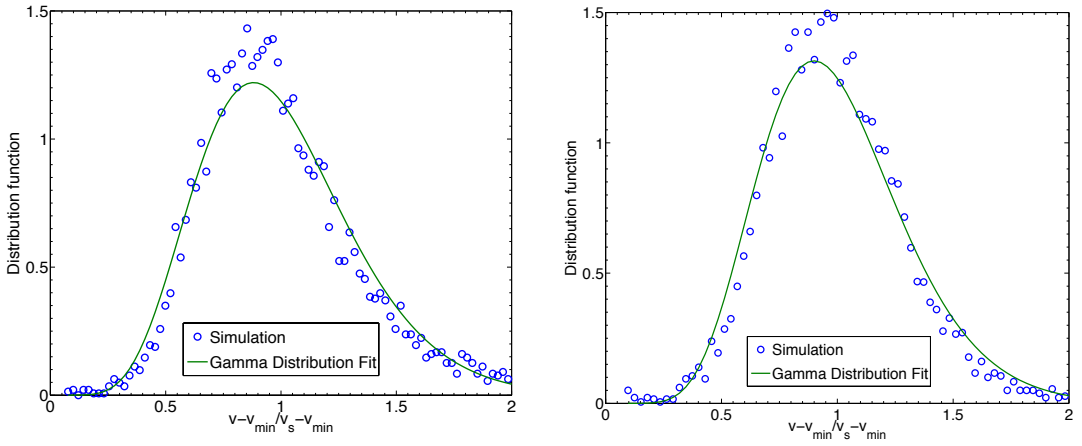

(a) (b)

Figure 7.15: Γ distribution fit for Voronoi volume for (a) Fixed bed (b) Expanded bed, with variable $V = V_v - V_{min}/ < V_v > -V_{min}$, normalised by its mean value. Here V_{min} is the smallest possible volume Voronoi cell could have, estimated as $0.693d^3$ (Aste *et al.* [2010] and $< V_v >$ is the averaged Voronoi volume.

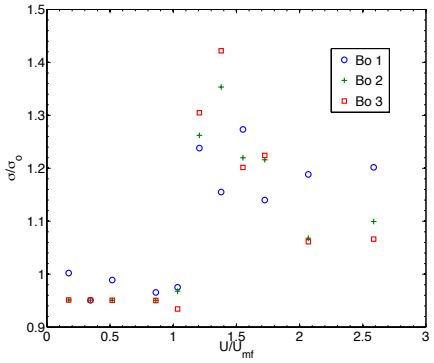

Figure 7.16: Normalised standard deviation plotted for increasing inlet velocity for different bond numbers. σ_o is the standard deviation of the distribution plot for fixed bed simulation of cohesion less granular static bed. Voronoi cell volume distribution is fitted with Γ distribution as explained in earlier figures.

This further validates the claim of preferential clustering in the expanded bed regime as an interplay between hydrodynamic and adhesive forces.

7.8 Conclusion to chapter

In this chapter, microstructural characterization of expanded bed regime was presented at different local length scales. Different microstructural tools studied are:

- Mechanical Coordination Number (MCN): Average number of meachanical contact per particle.

- Cohesion Coordination Number (CCN): Average number of cohesion contact per particle.
- Coarse grained solid fraction (ϕ_{av}): Particle concentration at the mesoscopic volume.
- Local solid fraction (ϕ_l): Local particle concentration based on the Voronoi cell tessellations.

The relevant length scales of the microstructural quantities are indicated in the figure 7.2. Fluidization procedure 1 was employed)(6.2.3) to study transition of averaged microstructural quantities from one regime to another and DEM data from procedure 2 was post-processed to characterize the expanded bed. Following note-worthy conclusions from this chapter are listed here:

- Variations of averaged solid fraction (ϕ_{av}), mechanical and cohesion coordination number (MCN and CCN) with increasing inlet velocities suggested agglomeration or cavities in the expanded bed regimes. It is concluded that the expanded bed expansion is not homogeneous with mesostructural inhomogeneities present.
- Fixed bed regime was identified to have a strong contact force network and just 20 % of strong force contacts could carry upto 70 % of the bed. Expanded bed had no such distinction, contact force distribution was even throughout the expanded bed. It was noted that, even though mechanical bonds were not broken in transition from fixed to expanded bed, but the magnitude of contact forces decreased to zero. It is further noted that the strong force network is minimally coordinated. Contact force distribution in an expanded bed is similar to the distribution in the bubbling bed indicating that the mechanical state of the expanded bed is more fluid-like.
- In the expanded bed, particles are in mechanical contacts but with minimal overlaps are just bind together by the adhesion forces. These bonds are kept together by the adhesive cohesion forces between particles until $U > U_{mb}$. Onset of bubbling is marked by the hydrodynamic forces able to break this cohesive bonds. This study brings out important role played by cohesive forces to suppress bubbling and formation of the expanded bed.
- Mechanical contacts formed a big part of the cohesion networks as well. It was noted that the mechanical contacts with the maximum cohesion forces are far more influential in governing dynamics than weak cohesion pairs that are not in mechanical contact.

- $S_{max} = 1.25d$ can be significantly reduced without affecting the dynamics of the system. It is further suggested that van der Waals model can be integrated to the contact model. A constant cohesion force equal to maximum van der Waals force can be given to each mechanical contact. This will save considerable computational time with hard disk space for storing cohesion contact data.

- Γ distribution function fits to the Voronoi distribution of different fluidization regimes with variable $V = V_v - V_{min}/ < V_v > -V_{min}$ normalised by its mean. Normalized standard deviation (σ/σ_o) is used to quantify clustering. It is found that the normalised standard deviation is 1.5 times more for expanded bed regimes than fixed bed regimes which quantifies agglomerate formation and cavities as evident from the local concentration plots. This validated the claim of preferential clustering in the expanded bed regime which are formed as an interplay between hydrodynamic and adhesive forces.

Chapter 8

Expanded bed: Stability and onset of bubbling

8.1 Introduction

Differences in liquid-solid and gas-solid fluidization behaviour is well established in literature. It is a general understanding that homogeneous bed expansion with increasing flow rate is a liquid-solid fluidization characteristic and bubble or slugs formation are associated with gas-solid fluidization at the onset of fluidization. These observations form just a part of complete fluidization spectrum first presented by Geldart [1973] and experimental evidences often pointed that even gas can fluidize a granular bed to homogeneously expanded bed [de Carvalho, 1981; Donsi and Massimilla, 1973]. However, much before Geldart [1973] distinguished between bubbling (aggregate) and non-bubbling (particulate) fluidization regimes by empirically relating particle and fluid properties to bulk behaviour, criterion on Froude number ($Fr_m = U_m^2/gd_p << 1$) was used to predict whether a granular bed would bubble or not [Wilhelm and Kwauk, 1948]. Both of these attempts to predict bubbling were based on experimental observations and could not establish a fully predictive criterion for transition from particulate to aggregate fluidization behaviour. Experimental findings on prediction of minimum bubbling conditions (U_{mb} and ϕ_{mb}) were mostly confined to limited operating conditions and particle properties [de Carvalho, 1981; Donsi and Massimilla, 1973]. Visual inspection was the only means to establish if a bed is bubbling or not.

For a more theoretical derivation of criterion to predict bubbling, linear stability theory was applied to the continuity and momentum equations by introducing small perturbations in the steady state voidage or particle velocity field. However, such analysis on

continuum momentum equations for gas fluidization process, showed it to be intrinsically unstable (Jackson [1963]). This theory essentially meant that hydrodynamic perturbations initiated by gas could only ramify into bubbles or slugs with the increase in the growth rate of these instabilities as wavelength tends to zero. A improvement over these non-physical predictions were soon followed by Anderson and Jackson [1967]; Pigford and Baron [1965] and a term representing viscous dissipation was added to the solid phase momentum equation, in order to correctly predict a bounded wavelength with increasing amplitude of instabilities. These predictions were contradicted by experimental observations of uniform stable expansion [Rietema, 1973; Rietema and Piepers, 1990]. A need of additional terms in the momentum equation was identified to explain the theoretical description and experimental evidences. Origin, form and the physics behind these extra terms has been much debated in the literature [Hou *et al.*, 2012]. An overview of this debate is presented in the literature review chapter of this thesis.

A generalized criterion to predict stability of fluidization based on wave propagations was first put forward by Wallis [1969] and later modified by Foscolo and Gibilaro [1987]; Gibilaro [2001]; Verloop and Heertjes [1970]. A concept of kinematic and dynamic wave propagation was introduced to explain the stability of uniformly expanded beds. Kinematic wave propagations are due to sudden changes in fluid flux, whereas sudden inertial changes lead to dynamic wave propagation. Each of these wave propagations depends upon the local structure of the expanded bed. The expressions of these would be presented in the later sections. The wave propagation theory was mostly developed under homogeneous structure assumptions. Based on propagation of these shock waves, criterion for the stability of the bed was established as ($u_D > u_K$), where u_D and u_K are the dynamic and kinematic wave velocities respectively [Wallis, 1969] . Predictions of u_D and u_K were modified to account for dynamic agglomerates with inclusion of granular Bond number and the agglomerate sizes by Millán [2012]. This chapter will study response of uniform expanded bed subjected to voidage and inertial shocks using DEM-CFD framework. Simulation results would be compared against theoretical predictions and effect of cohesion studied on the expanded bed stability. Following section elucidates aims and chapter structure and subsequent section will lay out literature and simulation methodology.

8.2 Aim of the chapter

In the last 2 chapters, DEM-CFD simulations were shown to be capable of capturing Geldart A fluidization behaviour by adding van der Waals model to the DEM force balance equation. In a granular assembly with $1 < Bo_g < 3$, fluid flux was suddenly

increased from 0 to U ($U_{mb} > U > U_{mf}$) resulting in an expanded bed regime and subsequently bubbling for ($U_{mb} < U$). Bed expansion can be studied by dividing into two stages: (1) incipient or start up phase (2) steady state phase. Incipient stage is an unsteady phase accompanied with wave propagation from bed bottom to the bed surface leading to a bed expansion but reaches a steady state when particles are immobile.

Chapter 5 characterized the steady state bed expansion with Richardson–Zaki correlation and ($U - \epsilon$) satisfied for an expanding bed and macroscopic particle velocities tending to zero. This chapter aims to capture unsteady aspects of expansion regime:

- Effect of cohesion and inlet superficial velocity change on kinematic wave propagation velocity (u_K), identified from DEM-CFD simulations presented in chapter 5.
- Reproduce dynamic wave propagation (u_D).
- Comparisons of predicted bubbling inlet velocity U_{mb} by DEM-CFD simulation with the theoretical predictions by Foscolo and Gibilaro [1984]; Valverde and Castellanos [2006].

8.3 Background and theory

8.3.1 Kinematic wave propagation

This section deals with the response of a static granular bed to a sudden influx of gas which results in the kinematic wave propagation. A fundamental assumption in formulation of wave propagation is that the steady state is a homogeneous state. This assumption might not completely hold true, as seen from chapter 7 of this thesis. It would be interesting to check the response of increased fluid flux on the local microstructure. A usual feature of gas-solid fluidization is that instabilities can develop from distributor plate and manifest fairly rapidly to form mesostructures leading to a heterogeneous bulk behaviour or to an homogeneous expansion. This section will focus on the situation when a stable expansion is found in the gas-solid fluidized bed.

The mechanism behind the stable bed expansion and the kinematic wave propagation was first explained by Foscolo and Gibilaro [1984]. Figure 8.1 illustrates the various stages of kinematic wave propagation when gas influx, subjected to a uniformly expanded bed, is suddenly increased from U_1 to U_2. In the present context, it should be assumed that inlet velocity U (U_1 or U_2) is in the range $U_{mf} < U < U_{mb}$. Figure 8.1a shows a steady bed state-1 at inlet velocity U_1 ($U_{mf} < U_1 < U_{mb}$) and bed porosity ϵ_1

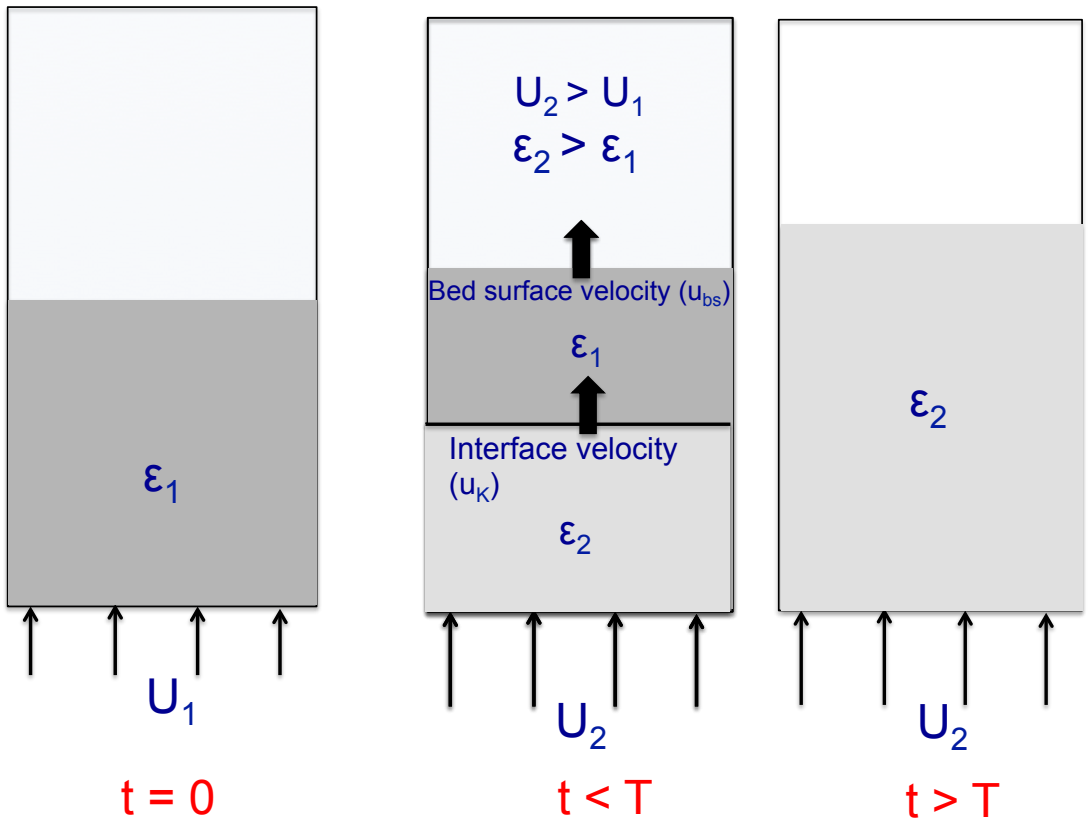

(a) (b) (c)

Figure 8.1: Idealized description of bed expansion and kinematic wave propagation, adapted from Gibilaro [2001]. T is the time required for the bed to reach the steady state after the kinematic shock.

(related by R–Z correlation Richardson and Zaki [1954]). Even though fluidized, bed gives smooth appearance and particles are immobile in the steady state.

At $t = (0 + \delta t)$, gas influx is suddenly changed from U_1 to U_2, such that $U_2 < U_{mb}$ and changes bed state from ϵ_1 to ϵ_2 ($\epsilon_2 > \epsilon_1$). A sudden increase of flux leads to an increase in hydrodynamic forces which further leads to an upward motion of particles. This manifests itself as an expanded bed with gradual decrease in particle concentration accompanied by a rise in the bed surface. This kinematic perturbation does not grow in amplitude and dissipates itself as it reaches the bed surface and a steady state 2 is reached. This final state is given by Figure 8.1c with steady state characteristics as (U_2, ϵ_2). The change from bed state-1 to 2 is gradual and accompanied by a wave propagation through the bed and rise in the bed height. It is reiterated that the state-2 is a steady state similar to state-1 again correlated by R–Z correlation.

To study intermediate stage, let us consider that this change in bed condition from

state-1 and 2 occur in finite time T. During this time, particles at the bottom of the bed accelerate first and pushes the disturbance to the rest of the bed giving a wave like appearance. Figure 8.1b, presents a bed state at a time t ($t < T$). As the particles accelerate up, bed can be divided in sections of higher (ϵ_2) and lower voidage (ϵ_1). Lower section would attain a porosity ϵ_2 (correlated to U_2 by R–Z correlation), and higher section is still at the initial steady state oblivious to the hydrodynamic changes occurring in lower section with initial porosity ϵ_1. Higher and lower voidage region interface travel from the distributor plate to the bed surface in time T and at time $t > T$ bed attains steady state-2 (U_2, ϵ_2) as shown in figure 8.1c, $t > T$. Interface travelling is identified as a kinematic shock wave and is accompanied by rise in bed surface and bed expansion.

Bed contraction is a process similar (as shown in figure 8.3) to expansion, except fluid influx is decreased ($U_1 > U_2$). Bed contraction and expansion are theoretically specular processes, however such a claim is questioned by Owoyemi and Lettieri [2008] pointing out that the bed contraction is stable while bed expansion is intrinsically unstable as lower porosity is at the bottom of the bed. The stability study by Owoyemi and Lettieri [2008] is based on purely hydrodynamic consideration and refutes the claim of adding solid stresses to the momentum equation to impart stability.

Wallis [1969] and Gibilaro [2001] explained kinematic disturbance propagation as a situation similar to one encountered in traffic engineering when a leading highway driver suddenly applies break [Lighthill and Whitham, 1955]. In order to maintain a constant head on distance between the vehicles, the next driver also applies break to avoid accident and this appears like a wave which propagates till the last driver in the lane. This is called a "traffic-concentration wave"which propagates at a constant speed from the first to last driver in the lane. However, this would present an ideal situation when no accident occurred and reaction times of each driver were fairly rapid to neglect any inertial effects. Local hydrodynamic changes are fairly rapid in the gas-solid fluidization processes and a assumption of constant speed propagation might not hold well.

Figure 8.2a and 8.2b gives the graphical representation of the bed surface rise and kinematic wave propagation during bed expansion and contraction, respectively. The bed height is plotted against the time t, ranging from kinematic shock wave initiation ($t = 0$, U suddenly changed from U_1 to U_2) to the time required for it to reach bed surface ($t = T$). Here, $L = 0$ is the distributor plate at the bottom of the granular bed; L_1 and L_2 are the steady state bed heights. Kinematic wave propagates from $L = 0$ to $L = L_2$ and the bed surface moves from L_1 to L_2 in time T. The slope of

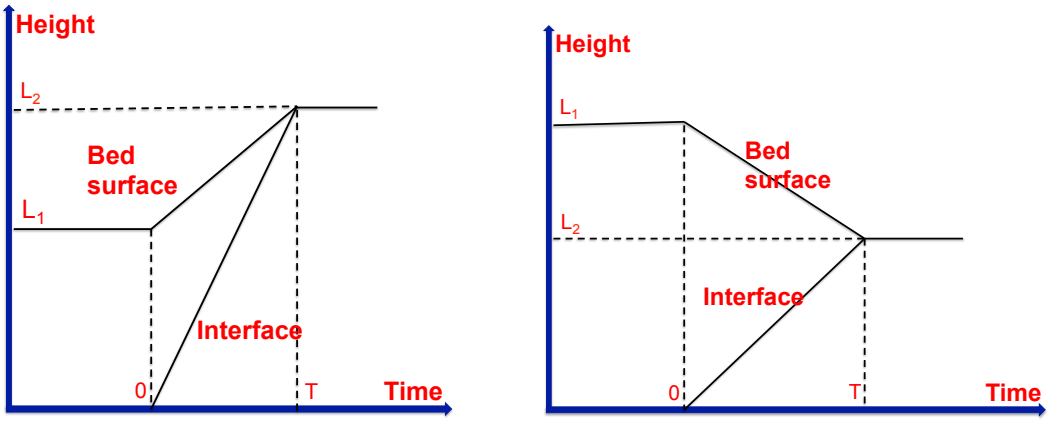

(a) (b)

Figure 8.2: Plot for height with time to describe kinematic wave propagation (u_K) and bed surface velocity (u_{bs} for (a) Bed expansion (b) Bed contraction. L_1 and L_2 are the bed heights at steady state 1 and 2 respectively. T is the total time for taken for bed expansion/contraction (adapted from Gibilaro [2001]).

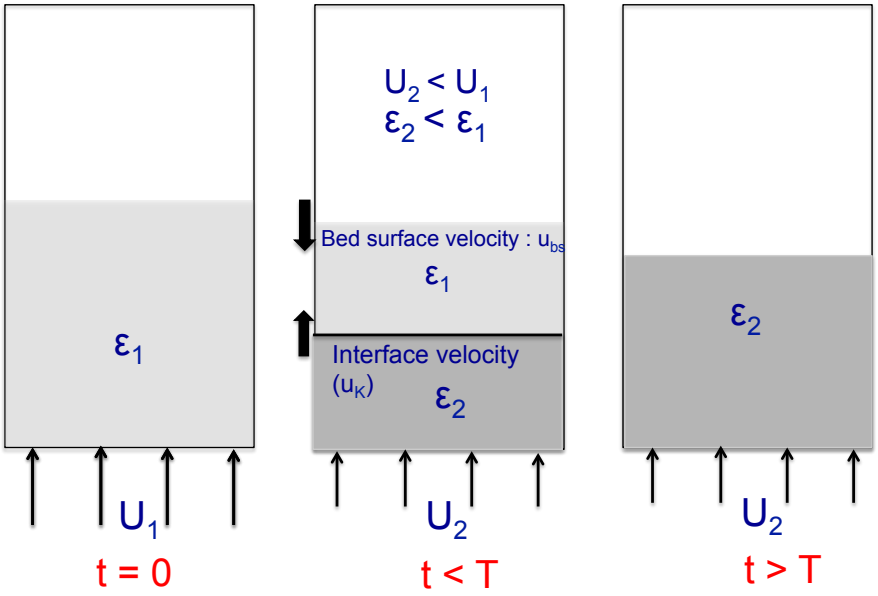

Figure 8.3: Idealized description of bed contraction and kinematic wave propagation, adapted from Gibilaro [2001].

these curves determine kinematic wave velocity (u_K) and bed surface velocity (u_{bs}). The expressions for these velocities in terms of the bed concentration and the inlet gas influx are given by equations 8.1 and 8.2 as presented by Foscolo and Gibilaro [1984]. Further details on the derivations of these equations can be found in chapters 4 and 5 of Gibilaro [2001].

$$u_{bs} = u_2 - u_1 \tag{8.1}$$

$$u_k = nu_t(1-\epsilon)\epsilon^{n-1} \tag{8.2}$$

where u_{bs} is the bed surface velocity, (u_1, ϵ_1) and (u_2, ϵ_2) are the steady state fluid inlet velocity and porosity at steady state-1 and 2, n is the R–Z correlation coefficient and u_t is the terminal velocity of free falling isolated particle (given by equation 6.13). ρ_p is the particle density, μ is the fluid viscosity, g is the gravitation constant, d_p is the particle diameter. u_t is correlated with n and Archimedes number Ar (given by equations 6.13 6.12, 6.11 respectively).

These predictions are theoretical and based on underlying assumption of uniform fluidization, Owoyemi and Lettieri [2008] further improved the kinematic wave velocity predictions by formulating a new drag closure and inclusion of elastic force term in the momentum exchange term. Inclusion of such a term is debated in literature but nevertheless resulted in a better prediction of stability criterion. These derivations of kinematic wave propagation velocity were done from purely hydrodynamic point of view and did not included inter particle force effects. A modelling approach for gas-solid fluidization of fine powders and was suggested by Valverde and Castellanos [2007*b*] which was an extension from liquid fluidization of non-cohesive particles and taking into account the effect of agglomerations. Although, Valverde and Castellanos [2007*b*] work was started for micron sized particles (used in this study) and later extended to the nano-powders successfully [van Ommen *et al.*, 2012]. A modified kinematic wave propagation expression by Valverde and Castellanos [2007*b*] is given by equation 8.3 which explicitly include the effect of cohesion in form of granular Bond number (Bo_g). The present work would attempt to reproduce the bed surface rise and kinematic wave propagation in a manner similar to theoretical works by Foscolo and Gibilaro [1987] using DEM-CFD methodology. The effects of cohesion will be included and u_K will be quantified by post processing DEM data and compared against the expressions by Millán [2012]; Valverde and Castellanos [2007*b*] given as,

$$u_{kb} = u_t(1-\epsilon)nBo^{2/(D+2)}[1-((1-\epsilon)Bo^{(3-D)/(D+2)})]^{n-1} \tag{8.3}$$

8.3.2 Dynamic wave propagation

Kinematic shock wave velocity formulation did not account for particle inertial response times, as seen in the previous section. In order to address stability issue, another velocity is defined to quantify inertial effect propagation through the system [Gibilaro, 2001] and is called dynamic wave propagation. These waves could be best understood as sonic waves that travel in the air as pressure waves as explained in Gibilaro [2001].

Gibilaro [2001] has explained the dynamic wave propagation with the help of figure 8.4. Dynamic waves are generated by bringing one particle layer closer to an upper adjacent layer rapidly and allowing this small compression to propagate throughout the system.

Consider an open cylinder with a piston under adiabatic conditions. If this piston is suddenly displaced upwardly, a sonic wave can travel as a pressure wave [Gibilaro, 2001]. This velocity expression can be given by 8.4 [Gibilaro, 2001], where P and ρ_f are the gas pressure and density, respectively. A similar experiment could be done with an expanded granular bed and distributor plate can be suddenly displaced upwardly to reproduce this wave propagation as seen in the figure 8.4. First layer of particle will come closer to the second layer and a decrease in voidage would result additional hydrodynamic force transmitted and lead to an inertial acceleration. This momentum exchange between the particles would be propagated to the top surface like an elastic wave. It should be noted that overall mechanism of wave propagation in the granular bed is different from that of sonic pressure wave. The expression for u_D is given by equation 8.5, where p is the particle phase pressure as a result of particle velocity fluctuations. The form of this expression for u_D is generally agreed upon in the literature as equation 8.5 but an expression for particle phase pressure ($p(\phi)$) as function of voidage or solid fraction (ϕ) is not [Guazzelli, 2004]. An expression for $p(\phi)$ for would account for p increasing with lower ϕ and decreasing for higher with a maxima in between [Sundaresan, 2003], hence a quadratic expression has been employed in the studies by Valverde and Castellanos [2007*b*]. Dynamic wave velocity expression was derived with underlying assumption that granular bed could be understood as a compressible fluid and given by equation 8.6 (for derivation of equation 8.6) from equation 8.5, refer to Gibilaro [2001]).

$$u_{SD} = \sqrt{\frac{\partial P}{\partial \rho_f}} \tag{8.4}$$

$$u_D = \sqrt{\frac{1}{\rho_p}\frac{\partial p}{\partial \phi}} \tag{8.5}$$

$$u_D = \sqrt{3.2 g d_p (1-\epsilon)(\rho_p - \rho_f)/\rho_p} \tag{8.6}$$

Through microstructural characterization of expanded bed in the chapter 6 and 7, it has been shown that the bed expansion is stable without mesostructural bubbling but not

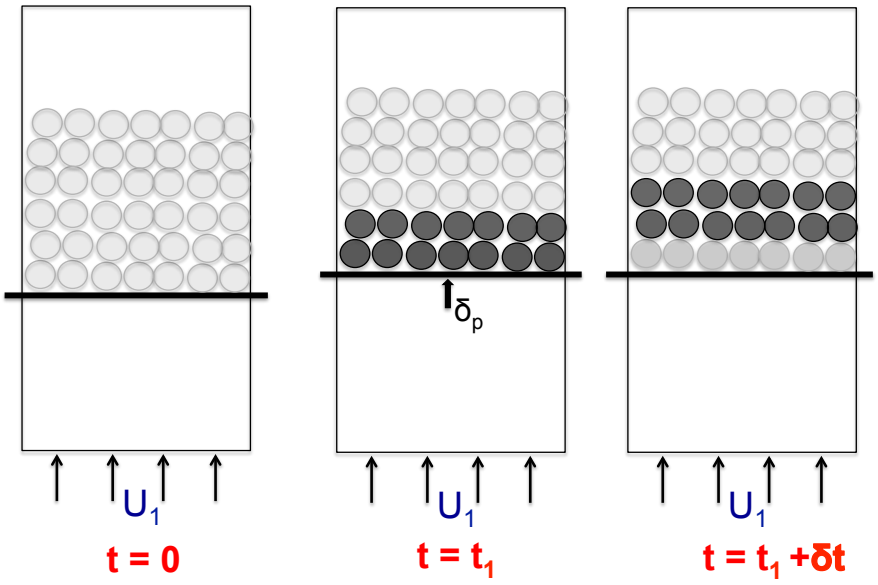

Figure 8.4: Idealized description of dynamic wave propagation when distributor plate is suddenly displaced up by distance δ_p, adapted from Gibilaro [2001].

homogeneous with the evidences of cavities and agglomeration. Furthermore, it should be pointed out that stable bed expansion caused due to cohesive stresses might only be a sufficient condition and not a necessary one. Simulations of gas-solid homogeneous fluidization in DEM-CFD framework, without including cohesive interactions are rare and even if reported, the underlying equations used are highly disputed [Hou *et al.*, 2012]. A significant gap remains to be covered to answer all these question regarding what is the underlying cause of this stable expansion and to what extent the bed can be considered as homogeneous. This brings out the significance of microstructural characterization done in chapter 7. Furthermore, force chains in fully fluidized expanded bed are very complex due to formation of agglomerates and the propagation of shocks might not be as idealized as presented in this section.

In order to account for the local structure difference present in an inhomogeneous but stable bed, Owoyemi and Lettieri [2008] pointed out that u_D calculations should also include local porosity along with the bulk porosity (ϵ). Fluid-particle drag closure derived in an earlier work [Mazzei, 2008] were based on similar principle and included a bed elasticity. Even though lacking a justification from a first principle derivation point of view, the expressions lead to a better predictive criterion for bubbling [Sundaresan, 2003]. Recently, u_D velocity formulation was further modified by Millán [2012]; Valverde [2013] to include effects of cohesion in terms of granular Bond number, similar to modifications done for kinematic wave velocity. The modified expressions for dynamic wave velocity (u_D^*) is given by equation 8.7. Bo_g is the granular Bond number

and D is a fractal dimension of the aggregates ($D = lnN/lnk$). Here, N is the number of particles in an aggregate and k is the ratio of aggregate to particle size. Furthermore, Bo_g and D can be related by equation 8.8 [Valverde and Castellanos, 2006].

$$u_D^* = \sqrt{g d_p (1-\epsilon) Bo_g^{(4-D)/(D+2)}} \tag{8.7}$$

$$Bo_g \sim Nk^2 = k^{D+2} \tag{8.8}$$

In the subsequent sections, steady state expanded granular bed would be subjected to sudden inertial effects by moving distributor plate by a distance $\delta = d/2$ using DEM-CFD simulations and the response will be recorded.

8.3.3 Stability criterion

After establishing theoretical calculations for u_K and u_D, the theory can be extended to give a predictive criterion on the stability of the bed: *the velocity of the dynamic wave must be greater than that of kinematic wave* [Gibilaro, 2001]. The idea is that, if the particle velocity fluctuations are more than the kinematic disturbance on the particle positions, then the bubbling can be suppressed. If inverse is true and the particle move around more freely, bubbling will occur. This stability criterion further establishes the granular temperature as an indicator to the bubbling as seen from chapter 6.

It should be further pointed out that theoretically smooth, non-bubbling fluidized bed behaviour should not necessarily imply stability [Koch and Sangani, 1999], an exception to this rule is fluidization of nano powders [van Ommen *et al.*, 2012]. To establish the stability criterion, even though [Foscolo and Gibilaro, 1984] invokes Wallis criterion Wallis [1969], Jackson [2000] proved that such a formulation is a mere algebraic rearrangement of linear stability analysis [Valverde, 2013]. It is noted here, that the applicability of linear stability analysis is much debated in the literature. However, its predictive capability is unquestionable for both liquid-solid and gas-solid fluidization behaviour. Experimental validation has been positive and lead to a general acceptance of the stability theory from the literature [Gibilaro, 2001]. Stability criterion for uniform fluidization can be simply expressed by: $u_D > u_K$ in its dimensionless form ($(u_D - u_K)/u_K = S$). Here, $S > 0$ indicates homogeneous expansion; $S = 0$ is the stability limit and $S < 0$ means bubbling fluidization. An expression for S can be given by equation 8.9 (Foscolo and Gibilaro [1984]) and is based on the underlying assumptions that transition of bubbling fully governed by hydrodynamic forces. The

theory was extended by Valverde [2013] and modified to include cohesion effects and stability criterion and S^* is given by equation 8.10.

$$S = \frac{1.79}{n}\left(\frac{gd_p}{u_t^2}\right)^{0.5}\left(\frac{\rho_p - \rho_f}{\rho_p}\right)^{0.5}\left(\frac{\epsilon^{1-n}}{(1-\epsilon)^{0.5}}\right) - 1 \tag{8.9}$$

$$S^* = 1 - 0.7n\frac{1}{160}\frac{\rho_p^2 g d_p^3}{\mu_f^2} Bo_g^{(2D-3)/(D+2)}\,(1-\epsilon)^{0.5}\,(\epsilon)^{n-1} \tag{8.10}$$

Here, d_p is the particle diameter; u_t is the terminal velocity for an isolated particle (defined earlier by equation 6.13); n is the R–Z coefficient (equation 6.11); Ar is the Archimedes number (given by equation 6.12); g is the gravitational constant; ϵ is the porosity of the bed at the onset of bubbling; ρ_p and ρ_f are particle and fluid density respectively, Bo_g is the granular bond number, D is the fractal dimension defined earlier.

8.4 Simulation set-up and methodology

DEM-CFD simulation parameters, geometry, mesh size and hydrodynamic parameters are same as used in the last chapter and are enlisted in table 6.1. From chapter 6, it has been identified that cohesive granular beds with the Bond numbers (Bo_g) ranging from 0.5 to 3 could reproduce an expanded bed regime with inlet velocities U/U_{mf} ranging from 1 to 2.5. This understanding would be used in this chapter to simulate the kinematic wave and dynamic wave propagation.

Kinematic wave propagation simulations require a sudden influx of inlet velocity in the region $U/U_{mf} = 1.1 - 2.0$. For initial 0.1 seconds inlet velocity was kept 0, at which point fluid flux was increased suddenly to U_2 ($U_2 < U_{mb}$). This lead to an unsteady transient wave propagation from bottom to the top surface of the bed leading to a bed surface rise and expansion, after which bed was in an *expanded bed state* with immobile particles. After 1.0 seconds of simulation time, fluid influx was again suddenly dropped to 0 in order to capture bed collapse wave propagation and simulations were allowed to run for another second. This was done for each cohesive bed simulation with Bo_g ranging from 0.5 to 3, U_1/U_{mf} ranging from 0 to 1 and U_2/U_{mf} ranging from 1-2.5.

Another set of simulations were carried out while varying initial inlet velocity (U_1/U_{mf}) from 0 to 1. Bond number was kept constant to quantify effects of contact stresses on the u_K, while keeping U_2 constant. Further, final inlet velocity U_2 was varied from U_{mf} to U_{mb} to capture effects of inlet velocity along with the Bond number change.

Dynamic wave propagation set up was similar to u_K set up, except when steady state was reached after 0.5 second of initiating a sudden increase of inlet velocity inertial disturbances were introduced. Distributor plate was suddenly displaced upwardly by $\delta = d/2$ distance, event was spanned $\delta t = 10^{-4}$ s. The value $\delta t = 10^{-4}s$ was chosen carefully after running simulations with values ranging from 10^{-3} to 10^{-6} s and accounting for numerical stability. Furthermore, amplitude of disturbance was also varied from δ = 0.1 to 1 d. Simulations were repeated with downward displacement of distributor plate instead of upwards to capture bed collapse dynamic wave propagation. These were repeated for each of the expanded regimes characterized in the chapter 6.

8.5 Results and discussion

The following section will attempt to simulate the kinematic and dynamic wave propagations in the expanded bed regimes as described earlier. It should be noted that, underlying assumptions of homogeneous expansion might not hold true and may hinder the exact reproduction of some of phenomenon. These wave propagation have been well identified with liquid fluidization but extended here and checked for gas-solid fluidization. The bubbling criterion developed by Foscolo and Gibilaro [1987] and Valverde [2013] will be compared with the DEM-CFD simulation predictions of U_{mb} with increasing cohesion Bo_g.

8.5.1 Kinematic wave propagation

DEM-CFD simulations of weakly cohesive granular bed ($1 < Bo_g < 3$) were conducted with bed subjected to a sudden influx of inlet velocity ($U < U_{mb}$) and transient wave propagation from bed bottom to the bed surface were observed. This process was accompanied by uniform bed expansion and rise of bed surface. After this transient phase, granular bed manifested a smooth appearance with immobile particles and attains an expanded bed state 2. From chapter 6, DEM-CFD simulations by accounting for inter-particle cohesion were able to capture this physical phenomenon and a window of stable expansion was identified. It was further noted that U_{mb} increases with an increase in the Bo_g. This sub-section will use the previous simulations and post process the DEM data to estimate u_K. The kinematic wave propagation will be studied here as a response to the voidage shocks, given to the weakly cohesive bed.

8.5.1.1 Bed surface velocity

Figure 8.6a plots bed surface height with time ($Bo_g = 1$) when bed is subjected to sudden influx of inlet velocity from $U_1 = U_{mf}$ to $U_2 = 1.2U_{mf}$. Analytical solution to

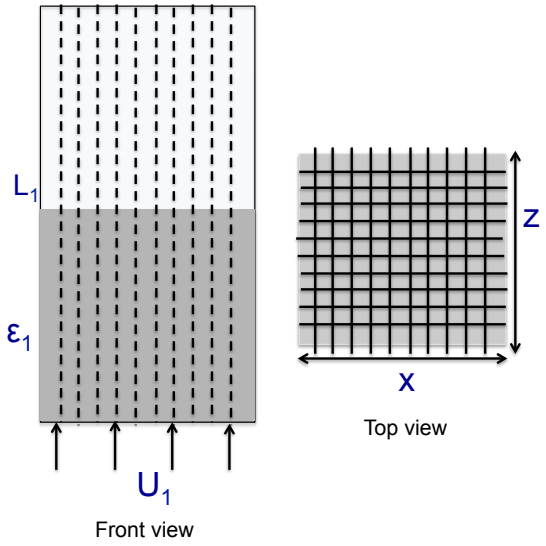

Figure 8.5: Bed division to calculated bed height by averaging over top 5 percentile particle Y coordinates in each of 100 parts (10 each in x and z directions).

bed rise height (L) is calculated by equation 8.11, where U_{bs} is the bed surface velocity given by equation 8.1; L is the instantaneous bed height; L_1 is the initial bed height and t is the time traversed from the start of the simulation. DEM-CFD simulation results are plotted by calculating the averaged bed height at any time instant t. In order to estimate the bed height, domain cross-section (x–z) of the bed is divided in 100 equal parts and averaged height coordinate of top 5 percentile particles is calculated for each part (figure 8.5). It should be further noted that during the uniform expansion, variance of the bed heights calculated should be very low. The variance of the bed height can also serve as an indicator if the bed was bubbling or expanding uniformly, but it is not a definite indicator and hence not employed to characterize expanding bed.

$$L = L_1 + U_{bs}t \tag{8.11}$$

From the DEM-CFD simulations, bed rise velocity (U_{2d}) can be calculated as a slope of height-time plot (figure 8.6a). The figure 8.6a shows a close match between the theoretical bed surface height and predicted DEM-CFD simulation results for initial times.

Different simulations with varying inlet velocity $U_2 = 1.1 - 1.6U_{mf}$ and Bond numbers $Bo_g = 0 - 1.5$ are run to calculate the bed rise velocity predicted by DEM-CFD simulations. Figure 8.6b plots the DEM-CFD simulation results for the difference of bed rise velocity (U_2) with the U_{mf} and normalized by U_{mf} with the theoretical predictions given by Foscolo and Gibilaro [1987] according to equation 8.1. The parity line

is plotted along with different Bond numbers to give an estimated deviation of DEM-CFD results from the theoretical results. $Bo_g = 0$ could not give a steady expanded state window, and bed height fluctuations were observed due to bubbling in the bed ($U_{mb} = U_{mf}$ for $Bo_g = 0$). For this case, bed rise velocities were averaged nevertheless for comparison sake and these showed over-prediction from the estimated U_{bs} and can be attributed to the bubbling and uncertainty in the bed height. Bond numbers 1 and 1.5 exhibited a window of uniform bed expansion and bed height did not fluctuate once the steady state was reached, bed surface velocity estimation is under predicted from equation 8.1. This can be explained by the cohesion dampening effect on the propagation of kinematic shock.

Similar 2D DEM-CFD simulations were conducted by Di Renzo and Di Maio [2007] to reproduce the bed expansion in a granular bed of particle size and density 70 μm and 1000 kg/m^3 respectively. These simulations did not include any cohesion effects and it was argued that hydrodynamic stability can be achieved from a purely hydrodynamic formulation. The bed surface velocities were reported to be captured accurately for both bed expansion and contraction. An interesting point noted was that the plots for bed height versus time for gas-solid fluidization showed fluctuations in the bed height even at the steady state. It is argued that the bed might be in sustained bubbling regime and not stable. It is hard to argue formation of a stable bed without adding bed elasticity terms in the momentum equation, when working in a purely hydrodynamic framework. It is again emphasized that cohesion effect on the formation of expanded bed is a sufficient condition and not a necessary one. It is interesting to note that within the expanded bed window, increase in the Bond number have an increasing dampening effect on the bed surface velocity. Transient bed surface velocity captured here is encouraging and serves as a validation to DEM-CFD Geldart A simulations.

8.5.1.2 Kinematic wave velocity

During the transient phase, the bed divides into porosity region of ϵ_1 and ϵ_2 associated with the steady state-1 and 2. The interface,marked by the boundary between ϵ_2 and ϵ_1, travels from the bottom to the top of the bed surface and the speed is said to be u_K. This phenomenon is reproduced in DEM-CFD simulations. Although the theoretical description is idealized, the interface can be identified as a high porosity region travelling throughout the bed with the region below and above the interface with porosity ϵ_2 and ϵ_1, respectively. In order to calculate and visualize the phenomenon, the coarse grained solid fraction is calculated for each fluid mesh by using DEM data. These calculations are done for every fluid time-step. Figure 8.7 shows the contour plots of solid fraction at different times at the middle x–z cross-section of the bed. The simulation shown here

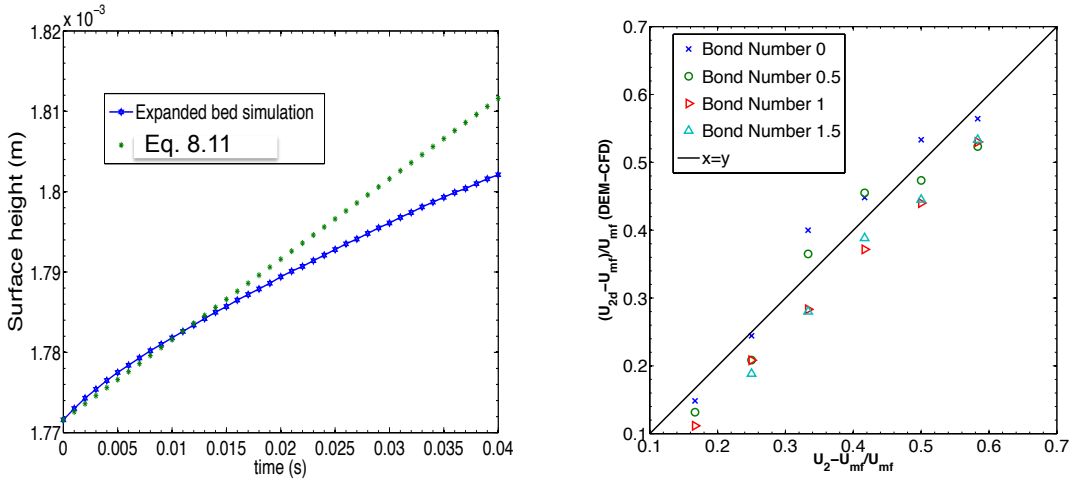

(a) (b)

Figure 8.6: (a) Plot of bed surface height versus time when granular bed (Bo number 1) is subjected to sudden influx of inlet velocity from $U_1 = U_{mf}$ to $U_2 = 1.2U_{mf}$. Green stars are the analytical solution which is calculated according to $L = L_1 + U_{bs}t$ where U_{bs} is the bed surface velocity given by equation 8.1. Blue stars are the expanded bed DEM-CFD simulation results of the bed surface height versus time. (b) Plot of bed rise velocity calculated as slope of bed surface versus time plots (normalized as U_{2d}/U_{mf}) from DEM-CFD simulations versus theoretical bed rise velocity U_{bs}, given by equation 8.1.

is done at U/U_{mf} = 1.4 and $Bo_g = 1$. The granular bed is subjected to the fluidizing air at t = 0.0 s (static bed). The color bar indicates local solid fraction (ϕ_l).

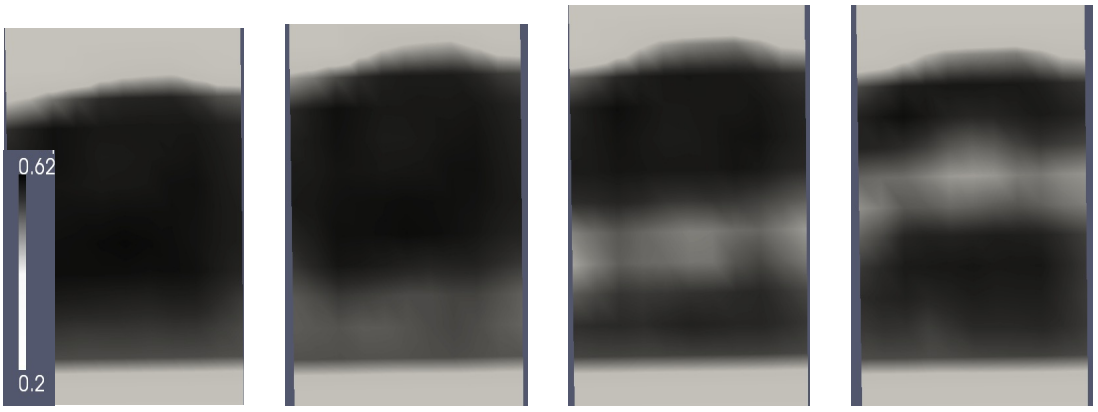

(a) (b) (c) (d)

Figure 8.7: DEM-CFD simulation of bed expansion and kinematic wave propagation (U_K, snapshots at time (a) 0.01 s (b) 0.03 s (c) 0.06 s (d) 0.09 s are shown here. Images are at grayscale and legend shown in image (a) is same for all the 4 snapshots. The legends indicates the solid fraction ϕ which is $1 - \epsilon$, color white indicates 0.2 porosity. A wave of low porosity is seen progressing in the granular bed (Bond number 1) from the time of kinematic shock ($U_1 = 0$ to $U_2 = 1.5U_{mf}$.

Dark space indicates regions of high particle concentration and white space indicate low porosity equalling 0.2 ($\epsilon = 1 - \phi_l$). Kinematic wave is indicated by a band of low

porosity separating the bed into 2 parts and can be seen moving from t = 0.01 to 0.09 seconds as shown in the Figure 8.7. This rapid rise of high voidage region is expected in the gas-solid fluidization and it is interesting that these voidage bands do not increase in the amplitude to form bubbles and instead forms an expanded bed. To identify the low and high porosity regions, the spatio-temporal plots will be shown in later sections (figure 8.9 and 8.8). In a liquid fluidization, interface between the high and lower voidage region travels gradually and exhibit classical kinematic wave propagation behaviour as seen in Di Renzo and Di Maio [2007]. Figure 8.7 also demonstrates rise in bed height progressively over time from t=0.0 to 0.09 s. From these observation and figure 8.7, it can be safely concluded that physical phenomenon is very well captured within DEM-CFD methodology.

Kinematic wave propagation velocity (u_K) can be quantified by plotting spatio-temporal plot for averaged bed solid fraction ($\phi_{av}(h,t)$). Solid fraction field is calculated over domain by coarse graining DEM particle positions and the volume occupied by them at each recorded DEM time-step on a 8 $\times$ 8 $\times$ 8 fixed grid over whole 3D domain. Spherical representative volume is chosen at each grid point of radius 2.5 times diameter of DEM particle (100 μm). Coarse-graining procedure is presented earlier in the post processing section of methodology chapter. This procedure will give ϕ_l as a function of $\phi_l(x,y,z,t)$, where x is the width of the bed, y is the height (positive in the anti-gravity direction) and z is the depth of the bed (figure 8.5). $\phi_l(x,y,z,t)$ is then averaged over depth (z) and width directions (x) to obtain $\phi_{av}(y,t)$. Contour plot of $\phi_{av}(y,t)$ is plotted as a spatio-temporal plot for for averaged bed solid fraction.

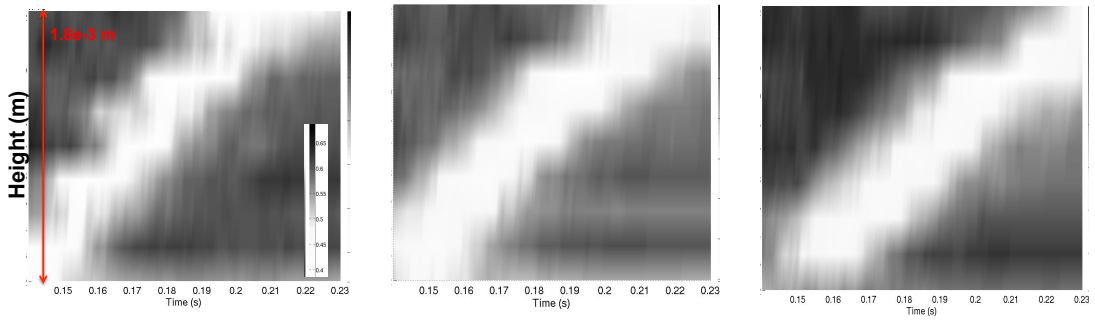

(a) (b) (c)

Figure 8.8: Spatio-temporal plot of ϕ_l for travelling kinematic wave from DEM-CFD fluidization simulation of particle size bed: 100 μm and density 1440 kg/m^3 at fluidizing velocity of 1.5U$_{mf}$ for Bond numbers (a) 1 (b) 2 (c) 3. Kinematic wave velocity (u_K) is calculated as slope of the plot. Solid fraction ϕ_l legend is shown in along Bond number 1 plot and same for all the plots. Kinematic shock is given at 0.10 s and the temporal range is from 0.15-0.23 s, 0.0018 m bed height is shown here. Dark region indicates particles are closely packed where as white region means higher voidage region. With increasing Bond number, u_K decreases.

Spatio-temporal plots of $\phi_{av}(y,t)$ for varying Bond number (1-3) at inlet velocity U/U_{mf} = 1.4 is presented in figure 8.8. The total height (h) of domain is 1.8×10^{-3} m. The legend indicates the solid fraction, white region is the high porosity $(1-\phi_{av})$ region and grey is low porosity region. The plot shows that the high porosity region vary linearly in height and time indicating a constant speed wave travelling from bottom ($h = 0$) to the top of the bed ($h = 1.8e-3$ m). High porosity band (white region in the plot) means that concentration of particle is very low in the region. The shock is given at $t = 0.10$ s and the time shown in the plot is the absolute time measured from $t = 0.0s$. This band further divides bed into two regions with porosity ϵ_1 and ϵ_2 ($\epsilon_2 > \epsilon_1$) and is an interface between the two regions as illustrated by figure 8.8. The kinematic wave velocity u_K can be approximately quantified as the slope of high porosity band. It should be noted that the width of the coarse graining bin in the depth direction is around 2 particles.

Figure 8.8 are plotted with increasing order of Bond number and u_K (slope of the high porosity band) is seen to be decreasing with increasing Bond number. This is expected and can be explained by the fact that the wave propagation will be dampened by the extra energy required to break cohesive bonds. For Bond numbers < 0.5, visual observation, averaged coarse grained particle velocity and the fluctuating bed height indicated highly mobile particles at the onset of fluidization and the high voidage bands seen at the bottom of the bed took form of bubbles indicating Geldart B behaviour. These simulations highlight role of cohesion in the formation of expanded bed. Adhesive forces are the binding forces which damp out the rapid kinematic disturbances. Since hydrodynamic forces are greater than the weight of the bed, the net upward forces that particles experience manifest themselves as uniform expansion instead of heterogeneous bubbling. If the Bond numbers are increased beyond Geldart A limits (> 3), it is observed that hydrodynamic forces are not greater enough to break all the cohesive bonds, hence cracks and channelling regime indicating of Geldart C fluidization. Yield stresses due to enduring particle contacts have been identified by Sundaresan [2003] responsible for uniform bed expansion and origin of these yield stresses were attributed to inter–particle adhesive forces by Rietema [1973] and Rietema and Piepers [1990]. These results from DEM-CFD simulations here supports the role of cohesion in uniform bed expansion and suppression of bubbling and in summary u_K decreases with increasing Bond number within Geldart A limits ($1 < Bo_g < 3$). To quantify u_K as a function of inlet velocity and Bo_g, more DEM-CFD simulations were run for different U/U_{mf} values in the region of $U < U_{mb}$ for $Bo_g = 0.5 - 3$.

Spatio-temporal plots of $\phi_{av}(y,t)$ for Bond number 2 but varying inlet velocity U_2 from 1.1 to 1.45 U_{mf} ($U_2 < U_{mb}$) are shown in figure 8.9. Slope of high porosity band (u_K) is seen increase with increase in inlet velocity U_2 and similar observation of high and low

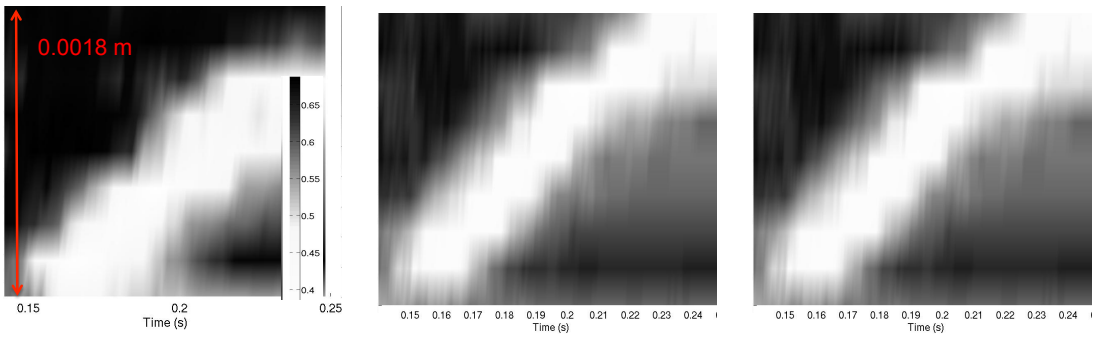

(a) (b) (c)

Figure 8.9: Spatio-temporal plot of ϕ_l for travelling kinematic wave from DEM-CFD fluidization simulation of particle size bed: 100 μm, density 1440 kg/m^3 and Bond number 2 at fluidizing velocity (a) 1.1U$_{mf}$ (b) 1.25U$_{mf}$ (c) 1.45U$_{mf}$. Kinematic wave velocity (u_K) is calculated as slope of the plot. Solid fraction ϕ_l legend is shown in along Bond number 1 plot and same for all the plots. Kinematic shock is given at 0.10 s and the temporal range is from 0.15-0.23 s, 0.0018 m bed height is shown here. Dark region indicates particles are closely packed where as white region means higher voidage region. With increasing Bond number, u_K decreases.

porosities regions are made as from the previous plots. The trend of increasing u_K with increasing inlet velocity is expected, as increase in hydrodynamic energy would lead to rapid rise of high porosity bands from bed bottom to top. An increase of U_2 beyond U$_{mb}$ would lead to bed bubbling as kinematic disturbances would exceed inertial particle responses. These plots bring out that the uniform expansion can be understood as an interplay between the hydrodynamic forces and the adhesive forces. In order to encompass full range of Geldart A, Bo_g and the inlet velocities, DEM-CFD simulations were run and u_K is quantified (not shown here).

Figure 8.10 presents a plot of u_K and inlet velocity U_2 for bed expansion in the observed window of expanded bed at different Bond numbers. Figure 8.10a gives theoretical predictions of u_K given by equation 8.3 based on modification of equation 8.2 by Millán [2012]. Equation 8.3 relates u_K to Bond number and solid fraction ϕ. In turn, ϕ can be related to inlet velocity U by Richardson-Zaki correlations. Hence an expression relating u_K to Bo_g and U is relatively straightforward. Figure 8.10b gives DEM-CFD simulation predictions of u_K for different Bond numbers with inlet velocities U_2 in the expanded bed regime window) predictions for u_K. Qualitative trends of decreasing u_K with increasing Bond numbers and decreasing inlet velocity (U_2) is well captured by DEM-CFD simulations as predicted by theoretical and experimental relations shown in figure 8.10a. These simulations results are successful in representing robust Geldart A fluidization regime features, but the simulation and theoretical prediction do not agree well quantitatively. These could be related to hydrodynamic modelling and inability of drag models to capture fluid-particle interaction accurately. The validation chapter

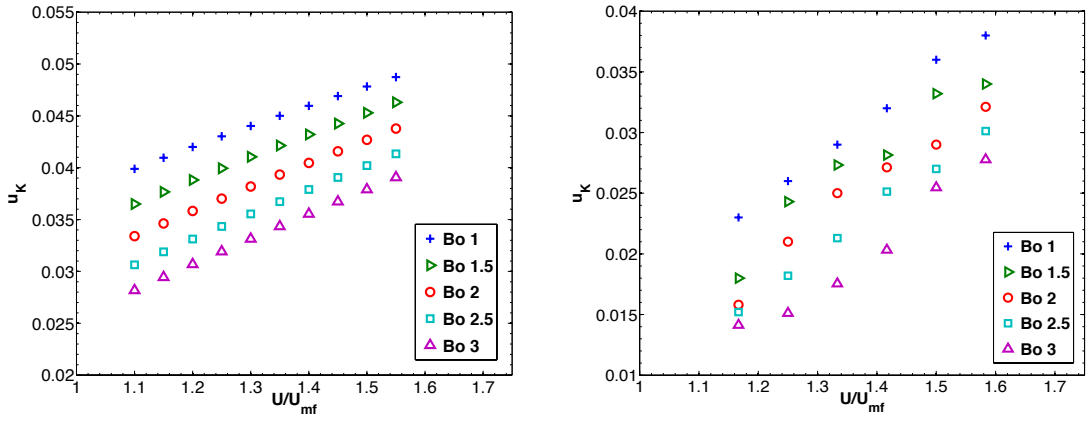

(a) (b)

Figure 8.10: Wave propagation velocity (u_K) versus a sudden wave propagation of velocity U/U_{mf} for different Bond numbers (1-3) for (a) Theoretical predictions by Valverde [2013] (b) DEM-CFD Geldart A simulations. Kinematic wave velocity is calculated as slope of spatiotemporal plots. Bed is static initially i.e. $U_1 = 0$. Increasing inlet velocity shock and decreasing Bo number increases u_K. Qualitative trends are captured by the simulations.

pointed out that the errors can be as high as 50% in Geldart B bubbling regime. It should again be pointed out that even the empirical correlations have not been rigorously tested before.

Furthermore, variation of initial state of the bed is important to be checked for effect on u_K. For this check, DEM-CFD simulations were run with initial bed states in the fixed regime and U_1 was varied from 0.0 to U_{mf} while keeping U_2 constant. For these studies $U_2 = 1.45$ and $Bo_g = 1$ were kept constant. From the conclusions of chapter 6, following features are noticed in the fixed bed regime ($0 < U < U_{mf}$):

- With increasing inlet velocity, the particle remain immobile and the particle velocities are in the order of 10^{-5} m/s.
- The cohesion stress almost constant and does not vary much throughout the bed even with increasing inlet velocity.
- The pressure drop across the bed increases with the increase in inlet velocity, until U_{mf}.
- Magnitude of gradient of contact stresses decreases with the increase in the inlet velocity.

For these simulations, two fixed bed states (a and b) are chosen as $U_{1a} = 0.2U_{mf}$ and $U_{1b} = 0.7U_{mf}$. Bed is fluidized to these velocities for 0.5 seconds and then a kinematic shock is given with $U_2 = 1.45U_{mf}$. For case $U_{1a} < U_{1b}$, based on chapter 6 conclusions,

$\sigma^a_{con} < \sigma^b_{con}$ and $\sigma^a_{cohe} = \sigma^b_{cohe}$. It was seen that the response of all the kinematic shocks at constant U_2 was same for all initial bed conditions in the fixed bed results. These result indicate that different initial contact stresses have no effect on u_K. These can be explained by the fact that the hydrodynamic forces during for all these simulations would be roughly similar.

Bed expansion simulations were allowed to a run longer time until steady state and then suddenly the velocity was decreased back to U_1 to capture the bed contraction. In theory, all the features of Geldart A regimes in bed expansion should also be present in the bed contraction. But these are under idealized conditions, when homogeneous expansion is assumed. The kinematic wave propagation was not identified for the bed contraction simulation. When the inlet velocity was lowered to U_1, almost instantly the bed state returned back to initial state. This can be due to the fact that the expanded bed is not a homogeneous bed with cavities and agglomeration as concluded from the microstructural characterization of the bed in chapter 7. Furthermore, it was concluded from chapter 6 that tensile stresses and high voidage spaces are present in some local regions of expanded bed (see figure 6.15). These findings on inhomogeneity of expanded bed in 2D beds were also reported by Hou *et al.* [2012] and Yang *et al.* [2013] recently through DEM-CFD simulations. The wave propagates through enduring contacts and is difficult to quantify in an inhomogeneous bed due to a complex network of force chains. As soon as the inlet velocity is lowered, particles around the cavity rearrange themselves to fill the void spaces.

8.5.2 Dynamic wave description

Kinematic wave propagations were based on voidage shocks and did not account for inertial effects of the particles. In this section, focus is on the Dynamic wave propagation which was first described by Verloop and Heertjes [1970] as a propagation velocity of an equilibrium disturbance. It is already well established that measurement of dynamic wave through inertial responses is difficult and not as straight forward as kinematic wave velocity [Di Renzo and Di Maio, 2007] both experimentally and by simulations. Wallis [1969] proposed a method to measure dynamic wave propagation velocity with help of a fluidization experiment. Particles were packed at the top of the bed against a mesh by giving them enough fluidizing velocity and the wave was generated by a shock impinging on the mesh. It was noted that generation of these shock waves require control in the experiments and homogeneous conditions.

In order to realize the dynamic wave propagation in DEM-CFD simulations of expanded beds, the distributor plate was suddenly moved upwards or downwards when the expanded bed is in the steady state. The amplitude and the time period of the shock was

set around 1 particle diameter and 10^{-4} s, respectively. The response of the expanded bed was visually inspected for a resultant longitudinal wave. Figure 8.11 gives the response of the granular bed ($Bo_g = 1$,operating conditions $U/U_{mf} = 1.45$) to the sudden upward displacement of the distributor plate. Figure 8.11a shows the contour plots of solid fraction for static fixed bed just before it was subjected to inlet velocity $U/U_{mf} = 1.45$. The local solid fraction is calculated by coarse graining the DEM particles position on the fluid mesh (table 6.1) by the opensource DEM-CFD code on the fly. The bed looks very homogeneous and calculated variance of the local solid fraction is as low as 1% of the mean. Figure 8.11b shows the state of the bed after 0.40 s of the simulation. The bed has reached a steady expanded state with particles highly immobile, though local inhomogeneities are pointed out. This is in line with microstructural characterization of the expanded state presented in chapter 7. At 0.4001 s, the distributor plate is suddenly displaced upwardly by a distance of 1 particle diameter (100 μm) while the bed is still fluidized with the same inlet velocity. Figure 8.11c gives the response of the bed to this sudden shock. There is no longitudinal wave propagation but instead the inhomogeneities in the bed grows. An idealized homogeneous scenario would have been that each particle around the distributor plate transfer the momentum gained to the particle directly above to them, leading a wave propagation. Furthermore figure 8.11c, gives the scenario after 0.1 seconds of the shock and it is observed that the particles have rearranged themselves and filled the void spaces, although not completely. It is further observed that in the long run, these void spaces do not form bubbles and remains stable, even though bed is still subjected to gas inlet velocity.

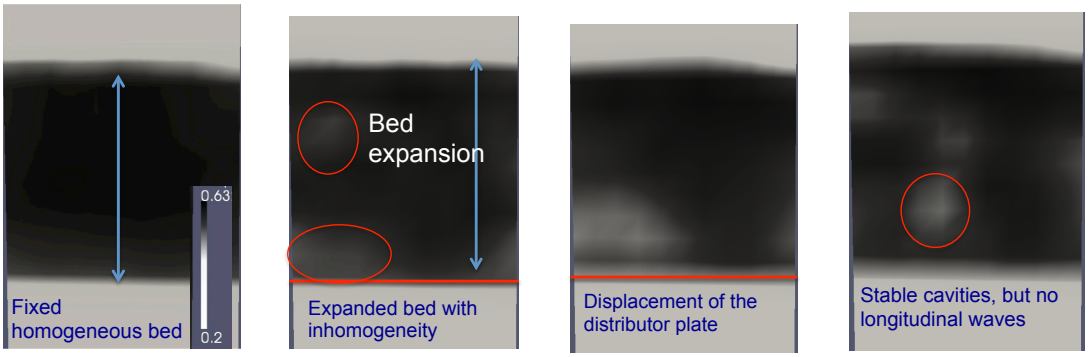

(a) (b) (c) (d)

Figure 8.11: Contours of solid fraction at the mid x–z cross-section of the granular bed by DEM-CFD simulations of weakly cohesive bed ($Bo_g = 1$) operated at $U/U_{mf} = 1.45$ (a) Fixed static bed, initial state (t=0.0 s) (b) Steady state expanded bed for the given conditions and inhomogeneities developed shown (t=0.4 s) (c) Sudden displacement of distributor plate by 1 particle diameter and response of the bed (t=0.42 s) (d) Final state of the bed after response of the dynamic shock with almost static cavities and no propagation of longitudinal wave (t=0.5 s). Images are at grayscale and legend shown in image (a) is same for all the 4 snapshots. The legends indicates the solid fraction ϕ which is $1 - \epsilon$, color white indicates 0.2 porosity.

In summary, due to inhomogeneities and agglomerates formed in the expanded bed regimes, the shock didn't propagate longitudinally. Just after the inertial shock, the particle velocities increased at the bottom of the bed, but the propagation of these shocks were highly non-uniform. Hence, the quantification of these disturbance propagation was not possible with DEM-CFD simulations. Figure 8.12 shows u_D with increasing inlet velocity and Bond numbers by theoretical predictions according to equation 8.7. These theoretical predictions are idealized situation of homogeneous expansion which are more likely to be applicable to liquid fluidized beds. Trends of the dynamic wave propagation (u_D) suggests that increase in Bond number would lead to an increase in u_D. These predictions are based on agglomerates formed according to equation 8.8. These light density agglomerate size increase with Bond number and form the governing dynamics of cohesive particles instead of particles themselves [Valverde, 2013]. Inertial effects would travel faster through these light density agglomerates if the cohesive strength is increased and it is observed that this response is opposite to the kinematic wave responses noted earlier.

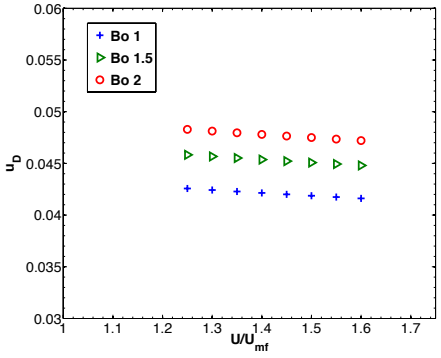

Figure 8.12: Dynamic wave propagation velocity (u_D) versus inlet velocity U/U_{mf} for different Bond numbers (1-2) for theoretical predictions by Valverde [2013].

8.6 Stability of the expanded bed

In chapter 6, minimum bubbling velocity (U_{mb}) was shown to be increasing function of the granular Bond number for Geldart A regime (table 6.2). U_{mb} was estimated by plotting kinetic stresses as a function of increasing inlet velocity for different Bond numbers (figure 8.13). The kinetic stress (similar to granular temperature), a measure of fluctuating velocity was shown to be an indicator of bubbling by Wang *et al.* [2011*a*]. Sudden jump in 2-3 orders of magnitude of kinetic stress can be seen at two distinct points, firstly at the onset of fluidization ($U = U_{mf}$) when the bed starts expanding and secondly at U_{mb} due to introduction of mesostructure, such as bubbles. Kinetic stresses during the expansion phase are mostly constant and no diffusion occurs, but kinetic

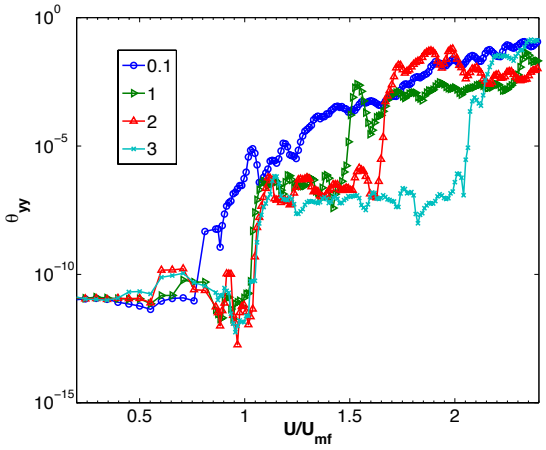

Figure 8.13: Bed division to calculated bed height by averaging over top 5 percentile particle Y coordinates in each of 100 parts (10 each in x and z).

stresses fluctuate after $U > U_{mb}$ due to increased diffusion by bubbling. This section will compare DEM-CFD predicted results for U_{mb} with those of bubbling criterion given by analysing the shock waves by Valverde [2013].

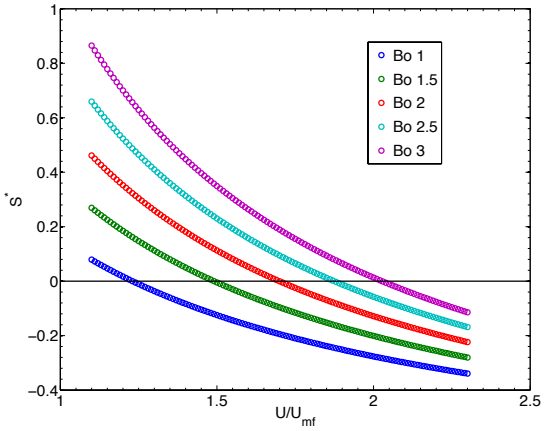

Figure 8.14: S plotted with increasing inlet velocity from theoretical predictions by Valverde [2013].

Stability criterion S^* by Valverde [2013] relates onset of bubbling with the minimum bubbling porosity ϵ_{mb}. Also, ϵ is related to superficial velocity by R–Z correlation Richardson and Zaki [1954] which is modified to account for agglomerates formation and effect of cohesion by Valverde and Castellanos [2006]. Figure 8.14 plots S^* with the inlet velocity normalized by U_{mf} for increasing Bond number (1-3). As stated earlier, bubbling is predicted when u_D or the inertial effects exceeds the kinematic effects u_K. Hence, $S^* = 0$ provides a criterion for minimum bubbling at different bond

numbers. Black line in the plot presents $S^* = 0$ and its intersection with each of Bond number plots will give U_{mb} prediction by the empirical relation by Valverde [2013].

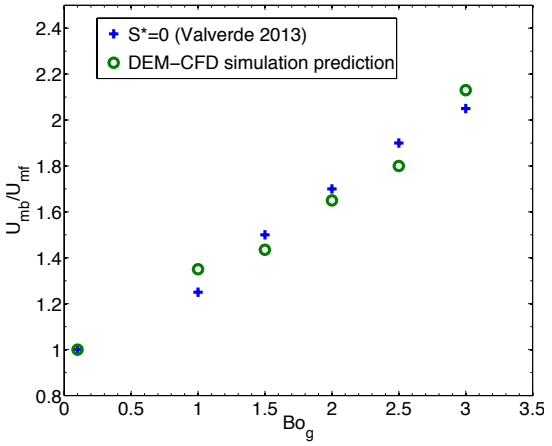

Figure 8.15: U_{mb} predictions by DEM-CFD simulations and theoretical predictions (Valverde [2013]), plotted with increasing Bo_g.

Figure 8.15 plots the U_{mb} predictions by DEM-CFD simulations and by empirical predictions based on experiments by Valverde [2013] with increasing Bo_g. Both the sets of the results are in remarkable agreement both qualitatively and quantitatively, despite DEM-CFD predictions are not able to capture u_D and u_K magnitude quantitatively. Although, similar qualitative observations of increasing U_{mb} with cohesion strength were made by Yang *et al.* [2013] and Ye *et al.* [2005] on a 2D bed, this is the first study to the author's knowledge that compares quantitatively to the theoretical predictions. U_{mb} predictions by DEM-CFD further serves as a validation of the code to capture Geldart A fluidization behaviour. It should be further pointed out that the predictions of the shock waves theory to discriminate between particulate and aggregative fluidization are reasonably accurate, even though based on questionable foundations.

8.7 Conclusion

This chapter aimed to study the effect of cohesion on stability of the expanded bed and the capability of the DEM-CFD code to predict onset of bubbling in weakly cohesive bed. Shock wave criterion established by Wallis [1969] and later modified to include the cohesion effects [Valverde, 2013] were employed for theoretical predictions of U_{mb} and compared against DEM-CFD predictions. Following conclusions were reached from this chapter:

- In the expanded bed regime, DEM-CFD simulation results for the bed surface velocity were in very close agreement with analytical solution given by Gibilaro

[2001]. Bed height fluctuations were observed for the fluidization simualtions of granular bed with Bond numbers less than 0.5 at inlet velocities greater than U_{mf}, but only for Bond numbers 1 and 1.5 for $U > U_{mb}$. Quantitatively, bed surface velocity is under predicted from equation 8.1 with increasing cohesion in the expanded bed regime. This was explained by the cohesion dampening effect on the propagation of kinematic shock.

- Kinematic wave propagation velocity (u_K) can be quantified by plotting spatio-temporal plot for averaged bed solid fraction ($\phi_{av}(h,t)$) in the expanded bed regime. It is observed that, u_K slow down with increasing Bond number and also with decreasing final velocity ($U_2 \geq U_{mb}$). These observations are in close agreement with the theoretical and empirical predictions by Valverde [2013] qualitatively. However, quantitatively the magnitudes are off by 50 % under-prediction which can be explained by inaccurate description of the hydrodynamics by the drag models employed.

- u_K does not depend upon initial bed states ($U_1 \geq U_{mf}$) and only cohesion stresses are responsible for change in stability behaviour. This is largely expected that because the hydrodynamic conditions of the final state is not changed. A more quantitative study is required to separate out role of contact and cohesion stresses in the expanded bed formation. This can be done by running simulations under some confining pressures.

- Dynamic wave and bed contraction is not reproduced by the DEM-CFD simulations. Due to inhomogeneities and agglomerates formed in the expanded bed regimes, the shocks did not propagate longitudinally. Just after the inertial shock, the particle velocities increased at the bottom of the bed, but the propagation of these shocks were highly non-uniform. Hence, the quantification of these disturbance propagation was not possible with DEM-CFD simulations.

- DEM-CFD simulation predictions of minimum bubbling velocity (U_{mb}) are in excellent agreement with stability predictions by Valverde [2013] based on shock waves. These findings are rather surprising as the DEM-CFD simulations are not able to reproduce kinematic wave propagation accurately.

Chapter 9

Conclusions and Recommendations

The research work reported in this thesis have been carried out to study fluidization regimes of Geldart A powders. A hybrid multi-scale model coupling the averaged Navier-Stokes equations for fluid with the discrete description of particles is employed to study hydrodynamics of Geldart A fluidization. Validation and verification of the DEM-CFD code is first laid out to check its implementation and ascertain its predictive capabilities to simulate real phenomenon. Various issues related to the expanded bed regime stability and microstructure have been addressed in this thesis. The thesis had following objectives:

- To perform verification and validation of an open source DEM-CFD code written from OpenFOAM and LAMMPS C++ libraries. This study was conducted to ascertain the strength and ability of the code to capture complex hydrodynamics of fluidization process.
- To check ability of the verified and validated code to check for reproducing hydrodynamics of weakly cohesive fluidization and its robust features such as pressure overshoot, uniform bed expansion and onset of bubbling. The overall idea was to keep the particle size and density in the region of Geldart A/B boundary and increase cohesive forces by changing cohesive model parameters. This would lead to systematic transition from Geldart B to C fluidization regimes.
- To conduct DEM-CFD parametric studies that has direct influence on the fluidization behaviour of weakly cohesive fluidization regimes, especially the expanded bed regime.

- To characterize the expanded bed by investigating microstructure at different local length scales. Statistical tools such as coordination numbers, coarse grained solid fraction and Vornoii cell tessellations were employed.
- To study stability of the expanded bed by shock wave criterion and prediction of the onset of bubbling as a function of increasing cohesion strength.

9.1 Conclusions on validation and verification study

Prior to employing the multiphase tool for prediction of flow regimes and design processes, a quantification of model sensitivity is required. This provides a realistic expectation as to what extent physics of the system can be captured by the model. Checking the implementation of the numerical method proposed and the solution errors for any computational code is termed as verification. An assessment exercise to know the capabilities and the extent of physics that can be captured by the tool is termed as validation. Validation exercises are always preceded by the verification of the code.

In this research, a careful verification is undertaken by employing test cases with increasing order of complexity. The cases are chosen according to the availability of simplified analytical solutions:

- Single particle sedimentation (SPS): SPS tested the DEM-CFD code implementation of fluid-particle coupling term in a very lean phase at low Reynolds number. A particle of diameter 100 μm is allowed to free fall in a tank of fluid with very wide finite boundaries. Different fluids with varying densities and viscosities are tested. Velocity of the particle as a function of time is calculated analytically and compared against DEM particle velocities. Maximum errors of 1-5 % were reported for all three fluids used: air, water, water-glycerol. Analytical solution is based on the assumption that the fluid flow is not disturbed by the particle motion (one–way coupling) where as DEM-CFD simulations are fully coupled, a source of error. Furthermore, issues of meshing, boundaries and statistical issues were addressed in DEM-CFD framework. A fake porosity as a numerical artefact is felt by the particle in case of a fine mesh, which resulted in errors upto 10% .
- Constant porosity Block (CPB): CPB tested the open source code implementation of fluid-particle coupling at finite solid fraction and the complex drag model implementation. A constant porosity block was created by placing equally spaced DEM particles in a regular lattice and fixed relatively to each other. CPB was allowed to sediment into a tank of water and an analytical solution of the terminal velocity was calculated based on the drag model employed [Di Felice, 1994]. A

maximum error of 5 % is reported and can be explained by the fact that analytical solutions do not account for motion of interstitial fluid.

- Pressure drop across a fixed CPB: This verification case tested the fluid particle interaction implementation at high solid fraction and Re number. A fixed porosity bed was fluidized with increasing inlet velocity. Analytical solution for pressure drop across the bed can be found by solving the force balance, with drag forces calculated at constant porosity. The pressure drop versus inlet velocity curve compared for the analytical solutions and the DEM-CFD simulations were in excellent agreement.

These three test cases provided a wide ranged flow and solid-fraction conditions. The fluid-particle coupling, numerical convergence and the drag model implementation was found to be bug-free. After any new capability is added to the code, these test cases are repeated to check for any bugs introduced. The next step is to check the physics captured by the equations. Such a step is important to understand the capabilities of the sub-models to capture different physical phenomenon. Validation studies were presented, covering a wide range of dense-phase fluidization studies. It should be noted that the DEM-CFD code is capable of handling wide range multiphase problems. However, in the present study, the scope of its application and validation is limited only to dense gas-solid fluidization process.

- Bubbling/slugging bed: Granular bed containing Geldart B/D particles was operated under a fully fluidized regime ($U = (2-3)U_{mf}$). The physical phenomenon was characterized using MR techniques [Müller *et al.*, 2008, 2009]. Pseudo 2-D fluidized bed phenomenon was simulated using the open source DEM-CFD code, the particle data was post processed and averaged to be compared against measured voidage, solid velocity and granular temperature at spatial resolutions comparable to the size of the fluidized particles. It was found that the simulations were able to capture macroscopic bulk phenomenon like the bubbling regime observed in the experiments; pressure drop fluctuations and its major frequency measured in the experiments and the minimum fluidization velocity captured by the experiments. Meso-scopic time averaged phenomenon like solid circulation pattern could also be reproduced qualitatively. However, quantitative discrepancies in the spatial-temporally averaged voidage, solid velocity and granular temperature profiles were noticeable near the wall regions and in the middle at the upper or lower bed. These discrepancies were related to the sub-model simplifications for the wall-particle interactions and the hydrodynamics of group

of non-spherical particles. It was found that the particle–wall interaction dominated the particle dynamics over the fluid–wall interaction in a wall boundary layer of about 5d wide. A solid wall with geometric resistance was simulated instead of planar frictional side walls. It was found that the wall with Coloumb friction was incapable of capturing physical phenomenon around the walls in a coarse grained DEM-CFD framework. The data suggested that the models of effective wall boundary conditions for solid velocity and granular temperature in a two-fluid model could be constructed using the particle dynamics data around the walls. The bed expansion and dynamics were found to be sensitive to the particle size, shape and particle bed height. Smaller particles have higher vertical velocities throughout the bed, which implies that size segregation could be a factor contributing to the over-(under-)prediction of velocities at the lower (upper) parts of the bed. The shape effect on fluid–particle interaction investigated through using a modified drag model led to appreciably closer agreement with the experimental solid velocities.

- Spouting bed: Spouting bed fluidization was studied to broaden the realm of validation. The study employed around 45K particles at much higher jet velocities (60 U_{mf}) and the physical phenomenon of different spouting fluidized bed was captured. Temporal and spatially averaged particle velocity profiles of the spouting bed was characterized by PEPT measurements [Link *et al.*, 2008]. In comparison with bubbling bed case, a much better agreement with the experiments was found. Although it was noted that there are still statistical averaging issues are apparent while using PEPT technique to characterize the fluidized bed hydrodynamics and subsequent comparisons with DEM-CFD simulations. Fluid-particle drag formulation was identified as a major cause of the discrepancies between numerical and the experimental data and emphasized that drag models used in the study were beyond their region of validity and employed in an ad-hoc manner.

- Bidisperse bed: In order to extend the validity limits, bidisperse fluidization was simulated by the DEM-CFD code. Random packing fraction and macroscopic trends like U_{mf} for different composition bidisperse bed were captured both qualitatively and quantitatively by DEM-CFD simulations. Segregation rates were captured by digital image analysis of bidisperse fluidization by Goldschmidt *et al.* [2003]. These experimental results were compared against DEM-CFD simulations. Different drag models from literature were identified and categorized according to their applicability to capture bidisperse bed phenomenon. It was noted that no single drag model was able to capture segregation rates accurately

and it was pointed out that the choice of the drag models employed to the bidisperse bed was not so straightforward. Recently proposed drag models, explicitly correcting for bi-dispersity and differences in the different species hydrodynamics [Holloway *et al.*, 2010], were employed to capture the segregation rates. This drag model HYS 2010 [Holloway *et al.*, 2010] was found to be reasonably better than other drag models employed. Furthermore, a systematic study is required by varying mass fraction, particle diameter ratio and inlet velocities to establish a strategy on drag model usage in bidisperse modelling with DEM-CFD.

From all the three case studies, it can be concluded that hydrodynamics of fluidized bed can be captured qualitatively by the open source DEM-CFD code. It should be noted that the validation studies were hampered by the fact that the sub-models such as drag model were employed outside the realms of their validity. This is a common practice in literature, because of lack of drag models which are valid in such a wide range of flow conditions as present in the fluidized beds. It was further noted that the multiphase experiments for the validation purposes are lacking in the literature. It is difficult to employ existing experimental data to validate DEM-CFD models hierarchically. Ideally, validation exercise should be done at the sub-model level such as fluid-particle drag model, particle-particle interactions. It should be noted that validation is a quantification of the errors in assessing reality. A multi-scale model is based on the constitutive laws derived from more resolved sub models and some information is lost while transferring to the next coarser level.

9.2 Conclusions on Geldart A fluidization study

DEM-CFD tool was employed to capture complex phenomenon of Geldart A fluidization regimes: fixed, expanded and bubbling bed. In particular, following questions were identified from the literature review:

- What is the role of inter-particle adhesive forces in the formation of expanded bed?
- What is the criterion on the onset of bubbling?
- What is the microstructural state of the uniformly expanded bed?

In this thesis, each of these issues were undertaken in chapters 5, 6 and 7. A considerable challenge was to reproduce different fluidization regimes numerically in the DEM-CFD framework. Cohesive inter-particle forces were captured using a van der

Waals force model. The cohesive strength of the bed was quantified using a dimensionless number, granular Bond number (Bo_g). Bo_g is defined as the ratio maximum van der Waals force that a particle is subjected to and the weight of the particle. In this 3D DEM-CFD study, the working methodology was increasing the Bo_g from 0-5, but keeping the particle size and density same. Physically, Bo_g increases with a decrease in the particle size, with Bo_g around 1 for particle sizes of few hundreds micrometer [Seville *et al.*, 2000]. Particle size (100 μm)and density (1440 kg/m^3) used in this study, lie on the A/B border of Geldart chart. Increase in Bo_g resulted in systematic transition from Geldart B to A to C behaviour. Based on a careful selection of the DEM-CFD parameters (not based on experiments) following conclusions were drawn from these studies:

- Robust feature of Geldart A fluidization reported in the literature: pressure overshoot phenomenon, macroscopic U_{mf} predictions, uniform stable bed expansion, delay in the onset of bubbling can be captured by DEM-CFD code. A quantitative assessment of U_{mf} revealed a closer match to the experiment and theoretical predictions.

- Transition between A/B and A/C were quantified to be around $Bo_g = 0.5$ and $Bo_g = 3$ respectively. This meant that Geldart A regime was found to be in between $0.5 < Bo_g < 3$.

- Expanded bed was rigorously characterized by satisfying two criterion: (1) Macroscopic averaged particle velocity tending to be almost zero ($< v_p >= 0$) (2) the bed expansion porosity related to the inlet velocity by Richardson–Zaki correlation. These criterion are popularly checked in the literature before for the same purpose.

- Stress analysis of the expanded bed revealed a presence of negative tensile stresses. As the inlet velocity is increased with $U < U_{mb}$, a longitudinal shift of these negative stresses was observed until it reached the bed surface. This highlight the role of cohesion stresses played in the formation of expanded bed and suppressing of bubbling. Microstructural changes were also observed in these negative tensile regions.

- At the minimum fluidization velocity, the negative tensile stresses at the bottom the bed can be linked to the pressure overshoot phenomenon. The magnitude of the pressure overshoot and tensile stresses were close and both were found to be increasing function of cohesion.

- Global granular temperature (θ), local porosity fluctuations and the pressure drop fluctuations were identified as indicators to determine U_{mb}. In particular, θ was

used extensively for this purposes, as a clear jump of 2 orders of magnitude was noticed at the onset of bubbling.

- U_{mb} was found to be an increasing function of the cohesive strength of the bed. Pressure overshoot magnitude also increased with the Bond number, but U_{mf} was found to be a constant. U_{mf} is a macroscopic quantity depending upon the particle size and density, calculated by force balance of the whole bed. U_{mb} does not have a clear physical meaning and simply signifies onset of bubbling, which is a meso-scopic phenomenon depending upon force balance at the particle scale.

- Discretization of the domain was found to be a key parameter for determination of U_{mb}. This signifies importance of resolving the meso-scopic structures within the DEM-CFD framework. It was noted that U_{mb} increased with employment of a coarser mesh. An optimized mesh size was identified as 2.5-3 times size of the particle.

- Different drag models were tested with both U_{mb} and U_{mf} are seen to be sensitive to them. Beetstra *et al.* [2007*a*] drag model was seen to be in closest agreement with empirical correlations.

9.2.1 Microstructural studies

The DEM-CFD simulations were successful in capturing stable expanded bed regime. DEM data was post-processed to study the structure of this stable expanded fluidized bed. The microstructural characterization of expanded bed regime was presented at different local length scales employing different tools:

- Mechanical Coordination Number (MCN): Average number of mechanical contact per particle.

- Cohesion Coordination Number (CCN): Average number of cohesion contact per particle.

- Coarse grained solid fraction (ϕ_{av}): Particle concentration at the meso-scopic volume.

- Local solid fraction (ϕ_l): Local particle concentration based on the Voronoi cell tessellations.

The relevant length scales of the microstructural quantities are indicated in the figure 7.2. Based on these quantities, following conclusions were drawn on the state of the bed:

- Definition of homogeneity in relation to the fluidization is rather obscure. The distinction is made on the macroscopic bed behaviour i.e. bubbling is regarded as heterogeneous fluidization where as absence of these meso-structures is regarded as a homogeneous bed. Motivation of this study is to check the homogeneity at microscopic level.

- Evidences of clustering, agglomeration and cavities were presented in the expanded bed through variations of averaged solid fraction (ϕ_{av}), mechanical and cohesion coordination number (MCN and CCN) with increasing inlet velocities (see figure 7.3 and 7.4). It is concluded that the expanded bed expansion is not homogeneous with meso-structural inhomogeneities present. This is contrary to the belief that stable expansion is actually homogeneous.

- Fixed bed regime was identified to have a strong contact force network and mere 20 % of strong force contacts could carry bulk of the bed. Expanded bed had no such distinction, contact force distribution was even throughout the expanded bed. It was noted that, even though mechanical bonds were not broken in transition from fixed to expanded bed, but the magnitude of contact forces decreased to zero. It is further noted that the strong force network is minimally coordinated.

- In the expanded bed, particles are in weak mechanical contacts but with minimal overlaps. The particle pairs are bind together by the adhesion forces. Bubbling is suppressed until these cohesive bonds are not broken ($U < U_{mb}$). Hence, a criterion on onset of bubbling can be marked by the dominance of hydrodynamic forces to be able to break cohesive bonds. This study could be further be used to explain role of cohesion forces in the stability and formation of expanded bed.

- Mechanical contacts formed a big part of the cohesion networks as well. It was noted that the mechanical contacts with the maximum cohesion forces are far more influential in governing dynamics than weak cohesion pairs that are not in mechanical contact.

- $S_{max} = 1.25d$ can be significantly reduced without affecting the dynamics of the system. It is further suggested that van der Waals model can be integrated to the contact model. A constant cohesion force equal to maximum van der Waals force can be given to each mechanical contact. This will save considerable computational time with hard disk space for storing cohesion contact data.

- Γ distribution function fits to the Voronoi distribution of different fluidization regimes with variable $V = (V_v - V_{min})/(< V_v > -V_{min})$ normalised by its mean. Normalized standard deviation (σ/σ_o) is used to quantify clustering. It

is found that the normalised standard deviation is 1.5 times more for expanded bed regimes than fixed bed regimes which quantifies agglomerate formation and cavities as evident from the local concentration plots. This validated the claim of preferential clustering in the expanded bed regime which are formed as an interplay between hydrodynamic and adhesive forces.

9.2.2 Stability of the expanded bed

Effect of cohesion on stability of the expanded bed and the capability of the DEM-CFD code to predict onset of bubbling in weakly cohesive bed were studied. Shock wave criterion established by Wallis [1969] and later modified to include the cohesion effects [Valverde, 2013] were employed for theoretical predictions of U_{mb} and compared against DEM-CFD predictions. Following conclusions were reached from this chapter:

- In the expanded bed regime, DEM-CFD simulation results for the bed surface velocity were in very close agreement with analytical solution given by Gibilaro [2001]. Bed height fluctuations were observed for the fluidization simulations of granular bed with Bond numbers less than 0.5 at inlet velocities greater than U_{mf}, but only for Bond numbers 1 and 1.5 for $U > U_{mb}$. Quantitatively, bed surface velocity is under predicted from equation 8.1 with increasing cohesion in the expanded bed regime. This was explained by the cohesion dampening effect on the propagation of kinematic shock.

- Kinematic wave propagation velocity (u_K) can be quantified by plotting spatio-temporal plot for averaged bed solid fraction ($\phi_{av}(h,t)$) in the expanded bed regime. It is observed that, u_K could slow down with increasing Bond number and also with decreasing final velocity ($U_2 \geq U_{mb}$). These observations are in close agreement with the theoretical and empirical predictions by Valverde [2013] qualitatively. However, quantitatively the magnitudes are off by 50% under-prediction which can be explained by inaccurate description of the hydrodynamics by the drag models employed.

- u_K does not depend upon initial bed states ($U_1 \geq U_{mf}$) and only cohesion stresses are responsible for change in stability behaviour. This is largely expected that because the hydrodynamic conditions of the final state is not changed. A more quantitative study is required to separate out role of contact and cohesion stresses in the expanded bed formation. This can be done by running simulations under some confining pressures.

- Dynamic wave and bed contraction is not reproduced by the DEM-CFD simulations. Due to inhomogeneities and agglomerates formed in the expanded bed

regimes, the shocks didn't propagate longitudinally. Just after the inertial shock, the particle velocities increased at the bottom of the bed, but the propagation of these shocks were highly non-uniform. Hence, the quantification of these disturbance propagation was not possible with DEM-CFD simulations.

- DEM-CFD simulation predictions of minimum bubbling velocity (U_{mb}) are in excellent agreement with stability predictions by Valverde [2013] based on shock waves. These findings are rather surprising as the DEM-CFD simulations are not able to reproduce kinematic wave propagation accurately.

9.3 Recommendations for future research

The thesis presented 3D DEM-CFD simulations of Geldart A fluidization behaviour and developed post processing tools for DEM-data. This research demonstrated capabilities of the DEM-CFD tool to capture the robust features of the fluidization regimes and opens a promising route to studies aimed at providing fundamental understanding of the process. From an industrial view-point, the tool has ability to capture the phenomenon both quantitatively and qualitatively and can help in up-scaling and design procedures. Nevertheless, there is a huge scope of improvement and some the recommendations for future studies are listed here:

- The study presented coarse-grained simulations of a process that is sensitive to changes at particle scales. It is suggested that a better fundamental understanding can be gained by resolving fluid field around the particles. DNS simulations of these weakly cohesive particles with same DEM parameters can be compared against present DEM-CFD simulations. These fully resolved simulations can be further used to improve/calibrate the existing drag models. This would be beneficial, in general, for continuum modelling tools to capture hydrodynamics of fluidized beds.

- The present study aimed at bringing out effects of cohesion in the formation of expanded bed. It should be noted here that, *cohesive interactions* in the granular bed is only shown as a sufficient condition and not a necessary one for the uniform bed expansion. One school of thought points out that the inter-particle friction or wall friction could also be sufficient in this regard. There is a need to segregate the effects of inter-particle friction, wall friction and cohesive forces to quantify the extent of role played by each of the parameter in uniform bed expansion. These studies can be done by a systematic variation of each parameter while keeping the other two as constants in the DEM-CFD framework.

- DEM-CFD studies with varying particle size distribution but keeping Hamaker constant (A) same can be conducted. These can be compared amongst current simulations for differences in the prediction of minimum bubbling velocity with a mean particle size. These studies would be directly the industries to use present DEM-CFD studies to their benefit, as often industrial powders are poly-disperse in nature. Segregation studies presented in the validation can help to suggest a drag model suitability.

- Constitutive laws for the solid stresses can be improved to include these cohesion stresses so as to improve TFM modelling of Geldart A fluidization. DEM-CFD simulations from the present studies can be extended to include more Bond number studies and the results could be coarse grained to find cohesion stresses.

- Parametric DEM-CFD studies from chapter 6 suggested a dependence of the results on the mesh discretization size. Even though, dependence of the length scale is inherent to the phenomenon itself, it is highly desired to segregate length scales of the phenomenon from the meshing dependence. This can be done by employing different meshes for solid and fluid phase in order to resolve the phases in a better way. The challenge would be to inter-link these meshes in a computationally efficient way.

- Various forms of DEM-CFD equations and implementations are used by research groups around the world. However, effect of these difference and the advantages of using one set over the others is not established. There is a growing need for guidelines of DEM-CFD best practices. It is proposed in future to check available implementation from the literature along with different averaging procedures within DEM-CFD framework. This would be a continued exercise for the validation and verification studies undertaken in this thesis.

List of References

Abrahamsen, A. and Geldart, D. (1980). Behaviour of gas-fluidized beds of fine powders part i. homogeneous expansion. *Powder technology*, **26**(1): pp. 35–46. (p. 4, 126, 127, 128, 129, 132, 136, 149)

Agrawal, K., Loezos, P.N., Syamlal, M., and Sundaresan, S. (2001). The role of meso-scale structures in rapid gasâĂŽĂĎÃňsolid flows. *Journal of Fluid Mechanics*, **445**: pp. 151–185, doi:10.1017/S0022112001005663. (p. 34, 38)

Anderson, T.B. and Jackson, R. (1967). Fluid mechanical description of fluidized beds. Equations of motion. *Industrial & Engineering Chemistry Fundamentals*, **6**(4): pp. 527–539. (p. 6, 24, 25, 28, 38, 42, 64, 133, 174)

André, J.M. (2014). The nobel prize in chemistry 2013. *Chemistry International*, **36**(2): pp. 2–7. (p. 22)

Andrews IV, A.T., Loezos, P.N., and Sundaresan, S. (2005). Coarse-grid simulation of gas-particle flows in vertical risers. *Industrial & engineering chemistry research*, **44**(16): pp. 6022–6037. (p. 38)

Anthony, E. (1995). Fluidized bed combustion of alternative solid fuels; status, successes and problems of the technology. *Progress in Energy and Combustion Science*, **21**(3): pp. 239–268. (p. 2)

Antony, S.J. (2000). Evolution of force distribution in three-dimensional granular media. *Physical Review E*, **63**(1): p. 011302. (p. 161)

Aoki, Y., Endrődi, G., Fodor, Z., Katz, S., and Szabo, K. (2006). The order of the quantum chromodynamics transition predicted by the standard model of particle physics. *Nature*, **443**(7112): pp. 675–678. (p. 21)

Aste, T., Delaney, G., and Di Matteo, T. (2010). kgamma distributions in granular packs. In: *American Institute of Physics Conference Series*, volume 1227, pp. 157–166. (p. xxv, 167, 169, 170)

Baeurle, S.A. (2009). Multiscale modeling of polymer materials using field-theoretic methodologies: a survey about recent developments. *Journal of mathematical chemistry*, **46**(2): pp. 363–426. (p. 21)

Bai, D., Grace, J.R., and Zhu, J.X. (1999). Characterization of gas fluidized beds of group c, a and b particles based on pressure fluctuations. *The Canadian Journal of Chemical Engineering*, **77**(2): pp. 319–324. (p. 86)

Batchelor, G. (1988). A new theory of the instability of a uniform fluidized bed. *Journal of Fluid Mechanics*, **193**: pp. 75–110. (p. 37)

Beetstra, R., der Hoef, M.A., and Kuipers, J.A.M. (2007*a*). Drag force of intermediate Reynolds number flow past mono-and bidisperse arrays of spheres. *AIChE Journal*, **53**(2): pp. 489–501. (p. 30, 50, 62, 70, 86, 87, 109, 113, 114, 124, 135, 136, 138, 148, 205)

Beetstra, R., der Hoef, M.A., and Kuipers, J.A.M. (2007*b*). Numerical study of segregation using a new drag force correlation for polydisperse systems derived from lattice-Boltzmann simulations. *Chemical Engineering Science*, **62**(1): pp. 246–255. (p. xxiii, 109, 136)

Benyahia, S., Syamlal, M., and O'Brien, T.J. (2006). Extension of hill–koch–ladd drag correlation over all ranges of reynolds number and solids volume fraction. *Powder Technology*, **162**(2): pp. 166–174. (p. 50)

Blair, D.L., Mueggenburg, N.W., Marshall, A.H., Jaeger, H.M., and Nagel, S.R. (2001). Force distributions in three-dimensional granular assemblies: Effects of packing order and interparticle friction. *Physical Review E*, **63**(4): p. 041304. (p. 161)

Boyce, C., Davidson, J., Holland, D., Scott, S., and Dennis, J. (2014). The origin of pressure oscillations in slugging fluidized beds: Comparison of experimental results from magnetic resonance imaging with a discrete element model. *Chemical Engineering Science*. (p. 86, 87)

Boyce, C.M., Holland, D.J., Scott, S.A., and Dennis, J.S. (2013). Adapting data processing to compare model and experiment accurately: a discrete element model and magnetic resonance measurements of a 3d cylindrical fluidized bed. *Industrial & engineering chemistry research*, **52**(50): pp. 18085–18094. (p. 84)

Busciglio, A., Micale, G., Vella, G., and Rizzuti, L. (2010). Linear stability analysis of gas-fluidized beds for the prediction of incipient bubbling conditions. *Chemical Engineering Journal*, **157**(2): pp. 489–500. (p. 139)

Capecelatro, J., Desjardins, O., and Fox, R.O. (2014). Numerical study of collisional particle dynamics in cluster-induced turbulence. *Journal of Fluid Mechanics*, **747**: p. R2. (p. 30)

Castellanos, a. (2005). *The relationship between attractive interparticle forces and bulk behaviour in dry and uncharged fine powders*, volume 54. ISBN 1746139050040, 263–376 pp., doi: 10.1080/17461390500402657. (p. 34)

Castellanos, A., Valverde, J., Pérez, A., Ramos, A., and Watson, P. (1999). Flow Regimes in Fine Cohesive Powders. *Physical Review Letters*, **82**(6): pp. 1156–1159, doi:10.1103/PhysRevLett.82.1156. (p. 16)

Cates, M., Wittmer, J., Bouchaud, J.P., and Claudin, P. (1998). Jamming, force chains, and fragile matter. *Physical review letters*, **81**(9): p. 1841. (p. 165)

Chaouki, J., Larachi, F., and Dudukovic, M.P. (1997). Noninvasive tomographic and velocimetric monitoring of multiphase flows. *Industrial & engineering chemistry research*, **36**(11): pp. 4476–4503. (p. 79)

Chaumeil, F. and Crapper, M. (2013). Dem simulations of initial deposition of colloidal particles around non-woven membrane spacers. *Journal of Membrane Science*, **442**: pp. 254–263. (p. 67)

Chung, Y. and Ooi, J. (2011). Benchmark tests for verifying discrete element modelling codes at particle impact level. *Granular Matter*, **13**(5): pp. 643–656. (p. 31, 62)

Cleary, P. (2001). Recent advances in dem modelling of tumbling mills. *Minerals Engineering*, **14**(10): pp. 1295–1319. (p. 27)

Cleary, P.W. and Sawley, M.L. (2002). Dem modelling of industrial granular flows: 3d case studies and the effect of particle shape on hopper discharge. *Applied Mathematical Modelling*, **26**(2): pp. 89–111. (p. 27)

Cody, G.D., Goldfarb, D.J., Storch Jr, G.V., and Norris, A.N. (1996). Particle granular temperature in gas fluidized beds. *Powder Technology*, **87**(3): pp. 211–232. (p. 37)

Colafigli, A., Mazzei, L., Lettieri, P., and Gibilaro, L. (2009). Apparent viscosity measurements in a homogeneous gas-fluidized bed. *Chemical Engineering Science*, **64**(1): pp. 144–152. (p. 128)

Cundall, P.A. and Strack, O.D.L. (1979). A discrete numerical model for granular assemblies. *Geotechnique*, **29**(1): pp. 47–65. (p. 26, 27, 43, 46)

Dan, S., Shuyan, W., Huilin, L., Zhiheng, S., Xiang, L., Shuai, W., Yunhua, Z., and Lixin, W. (2009). A second-order moment method of dense gas–solid flow for bubbling fluidization. *Chemical Engineering Science*, **64**(23): pp. 5013–5027. (p. 82)

de Carvalho, J. (1981). Dense phase expansion in fluidised beds of fine particles: the effect of pressure on bubble stability. *Chemical Engineering Science*, **36**(2): pp. 413–416. (p. 173)

de Pablo, J.J. (2011). Coarse-grained simulations of macromolecules: from dna to nanocomposites. *Annual review of physical chemistry*, **62**: pp. 555–574. (p. 21)

Deen, N.G., Van Sint Annaland, M., der Hoef, M.A., and Kuipers, J.A.M. (2007). Review of discrete particle modeling of fluidized beds. *Chemical Engineering Science*, **62**(1): pp. 28–44. (p. 6, 61, 122)

Derjaguin, B., Muller, V., and Toporov, Y. (1980). On different approaches to the contact mechanics. *Journal of Colloid and Interface Science*, **73**(1): pp. 293–294. (p. 46)

Di Felice, R. (1994). The voidage function for fluid-particle interaction systems. *International Journal of Multiphase Flow*, **20**(1): pp. 153–159. (p. 48, 49, 70, 74, 86, 104, 200)

Di Felice, R. and Rotondi, M. (2012). Fluid-particle Drag Force in Binary-solid Suspensions. *International Journal of Chemical Reactor Engineering*, **10**(1), doi:10.1515/1542-6580.3000. (p. 126)

Di Renzo, A. and Di Maio, F.P. (2007). Homogeneous and bubbling fluidization regimes in dem–cfd simulations: hydrodynamic stability of gas and liquid fluidized beds. *Chemical Engineering Science*, **62**(1): pp. 116–130. (p. 29, 34, 38, 40, 41, 128, 186, 188, 192)

Dijkhuizen, W., Bokkers, G.A., Deen, N.G., Annaland, M.V.S., and Kuipers, J.A.M. (2007). Extension of PIV for measuring granular temperature field in dense fluidized beds. *AIChE journal*, **53**(1): pp. 108–118, doi:10.1002/aic. (p. 79)

Ding, J. and Gidaspow, D. (1990). A bubbling fluidization model using kinetic theory of granular flow. *AIChE Journal*, **36**(4): pp. 523–538. (p. 25)

Donsi, G. and Massimilla, L. (1973). Bubble-free expansion of gas-fluidized beds of fine particles. *AIChE Journal*, **19**(6): pp. 1104–1110. (p. 128, 173)

Dry, M.E. (2002). The fischer–tropsch process: 1950–2000. *Catalysis today*, **71**(3): pp. 227–241. (p. 2)

Ebrahimi, M., Crapper, M., and Ooi, J.Y. (2014). Experimental and simulation studies of dilute horizontal pneumatic conveying. *Particulate Science and Technology*, **32**(2): pp. 206–213. (p. 27)

El-Kaissy, M. and Homsy, G. (1976). Instability waves and the origin of bubbles in fluidized beds: Part 1: Experiments. *International Journal of Multiphase Flow*, **2**(4): pp. 379–395. (p. 37)

Elnashaie, S. and El-Hennawi, I. (1979). Multiplicity of the steady state in fluidized bed reactorsâĂŤiv. fluid catalytic cracking (fcc). *Chemical Engineering Science*, **34**(9): pp. 1113–1121. (p. 2)

Ergun, S. (1952). Fluid flow through packed columns. *Chem. Eng. Prog.*, **48**. (p. 4, 7, 30, 48, 105, 126, 135)

Ergun, S. and Orning, A.A. (1949). Fluid flow through randomly packed columns and fluidized beds. *Industrial & Engineering Chemistry*, **41**(6): pp. 1179–1184. (p. 72)

Espin, M., Valverde, J., Quintanilla, M., and Castellanos, A. (2011). Stabilization of gas-fluidized beds of magnetic powders by a cross-flow magnetic field. *Journal of Fluid Mechanics*, **680**: pp. 80–113. (p. 144)

Fedors, R. and Landel, R. (1979). An empirical method of estimating the void fraction in mixtures of uniform particles of different size. *Powder Technology*, **23**(2): pp. 225–231. (p. 108)

Felipe, C.A.S. and Rocha, S. (2004). Time series analysis of pressure fluctuation in gas-solid fluidized beds. *Brazilian Journal of Chemical Engineering*, **21**(3): pp. 497–507. (p. 86)

Feng, Y.Q. and Yu, A.B. (2004). Assessment of model formulations in the discrete particle simulation of gas-solid flow. *Industrial & engineering chemistry research*, **43**(26): pp. 8378–8390. (p. 29, 42, 122)

Feng, Y.Q. and Yu, A.B. (2007). Microdynamic modelling and analysis of the mixing and segregation of binary mixtures of particles in gas fluidization. *Chemical engineering science*, **62**(1): pp. 256–268. (p. 29)

Feng, Z.G. and Michaelides, E.E. (2004). The immersed boundary-lattice boltzmann method for solving fluid–particles interaction problems. *Journal of Computational Physics*, **195**(2): pp. 602–628. (p. 64, 67)

Forsyth, A.J. and Rhodes, M.J. (2000). A simple model incorporating the effects of deformation and asperities into the van der waals force for macroscopic spherical solid particles. *Journal of colloid and interface science*, **223**(1): pp. 133–138. (p. 36)

Foscolo, P. and Gibilaro, L. (1987). Fluid dynamic stability of fluidised suspensions: the particle bed model. *Chemical Engineering Science*, **42**(6): pp. 1489–1500. (p. 38, 174, 179, 184, 185)

Foscolo, P.U. and Gibilaro, L.G. (1984). A fully predictive criterion for the transition between particulate and aggregate fluidization. *Chemical engineering science*, **39**(12): pp. 1667–1675. (p. 9, 37, 38, 39, 175, 178, 182)

Garg, R., Galvin, J., Li, T., and Pannala, S. (2010). Documentation of open-source mfix–dem software for gas-solids flows. *From URL https://mfix. netl. doe. gov/documentation/dem doc*. (p. 32, 63)

Garg, R., Galvin, J., Li, T., and Pannala, S. (2012). Open-source mfix-dem software for gas–solids flows: Part iâĂŤverification studies. *Powder Technology*, **220**: pp. 122–137. (p. 7, 32, 63)

Garg, S. and Pritchett, J. (1975). Dynamics of gas-fluidized beds. *Journal of Applied Physics*, **46**(10): pp. 4493–4500. (p. 37)

Gel, A., Li, T., Gopalan, B., Shahnam, M., and Syamlal, M. (2013). Validation and uncertainty quantification of a multiphase computational fluid dynamics model. *Industrial & Engineering Chemistry Research*, **52**(33): pp. 11424–11435. (p. 32)

Geldart, D. (1973). Types of gas fluidization. *Powder technology*, **7**(5): pp. 285–292. (p. 5, 8, 14, 16, 17, 18, 19, 36, 37, 127, 128, 173)

Geldart, D. (1986). Gas fluidization technology. (p. 5)

Gibilaro, L. (2001). *Fluidization dynamics*. Butterworth-Heinemann. (p. xxv, 36, 37, 174, 176, 177, 178, 179, 180, 181, 182, 196, 207)

Gidaspow, D. (1994). *Multiphase flow and fluidization: continuum and kinetic theory descriptions*. Academic press. (p. xxii, xxiii, 28, 48, 70, 71, 82, 86, 108, 109, 110, 112, 113, 114, 135, 136)

Goldenberg, C., Atman, A.P.F., Claudin, P., Combe, G., and Goldhirsch, I. (2006). Scale separation in granular packings: stress plateaus and fluctuations. *Physical review letters*, **96**(16): p. 168001. (p. 56)

Goldenberg, C. and Goldhirsch, I. (2004). Small and large scale granular statics. *Granular Matter*, **6**(2-3): pp. 87–96. (p. 54)

Goldhirsch, I. and Goldenberg, C. (2002). On the microscopic foundations of elasticity. *The European Physical Journal E*, **9**(3): pp. 245–251. (p. 54)

Goldschmidt, M., Kuipers, J., and Van Swaaij, W. (2001). Hydrodynamic modelling of dense gas-fluidised beds using the kinetic theory of granular flow: effect of coefficient of restitution on bed dynamics. *Chemical Engineering Science*, **56**(2): pp. 571–578. (p. 131)

Goldschmidt, M.J.V., Link, J.M., Mellema, S., and Kuipers, J.A.M. (2003). Digital image analysis measurements of bed expansion and segregation dynamics in dense gas-fluidised beds. *Powder Technology*, **138**(2): pp. 135–159. (p. 6, 8, 62, 79, 99, 105, 106, 107, 108, 109, 110, 111, 112, 115, 116, 202)

González-Montellano, C., Ayuga, F., and Ooi, J. (2011). Discrete element modelling of grain flow in a planar silo: influence of simulation parameters. *Granular Matter*, **13**(2): pp. 149–158. (p. 27)

Goossens, W.R. (1998). Classification of fluidized particles by archimedes number. *Powder technology*, **98**(1): pp. 48–53. (p. 18)

Grace, J.R. (1986). Contacting modes and behaviour classification of gasâĂŤsolid and other two-phase suspensions. *The Canadian Journal of Chemical Engineering*, **64**(3): pp. 353–363. (p. xix, 5, 18, 19)

Grace, J.R. and Taghipour, F. (2004). Verification and validation of cfd models and dynamic similarity for fluidized beds. *Powder Technology*, **139**(2): pp. 99–110. (p. 32)

Guazzelli, É. (2004). Fluidized beds: from waves to bubbles. *The Physics of Granular Media*: pp. 211–232. (p. 180)

Guo, Y., Wu, C.Y., and Thornton, C. (2013). Modeling gas-particle two-phase flows with complex and moving boundaries using dem-cfd with an immersed boundary method. *AIChE Journal*, **59**(4): pp. 1075–1087. (p. 6, 27)

Haber, H.E. and Kane, G.L. (1985). The search for supersymmetry: probing physics beyond the standard model. *Physics Reports*, **117**(2): pp. 75–263. (p. 21)

Haider, A. and Levenspiel, O. (1989). Drag coefficient and terminal velocity of spherical and nonspherical particles. *Powder technology*, **58**(1): pp. 63–70. (p. 49, 82, 86, 95)

Hakim, L.F., Portman, J.L., Casper, M.D., and Weimer, A.W. (2005). Aggregation behavior of nanoparticles in fluidized beds. *Powder Technology*, **160**(3): pp. 149–160. (p. 150)

Hamaker, H. (1937). The londonâĂŤvan der waals attraction between spherical particles. *physica*, **4**(10): pp. 1058–1072. (p. 35)

Hartman, M., Trnka, O., and Svoboda, K. (2009). Use of Pressure Fluctuations to Determine Online the Regime of GasâĂŽĂăÃ■Solids Suspensions from Incipient Fluidization to Transport. *Industrial & Engineering Chemistry Research*, **48**(14): pp. 6830–6835, doi: 10.1021/ie900055x. (p. 132)

Hill, R.J., Koch, D.L., and Ladd, A.J. (2001*a*). The first effects of fluid inertia on flows in ordered and random arrays of spheres. *Journal of Fluid Mechanics*, **448**: pp. 213–241. (p. 49)

Hill, R.J., Koch, D.L., and Ladd, A.J. (2001*b*). Moderate-reynolds-number flows in ordered and random arrays of spheres. *Journal of Fluid Mechanics*, **448**: pp. 243–278. (p. 49)

Hjelmfelt Jr, A. and Mockros, L. (1966). Motion of discrete particles in a turbulent fluid. *Applied Scientific Research*, **16**(1): pp. 149–161. (p. 33)

Holland, D.J., Müller, C.R., Dennis, J.S., Gladden, L.F., and Sederman, A.J. (2008). Spatially resolved measurement of anisotropic granular temperature in gas-fluidized beds. *Powder Technology*, **182**(2): pp. 171–181. (p. xx, 6, 54, 79, 81, 82, 84, 85, 87, 88)

Holloway, W., Yin, X., and Sundaresan, S. (2010). Fluid-particle drag in inertial polydisperse gas–solid suspensions. *AIChE Journal*, **56**(8): pp. 1995–2004. (p. 51, 109, 111, 112, 113, 114, 116, 203)

Holst, J., Ooi, J., Rotter, J., and Rong, G. (1999). Numerical modeling of silo filling. ii: Discrete element analysis. *J. Engng. Mech., ASCE*, **125**(1): pp. 104–110. (p. 27, 31)

Hoomans, B.P.B., Kuipers, J.A.M., Briels, W.J., and Van Swaaij, W.P.M. (1996). Discrete particle simulation of bubble and slug formation in a two-dimensional gas-fluidised bed: a hard-sphere approach. *Chemical Engineering Science*, **51**(1): pp. 99–118. (p. 27, 29)

Hoomans, B.P.B., Kuipers, J.A.M., and Van Swaaij, W.P.M. (2000). Granular dynamics simulation of segregation phenomena in bubbling gas-fluidised beds. *Powder Technology*, **109**(1): pp. 41–48. (p. 29)

Hou, Q., Zhou, Z., and Yu, A. (2012). Micromechanical modeling and analysis of different flow regimes in gas fluidization. *Chemical Engineering Science*, **84**: pp. 449–468. (p. 9, 38, 39, 40, 119, 121, 122, 124, 127, 131, 136, 150, 159, 160, 174, 181, 192)

Hristov, J. (2007). Magnetic field assisted fluidizationâĂŤdimensional analysis addressing the physical basis. *China Particuology*, **5**(1): pp. 103–110. (p. 36)

Huber, N. and Sommerfeld, M. (1998). Modelling and numerical calculation of dilute-phase pneumatic conveying in pipe systems. *Powder Technology*, **99**(1): pp. 90–101. (p. 27)

Igci, Y. and Sundaresan, S. (2011). Constitutive models for filtered two-fluid models of fluidized gas–particle flows. *Industrial & Engineering Chemistry Research*, **50**(23): pp. 13190–13201. (p. 39, 134)

Ishii, M. (1975). Thermo-fluid dynamic theory of two-phase flow. *NASA STI/Recon Technical Report A*, **75**: p. 29657. (p. 25)

Israelachvili, J.N. (2011). *Intermolecular and surface forces: revised third edition*. Academic press. (p. 35, 122, 123)

Jackson, R. (1963). The mechanics of fluidized beds. i. the stability of the state of uniform fluidization. *Trans. Inst. Chem. Eng*, **41**: pp. 13–21. (p. 14, 36, 37, 38, 174)

Jackson, R. (1997). Locally averaged equations of motion for a mixture of identical spherical particles and a Newtonian fluid. *Chemical Engineering Science*, **52**(15): pp. 2457–2469. (p. 42)

Jackson, R. (2000). *The dynamics of fluidized particles*. Cambridge University Press. (p. 141, 182)

Jaeger, H.M., Nagel, S.R., and Behringer, R.P. (1996). Granular solids, liquids, and gases. *Reviews of Modern Physics*, **68**(4): p. 1259. (p. 1)

Jaeger, H.M., Nagel, S.R., and Behringer, R.P. (2008). The physics of granular materials. *Physics Today*, **49**(4): pp. 32–38. (p. 1)

Jing, L. and Stephansson, O. (2007). Fundamentals of discrete element methods for rock engineering-theory and applications. (p. 27)

Johnson, K., Kendall, K., and Roberts, A. (1971). Surface energy and the contact of elastic solids. *Proceedings of the royal society of London. A. mathematical and physical sciences*, **324**(1558): pp. 301–313. (p. 46)

Jonke, A., Levitz, N., Litty, A., and Lawroski, S. (1958). Fluidization techniques in producing refined uranium from ore concentrates. *Industrial & Engineering Chemistry*, **50**(12): pp. 1739–1743. (p. 2)

Jop, P., Forterre, Y., and Pouliquen, O. (2006). A constitutive law for dense granular flows. *Nature*, **441**(7094): pp. 727–730. (p. 26)

Kafui, K.D., Thornton, C., and Adams, M.J. (2002). Discrete particle-continuum fluid modelling of gas–solid fluidised beds. *Chemical Engineering Science*, **57**(13): pp. 2395–2410. (p. 7, 29, 122)

Kage, H., Agari, M., Ogura, H., and Matsuno, Y. (2000). Frequency analysis of pressure fluctuation in fluidized bed plenum and its confidence limit for detection of various modes of fluidization. *Advanced Powder Technology*, **11**(4): pp. 459–475. (p. 86)

Kamrin, K. and Bazant, M.Z. (2007). Stochastic flow rule for granular materials. *Physical Review E*, **75**(4): p. 041301. (p. 26)

Kenning, V.M. and Crowe, C.T. (1997). On the effect of particles on carrier phase turbulence in gas-particle flows. *International journal of multiphase flow*, **23**(2): pp. 403–408. (p. 33)

Kinloch, A.J. (1987). *Adhesion and adhesives: science and technology*. Springer. (p. 34)

Kobayashi, T., Kawaguchi, T., Tanaka, T., and Tsuji, Y. (2002). Dem analysis on flow pattern of geldart's group a particles in fluidized bed. In: *Proceedings of the World Congress on Particle Technology*, volume 4, pp. 21–25. (p. 29, 130)

Kobayashi, T., Tanaka, T., Shimada, N., and Kawaguchi, T. (2013). Dem–cfd analysis of fluidization behavior of geldart group a particles using a dynamic adhesion force model. *Powder Technology*, **248**: pp. 143–152. (p. 40, 121)

Koch, D.L. and Hill, R.J. (2001). Inertial effects in suspension and porous-media flows. *Annual Review of Fluid Mechanics*, **33**(1): pp. 619–647. (p. 101)

Koch, D.L. and Sangani, A.S. (1999). Particle pressure and marginal stability limits for a homogeneous monodiperse gas-fluidized bed: Kinetic theory and numerical simulations. *Journal of Fluid Mechanics*, **400**(1): pp. 229–263. (p. 182)

Kono, H.O., Narasimhan, S., Richman, L.M., and Ohtake, T. (2002). Flow properties of homogeneously aerated, expanded emulsion phase of fine powders (quasi-solid emulsion phase viscosity). *Powder technology*, **122**(2): pp. 168–176. (p. 128)

Krupp, H. (1967). *Particle adhesion, theory and experiment*. Advan. Colloid Interface Sci. 1 (1967), 111-239. (p. 17)

Kunii, D. and Levenspiel, O. (1969). Fluidization engineering. (p. xix, 2, 3, 5)

Laverman, J.A., Roghair, I., Annaland, M.v.S., and Kuipers, H. (2008). Investigation into the hydrodynamics of gas-solid fluidized beds using particle image velocimetry coupled with digital image analysis. *The Canadian Journal of Chemical Engineering*, **86**(3): pp. 523–535. (p. 6, 79)

Lettieri, P., Newton, D., and Yates, J. (2002). Homogeneous bed expansion of fcc catalysts, influence of temperature on the parameters of the richardson–zaki equation. *Powder Technology*, **123**(2): pp. 221–231. (p. 127, 149)

Li, T., Dietiker, J.F., and Shahnam, M. (2012*a*). Mfix simulation of netl/psri challenge problem of circulating fluidized bed. *Chemical Engineering Science*, **84**: pp. 746–760. (p. 32)

Li, T., Garg, R., Galvin, J., and Pannala, S. (2012*b*). Open-source mfix-dem software for gas-solids flows: Part iiâĂŤvalidation studies. *Powder Technology*, **220**: pp. 138–150. (p. 7, 32, 61, 63, 81, 82, 92, 99, 101, 103, 108, 112)

Li, X., Grace, J., Lim, C., Watkinson, A., Chen, H., and Kim, J. (2004). Biomass gasification in a circulating fluidized bed. *Biomass and bioenergy*, **26**(2): pp. 171–193. (p. 2)

Lighthill, M.J. and Whitham, G.B. (1955). On kinematic waves. ii. a theory of traffic flow on long crowded roads. *Proceedings of the Royal Society of London. Series A. Mathematical and Physical Sciences*, **229**(1178): pp. 317–345. (p. 177)

Link, J., Cuypers, L., Deen, N., and Kuipers, J. (2005). Flow regimes in a spout–fluid bed: A combined experimental and simulation study. *Chemical Engineering Science*, **60**(13): pp. 3425–3442. (p. 99)

Link, J.M., Deen, N.G., Kuipers, J.A.M., Fan, X., Ingram, A., Parker, D.J., Wood, J., and Seville, J.P.K. (2008). PEPT and discrete particle simulation study of spout-fluid bed regimes. *AIChE Journal*, **54**(5): pp. 1189–1202. (p. 6, 8, 79, 99, 100, 101, 102, 103, 115, 116, 202)

Liu, D., Kwauk, M., and Li, H. (1996). Aggregative and particulate fluidizationâĂŤthe two extremes of a continuous spectrum. *Chemical Engineering Science*, **51**(17): pp. 4045–4063. (p. 20)

Liu, S., Chen, Q., Wang, H., Jiang, F., Ismail, I., and Yang, W. (2005). Electrical capacitance tomography for gas–solids flow measurement for circulating fluidized beds. *Flow Measurement and Instrumentation*, **16**(2): pp. 135–144. (p. 80)

Loezos, P.N., Costamagna, P., and Sundaresan, S. (2002). The role of contact stresses and wall friction on uidization. *Chemical Engineering Science*, **57**(24): pp. 5123–5141. (p. 37, 38, 72, 141, 142)

Luding, S. (2004). Molecular dynamics simulations of granular materials. *The physics of granular media*: pp. 297–324. (p. 27)

Luding, S. (2008). Cohesive, frictional powders: contact models for tension. *Granular matter*, **10**(4): pp. 235–246. (p. 46)

Majmudar, T.S. and Behringer, R.P. (2005). Contact force measurements and stress-induced anisotropy in granular materials. *Nature*, **435**(7045): pp. 1079–1082. (p. 152)

Matsuda, S., Hatano, H., and Tsutsumi, A. (2001). Ultrafine particle fluidization and its application to photocatalytic no< sub> x</sub> treatment. *Chemical Engineering Journal*, **82**(1): pp. 183–188. (p. 2)

Mazzei, L. (2008). *Eulerian modelling and computational fluid dynamics simulation of mono and polydisperse fluidized suspension*. Ph.D. thesis, UCL (University College London). (p. 128, 181)

Mazzei, L. and Lettieri, P. (2008). Cfd simulations of expanding/contracting homogeneous fluidized beds and their transition to bubbling. *Chemical Engineering Science*, **63**(24): pp. 5831–5847. (p. 9, 38, 39, 127, 128)

Mckeen, T. and Pugsley, T. (2003). Simulation and experimental validation of a freely bubbling bed of fcc catalyst. *Powder Technology*, **129**(1): pp. 139–152. (p. 127)

Menon, N. and Durian, D.J. (1997*a*). Diffusing-wave spectroscopy of dynamics in a three-dimensional granular flow. *Science*, **275**(5308): pp. 1920–1922. (p. 6, 80)

Menon, N. and Durian, D.J. (1997*b*). Particle motions in a gas-fluidized bed of sand. *Physical review letters*, **79**(18): pp. 3407–3410. (p. 38, 80, 160)

Mercado, J.M., Prakash, V.N., Tagawa, Y., Sun, C., Lohse, D., *et al.* (2012). Lagrangian statistics of light particles in turbulence. *Physics of Fluids (1994-present)*, **24**(5): p. 055106. (p. 166)

Mikami, T., Kamiya, H., and Horio, M. (1998). Numerical simulation of cohesive powder behavior in a fluidized bed. *Chemical Engineering Science*, **53**(10): pp. 1927–1940. (p. 29)

Millán, J.M.V. (2012). *Fluidization of fine powders: cohesive versus dynamical aggregation*. Springer. (p. 174, 179, 181, 190)

Mishra, B. and Rajamani, R.K. (1992). The discrete element method for the simulation of ball mills. *Applied Mathematical Modelling*, **16**(11): pp. 598–604. (p. 27)

Molerus, O. (1982). Interpretation of geldart's type a, b, c and d powders by taking into account interparticle cohesion forces. *Powder technology*, **33**(1): pp. 81–87. (p. 16, 17, 128)

Mueth, D.M., Jaeger, H.M., and Nagel, S.R. (1998). Force distribution in a granular medium. *Physical Review E*, **57**(3): p. 3164. (p. 160, 161)

Müller, C.R., Holland, D.J., Sederman, A.J., Scott, S.A., Dennis, J.S., and Gladden, L.F. (2008). Granular temperature: comparison of magnetic resonance measurements with discrete element model simulations. *Powder Technology*, **184**(2): pp. 241–253. (p. 8, 79, 81, 82, 84, 201)

Müller, C.R., Scott, S.A., Holland, D.J., Clarke, B.C., Sederman, A.J., Dennis, J.S., and Gladden, L.F. (2009). Validation of a discrete element model using magnetic resonance measurements. *Particuology*, **7**(4): pp. 297–306. (p. 8, 81, 82, 85, 94, 97, 115, 201)

Mutsers, S. and Rietema, K. (1977). The effect of interparticle forces on the expansion of a homogeneous gas-fluidized bed. *Powder Technology*, **18**(2): pp. 239–248. (p. 38, 149)

Nilsen, C., Andersson, H.I., and Zhao, L. (2013). A voronoï analysis of preferential concentration in a vertical channel flow. *Physics of Fluids (1994-present)*, **25**(11): p. 115108. (p. 166)

Nwose, E.N., Pei, C., and Wu, C.Y. (2012). Modelling die filling with charged particles using dem/cfd. *Particuology*, **10**(2): pp. 229–235. (p. 27)

Oberkampf, W.L. and Blottner, F.G. (1998). Issues in computational fluid dynamics code verification and validation. *AIAA journal*, **36**(5): pp. 687–695. (p. 7, 30, 78)

Oberkampf, W.L. and Trucano, T.G. (2002). Verification and validation in computational fluid dynamics. *Progress in Aerospace Sciences*, **38**(3): pp. 209–272. (p. 30, 63, 77)

Okabe, A., Boots, B., Sugihara, K., and Chiu, S.N. (2009). *Spatial tessellations: concepts and applications of Voronoi diagrams*, volume 501. John Wiley & Sons. (p. 154)

Oltrogge, R.D. (1972). *Gas fluidized beds of fine particles*. Ph.D. thesis, University of Michigan. (p. 19, 20)

Ooi, J.Y. (2013). Establishing predictive capabilities of dem–verification and validation for complex granular processes. In: *POWDERS AND GRAINS 2013: Proceedings of the 7th International Conference on Micromechanics of Granular Media*, AIP Publishing, pp. 20–24. (p. 31, 63)

Owoyemi, O. and Lettieri, P. (2008). Stability analysis and cfd validation of a new fluid–particle interaction force for mono-component gas–solid fluidized beds. *Powder Technology*, **183**(1): pp. 27–36. (p. 177, 179, 181)

Pain, C., Mansoorzadeh, S., and De Oliveira, C. (2001). A study of bubbling and slugging fluidised beds using the two-fluid granular temperature model. *International Journal of Multiphase Flow*, **27**(3): pp. 527–551. (p. 6)

Pandit, J.K., Wang, X., and Rhodes, M. (2005). Study of Geldart's Group A behaviour using the discrete element method simulation. *Powder Technology*, **160**(1): pp. 7–14, doi:10.1016/j.powtec.2005.04.044. (p. 39)

Pandit, J.K., Wang, X., and Rhodes, M. (2006). On geldart group a behaviour in fluidized beds with and without cohesive interparticle forces: A dem study. *Powder technology*, **164**(3): pp. 130–138. (p. 39, 121)

Paola, C. and Voller, V. (2005). A generalized exner equation for sediment mass balance. *Journal of Geophysical Research: Earth Surface (2003–2012)*, **110**(F4). (p. 63)

Peters, J., Muthuswamy, M., Wibowo, J., and Tordesillas, A. (2005). Characterization of force chains in granular material. *Physical review E*, **72**(4): p. 041307. (p. 160)

Pigford, R.L. and Baron, T. (1965). Hydrodynamic stability of a fluidized bed. *Industrial & Engineering Chemistry Fundamentals*, **4**(1): pp. 81–87. (p. 14, 37, 174)

Plimpton, S. (1995). Fast parallel algorithms for short-range molecular dynamics. *Journal of Computational Physics*, **117**(1): pp. 1–19. (p. 41, 154)

Plimpton, S. (2005). Lammps userâĂŹs manual. *Sandia National Laboratory*. (p. 44, 46)

Radjai, F., Roux, S., and Moreau, J.J. (1999). Contact forces in a granular packing. *Chaos: An Interdisciplinary Journal of Nonlinear Science*, **9**(3): pp. 544–550. (p. 161)

Rhodes, M., Wang, X., and Nguyen, M. (2001*a*). Use of discrete element method simulation in studying fluidization characteristics : infuence of interparticle force. *Chemical Engineering . . .*, **56**: pp. 69–76. (p. 29, 39, 124, 130)

Rhodes, M., Wang, X.S., Nguyen, M., Stewart, P., and Liffman, K. (2001*b*). Onset of cohesive behaviour in gas fluidized beds: a numerical study using dem simulation. *Chemical Engineering Science*, **56**(14): pp. 4433–4438. (p. 39)

Rhodes, M.J., Wang, X.S., Nguyen, M., Stewart, P., and Li, K. (2001*c*). Onset of cohesive behaviour in gas fluidized beds: a numerical study using DEM simulation. *Chemical Engineering Science*, **56**(14): pp. 4433–4438. (p. 128)

Richardson, J. and Zaki, W. (1954). The sedimentation of a suspension of uniform spheres under conditions of viscous flow. *Chemical Engineering Science*, **3**(2): pp. 65–73. (p. 48, 49, 139, 140, 176, 195)

Rietema, K. (1973). The effect of interparticle forces on the expansion of a homogeneous gas-fluidised bed. *Chemical Engineering Science*, **28**(7): pp. 1493–1497. (p. 37, 38, 174, 189)

Rietema, K. and Piepers, H. (1990). The effect of interparticle forces on the stability of gas-fluidized bedsâĂŤi. experimental evidence. *Chemical Engineering Science*, **45**(6): pp. 1627–1639. (p. 35, 38, 174, 189)

Robinson, M., Ramaioli, M., and Luding, S. (2014). Fluid–particle flow simulations using two-way-coupled mesoscale sph–dem and validation. *International journal of multiphase flow*, **59**: pp. 121–134. (p. 64, 70)

Rowe, P. (1987). A convenient empirical equation for estimation of the richardson-zaki exponent. *Chemical Engineering Science*, **42**(11): pp. 2795–2796. (p. 140)

Rumpf, H. (1990). *Mechanische Verfahrenstechnik*. Taylor & Francis. (p. 35)

Rusche, H. (2003). *Computational fluid dynamics of dispersed two-phase flows at high phase fractions*. Ph.D. thesis, Imperial College London (University of London). (p. 41)

Sanad, A., Ooi, J., Holst, J., and Rotter, J. (2001). Computations of granular flow and pressures in a flat-bottomed silo. *Journal of engineering mechanics*, **127**(10): pp. 1033–1043. (p. 31)

Savage, S. (1998). Analyses of slow high-concentration flows of granular materials. *Journal of Fluid Mechanics*, **377**: pp. 1–26. (p. 26)

Schuck, P. (2000). Size-distribution analysis of macromolecules by sedimentation velocity ultracentrifugation and lamm equation modeling. *Biophysical journal*, **78**(3): pp. 1606–1619. (p. 64)

Schwer, L. (2006). An overview of the asme guide for verification and validation in computational solid mechanics. *LS-DYNA Anwenderforum*. (p. 63)

Schwer, L. *et al.* (2006). Guide for verification and validation in computational solid mechanics. *American Society of Mechanical Engineers, ASME V&V*: pp. 10–2006. (p. 7, 31)

Schwer, L.E. (2007). An overview of the ptc 60/v&v 10: guide for verification and validation in computational solid mechanics. *Engineering with Computers*, **23**(4): pp. 245–252. (p. 31)

Sederman, A., Alexander, P., and Gladden, L. (2001). Structure of packed beds probed by magnetic resonance imaging. *Powder Technology*, **117**(3): pp. 255–269. (p. 93)

Seville, J. and Clift, R. (1984). The effect of thin liquid layers on fluidisation characteristics. *Powder Technology*, **37**(1): pp. 117–129. (p. 16)

Seville, J., Willett, C., and Knight, P. (2000). Interparticle forces in fluidisation: a review. *Powder Technology*, **113**(3): pp. 261–268. (p. vii, 129, 204)

Shäfer, J., Dippel, S., and Wolf, D. (1996). Force schemes in simulations of granular materials. *Journal de physique I*, **6**(1): pp. 5–20. (p. 27)

Silbert, L.E., Grest, G.S., and Landry, J.W. (2002). Statistics of the contact network in frictional and frictionless granular packings. *Physical Review E*, **66**(6): p. 061303. (p. 151, 161, 163, 164)

Simone, S. and Harriott, P. (1980). Fluidization of fine powders with air in the particulate and the bubbling regions. *Powder Technology*, **26**(2): pp. 161–167. (p. 127, 128)

Simpson, H. and Rodger, B. (1961). The fluidization of light solids by gases under pressure and heavy solids by water: a study of the transition between aggregative and particulate fluidization. *Chemical Engineering Science*, **16**(3): pp. 153–180. (p. 14)

Socolar, J., Schaeffer, D.G., and Claudin, P. (2002). Directed force chain networks and stress response in static granular materials. *The European Physical Journal E: Soft Matter and Biological Physics*, **7**(4): pp. 353–370. (p. 163)

Sommerfeld, M. and Kussin, J. (2003). Analysis of collision effects for turbulent gas-particle flow in a horizontal channel. Part II. Integral properties and validation. *International journal of multiphase flow*, **29**(4): pp. 701–718. (p. 53)

Srivastava, A. and Sundaresan, S. (2002). Role of wall friction in fluidization and standpipe flow. *Powder technology*, **124**(1): pp. 45–54. (p. 141)

Steinhauser, M.O. (2008). *Computational Multiscale Modeling of Fluids and Solids*, volume 60. Springer. (p. 21)

Stokes, G.G. (1851). *On the effect of the internal friction of fluids on the motion of pendulums*, volume 9. Pitt Press. (p. 33)

Sturm, M., Wirtz, S., Scherer, V., and Denecke, J. (2010). Coupled dem-cfd simulation of pneumatically conveyed granular media. *Chemical Engineering & Technology*, **33**(7): pp. 1184–1192. (p. 27)

Sun, J. and Battaglia, F. (2006). Hydrodynamic modeling of particle rotation for segregation in bubbling gas-fluidized beds. *Chemical Engineering Science*, **61**(5): pp. 1470–1479. (p. 111)

Sun, J. and Sundaresan, S. (2011). A constitutive model with microstructure evolution for flow of rate-independent granular materials. *Journal of Fluid Mechanics*, **682**(1): pp. 590–616. (p. 150)

Sundaresan, S. (2003). Instabilities in fluidized beds. *Annual review of fluid mechanics*, **35**(1): pp. 63–88. (p. 8, 38, 81, 144, 180, 181, 189)

Sutkar, V.S., Deen, N.G., and Kuipers, J. (2013). Spout fluidized beds: Recent advances in experimental and numerical studies. *Chemical Engineering Science*, **86**: pp. 124–136. (p. 98)

Syamlal, M. and O'Brien, T.J. (1987). A generalized drag correlation for multiparticle systems. *Unpublished report*. (p. xxiii, 30, 49, 70, 86, 101, 104, 109, 113, 114, 126, 135, 136)

Tagawa, Y., Mercado, J.M., Prakash, V.N., Calzavarini, E., Sun, C., and Lohse, D. (2012). Three-dimensional lagrangian voronoï analysis for clustering of particles and bubbles in turbulence. *Journal of Fluid Mechanics*, **693**: pp. 201–215. (p. 151, 154, 166, 167)

Ten Cate, A., Nieuwstad, C., Derksen, J., and Van den Akker, H. (2002). Particle imaging velocimetry experiments and lattice-boltzmann simulations on a single sphere settling under gravity. *Physics of Fluids (1994-present)*, **14**(11): pp. 4012–4025. (p. 64)

Thakur, S.C., Morrissey, J.P., Sun, J., Chen, J., and Ooi, J.Y. (2014). Micromechanical analysis of cohesive granular materials using the discrete element method with an adhesive elasto-plastic contact model. *Granular Matter*, **16**(3): pp. 383–400. (p. 46)

Thornton, C. (1997). Coefficient of restitution for collinear collisions of elastic-perfectly plastic spheres. *Journal of Applied Mechanics*, **64**(2): pp. 383–386. (p. 46)

Thornton, C. and Ning, Z. (1998). A theoretical model for the stick/bounce behaviour of adhesive, elastic-plastic spheres. *Powder technology*, **99**(2): pp. 154–162. (p. 40, 46, 151)

Tsuji, T., Narita, E., and Tanaka, T. (2013). Effect of a wall on flow with dense particles. *Advanced Powder Technology*, **24**(2): pp. 565–574. (p. 90)

Tsuji, Y., Kawaguchi, T., and Tanaka, T. (1993). Discrete particle simulation of two-dimensional fluidized bed. *Powder technology*, **77**(1): pp. 79–87. (p. 7, 28, 29)

Tsuji, Y., Tanaka, T., and Ishida, T. (1992). Lagrangian numerical simulation of plug flow of cohesionless particles in a horizontal pipe. *Powder technology*, **71**(3): pp. 239–250. (p. 46)

Valverde, J., Castellanos, a., Mills, P., and Quintanilla, M. (2003). Effect of particle size and interparticle force on the fluidization behavior of gas-fluidized beds. *Physical Review E*, **67**(5): p. 016303, doi:10.1103/PhysRevE.67.051305. (p. 128, 140)

Valverde, J.M. (2013). Fluidization of fine powders: Cohesive versus dynamic aggregation. (p. vii, xxvi, 150, 181, 182, 183, 184, 191, 194, 195, 196, 197, 207, 208)

Valverde, J.M. and Castellanos, A. (2006). Fluidization of nanoparticles: A modified Richardson-Zaki Law. *AIChE journal*, **52**(2): pp. 838–842. (p. 175, 182, 195)

Valverde, J.M. and Castellanos, A. (2007*a*). Fluidization, bubbling and jamming of nanoparticle agglomerates. *Chemical Engineering Science*, **62**(23): pp. 6947–6956. (p. 8)

Valverde, J.M. and Castellanos, A. (2007*b*). Types of gas fluidization of cohesive granular materials. *Physical Review E*, **75**(3): p. 031306, doi:10.1103/PhysRevE.75.031306. (p. 16, 140, 179, 180)

Valverde, J.M. and Castellanos, A. (2008). Fluidization of nanoparticles: a simple equation for estimating the size of agglomerates. *Chemical Engineering Journal*, **140**(1): pp. 296–304. (p. 16)

van der Hoef, M., Ye, M., van Sint Annaland, M., Andrews, A., Sundaresan, S., and Kuipers, J. (2006). Multiscale modeling of gas-fluidized beds. *Advances in Chemical Engineering*, **31**: pp. 65–149. (p. xix, xxvii, 24, 28, 30)

van der Hoef, M.A., Beetstra, R., and Kuipers, J.A.M. (2005). Lattice-Boltzmann simulations of low-Reynolds-number flow past mono-and bidisperse arrays of spheres: results for the permeability and drag force. *J. Fluid Mech*, **528**: pp. 233–254. (p. 30, 33, 49)

van der Hoef, M.A., van Sint Annaland, M., Deen, N.G., and Kuipers, J.A.M. (2008). Numerical simulation of dense gas-solid fluidized beds: A multiscale modeling strategy. *Annu. Rev. Fluid Mech.*, **40**: pp. 47–70. (p. xix, 6, 22, 23, 24, 26)

van Ommen, J.R., Valverde, J.M., and Pfeffer, R. (2012). Fluidization of nanopowders: a review. *Journal of nanoparticle research*, **14**(3): pp. 1–29. (p. 16, 150, 158, 179, 182)

van Sint Annaland, M., Bokkers, G., Goldschmidt, M., Olaofe, O., Van Der Hoef, M., and Kuipers, J. (2009). Development of a multi-fluid model for poly-disperse dense gas–solid fluidised beds, part ii: Segregation in binary particle mixtures. *Chemical Engineering Science*, **64**(20): pp. 4237–4246. (p. 112)

Verloop, J. and Heertjes, P. (1970). Shock waves as a criterion for the transition from homogeneous to heterogeneous fluidization. *Chemical Engineering Science*, **25**(5): pp. 825–832. (p. 19, 37, 174, 192)

Wallis, G.B. (1969). One-dimensional two-phase flow. (p. 174, 177, 182, 192, 196, 207)

Walton, O.R. and Braun, R.L. (1986). Viscosity, granular-temperature, and stress calculations for shearing assemblies of inelastic, frictional disks. *Journal of Rheology (1978-present)*, **30**(5): pp. 949–980. (p. 46)

Wang, J. (2009). A review of eulerian simulation of geldart a particles in gas-fluidized beds. *Industrial & Engineering Chemistry Research*, **48**(12): pp. 5567–5577. (p. 120)

Wang, J., Tan, L., van der Hoef, M., van Sint Annaland, M., and Kuipers, J. (2011*a*). From bubbling to turbulent fluidization: Advanced onset of regime transition in micro-fluidized beds. *Chemical Engineering Science*, **66**(9): pp. 2001–2007, doi:10.1016/j.ces.2011.02.003. (p. 127, 128, 194)

Wang, J., Van der Hoef, M., and Kuipers, J. (2009). Why the two-fluid model fails to predict the bed expansion characteristics of geldart a particles in gas-fluidized beds: a tentative answer. *Chemical Engineering Science*, **64**(3): pp. 622–625. (p. 39, 120, 131)

Wang, J., Van der Hoef, M., and Kuipers, J. (2011*b*). The role of scale resolution versus inter-particle cohesive forces in two-fluid modeling of bubbling fluidization of geldart a particles. *Chemical Engineering Science*, **66**(18): pp. 4229–4240. (p. 25, 39, 131, 133, 135)

Wang, J., van der Hoef, M., and Kuipers, J. (2013). Particle granular temperature of geldart a, a/b and b particles in dense gas-fluidized beds. *Chemical Engineering Science*, **97**: pp. 264–271. (p. xxii, 128, 129, 132)

Warsito, W. and Fan, L.S. (2001). Measurement of real-time flow structures in gas–liquid and gas–liquid–solid flow systems using electrical capacitance tomography (ECT). *Chemical Engineering Science*, **56**(21): pp. 6455–6462. (p. 6)

Wee Chuan Lim, E., Wang, C.H., and Yu, A.B. (2006). Discrete element simulation for pneumatic conveying of granular material. *AIChE journal*, **52**(2): pp. 496–509. (p. 27)

Wen, C.Y. and Yu, Y.H. (1966). A generalized method for predicting the minimum fluidization velocity. *AIChE Journal*, **12**(3): pp. 610–612. (p. 48, 135)

Wilhelm, R.H. and Kwauk, M. (1948). Fluidization of solid particles. *Chemical Engineering Progress*, **44**(3): pp. 201–218. (p. 13, 173)

Wu, C.Y. (2012). *Discrete Element Modelling of Particulate Media*, volume 339. Royal Society of Chemistry. (p. 27)

Wu, C.Y. and Guo, Y. (2012). Numerical modelling of suction filling using dem/cfd. *Chemical Engineering Science*, **73**: pp. 231–238. (p. 27)

Xiao, H. and Sun, J. (2011). Algorithms in a Robust Hybrid CFD-DEM Solver for Particle-Laden Flows. *Communications in Computational Physics*, **9**(2): p. 297. (p. 41, 42, 47, 53, 134)

Xie, H.Y. and Geldart, D. (1995). Fluidization of fcc powders in the bubble-free regime: effect of types of gases and temperature. *Powder technology*, **82**(3): pp. 269–277. (p. 127)

Xiong, Q., Zhou, G., Li, B., Xua, J., Fang, X., Wang, J., He, X., Wang, X., Wang, L., Ge, W., *et al.* (2010). Large-scale dns of gas-solid flow on mole-8.5. *arXiv preprint arXiv:1011.2613*. (p. 6)

Xu, B.H. and Yu, A.B. (1997). Numerical simulation of the gas-solid flow in a fluidized bed by combining discrete particle method with computational fluid dynamics. *Chemical Engineering Science*, **52**(16): pp. 2785–2809. (p. 7, 28, 29, 30)

Yang, F., Thornton, C., and Seville, J. (2013). Effect of surface energy on the transition from fixed to bubbling gas-fluidised beds. *Chemical Engineering Science*, **90**: pp. 119–129. (p. 9, 39, 40, 131, 150, 192, 196)

Yang, N., Wang, W., Ge, W., and Li, J. (2003). Cfd simulation of concurrent-up gas–solid flow in circulating fluidized beds with structure-dependent drag coefficient. *Chemical Engineering Journal*, **96**(1): pp. 71–80. (p. 39)

Yang, N., Wang, W., Ge, W., Wang, L., and Li, J. (2004). Simulation of heterogeneous structure in a circulating fluidized-bed riser by combining the two-fluid model with the emms approach. *Industrial & engineering chemistry research*, **43**(18): pp. 5548–5561. (p. 39)

Yang, R., Zou, R., and Yu, A. (2000). Computer simulation of the packing of fine particles. *Physical Review E*, **62**(3): p. 3900. (p. 107)

Yang, W.c. (2003). *Handbook of fluidization and fluid-particle systems*. CRC Press. (p. 48)

Yang, W.C. (2007). Modification and re-interpretation of geldart's classification of powders. *Powder technology*, **171**(2): pp. 69–74. (p. xix, 16, 19, 20)

Yao, W., Guangsheng, G., Fei, W., and Jun, W. (2002). Fluidization and agglomerate structure of sio< sub> 2</sub> nanoparticles. *Powder Technology*, **124**(1): pp. 152–159. (p. 150)

Yates, J. (1983). Fundamentals of fluidized bed chemical processes. (p. xix, 15)

Ye, M., Van der Hoef, M., and Kuipers, J. (2004). A numerical study of fluidization behavior of geldart a particles using a discrete particle model. *Powder Technology*, **139**(2): pp. 129–139. (p. 39, 40, 121, 124)

Ye, M., Van der Hoef, M., and Kuipers, J. (2005). The effects of particle and gas properties on the fluidization of geldart a particles. *Chemical Engineering Science*, **60**(16): pp. 4567–4580. (p. xxii, 39, 40, 123, 127, 128, 130, 131, 137, 196)

Yin, X. and Sundaresan, S. (2008). Drag Law for Bidisperse Gas- Solid Suspensions Containing Equally Sized Spheres. *Industrial & Engineering Chemistry Research*, **48**(1): pp. 227–241. (p. 51, 70)

Yu, A. and Standish, N. (1987). Porosity calculations of multi-component mixtures of spherical particles. *Powder Technology*, **52**(3): pp. 233–241. (p. 108)

Yu, A.B. and Xu, B.H. (2003). Particle-scale modelling of gas–solid flow in fluidisation. *Journal of Chemical Technology and Biotechnology*, **78**(2-3): pp. 111–121. (p. 39, 122, 158, 159, 160)

Zhang, J. and Tang, F. (2004). Classification and determination of flow regimes in spout–fluidized beds. In: *Proceedings of the 11th International Conference on Fluidization*, volume 491. (p. 99, 101)

Zhou, Z., Yu, A., and Zulli, P. (2009). Particle scale study of heat transfer in packed and bubbling fluidized beds. *AIChE Journal*, **55**(4): pp. 868–884. (p. 152)

Zhu, H.P., Zhou, Z.Y., Yang, R.Y., and Yu, A.B. (2007). Discrete particle simulation of particulate systems: theoretical developments. *Chemical Engineering Science*, **62**(13): pp. 3378–3396. (p. 33, 39)

Zhu, H.P., Zhou, Z.Y., Yang, R.Y., and Yu, A.B. (2008). Discrete particle simulation of particulate systems: A review of major applications and findings. *Chemical Engineering Science*, **63**(23): pp. 5728–5770. (p. 27)

Zhu, Q. and Li, H. (1996). Study on magnetic fluidization of group c powders. *Powder Technology*, **86**(2): pp. 179–185. (p. 36)